Vertical decorrelation of a vortex by an external shear flow in a strongly stratified fluid

Julien Bonnici

université PARIS-SACLAY

NNT : 2018SACLX024

Thèse de doctorat

Décorrélation verticale d'un tourbillon soumis à un champ de cisaillement dans un fluide fortement stratifié

Thèse de doctorat de l'Université Paris-Saclay
préparée à l'École polytechnique

École doctorale n°579, Sciences mécaniques et énergétiques, matériaux et géosciences, SMEMAG
Spécialité de doctorat : Mécanique des fluides

Thèse présentée et soutenue à Palaiseau, le 6 avril 2018, par

Julien Bonnici

Composition du Jury :

Riwal Plougonven Professeur chargé de cours, École polytechnique (LMD)	Président
Fabien Godeferd Directeur de Recherche CNRS, École Centrale de Lyon (LMFA)	Rapporteur
Stéphane Le Dizès Directeur de Recherche CNRS, Institut de Recherche sur les Phénomènes Hors Équilibre (IRPHE)	Rapporteur
Ivan Delbende Maître de conférences, Université Pierre et Marie Curie (LIMSI)	Examinateur
Ludivine Oruba Maître de conférences, Université Pierre et Marie Curie (LATMOS)	Examinatrice
Paul Billant Directeur de Recherche CNRS, École polytechnique (LADHYX)	Directeur de thèse

Merci !

Je remercie tout d'abord mon directeur de thèse, Paul Billant, pour de très nombreuses raisons qu'il serait trop long d'énumérer ici. Je citerai néanmoins les principales : Paul, merci pour ta disponibilité sans failles et ta bienveillance en toutes circonstances, y compris dans les moments les plus délicats de cette thèse qui m'aura donné bien du fil à retordre ! Je retiens également la liberté que tu m'as laissée tout au long de la thèse, une liberté telle qu'elle m'a permis de continuer à m'épanouir dans mes passions et en particulier d'assurer la dizaine d'heures d'entraînement hebdomadaires dont j'ai tant besoin pour garder mon discernement et mon équilibre au quotidien. Enfin, comment ne pas mentionner le travail colossal abattu lors de cette étape très éprouvante qu'est la rédaction ? Si toutefois je ne devais retenir qu'une chose parmi tout ce que cette thèse a exacerbé en moi, ce serait sans aucun doute la ténacité, car c'est là ce qui a, en fin de compte, le plus d'importance, puisque cela continuera de me servir quotidiennement à l'avenir, aussi bien dans le cadre professionnel que sur un plan plus personnel. Je te remercie donc tout simplement pour m'avoir guidé patiemment et avec subtilité tout au long de cette longue mais inestimable progression.
J'en profite pour saluer le petit comité des numériciens, à savoir Ernesto, Eunok, Gaétan, Guillaume, Jérémy, Léopold, Lutz, Mathieu B., Océane, et Tristan. Je dois cependant des remerciements spéciaux à Léopold, Océane et Tristan, pour toutes les choses que nous avons partagées ces dernières années, mais aussi pour votre gentillesse, votre intelligence, et votre discernement. Merci également à Adrien Saint-S., Camille, Caroline C., Caroline F., Emmanuel de L., Jean-Philippe et Vincent pour votre sympathie.
Merci par ailleurs aux secrétaires, Delphine, Magali, Sandrine et Thérèse, pour faciliter toutes nos démarches administratives avec le sourire, ainsi qu'à Daniel et Toai pour vous assurer que les problèmes d'ordre numérique trouvent des solutions rapides et efficaces.
Je me dois bien évidemment de remercier les membres de mon jury de thèse, et notamment mes deux rapporteurs, pour avoir accepté d'évaluer mes travaux, en particulier au vu des efforts et de l'attention que les modélisations théoriques du quatrième chapitre requièrent, mais aussi pour la curiosité et l'intérêt que vous avez tous témoigné à l'égard de mes travaux.

Ma thèse, bien qu'académique, ne s'est toutefois pas bornée au laboratoire puisque j'ai également eu la chance d'effectuer une activité complémentaire en entreprise en parallèle de celle-ci. Parmi toutes les personnes que j'ai pu côtoyer dans ce cadre-là, j'adresse des remerciements tout particuliers à Antoine, Jegan, Mohamed et Zahra. Une multitude de raisons me viennent à l'esprit pour vous exprimer ma profonde gratitude.
Antoine, merci pour ton franc-parler, ton humanité et pour toutes tes histoires qui

égayaient souvent mes journées à GTT, ainsi que pour ton soutien en fin de thèse.
Jegan, merci pour tout le temps que tu m'as consacré durant mon passage à GTT, mais surtout pour ta bienveillance, ton estime, la confiance que tu m'as accordée, et tous les précieux enseignements que j'ai retirés de nos conversations !
Mohamed, merci pour ton honnêteté, ta sympathie, ta bonne humeur et ta curiosité.
Enfin, Zahra, merci pour ta gentillesse, ta finesse, ton ouverture d'esprit et toutes tes attentions à mon égard. J'espère m'en être montré digne et en particulier t'avoir aidée et soutenue comme tu le méritais au cours de ces derniers mois.

Sur un tout autre plan, je remercie chaleureusement mes amis de la section « Musculation » du club sportif de l'Ecole polytechnique : Christophe, Marie, Marwane, Paul C., et Yannick, pour avoir contribué, chacun à votre façon, à me distraire aussi bien durant nos entraînements qu'en dehors. Un grand merci à Christophe et Marie pour les (longs !) entraînements du week-end ! Christophe, je garde un souvenir particulier de ton état d'esprit authentique, et de cet inébranlable enthousiasme que l'on partage à toujours tenter de repousser nos limites sans crainte des éventuels échecs. Marie, je salue ta gentillesse et ta patience ! Marwane, merci pour tes conseils avisés lorsqu'il s'agissait de parfaire ma technique sur certains exercices ! Un merci spécial à Paul C. pour tous les entraînements en extérieur, aussi bien à Gif-sur-Yvette qu'à Massy, par grand beau temps comme sous une pluie battante, mais avec le sourire quelles qu'aient pu être les circonstances ! Je pense que les poteaux des terrains de rugby de Gif se souviennent encore de nos passages improvisés aux anneaux ! J'espère que l'on parviendra un jour tous les deux à maîtriser ce fameux Graal que constitue la « full planche », voire, soyons ambitieux (il faut l'être), la « maltese » ! Enfin, Yannick, un grand merci, tu sais pourquoi. Je mentionne tout de même que je suis désolé pour les « quelques » grognements que j'ai parfois laissé échapper au cours de mes entraînements, ainsi que pour les quelques séismes occasionnés par mes séances de soulevé de terre...

Mes derniers mots vont à mes amis de longue date, Adrien D., Cristian, Mathieu M. notamment, ainsi qu'à mes parents, et plus largement aux personnes qui m'ont soutenu de quelque manière que ce soit durant toutes ces années, et à qui j'adresse ma sincère gratitude.

Palaiseau, le 24 avril 2018.

Contents

Chapter 1

Introduction

The context of the present dissertation is that of Geophysical Fluid Dynamics (GFD). GFD is a branch of fluid mechanics that is concerned with the dynamics of atmospheric and oceanic flows such as cyclones, jets, or streams for example.

1.1 Geophysical flows

1.1.1 Structure and classification

The atmosphere and the oceans both consist of shallow layers of fluid: their thickness is small relative to their horizontal extent. For example, hurricanes generally exhibit a diameter of the order of 100 km. In the vertical direction however, they remain confined to the bottom layer of the atmosphere, i.e. the troposphere whose thickness is about 10 km. Therefore, their aspect ratio is of the order of 0.1 and is thus well below unity. As for oceans, their maximum depth is reached in the Mariana Trench, and is also 10 km approximately. Since they extend over more than hundreds of kilometers in the horizontal, it is clear that their aspect ratio is small as well.

A direct consequence is that geophysical flows are classified in terms of their horizontal length scale. Hurricanes are planetary scale flows, whereas tornadoes for instance are much more local eddies. This variety of scales is illustrated in figure 1.1, which is a satellite image of the Oyashio Current that displays multiple eddies of various diameters.

The notion of coherent structures is also quite frequently mentioned in GFD. In most cases, these coherent structures refer to vortices, because they are ubiquitous components of geophysical flows as indirectly suggested previously.

1.1.2 Central physical effects

As underlined in many books about GFD (Gill, 1982; Pedlosky, 1987; Vallis, 2006; Cushman-Roisin and Beckers, 2011), the dynamics of atmospheric and oceanic flows is constrained by two physical effects, namely the ambient stable stratification and the rotation of the Earth.

The stratification is the result of density variations along the vertical. These changes in the density arise from fluctuating temperature and pressure in the atmosphere, and from varying temperature and salinity in the oceans. In general, the density decreases upwards, resulting in a configuration where lighter layers of fluid are located above

Figure 1.1: Photograph taken from space in March, 1992, of eddies in the Oyashio Current. Sea-ice allows visualizing the flow. It is reproduced from Vallis (2006).

the heavier fluid. Thus, the stratification is usually stable. If we consider a stratified flow at rest, then the isopycnals - i.e. the lines of constant density - are rigorously horizontal. Under the effect of any disturbance, the parcels of fluid will depart from their equilibrium position by oscillating vertically around this mean position, at a typical frequency called Brunt-Väisälä frequency. These oscillations are due to the fact that the stratification acts like a spring, whose stiffness would be the equivalent of the intensity of the stratification. A strong stable stratification therefore tends to inhibit vertical motions of large amplitude.

The dynamics of geophysical flows is also affected by the Earth's rotation through the existence of a Coriolis force. How influential stratification and rotation are actually depends on the length scale of the flow. Indeed, they are both significant at the largest geophysical scales. In contrast, there exist length scales where stratification prevails over the Earth's rotation, namely the atmospheric mesoscales, comprised between 1 km and 100 km globally, and the oceanic sub-mesoscales that range from 10 m to 10 km approximately. The present dissertation deals with the stratified regime only.

1.2 Notion of turbulence

Geophysical flows exhibit a large length scale even in the purely stratified regime. Thus, their Reynolds number is very large as well. In other words, inertia effects largely dominate the viscous dissipation. Such conditions are conducive to the generation of turbulence (Lesieur, 2008), which is why we briefly discuss this concept in the following.

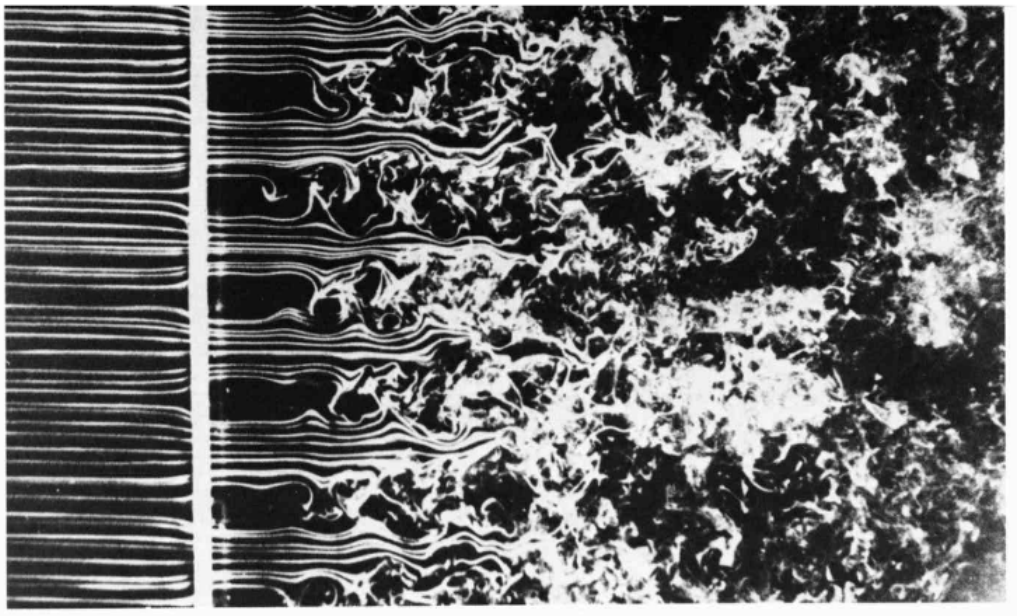

Figure 1.2: Generation of turbulence by a grid. The turbulent part of the flow, visible in the downstream region, is chaotic, disordered, without any clear trend in the motion of the fluid parcels in strong contrast with the far field laminar flow of the upstream region. Reproduced from Van Dyke (1982).

1.2.1 Global features

Turbulent motions share a variety of typical features. First, they are disordered: the motion of the fluid does not exhibit any clear trend because the fluid parcels, since they move erratically, cannot be clearly distinguished from each other. This is illustrated in figure 1.2, which shows a turbulent motion generated by a grid. In the upstream region at the left of the grid, the incident flow is uniform and laminar: the streamlines can be clearly distinguished. In contrast, in the downstream region, the streamlines are tightened. There is a first sub-region where they still can be identified, but the fact that they are closer to each other implies the existence of shear layers. Their destabilisation ultimately leads to a transition towards turbulence, after which the flow no longer exhibits any clear structure.

Then, turbulence is a chaotic phenomenon. For example, it is very sensitive to the conditions imposed at the onset of the motion. More generally, the local evolution of any turbulent flow is not deterministic and is therefore not predictable from the classical Navier-Stokes equations. For this reason, the dynamics is preferentially characterized on the basis of statistical averages.

Finally, turbulent flows are generally seen as complex flows made of a flurry of vortices of various sizes that interact with each other. This is at the origin of energy and enstrophy - the vorticity squared - transfers. The dynamics of these exchanges will be discussed in the following, because it actually depends on the nature of the turbulent motions.

1.2.2 Three- and two-dimensional turbulence

Three-dimensional isotropic homogeneous turbulence

Isotropic homogeneous turbulence is the model case of reference. It has been considered at the origin by Kolmogorov (1941), who derived a number of theoretical results regarding its spectral properties. In particular, Kolmogorov has demonstrated the famous law which states that the kinetic energy spectrum $E(k)$ varies like $k^{-5/3}$, where $k \sim 1/l$ is the wavenumber associated with the length scale l of the turbulent motion.

It is worth stressing that this spectrum is in fact very robust in the sense that it accounts for the dynamics of a wide variety of turbulent flows. Notably, stratified turbulence, which will be extensively discussed further, is characterized by this spectrum, although it is strongly anisotropic in sharp contrast with isotropic homogeneous turbulence.

In isotropic homogeneous turbulence, the energy is transferred from the largest towards the finest scales through a so-called direct energy cascade. The acting process is referred to as vortex stretching. Basically, the largest structures provide some part of their energy to smaller structures through non-linear inertial mechanisms and so on until the so-called Kolmogorov scale, where the energy is ultimately dissipated by viscosity. Indeed, this scale is defined as the scale at which the Reynolds number is of order unity. To put it another way, inertial effects are balanced by viscous effects below this threshold. Statistically, the turbulent motion is evenly distributed along the three dimensions.

Two-dimensional turbulence

Besides three-dimensional isotropic turbulence, another essential concept in turbulence is that of two-dimensional turbulence (Kraichnan, 1967, 1971; Lilly, 1969), first for its strong theoretical interest, and then because geophysical turbulence resembles bidimensional turbulence in a certain regime (Charney, 1971).

From a theoretical point of view, this kind of turbulence clearly departs from its three-dimensional counterpart in that the stretching of the vorticity is no longer possible geometrically. This is at the origin of the conservation of the vorticity and enstrophy in the inviscid limit. As a result, the energy transfers are tremendously affected, since a forward cascade (towards small scales as in three-dimensional turbulence) can no longer settle. A simple demonstration is provided by Augier (2011), which is essentially based on the fact that the enstrophy is proportional to the energy in spectral space. It therefore turns out that two-dimensional turbulence is characterized by an inverse energy cascade, namely from the smallest towards the largest scales.

1.2.3 Geophysical turbulence

Global issues

The early work by Lumley (1964) dealt with the nature of stratified turbulence. This investigation as well as others (Kraichnan, 1967, 1971; Lilly, 1969) participated in motivating a flurry of subsequent studies regarding the dynamics of turbulence in the atmosphere and the oceans.

In particular, Charney (1971) focused on the dynamics of quasi-geostrophic turbulence, which takes place in atmospheric and oceanic flows whose horizontal length

scale is large enough to ensure that the stratification as well as the Earth's rotation are strongly influential in determining the motion of the flow. In his paper, Charney underlined that quasi-geostrophic turbulence, although not rigorously bidimensional, resembles two-dimensional turbulence, hence the importance of this model case. This finding has naturally suggested that the energy cascades towards large scales in a certain range of length scales in the atmosphere and the oceans, thus asking the question of how energy can be dissipated at smaller scales. A global concern has therefore been to identify the nature and mechanisms of the energy cascades in geophysical media, i.e. to understand the physical processes that characterize purely stratified turbulence on one hand and stratified-rotating turbulence on the other hand.

Stratified turbulence

Gage (1979) argued that the atmospheric mesoscale kinetic energy spectrum results from an inverse energy cascade through two-dimensional turbulence as described by Kraichnan (1967). Lilly (1983) supported this analysis. Atmospheric mesoscales correspond to length scales that are essentially influenced by a strong stratification. It has been conjectured that stably stratified flows exhibit a two-dimensional dynamics when the stratification is strong, notably because vertical motions are then inhibited (Riley et al., 1981; Lilly, 1983; Lilly et al., 1998; Riley and Lelong, 2000). Thus, stratified turbulence is strongly anisotropic, and mainly concentrated in the horizontal direction. The latter result effectively tends to indicate that the dynamics of the energy and enstrophy transfers at atmospheric mesoscales can be properly explained on the basis of two-dimensional turbulence.

Nevertheless, considering the two-dimensional limit is valid only if vertical gradients are not too intense. For this reason, several authors have questioned the hypothesis that strongly stratified flows behave as nearly two-dimensional flows. Indeed, Herring and Métais (1989); Métais and Herring (1989); Park et al. (1994); Godeferd and Staquet (2003); Waite and Bartello (2004); Lindborg and Brethouwer (2007) report that strongly stratified turbulence is made of thin horizontal layers, hence implying the existence of strong vertical variations. This layering is clearly visible in figure 1.3, which shows vertical cross-sections of typical turbulent velocity fields in presence of a strong stratification. Billant and Chomaz (2001) clearly confirmed the idea of strong vertical variations. This result has therefore motivated additional studies in order to clarify the nature of the energy cascade that is characteristic of stratified turbulence. Notably, Lindborg (1999) and Cho and Lindborg (2001) invalidated Gage's (Gage, 1979) and Lilly's proposal (Lilly, 1983) that the mesoscale range of the atmosphere is the seat of an inverse energy cascade due to bidimensional turbulence. Indeed, by studying structure functions, Lindborg (1999) and Cho and Lindborg (2001) have demonstrated that the energy is actually transferred downscale. Evidence supporting this theory have been brought in more recent papers such as Lindborg (2006), Brethouwer et al. (2007), and Riley and Lindborg (2008). Besides, this result has been extended in the presence of a background rotation since Lindborg (2005) has shown that this energy cascade can actually prevail as long as the Rossby number, which is the ratio of inertial to Coriolis effects, is larger than ~ 0.1.

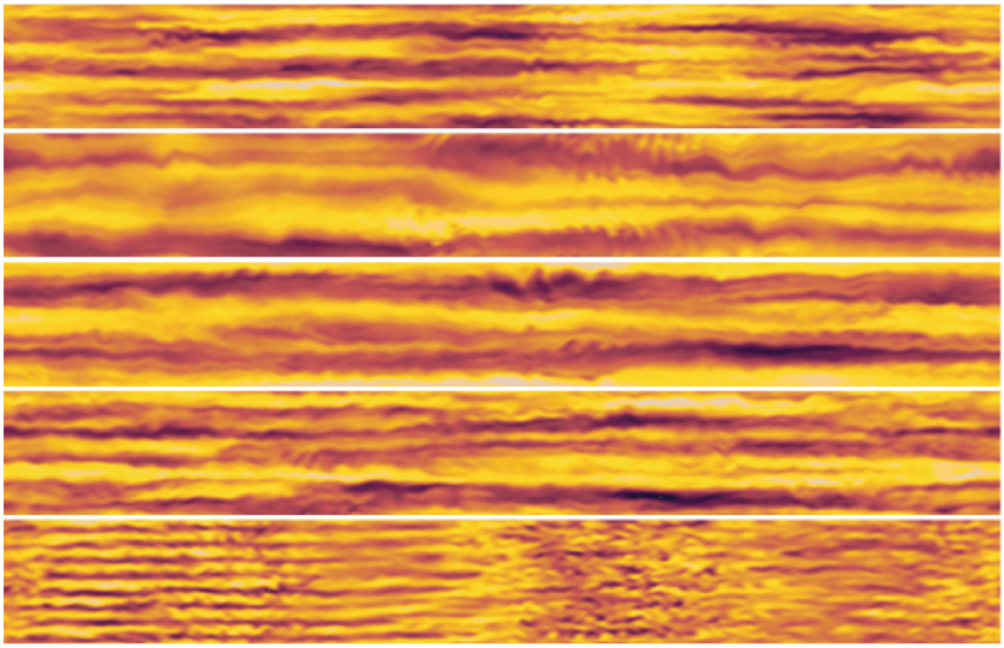

Figure 1.3: Vertical cross-sections of horizontal velocity fields taken from Direct Numerical Simulations of stratified turbulence. The snapshots are reproduced from Lindborg and Brethouwer (2007).

Stratified-rotating turbulence

Stratified-rotating turbulence is influenced by rotation besides stratification. It therefore takes place beyond the mesoscale and sub-mesoscale ranges in the atmosphere and the oceans respectively. Thus, quasi-geostrophic scales are the seat of a stratified-rotating turbulence. As already mentioned, Charney (1971) discussed the similarities between quasi-geostrophic turbulence and bidimensional turbulence, hence suggesting the existence of an inverse cascade of energy in quasi-geostrophic turbulence as in two-dimensional turbulence.

More generally, stratified-rotating turbulence is characterized by an inverse cascade of energy (Métais et al., 1996), from smaller towards larger scales. This is due to the existence of a competition between stratification and rotation, in the sense that they have antagonistic effects. Although they both tend to inhibit vertical motions, the vertical scale of the flow depends on their respective strengths: the stratification tends to diminish vertical scales whereas the rotation tends to stretch them. For example, applying a background rotation to three-dimensional turbulence generates vertical coherence (Bartello et al., 1994). More precisely, the dynamics of the energy transfers accross the different scales is complex in that downscale and upscale energy cascades coexist (Pouquet and Marino, 2013). Numerical studies of stably stratified and rotating turbulence have led to the conclusion that the amount of energy transferred downscale is dependent upon the magnitude of the rotation: a larger stratification enhances downscale transfers while a larger rate of rotation inhibits downscale transfers of energy (Vallgren et al., 2011; Deusebio et al., 2013). Deusebio et al. (2014) supported these results by showing that the rotation strengthens upscale transfers at the expense of the direct energy cascade, and that this is achieved through the suppression of the enstrophy production, i.e through the reduction of the dissipation. Interestingly, their results indicated that even in the presence of a rapid rotation, the inverse cascade of

energy may eventually vanish when the vertical scale of the flow is large enough relative to the forcing scale at which the energy is injected, hence underlining the complexity of systems influenced by a strong stratification as well as a rapid rotation.

1.3 Routes to dissipation

A global paradox

To briefly sum things up, the previous discussion has shown that:

1. Stratified rapidly rotating turbulence is the seat of an inverse cascade of energy, i.e. from smaller to larger scales. In the atmosphere and the oceans, this behaviour typically occurs at the largest scales.

2. Purely stratified turbulence is in contrast characterized by a forward cascade of energy as in three-dimensional turbulence: the energy is transferred from the largest to the smallest scales. This cascade takes place in an intermediate range of length scales in geophysical media, namely the mesoscale range in the atmosphere and the sub-mesoscale range in the oceans.

Thus, the dynamics is complex in that the energy is not directly transferred downscale throughout the whole range of geophysical scales as is the case in three-dimensional isotropic turbulence. Identifying the mechanisms responsible for the dynamical transition from a 2D-like turbulence at large scales and a more isotropic 3D-like turbulence at small enough scales actually remains a central question in the study of GFD (Molemaker et al., 2005; Müller et al., 2005; Ferrari and Wunsch, 2009).

Since quasi-geostrophic turbulence behaves like bidimensional turbulence as indicated by Charney (1971), a transfer of energy towards small scales is possible only through so-called ageostrophic, i.e. unbalanced motions. Precisely, recent numerical simulations of stratified rotating turbulence (Bartello, 2010; Vallgren et al., 2011; Deusebio et al., 2013; Pouquet and Marino, 2013) have proved that an ageostrophic cascade of energy towards small scales exists. Although this mechanism seems promising to account for the dynamical transition between the large and small scale turbulent regimes, the nature of the non-linearities that are involved in this process remains unclear.

The zigzag and Kelvin-Helmholtz instabilities

Stratified fluids are the seat of three-dimensional instabilities, which are good candidates for the generation of small scales since they typically intervene in the transition towards turbulence.

A central instability that develops in the presence of an ambient stratification is the so-called zigzag instability. To briefly explain its principle, this instability acts on a pair of vertical vortices. It bends the pair as a whole in a zigzag as illustrated in figure 1.4. It is antisymmetric with respect to the plane that separates the two vortices. An important feature is that this instability does not saturate and results in the slicing of the pair in independent pancake dipoles (Beckers et al., 2001) in the ultimate stages of its evolution.

It has been discovered experimentally by Billant and Chomaz (2000a) and then studied theoretically and numerically (Billant and Chomaz, 2000b,c) in the case of

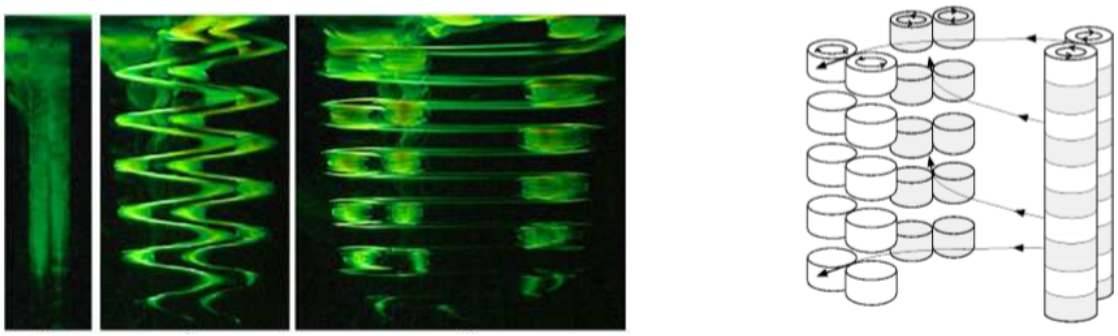

Figure 1.4: Illustration of the development of the zigzag instability in the case of a pair of counter-rotating vortices. Reproduced from the experiments presented in Billant and Chomaz (2000a).

counter-rotating vortices. These preliminary investigations have then been extended to the case of co-rotating vortices (Otheguy et al., 2006, 2007). These analyses were finally reconciled and extended to the stratified-rotating case by Billant (2010); Billant et al. (2010).

Interestingly, Deloncle et al. (2008) have shown, by means of a numerical analysis, that the zigzag instability transfers the energy from large to small dissipative scales, and as such represents a contributor of the direct energy cascade that characterizes strongly stratified turbulence. Along with the fact that it slices vortices into smaller pancake-like vortices, and as such may explain the layering which is typical of stratified turbulence, this suggests that the zigzag instability is actually an essential mechanism in stratified flows.

Another major characteristic of this instability is that it is at the origin of an intense growth of the vertical shear. In fact, this intensification can even be sufficient to trigger the Kelvin-Helmholtz (KH) instability (Thorpe, 1968; Drazin, 1970) as a secondary instability, as reported by Deloncle et al. (2008); Augier and Billant (2011); Augier et al. (2012).

The KH instability is typically generated at the interface between two flows moving with constant and opposite velocities. Depending on the conditions, the interface can be destabilized and be the seat of roll-up events referred to as KH billows. A model experiment where this instability is studied is described in Thorpe (1968). An illustration of the billows resulting from the KH instability is provided in figure 1.5. In practice, the KH instability is likely to be triggered as soon as the vertical shear of the horizontal velocity of the flow is large enough according to Miles & Howard criterion (Miles, 1961; Howard, 1961). As such, it can occur in any vertically sheared flow *a priori*.

Vertical decorrelation of a structure by an environmental shear flow

A mechanism of generation of small scales has been proposed by Lilly (1983) for strongly stratified flows. It consists in a process of vertical decorrelation of a structure by an environmental, vertically sheared flow. Under the assumptions that the horizontal velocity of the structure is purely advected by the shear flow and that no vertical velocity arises, Lilly demonstrated that the vertical shear of the horizontal velocity grows algebraically as time evolves. Hence, on the grounds of Miles & Howard criterion (Miles,

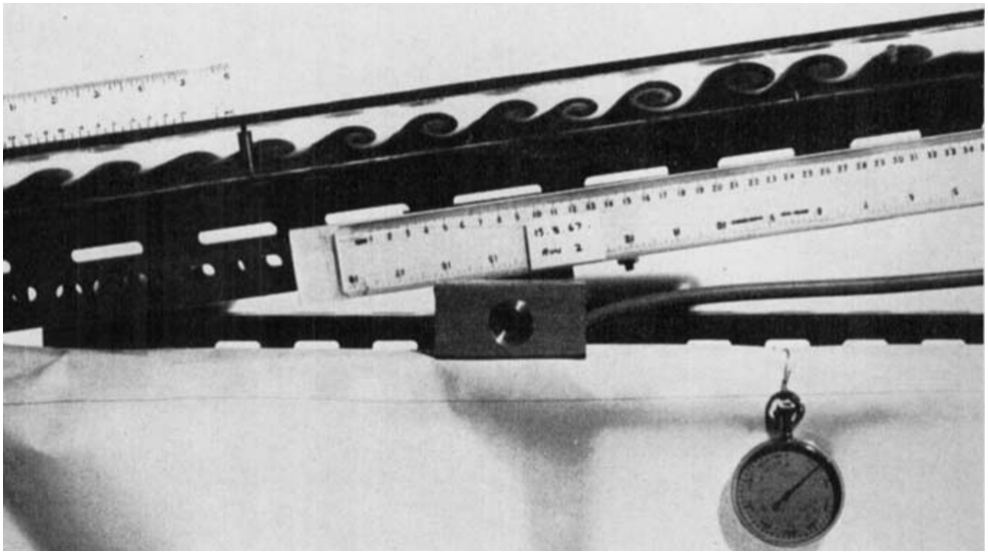

Figure 1.5: Example of experiment showing the KH instability of an interface between two fluids of equal depth and different densities in relative motion. Reproduced from Thorpe (1968).

1961; Howard, 1961), one would expect the shear instability to be triggered unconditionally after a certain time that notably depends on the intensity of the advection due to the shear flow. This analysis suggests that stratified turbulence should be rapidly turned into three-dimensional turbulence via the shear instability.

Several studies have revealed that the KH instability effectively exists in strongly stratified turbulence, as predicted by Lilly (1983). More precisely, Smyth and Moum (2000); Riley and deBruynKops (2003); Godoy-Diana et al. (2004); Brethouwer et al. (2007); Bartello and Tobias (2013) indicate that the so-called buoyancy Reynolds number is crucial for characterizing the dynamics of stratified turbulence, and especially for discriminating whether conditions are conducive to the onset of the shear instability or not. Indeed, Brethouwer et al. (2007) report the existence of KH billows in their simulations when this quantity is larger than the unit. On the contrary, they observe that the shear instability leaves place to wave-like localized disturbances as the buoyancy Reynolds number is lessened below the unit. These findings are consistent with Riley and deBruynKops (2003), who argued that the local Richardson number scales as the inverse of the buoyancy Reynolds number. Thus, if the buoyancy Reynolds number is large enough, then the local Richarsdon number can be smaller than the critical threshold 1/4 below which the KH instability is likely to develop (Miles, 1961; Howard, 1961). Note that Riley and deBruynKops (2003) also report the presence of a KH instability in their numerical simulations. Aside from these papers, numerous complementary studies have testified of the occurrence of shear instabilities in strongly stratified flows, such as Deloncle et al. (2008) and Augier and Billant (2011). In these cases, the shear instability manifested itself as a secondary instability on the zigzag instability. These advances suggest that, apart from the zigzag instability previously described, the KH instability is a central mechanism of the direct energy cascade that is characteristic of strongly stratified turbulence, as pointed out by Waite (2013). Indeed, it generates small scales by making the flow transition into three-dimensional turbulence locally.

Therefore, an open question is: does the process of vertical decorrelation imagined

by Lilly always result in the trigger of the shear instability and ultimately in the generation of small scales via this mechanism ?

1.4 Goals of the dissertation

1.4.1 Dynamics of a vortex embedded in an environmental shear flow

The dynamics of the process of vertical decorrelation considered by Lilly (1983) has been the subject of a variety of other investigations (Marshall and Parthasarathy, 1993; Jones, 1995; DeMaria, 1996; Smith et al., 2000; Vandermeirsch et al., 2002; Jones, 2004) that dealt with the case of a cyclone-like vortex subjected to an environmental shear flow. The underlying motivation of these works was to understand the different facets of the resiliency of the vortex to the external shear flow.

Although the conclusions of these papers are not directly transposable to the purely stratified case (Lilly, 1983) because a background rotation is taken into account, they have not only shown that a vertical velocity exists due to the tilting of the vortex, but that it actually represents a major component of the global dynamics (Jones, 1995; Frank and Ritchie, 1999; Jones, 2000b). Hence, the fact that Lilly (1983) ignores the vertical velocity in his analysis appears debatable.

This is not the only objection that can be raised regarding the interpretation of Lilly. Indeed, Marshall and Parthasarathy (1993) have studied the dynamics of an initially aligned vortex embedded in a current difference in a two-layer quasigeostrophic flow. Their investigation has led to the conclusion that two distinct regimes exist: when the intensity of the current is weak enough compared to the vortex strength, the vortex is simply advected while remaining coherent along the vertical. This regime has been called non-tearing regime by the authors. In contrast, when the advection by the current is strong relative to the vortex, this one is progressively torn apart into two smaller vortices. This regime is called tearing regime. Hence, discriminating whether the vortex will be torn or not by the current is possible only by examining the competition between the external advection and the strength of the vortex, which is measured by its ability to remain coherent vertically. We stress that the analysis by Marshall and Parthasarathy (1993) is valid in the presence of a rapid background rotation. However, this competition still exists in purely stratified flows. Therefore, neglecting the vertical coupling as done by Lilly (1983) may not be appropriate in general.

1.4.2 Global problem

In light of the previous discussions, an important issue is to be able to state whether the vertical decorrelation of a flow structure by an environmental shear flow is a relevant and efficient mechanism of generation of small scales via the shear instability in stratified fluids or not. To say things more simply, the problem is to test Lilly's hypothesis. Hence, the concern of the present dissertation is the investigation of the dynamics of an initially vertical vortex in a stratified shear flow. Indeed, although Lilly (1983) cleverly predicted the possibility of encountering shear instabilities in strongly stratified flows, recent findings (Jones, 1995; Riley and deBruynKops, 2003; Brethouwer et al., 2007) have demonstrated that his reasoning is insufficient to predict their occurrence in so

far as it neglects important physical effects - including the vertical velocity and the vertical coupling of the velocity field - on one hand and that, on the other hand, the development of the instability is not unconditional, which directly contradicts Lilly's predictions.

1.4.3 Outline of the thesis

In the aim of testing Lilly's conjecture for the growth of the vertical shear, we will investigate the dynamics of a Lamb-Oseen vortex in a shear flow uniform in the horizontal and sinusoidally sheared along the vertical. We will rely on the full Navier-Stokes equations under the Boussinesq approximation to perform Direct Numerical Simulations (DNS) as well as theoretical asymptotic analyses of the dynamics of the vortex.

Before explaining the concrete results of the thesis, the **chapter 2** is dedicated to the description of the numerical method. Some hints regarding the numerical simulations are also briefly given.

Then, in **chapter 3**, we investigate the volume-integrated budgets of kinetic energy and enstrophy. The goal of this study is to understand how the control parameters affect the saturation of the enstrophy. Indeed, when vertical gradients are large, the enstrophy is equivalent to the vertical shear of the horizontal velocity, which is a crucial quantity to predict the onset of the shear instability. It will be shown that the analysis of these global budgets is actually insufficient to account for the effect of the stratification on the variations of the enstrophy. This has therefore motivated local analyses.

These local analyses are carried out in **chapter 4**. The first analysis will consist in an asymptotic expansion for small times starting from the initial conditions. It will be shown that the initial response of the vortex is non-hydrostatic whatever the magnitude of the stratification. The second asymptotic analysis is conducted for long vertical wavelength following a similar approach as used by Billant (2010) to describe the unstable interaction between columnar vortices in stratified-rotating fluids. This analysis will provide the governing equations for the displacements of the vortex center and its structure evolution due to the shear flow. We shall see that the vortex is not only advected in the direction of the shear flow but also in the orthogonal direction owing to its self-induced motion. In addition, it will be demonstrated that the vertical vorticity of the vortex decreases with time owing to dynamic and viscous effects. The initial non-hydrostatic regime evidenced in the first asymptotic analysis will be related to the transient excitation of internal waves at the start-up of the motion.

These theoretical results will eventually be discussed against numerical results from the DNS in **chapter 5**. A very good agreement will be observed. Hence, on the basis of these results, an estimation of the minimum local Richardson number will be derived in terms of the control parameters in the limit of strong stratification. This will allow concluding regarding the possibility of encountering the shear instability in strongly stratified fluids via the process of vertical decorrelation suggested by Lilly (1983).

A general conclusion as well as perspectives will be given ultimately in **chapter 6**.

Chapter 2

Numerical method

The numerical program, called NS3D, that allowed us to perform direct numerical simulations (DNS) on parallel computers is presented in this chapter. Another post-processing program has been developed in order to compute a variety of quantities that derive from the fields computed by NS3D. This Data Analysis Program (DAP) works on parallel architectures as well. It is described in a second time.

2.1 Governing equations

The dynamics of any flow in a stably stratified fluid is governed by the incompressible Navier-Stokes equations under the Boussinesq approximation. In dimensional form, they read

$$\boldsymbol{\nabla} \cdot \boldsymbol{u} = 0, \tag{2.1}$$

$$\frac{\partial \boldsymbol{u}}{\partial t} = \boldsymbol{u} \times \boldsymbol{\omega} - \boldsymbol{\nabla} \left[\frac{p}{\rho_0} + \frac{\boldsymbol{u}^2}{2} \right] + b\boldsymbol{e}_z + \nu \boldsymbol{\nabla}^2 \boldsymbol{u}, \tag{2.2}$$

$$\frac{\partial b}{\partial t} + \boldsymbol{u} \cdot \boldsymbol{\nabla} b + N^2 w = \frac{\nu}{Sc} \nabla^2 b, \tag{2.3}$$

with $\boldsymbol{u} = (u, v, w)$ being the velocity field, $\boldsymbol{\omega}$ its curl, p the pressure, b the buoyancy, $\boldsymbol{e}_z$ the vertical unit vector oriented upwards, ν the viscosity, and Sc the Schmidt number. The total density field ρ_t has been decomposed as $\rho_t(\boldsymbol{x}, t) = \rho_0 + \bar{\rho}(z) + \rho(\boldsymbol{x}, t)$, ρ_0 being a constant reference density, $\bar{\rho}$ a linear mean density profile varying with the vertical coordinate z, and $\rho(\boldsymbol{x}, t)$ a perturbation density which is related to the buoyancy b by $b = -g\rho/\rho_0$. The Brunt-Väisälä frequency N measuring the ambient stable stratification is

$$N = \sqrt{-\frac{g}{\rho_0} \frac{\mathrm{d}\bar{\rho}}{\mathrm{d}z}}. \tag{2.4}$$

2.2 Direct Numerical Simulations

2.2.1 Global features

NS3D integrates the equations (2.1-2.3) in a parallelepipedic domain of dimensions $l_x \times l_y \times l_z$ with $n_x \times n_y \times n_z$ collocation points. Triply periodic boundary conditions are implemented, i.e.:

$$\boldsymbol{q}(x + l_x, y + l_y, z + l_z, t) = \boldsymbol{q}(x, y, z, t), \tag{2.5}$$

where the vector $\boldsymbol{q} = (u, v, w, p, b)$ gathers the unknowns of the problem. Since periodic boundary conditions are used, pseudo-spectral methods are particularly suited for resolving the problem numerically. Their principle is addressed in the following.

2.2.2 Formulation of the equations in spectral space

Let φ be a scalar periodic quantity, hence satisfying (2.5). Its three-dimensional Fourier transform $\hat{\mathcal{F}}$ is given by:

$$\hat{\mathcal{F}}(\varphi)(k_x, k_y, k_z, t) = \int_0^{l_z} \int_0^{l_y} \int_0^{l_x} \varphi(x, y, z, t)\, \mathrm{e}^{-i(k_x x + k_y y + k_z z)}\, \mathrm{d}x\mathrm{d}y\mathrm{d}z, \tag{2.6}$$

where $\boldsymbol{k} = (k_x, k_y, k_z)$ is the total wavenumber and $i^2 = -1$. Thanks to the periodicity, a fundamental property of the Fourier transform is

$$\hat{\mathcal{F}}\left(\frac{\partial \varphi}{\partial x_j}\right) = i k_j \hat{\mathcal{F}}(\varphi), \tag{2.7}$$

with x_j being any space variable and k_j the corresponding component in $\boldsymbol{k}$. This property is essential for formulating the Boussinesq equations in spectral space. In the following, we derive the spectral form of the momentum equation (2.2) so as to illustrate some subtle aspects of pseudo-spectral methods. The spectral form of the thermodynamic equation will be given directly since it is based on a similar reasoning.

First, applying the 3D Fourier transform to (2.1) yields:

$$\boldsymbol{k} \cdot \hat{\boldsymbol{\mathcal{F}}}(\mathbf{u}) = 0. \tag{2.8}$$

Thus, in spectral space, the velocity field is orthogonal to the wave vector.

Then, by taking the divergence of (2.2), the dynamic pressure per unit mass $p^* = p/\rho_0 + \boldsymbol{u}^2/2$ is found to satisfy the following Poisson equation:

$$\nabla^2 p^* = \boldsymbol{\nabla} \cdot \left[\boldsymbol{u} \times \boldsymbol{\omega} + b\boldsymbol{e}_z + \nu \boldsymbol{\nabla^2 u}\right]. \tag{2.9}$$

As a result, we have

$$\hat{\mathcal{F}}(p^*) = -i \frac{\boldsymbol{k}}{\boldsymbol{k}^2} \cdot \hat{\boldsymbol{\mathcal{F}}}(\boldsymbol{a}), \tag{2.10}$$

where the acceleration $\boldsymbol{a}$ is defined as $\boldsymbol{a} = \boldsymbol{u} \times \boldsymbol{\omega} + b\boldsymbol{e}_z$.

Finally, the Fourier transform is applied to the momentum equation (2.2). By introducing the unit vector $\boldsymbol{e}_k$ such that

$$\boldsymbol{e}_k = \frac{\boldsymbol{k}}{||\boldsymbol{k}||}, \tag{2.11}$$

where $||\boldsymbol{k}||$ is the norm of $\boldsymbol{k}$, and by taking advantage of the previous results, we find:

$$\left[\frac{\partial}{\partial t} + \nu \boldsymbol{k}^2\right] \hat{\boldsymbol{\mathcal{F}}}(\mathbf{u}) = \hat{\boldsymbol{\mathcal{F}}}(\boldsymbol{a}) - \left[\boldsymbol{e}_k \cdot \hat{\boldsymbol{\mathcal{F}}}(\boldsymbol{a})\right] \boldsymbol{e}_k. \tag{2.12}$$

The right-hand side of (2.12) can be rewritten

$$\hat{\mathcal{F}}_m(\boldsymbol{a})\boldsymbol{e}_m - \left[\hat{\mathcal{F}}_n(\boldsymbol{a}) \frac{k_n}{||\boldsymbol{k}||}\right] \frac{k_m}{||\boldsymbol{k}||} \boldsymbol{e}_m = \left[\delta_{mn} - \frac{k_m k_n}{\boldsymbol{k}^2}\right] \hat{\mathcal{F}}_n(\boldsymbol{a}) \boldsymbol{e}_n = \mathcal{P}_\perp(\hat{\boldsymbol{\mathcal{F}}}(\boldsymbol{a})), \tag{2.13}$$

where the tensor $\mathcal{P}_\perp(\boldsymbol{k})$ represents the projection on the space of solenoidal fields $\mathcal{D}(\boldsymbol{e_k})^\perp$:

$$\mathcal{P}_\perp(\boldsymbol{k}) = \left[\delta_{mn} - \frac{k_m k_n}{\boldsymbol{k}^2}\right]_{1\leqslant m,n\leqslant 3}, \tag{2.14}$$

where $\delta_{mn} = 0$ if $m \neq n$ and $\delta_{mn} = 1$ if $m = n$. These results are not valid when the total wavenumber is zero. However, the incompressibility condition is automatically satisfied in this case, thus resolving the problem.

It eventually turns out that we can formulate (2.2) and (2.3) in spectral space in the form

$$\frac{\partial \hat{\boldsymbol{\mathcal{F}}}(\mathbf{u})\, \mathrm{e}^{\nu \boldsymbol{k}^2 t}}{\partial t} = \mathcal{P}_\perp \left(\hat{\boldsymbol{\mathcal{F}}}(\boldsymbol{a})\right) \mathrm{e}^{\nu \boldsymbol{k}^2 t}, \tag{2.15}$$

$$\frac{\partial \hat{\mathcal{F}}(b)\, \mathrm{e}^{\nu \boldsymbol{k}^2 t/Sc}}{\partial t} = -\left[i\boldsymbol{k} \cdot \hat{\boldsymbol{\mathcal{F}}}(b\boldsymbol{u}) + N^2 \hat{\mathcal{F}}(w)\right] \mathrm{e}^{\nu \boldsymbol{k}^2 t/Sc}. \tag{2.16}$$

The central features of the method are summarized below:

(i) In spectral space, the incompressibility imposes that the wave vector is orthogonal to the velocity field.

(ii) A projection operator, which appears in the form of a second-order tensor in the spectral formulation of the momentum equation, enforces the incompressibility.

(iii) The introduction of this projector is at the origin of the disappearance of the pressure field in the spectral formulation (2.15) of the momentum equation. Therefore, computing the pressure is actually not necessary for determining the remaining unknowns. However, it can be directly deduced from $\boldsymbol{u}$ and b if needed.

2.2.3 Time integration and pseudo-spectral method

Equations (2.15) and (2.16) are integrated in time using a fourth-order Runge-Kutta scheme. The core of the program is the algorithm implemented for computing the nonlinear terms found in these two equations. The procedure is the following:

1. The vorticity is calculated in spectral space, i.e. $\hat{\boldsymbol{\mathcal{F}}}(\boldsymbol{\omega}) = i\boldsymbol{k} \times \hat{\boldsymbol{\mathcal{F}}}(\boldsymbol{u})$.
2. Backward Fourier transforms are applied to $\hat{\boldsymbol{\mathcal{F}}}(\boldsymbol{u})$, $\hat{\boldsymbol{\mathcal{F}}}(\boldsymbol{\omega})$, and $\hat{\mathcal{F}}(b)$. In this way, the fields $\boldsymbol{u}$, $\boldsymbol{\omega}$, and b are found in physical space.
3. $\boldsymbol{u} \times \boldsymbol{\omega}$ and $b\boldsymbol{u}$ are computed in the physical space.
4. $\hat{\boldsymbol{\mathcal{F}}}(\boldsymbol{u} \times \boldsymbol{\omega})$ and $\hat{\boldsymbol{\mathcal{F}}}(b\boldsymbol{u})$ are deduced from the previous quantities by applying a forward Fourier transform. This yields the nonlinear terms found in (2.15) and (2.16).
5. The time advancement is performed.

This algorithm makes an extensive use of Discrete Fourier Transforms. They are calculated with a Fast-Fourier Transform (FFT) algorithm. The parallelization of NS3D and the assessment of its performances have been performed by Deloncle (2007, 2014), which offers a comprehensive description of the optimization of the whole program. The most limiting tasks in terms of computations are precisely the FTTs, which consume from 70 to 95% of the total computational time.

2.2.4 Aliasing

The Discrete Fourier Transform of a periodic field is responsible for the existence of so-called aliasing errors. They arise when nonlinear quantities are computed. To be more specific, the aliasing affects the accuracy of high-order modes by polluting their top one-third, as pointed out by Orszag (1971). Delbende (1998) illustrates how aliasing errors are produced in a single dimension space.

Therefore, NS3D offers the possibility to truncate high order modes. Formally, we introduce the truncation radii R_{xs}, R_{ys}, and R_{zs} and the maximum wavenumbers $\max(k_x)$, $\max(k_y)$, and $\max(k_z)$ along the three spectral directions. We apply an elliptic aliasing removal. Mathematically, this means that spectral quantities are set to zero for the wavenumbers (k_x, k_y, k_z) that satisfy the condition

$$\left[\frac{k_x}{R_{xs}\max(k_x)}\right]^2 + \left[\frac{k_y}{R_{ys}\max(k_y)}\right]^2 + \left[\frac{k_z}{R_{zs}\max(k_z)}\right]^2 > 1. \tag{2.17}$$

All the simulations presented in this dissertation have been performed using a classical two-third rule: $R_{xs} = R_{ys} = R_{zs} = 2/3$.

2.3 Specificities of the present DNS

2.3.1 Initial state

The version of NS3D described in Deloncle (2014) has been adapted in order to simulate the dynamics of an isolated columnar vortex subjected to a vertically sheared flow.

More precisely, the initial state comprises a columnar Lamb-Oseen vortex embedded in a sinusoidal shear flow whose velocity field will be denoted $U(z)\boldsymbol{e}_x$ with $U(z) = U_S \sin(k_z z)$, $\boldsymbol{e}_x$ being the streamwise unit vector. The amplitude U_S simply sets the intensity of the advection. The wavenumber k_z of the profile $U(z)$ is $k_z = 2\pi/l_z$ so that a single wavelength is simulated. We have opted for a sinusoidal shear flow because it is straightforward to handle since periodic boundary conditions are implemented in NS3D. The vortex is purely vertical at $t = 0$. Initially, its vorticity field, in dimensional form, reads

$$\boldsymbol{\omega} = \zeta \boldsymbol{e}_z = \frac{\Gamma}{\pi a_0^2} \mathrm{e}^{-r^2/a_0^2} \boldsymbol{e}_z, \tag{2.18}$$

where Γ is the circulation, a_0 the vortex radius, and r the radial coordinate. Using a Fast Fourier Transform, this vorticity field is inverted to obtain the corresponding velocity field in the computational domain. If the domain were infinite and non-periodic, this velocity field would be the Lamb-Oseen profile

$$\boldsymbol{u}_v = u_\theta(r)\boldsymbol{e}_\theta = \frac{\Gamma}{2\pi r}\left[1 - \mathrm{e}^{-r^2/a_0^2}\right]\boldsymbol{e}_\theta, \tag{2.19}$$

$\boldsymbol{e}_\theta$ being the azimuthal unit vector. However, the actual profile differs from this Lamb-Oseen profile for large radius since the total circulation has to vanish in a periodic domain (Pradeep and Hussain, 2004).

Therefore, the total velocity field is purely horizontal initially. For this reason, the vertical velocity w and the buoyancy b are zero at $t = 0$.

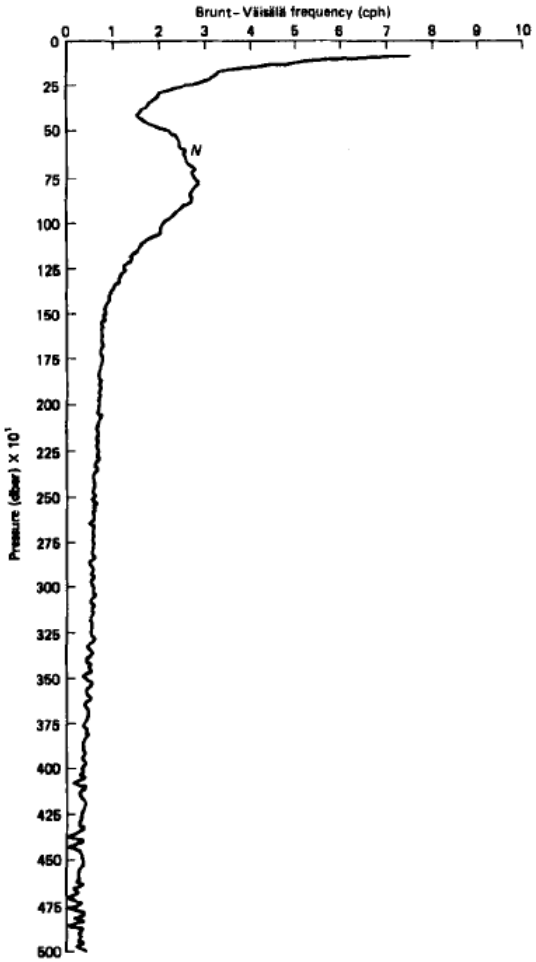

Figure 2.1: A typical profile of the Brunt-Väisälä frequency in the ocean. The measurement was performed in the North Atlantic ocean, near 28° North, 70° West. It is reproduced from Gill (1982).

The Reynolds number Re and the Froude number F_h are based on the initial conditions:

$$Re = \frac{|\Gamma|}{2\pi\nu}, \quad F_h = \frac{|\Gamma|}{2\pi a_0^2 N}. \tag{2.20}$$

This implies that the time and length units are chosen as $2\pi a_0^2/|\Gamma|$ and a_0 respectively. Accordingly, U_S is non-dimensionalized by $|\Gamma|/2\pi a_0$ and k_z by $1/a_0$:

$$U_S^* = \frac{2\pi a_0}{|\Gamma|} U_S, \quad k_z^* = a_0 k_z. \tag{2.21}$$

In the following, the stars will be dropped for simplicity. We will no longer consider dimensional variables unless explicitly mentioned. All dimensionless quantities will be denoted like their dimensional counterparts for simplicity as well, as done for U_S and k_z.

The Brunt-Väisälä frequency varies with altitude in the atmosphere and with depth in the oceans, as illustrated in figure 2.1, which displays a typical vertical profile of N in the ocean. To simplify things, it will be assumed that N is independent of the vertical coordinate z throughout this dissertation. Thus, the Froude number will be varied by simply setting N to the proper constant value.

It is worth stressing that we focus on flows such that the vortex is stronger than the external shear flow, i.e. $|U_S| < 1$ in dimensionless form. We will also consider that the vortex circulation is positive, since there is no loss of generality in making this assumption.

Therefore, the control parameters of the problem are F_h, Re, and the dimensionless velocity U_S and wavenumber k_z.

2.3.2 On the triply periodic boundary conditions

Periodic boundary conditions are commonly implemented in numerical programs that aim at investigating the dynamics of vortices beyond the range of parameters reachable in laboratory experiments. Nevertheless, such boundary conditions can disrupt the physics, leading to at least partially incorrect numerical results as pointed out by Pradeep and Hussain (2004).

For example, a pair of interacting vortices in a parallelepipedic box is actually embedded in a strain field that arises from the existence of an infinite number of pairs of vortices located in the virtual boxes that are adjacent to the domain which is simulated. This effect is precisely due to the periodicity constraint. Depending on the conditions, this strain may exert a strong influence on the pair of vortices under consideration, and, in turn, make its dynamics depart from the behaviour that should be observed normally, i.e. without any strain field.

Pradeep and Hussain (2004) also stress that the net circulation of the flow within the numerical domain should be zero because of the periodic boundary conditions. The flow considered throughout this dissertation comprises a single vortex, which is at the origin of the existence of a non-zero circulation at the boundaries. In order to suppress this effect, Otheguy et al. (2006) have proposed to add the appropriate background rotation that compensates this net circulation. This background rotation can be estimated from the mean vertical vorticity uniformly generated by the vortex in the domain, which is equal to $\Gamma/l_x l_y$.

Rennich and Lele (1997) also provided a method to deal with problems related to periodic boundary conditions.

However, in order to mitigate the effect of periodicity, the simplest solution consists in attributing sufficiently large values to the domain dimensions, as in Deloncle et al. (2008). Obviously, this requires carrying out a careful preliminary analysis for identifying the proper values of the different parameters.

We have opted for the latest option for a variety of reasons, and notably because:

1. Implementing a method such as proposed by Rennich and Lele (1997) would have required to profoundly modify NS3D.

2. The strain due to the artificial images of the flow is inversely proportional to the square of the horizontal dimension of the numerical domain. As such, it is weak when l_x and l_y are large. This is valid also regarding the net circulation.

In the case of the model flow that we focus on in this dissertation, we have observed that the dimensions of the fluid domain should be adjusted depending on the intensity of the advection U_S. This point will be detailed later since, to be explained satisfactorily, it requires introducing several intermediate notions.

2.4 Post-processing

NS3D computes the velocity field $\boldsymbol{u} = (u, v, w)$, its curl $\boldsymbol{\omega} = (\omega_x, \omega_y, \zeta)$, and the buoyancy b. A Data Analysis Program (DAP) has been therefore developed from NS3D in order to carry out further calculations from these fields. Its architecture is very similar to that of NS3D.

Since a wide variety of post-processing routines have been implemented, we will not describe the DAP in details. Instead, we will put the emphasis on the computation and processing of a crucial quantity for analysing the vortex deformations, namely the potential vorticity. The other tasks performed by the DAP will be listed and their subtleties will be briefly pointed out if needed.

2.4.1 Potential vorticity

The potential vorticity Π is an inviscid invariant of the governing equations (2.1-2.3), i.e.:

$$\frac{\mathrm{D}\Pi}{\mathrm{D}t} = 0, \quad \frac{\mathrm{D}}{\mathrm{D}t} = \frac{\partial}{\partial t} + \boldsymbol{u} \cdot \boldsymbol{\nabla}. \tag{2.22}$$

In a stratified fluid, its expression, in dimensional form, is:

$$\Pi = \boldsymbol{\omega} \cdot \left[\boldsymbol{\nabla} b + N^2 \boldsymbol{e}_z \right]. \tag{2.23}$$

The potential vorticity is one of the most challenging quantities to compute from the basic fields because it is the sum of three nonlinear terms. As such, it is *a priori* sensitive to aliasing errors. For this reason, we have computed this quantity without introducing any truncation of the high-order modes in the first instance. In a second time, it has been calculated by applying the same truncation as in NS3D, namely an elliptic dealiasing following the two-third rule by Orszag (1971).

The comparison of the numerical results has revealed that differences are insignificant provided that the simulation is properly resolved. In contrast, they can grow quite significantly when the mesh is coarse, and especially when a shear instability is under-resolved. In order to illustrate that the computation of the potential vorticity is largely insensitive to the aliasing removal in properly resolved cases, figure 2.2 reports the evolution of the potential vorticity maxima computed in the horizontal planes $z = l_z/4$, where the advection is the strongest and the vertical shear of the horizontal velocity is the weakest, and $z = l_z/2$, where the advection is zero and the vertical shear of the horizontal velocity reaches its peak. The control parameters are $F_h = 0.5$, $k_z = \pi/2$, $U_S = 0.2$, and $Re = 6000$. The dimensions of the box are $l_x = l_y = 18$ and $l_z = 4$. This run has been performed using $n_x = n_y = 512$ and $n_z = 256$ collocation points. The fact that the curves are collapsed confirms the previous statement. For this reason, the DAP actually computes the potential vorticity without truncating the top one-third modes.

2.4.2 Tracking the vortex position

It will be useful to locate the vortex as time evolves. This is done by computing the position of the vortex center in each horizontal plane, which provides a representation of the deformations of the vortex axis.

A panel of different methods can be implemented, depending on how we define the center. In a similar study, Jones (2004) stressed that the outer regions of the vortex

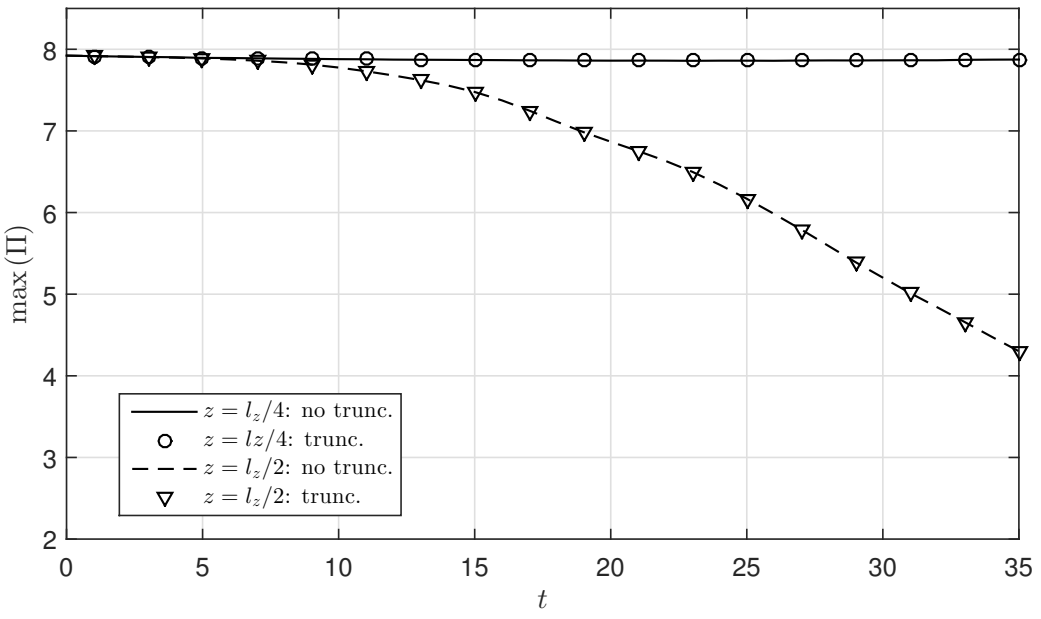

Figure 2.2: Evolution of the potential vorticity maxima computed in the planes $z = l_z/4$, without any aliasing removal (solid line) and with a dealiasing (open circles), and $z = l_z/2$, without any aliasing removal (dashed line) and with a dealiasing (triangles). The elliptic dealiasing cancels the top one-third modes following Orszag (1971). The control parameters are $F_h = 0.5$, $k_z = \pi/2$, $U_S = 0.2$, and $Re = 6000$.

were more strongly tilted than its inner core, in agreement with former investigations such as Jones (1995) and Jones (2000a). She emphasizes that, in such cases, defining the position of the vortex center as that of the maximum vertical vorticity does not provide reliable indications about the bending of the vortex because of the non-uniformity of the vortex tilt. This is the reason why we have opted for a similar definition as in Jones (2004), which is precisely based on the use of the potential vorticity. To be more specific, the position of the vortex $(x_c(z,t), y_c(z,t))$ in each horizontal plane has been obtained from the potential vorticity centroids:

$$x_c(z,t) = \frac{\langle x\Pi \rangle_h}{\langle \Pi \rangle_h}, \quad y_c(z,t) = \frac{\langle y\Pi \rangle_h}{\langle \Pi \rangle_h}, \tag{2.24}$$

where the brackets denote the horizontal averaging operator:

$$\langle \varphi \rangle_h = \int_{\Pi > \Pi_c} \varphi(x,y,z,t) \mathrm{d}x\mathrm{d}y. \tag{2.25}$$

The horizontal integration is carried out only in the regions where the potential vorticity is larger than a threshold Π_c in order to avoid taking into account the small background vorticity due to the fact that the total vorticity is zero owing to the use of periodic boundary conditions. This threshold being defined as $\Pi_c = \eta \max_{t=0}(\Pi)$, several tests have been done in order to set the coefficient η properly, that is for ensuring that the numerical results are independent of the size of the computational domain and of the particular value of Π_c. This investigation has revealed that taking $\eta = 0.05$ was sufficient. Indeed, figure 2.3 displays four trajectories of the vortex center computed as previously explained, that correspond to four values of the parameter η, namely $\eta = 0.05$, $\eta = 0.1$, $\eta = 0.5$, and $\eta = 0.9$. The control parameters are $F_h = 0.5$,

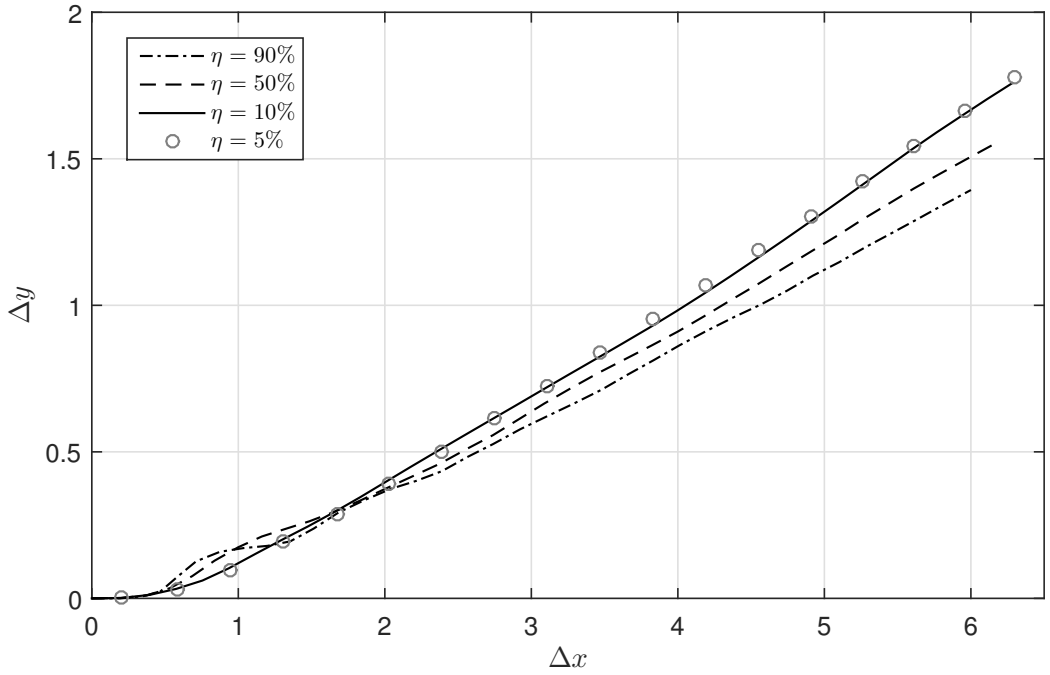

Figure 2.3: Displacement of the vortex with respect to its initial position, in the plane $z = l_z/4$. Four trajectories are reported, respectively corresponding to $\eta = 90\%$ (black dash-dotted line), $\eta = 50\%$ (black dashed line), $\eta = 10\%$ (black solid line) and $\eta = 5\%$ (grey open circles). The sampling times range from $t = 0$ up to $t = 35$. The control parameters are $F_h = 0.5$, $k_z = \pi/2$, $U_S = 0.2$, and $Re = 6000$. The horizontal dimensions of the domain are $l_x = l_y = 18$.

$k_z = \pi/2$, $U_S = 0.2$, and $Re = 6000$. The horizontal dimensions of the box are $l_x = l_y = 18$. The displacements Δx and Δy that are plotted are the displacements of the vortex with respect to its initial position, in the plane $z = l_z/4$ where the advection is the strongest. They are reported for $0 \leqslant t \leqslant 35$. It is seen that the trajectories are converged for $\eta \leqslant 0.1$, hence confirming that $\eta = 0.05$ is an optimal choice.

It is worth mentioning that the same method has been also implemented to locate the vortex on the basis of the vertical vorticity field. This simply consists in replacing Π by ζ in (2.24). This is different from the method that consists in assimilating the vortex center to the point where the vertical vorticity is maximum since the horizontal average will take the potential asymmetries into account and will therefore offer an adequate representation of the bending of the vortex. This is not the only advantage of such a method since it will also allow estimating the consistency of such a representation of the vortex deformations. Indeed, in chapter 5, we will show that apart from an initial transient stage, this computation of the vortex center provides nearly identical results whether Π or ζ is used.

2.4.3 Mitigation of the effect of periodic boundary conditions

As already mentioned, we have simulated the dynamics of the flow in a box whose horizontal dimensions are large enough to significantly weaken the effect of the periodic boundary conditions.

A careful analysis has revealed that a good indicator of how influential periodic

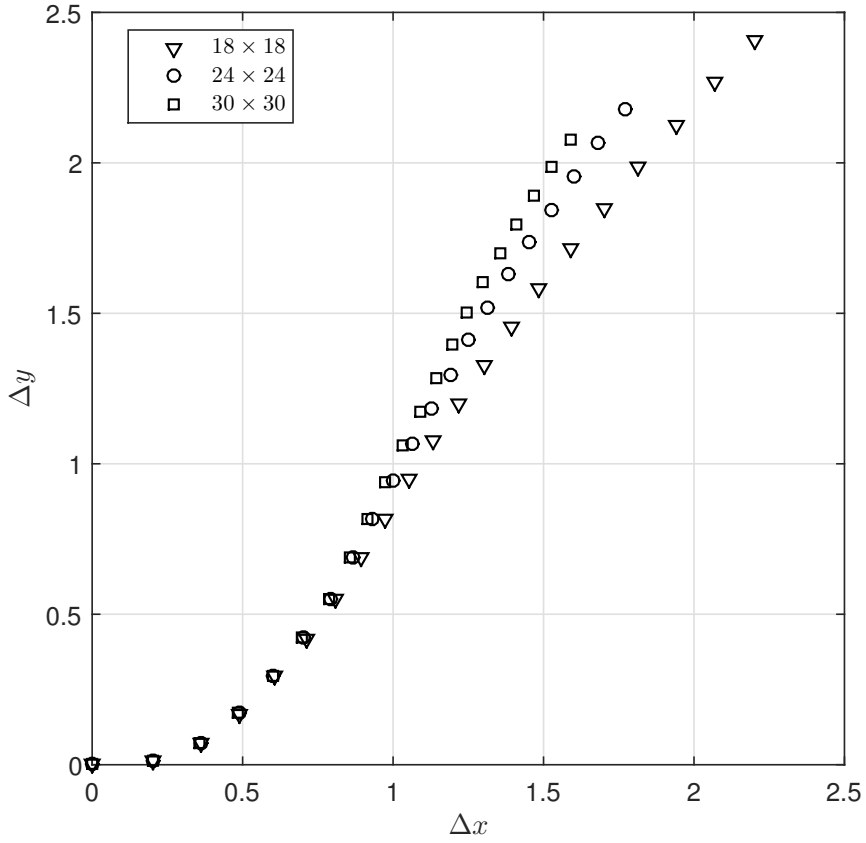

Figure 2.4: Displacement of the vortex with respect to its initial position, in the plane $z = l_z/4$. Three trajectories are reported, respectively corresponding to $l_x = l_y = 18$ (triangles), $l_x = l_y = 24$ (circles), and $l_x = l_y = 30$ (squares). The sampling times range from $t = 0$ up to $t = 40$. The control parameters are $F_h = 0.5$, $k_z = \pi$, $U_S = 0.1$, and $Re = 6000$. The displacements are those of the potential vorticity centroid obtained with $\eta = 5\%$.

boundary conditions are is the convergence of the vortex trajectory when l_x and l_y are varied, following the same idea as in figure 2.3.

More precisely, to any value U_S of the advection corresponds a minimal threshold for l_x and l_y beyond which the vortex trajectories - as previously computed - are independent of the box dimensions, i.e. insensitive to the periodic boundary conditions. Without presenting the whole set of investigations that have been carried out, figure 2.4 shows that for $U_S = 0.1$, the horizontal dimensions of the box must be $l_{x,y} \geqslant 24$ to ensure that the vortex trajectory is reasonably converged. Such a large domain requires introducing a large number of collocation points to properly resolve the finest scales. These requirements are actually too constraining in terms of computational resources. Instead, for $U_S = 0.2$, setting $l_{x,y} \geqslant 18$ is sufficient and allows using an affordable number of collocation points to properly resolve the dynamics. The latest compromise being the best to reconcile numerical issues and the condition $|U_S| < 1$, the vast majority of the simulations presented in this dissertation have been performed with $l_x = l_y = 18$ and U_S comprised between 0.2 and 0.4.

2.4.4 Listing of the post-processing routines

To finish, we provide a list of the main routines that have been implemented in the DAP:

1. The potential vorticity field is computed without applying any dealiasing. Its maximum is also computed and located in each plane $z = cte$. Similarly, the position of its centroid is calculated in each of these planes.

2. The global budgets of kinetic and potential energies, enstrophy and potential enstrophy are computed from the basic fields determined by NS3D.

3. The total flow is decomposed into a mean component corresponding to a purely horizontal, vertically sheared flow, and a residual component which is in fact assimilable to the vortex flow. This is demonstrated in details in the next chapter.

4. The global and local budgets of kinetic energy and enstrophy associated with these two components are computed.

5. The vertical shear of horizontal velocity is computed for the total flow, the mean flow, and the vortex flow. The corresponding maxima are also determined in each plane $z = cte$. Similarly, the vertical shear of the total horizontal velocity on one hand, and of the vortex horizontal velocity on the other hand, are determined at the center of the vortex, in the plane $z = l_z/2$ where the vertical shear is the most intense. Indeed, it will be shown that this quantity is essential to predict whether the shear instability can be triggered or not.

6. The vertical buoyancy gradient as well as the local Richardson number (see its definition further) are computed. A quantity of utmost importance for examining the onset of the shear instability is the minimum Richardson number, which is therefore determined in each horizontal plane. We do not apply any dealiasing to compute the Richardson number.

7. Globally, the DAP allows determining the vertical profiles of the minimum and maximum values of any field. In particular, this is done for the vertical velocity and the buoyancy, in addition to the fields already mentioned.

8. The profile of the mean flow velocity is also computed by the program.

2.5 Towards practical numerical simulations

We finish this chapter by giving some preliminary hints regarding the DNS.

As already mentioned, the present investigation aims at discriminating whether shear instabilities are likely to be triggered or not, depending on the values attributed to the control parameters. Following Miles (1961) and Howard (1961), a necessary condition for the KH instability to develop in a stratified fluid is that the local Richardson number falls below 1/4 somewhere in the flow. Recent studies, such as Riley and deBruynKops (2003), Brethouwer et al. (2007) and Bartello and Tobias (2013), have shown that the buoyancy Reynolds number ReF_h^2 (where Re is the Reynolds number and F_h the Froude number) is of utmost importance in determining the dynamics of stratified turbulence. Riley and deBruynKops (2003) and Deloncle et al. (2008),

besides reporting the existence of shear instabilities in strongly stratified flows, both proposed that the local Richardson number is inversely proportional to ReF_h^2. Thus, a large buoyancy Reynolds number is *a priori* conducive to the occurrence of the KH instability.

This is important for setting the horizontal Froude number as well as the Reynolds number in the numerical simulations. On one hand, the fact that the fluid is strongly stratified imposes $F_h < 1$, and, if possible, $F_h \ll 1$. On the other hand however, since ReF_h^2 must be at least reasonably large to favor the onset of shear instabilities, say $ReF_h^2 \gg 1$, decreasing F_h requires increasing Re if ReF_h^2 is kept constant. Therefore, tending to the strongly stratified regime at a constant buoyancy Reynolds number requires increasing the resolution so as to resolve the finest scales, hence requiring larger computational resources. Thus, the setting of F_h and Re is a matter of compromises. A variety of tests have shown that these issues are reconciled by choosing $F_h = 0.5$ and increasing Re up to ~ 7000 for example, whereas with $F_h = 0.1$ the Reynolds number can be set up to $Re \sim 10000$. With these settings, good but affordable resolutions are sufficient for properly resolving all the scales.

Note that, due to the Schmidt number Sc, the competition between inertial and viscous effects is not the same in the thermodynamic equation (2.3) as in the momentum equation (2.2). This is at the origin of another numerical difficulty. Indeed, for salt in the oceans for example, we have $Sc \sim 700$. The "equivalent" Reynolds number that intervenes in (2.3) is therefore 700 times larger than in (2.2). Thus, in the DNS, if we opt for $Re = 6000$ by keeping $Sc = 700$ at the same time, then the actual Reynolds number in (2.3) is $\sim 4.2 \times 10^6$. Even with $Sc = 7$, we would have an equivalent Reynolds number $\sim 4.2 \times 10^4$. Both cases are out of reach numerically if simulated through DNS. For numerical convenience, we have therefore opted for keeping $Sc = 1$.

Chapter 3

Preliminary study: global energy and enstrophy budgets

In this preliminary investigation, we examine the global energy and enstrophy budgets in order to get some insights on the effects of the control parameters on the dynamics of the flow. Especially, the present analysis aims at understanding how the enstrophy is affected when the control parameters vary. Indeed, as this quantity is nearly equivalent to the vertical shear of the horizontal velocity when vertical gradients are large, this study is a first step to predict the development of the shear instability.

3.1 Example of a simulation

Before discussing the energy and enstrophy budgets, we show in figure 3.1 the evolution of the potential vorticity field and the vertical shear of the horizontal velocity for the parameters $F_h = 0.5$, $k_z = \pi$, $U_S = 0.2$, and $Re = 6000$. The purpose is here to just give a brief idea of the flow evolution. This evolution will be discussed in more details in chapter 5.

3.2 Decomposition of the flow

In order to understand the mechanisms at work in the flow, it is interesting to decompose the total flow as

$$\boldsymbol{u} = \bar{\boldsymbol{u}} + \boldsymbol{u}^*, \tag{3.1}$$

where the operator $\bar{\cdot}$ denotes the horizontal average which for any quantity q is defined as

$$\bar{q} = \frac{1}{l_x l_y} \int_0^{l_y} \int_0^{l_x} q(x, y, z, t) \mathrm{d}x \mathrm{d}y. \tag{3.2}$$

Thus, $\bar{\boldsymbol{u}}$ is a mean flow varying only along the vertical and with time. The horizontal average of the complementary flow $\boldsymbol{u}^*$ is zero by definition. At $t = 0$, we have $\bar{\boldsymbol{u}} = U(z)\boldsymbol{e}_x$ and $\boldsymbol{u}^* = \boldsymbol{u}_v$ so that $\boldsymbol{u}^*$ will be called "vortex flow".

Applying the horizontal average operator to the dimensionless version of (2.1-2.3) leads to:

$$\frac{\partial \bar{w}}{\partial z} = 0, \tag{3.3}$$

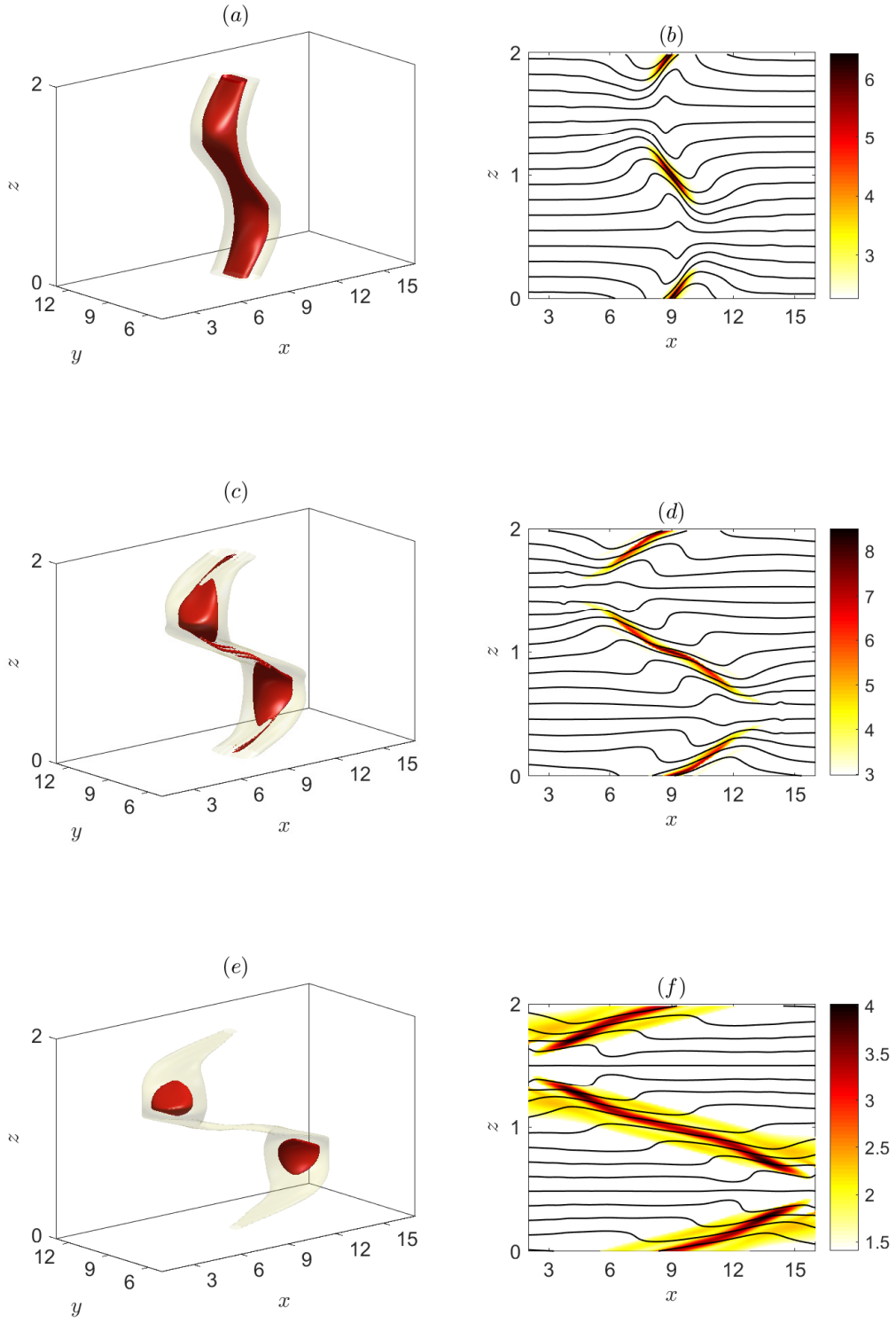

Figure 3.1: Left column: three-dimensional contours of the potential vorticity at different times for $F_h = 0.5$, $k_z = \pi$, $U_S = 0.2$, $Re = 6000$. Right column: corresponding vertical cross-sections of the shear $\sqrt{S_z} = \sqrt{(\partial u/\partial z)^2 + (\partial v/\partial z)^2}$ (color) and of the total density ρ_t (black contour lines) in the plane $y = 9$. The times shown are (a,b) $t = 12$, (c,d) $t = 24$, (e,f) $t = 36$. In (a,c,e), the isocontours correspond to 20% (yellow) and 60% (red) of the initial maximum value.

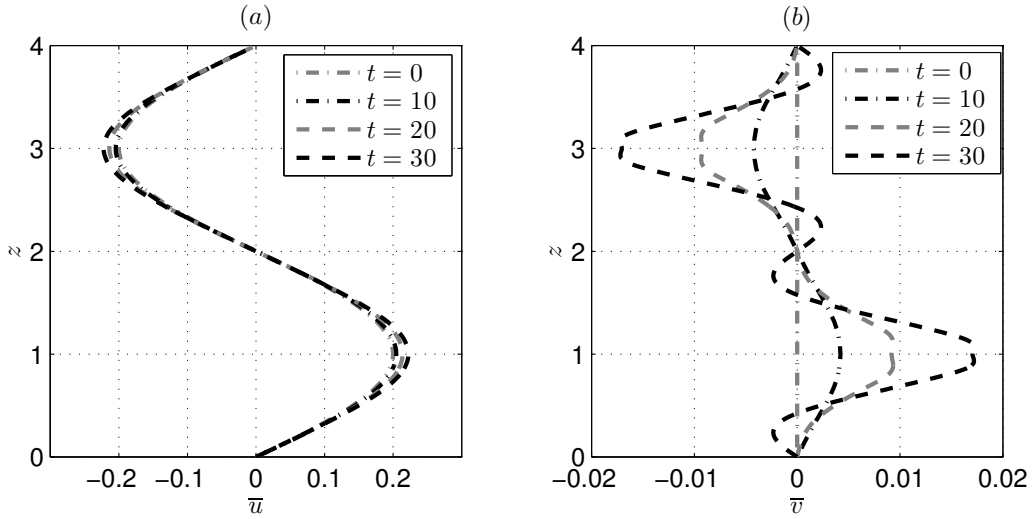

Figure 3.2: Vertical profiles of (a) the streamwise velocity component $\bar{u}$ and (b) the spanwise velocity component $\bar{v}$ of the mean flow. The profiles are shown at four different times $t = 0$ (grey dash-dotted line), $t = 10$ (black dash-dotted line), $t = 20$ (grey dashed line) and $t = 30$ (black dashed line). The control parameters are $F_h = 0.5$, $k_z = \pi/2$, $U_S = 0.2$, and $Re = 6000$. The left picture (a) clearly shows that the departures from the initial sinusoidal profile are insignificant, whereas the right picture (b) indicates that a spanwise component grows as time evolves, but remains small relative to the streamwise flow.

$$\frac{\partial \bar{\boldsymbol{u}}}{\partial t} + \frac{\partial \overline{w\,(\bar{\boldsymbol{u}} + \boldsymbol{u}^*)}}{\partial z} = -\frac{\partial \bar{p}}{\partial z}\boldsymbol{e}_z + \bar{b}\boldsymbol{e}_z + \frac{1}{Re}\frac{\partial^2 \bar{\boldsymbol{u}}}{\partial z^2}, \tag{3.4}$$

$$\frac{\partial \bar{b}}{\partial t} + \frac{\partial \overline{w b}}{\partial z} = -\frac{\bar{w}}{F_h^2} + \frac{1}{ReSc}\frac{\partial^2 \bar{b}}{\partial z^2}, \tag{3.5}$$

where the periodicity of $(\boldsymbol{u}, p, b)$ has been used. Equation (3.3) implies $\bar{w} = 0$. Indeed, this equation rigorously indicates that $\bar{w}$ depends on t only. However, an integration along the vertical then yields this result. Thus, the mean flow is purely horizontal and governed by

$$\frac{\partial \bar{\boldsymbol{u}}_h}{\partial t} = -\frac{\partial \overline{w^* \boldsymbol{u}_h^*}}{\partial z} + \frac{1}{Re}\frac{\partial^2 \bar{\boldsymbol{u}}_h}{\partial z^2}. \tag{3.6}$$

The equations for $\boldsymbol{u}^*$ can be obtained by subtracting (3.6) from the dimensionless form of (2.2).

Interestingly, the analysis of the numerical results indicates that the mean flow exhibits a velocity field which closely resembles the sinusoidal profile imposed initially. This is illustrated in figure 3.2, where the vertical profiles of each component $\bar{u}$ and $\bar{v}$ of the mean flow are reported at four different times $t = 0$, $t = 10$, $t = 20$ and $t = 30$, for $F_h = 0.5$, $k_z = \pi/2$, $U_S = 0.2$, and $Re = 6000$. It is seen that the departures from the initial sinusoidal profile are small. Hence, $\bar{\boldsymbol{u}}_h = U(z)\boldsymbol{e}_x$ is an accurate approximation of the mean flow velocity at any time.

3.3 Kinetic and potential energies

3.3.1 Definitions

First, we define the volume-integrated kinetic energies of the mean flow on one hand, and of the vortex on the other hand, following the decomposition of the total flow introduced previously. The global kinetic energy of the mean flow simply reads:

$$\bar{E}_k = \frac{1}{l_z}\int_\vartheta \frac{\bar{\boldsymbol{u}}_h{}^2}{2}\mathrm{d}\vartheta, \tag{3.7}$$

where ϑ stands for the numerical domain. The integral over ϑ is the triple integral over the fluid domain. The normalisation by l_z allows performing comparisons between cases associated with distinct wavelengths (Deloncle et al., 2008). We also define:

$$E^*_{kh} = \frac{1}{l_z}\int_\vartheta \frac{\boldsymbol{u}^{*2}_h}{2}\mathrm{d}\vartheta, \quad E^*_{kz} = \frac{1}{l_z}\int_\vartheta \frac{w^{*2}}{2}\mathrm{d}\vartheta, \quad E^*_k = E^*_{kh} + E^*_{kz}, \tag{3.8}$$

where E^*_{kh} is the global horizontal kinetic energy of the vortex and E^*_{kz} its vertical counterpart. Hence, E^*_k is the total kinetic energy of the vortex per vertical length unit.

In addition, the potential energy per vertical length unit is:

$$E_p = \frac{1}{l_z}\int_\vartheta \frac{F_h^2 b^2}{2}\mathrm{d}\vartheta. \tag{3.9}$$

3.3.2 Volume-integrated budgets

The volume-integrated budgets that describe the variations of the kinetic energies are found to be

$$\frac{\mathrm{d}\bar{E}_k}{\mathrm{d}t} = -T + \bar{D} \tag{3.10}$$

for the mean flow, and

$$\frac{\mathrm{d}E^*_k}{\mathrm{d}t} = \mathcal{C}^* + T + D^*_h + D^*_z + D_w \tag{3.11}$$

for the vortex.

In these budgets, the transfer terms read

$$T = \frac{1}{l_z}\int_\vartheta \bar{\boldsymbol{u}}_h \cdot \frac{\partial \overline{w^* \boldsymbol{u}^*_h}}{\partial z}\mathrm{d}\vartheta, \quad \mathcal{C}^* = \frac{1}{l_z}\int_\vartheta w^* b \mathrm{d}\vartheta, \tag{3.12}$$

and the dissipation terms are

$$\bar{D} = -\frac{1}{l_z Re}\int_\vartheta \left(\frac{\partial \bar{\boldsymbol{u}}_h}{\partial z}\right)^2 \mathrm{d}\vartheta, \tag{3.13}$$

$$D^*_h = -\frac{1}{l_z Re}\int_\vartheta \left[\left(\frac{\partial \boldsymbol{u}^*_h}{\partial x}\right)^2 + \left(\frac{\partial \boldsymbol{u}^*_h}{\partial y}\right)^2\right]\mathrm{d}\vartheta, \quad D^*_z = -\frac{1}{l_z Re}\int_\vartheta \left(\frac{\partial \boldsymbol{u}^*_h}{\partial z}\right)^2 \mathrm{d}\vartheta, \tag{3.14}$$

$$D_w = -\frac{1}{l_z Re}\int_\vartheta \left[\left(\frac{\partial w^*}{\partial x}\right)^2 + \left(\frac{\partial w^*}{\partial y}\right)^2 + \left(\frac{\partial w^*}{\partial z}\right)^2\right]\mathrm{d}\vartheta. \tag{3.15}$$

The kinetic energy $\bar{E}_k$ of the mean flow varies because of two terms: a transfer term T from the mean flow to the vortex and the dissipative term $\bar{D}$ which results from the vertical shear of the mean flow. The budget of the kinetic energy E_k^* of the vortex is more complex and contains:

1. the transfer term T and the conversion of the potential energy into kinetic energy $\mathcal{C}^*$.

2. two dissipative terms related to the horizontal shear and the vertical shear of the vortex horizontal velocity (3.14). We stress that these two contributions have been distinguished in the total dissipation for convenience in anticipation of further analyses.

3. the dissipative term (3.15) related to the vertical velocity.

Finally, the total potential energy satisfies:

$$\frac{\mathrm{d}E_p}{\mathrm{d}t} = -\mathcal{C}^* - \frac{F_h^2}{l_z ReSc}\int_\vartheta (\boldsymbol{\nabla} b)^2 \mathrm{d}\vartheta. \tag{3.16}$$

Since this equation only involves the vertical velocity $w = w^*$, it remains the same whether the total horizontal velocity field is decomposed into a mean component and a residual part or not.

3.4 Enstrophy

3.4.1 Definitions

From the velocity field decomposition defined previously, the vorticity $\boldsymbol{\omega} = \boldsymbol{\nabla} \times \boldsymbol{u}$ of the global flow can be expressed as:

$$\boldsymbol{\omega} = \bar{\boldsymbol{\omega}} + \boldsymbol{\omega}^*, \quad \bar{\boldsymbol{\omega}} = \boldsymbol{\nabla} \times \bar{\boldsymbol{u}}_h, \quad \boldsymbol{\omega}^* = \boldsymbol{\nabla} \times \boldsymbol{u}^*. \tag{3.17}$$

As such, $\bar{\boldsymbol{\omega}}$ and $\boldsymbol{\omega}^*$ respectively stand for the vorticities associated with the mean flow and the vortex.

Hence, we define:

$$\bar{Z} = \frac{1}{l_z}\int_\vartheta \frac{\bar{\boldsymbol{\omega}}^2}{2}\mathrm{d}\vartheta, \quad Z^* = \frac{1}{l_z}\int_\vartheta \frac{\boldsymbol{\omega}^{*2}}{2}\mathrm{d}\vartheta, \tag{3.18}$$

$\bar{Z}$ being the volume-integrated enstrophy associated with the mean flow and Z^* the global enstrophy of the vortex. Note that $\bar{\boldsymbol{\omega}}$ is purely horizontal since $\bar{\boldsymbol{u}}$ depends on z only. The application of the horizontal average to the non-dimensional vorticity equation gives:

$$\frac{\partial \bar{\boldsymbol{\omega}}}{\partial t} + \frac{\partial \overline{w^* \boldsymbol{\omega}^*}}{\partial z} = \frac{\partial \overline{\omega_z^* \boldsymbol{u}^*}}{\partial z} + \frac{1}{Re}\frac{\partial^2 \bar{\boldsymbol{\omega}}}{\partial z^2}. \tag{3.19}$$

The equation for $\boldsymbol{\omega}^*$ can be easily obtained by subtracting (3.19) from the full vorticity equation.

3.4.2 Volume-integrated budgets

The global enstrophy budgets can be written in the form

$$\frac{\mathrm{d}\bar{Z}}{\mathrm{d}t} = -\mathcal{T} + \bar{\mathcal{S}} + \bar{\mathcal{D}} \tag{3.20}$$

in the case of the mean flow, and

$$\frac{\mathrm{d}Z^*}{\mathrm{d}t} = \mathcal{T} + \mathcal{S}^* + \bar{\mathcal{S}}^* + \mathcal{B}^* + \mathcal{D}^* \tag{3.21}$$

regarding the vortex. The different terms read:

$$\mathcal{T} = \frac{1}{l_z}\int_\vartheta \bar{\boldsymbol{\omega}} \cdot \frac{\partial \overline{w^* \boldsymbol{\omega}^*}}{\partial z}\mathrm{d}\vartheta, \tag{3.22}$$

$$\bar{\mathcal{S}} = \frac{1}{l_z}\int_\vartheta \bar{\boldsymbol{\omega}} \cdot \frac{\partial \overline{\omega_z^* \boldsymbol{u}^*}}{\partial z}\mathrm{d}\vartheta, \tag{3.23}$$

$$\mathcal{S}^* = \frac{1}{l_z}\int_\vartheta \boldsymbol{\omega}^* \cdot \left[(\boldsymbol{\omega}^* \cdot \boldsymbol{\nabla})\,\boldsymbol{u}^*\right]\mathrm{d}\vartheta, \quad \bar{\mathcal{S}}^* = \frac{1}{l_z}\int_\vartheta \boldsymbol{\omega}^* \cdot \left[(\bar{\boldsymbol{\omega}} \cdot \boldsymbol{\nabla})\boldsymbol{u}^* + (\boldsymbol{\omega}^* \cdot \boldsymbol{\nabla})\bar{\boldsymbol{u}}_h\right]\mathrm{d}\vartheta, \tag{3.24}$$

$$\mathcal{B}^* = \frac{1}{l_z}\int_\vartheta \boldsymbol{\omega}^* \cdot (\boldsymbol{\nabla} b \times \boldsymbol{e_z})\,\mathrm{d}\vartheta, \tag{3.25}$$

$$\bar{\mathcal{D}} = -\frac{1}{l_z Re}\int_\vartheta \left(\frac{\partial^2 \bar{\boldsymbol{u}}_h}{\partial z^2}\right)^2 \mathrm{d}\vartheta, \quad \mathcal{D}^* = -\frac{1}{l_z Re}\int_\vartheta \left[(\boldsymbol{\nabla}\omega_x^*)^2 + (\boldsymbol{\nabla}\omega_y^*)^2 + (\boldsymbol{\nabla}\omega_z^*)^2\right]\mathrm{d}\vartheta. \tag{3.26}$$

The term $\mathcal{T}$ represents a transfer from the enstrophy of the mean flow to the enstrophy of the vortex. The term $\bar{\mathcal{S}}$ represents the effect of the stretching and tilting of the vortex on the mean flow. Conversely, $\bar{\mathcal{S}}^*$ is the stretching and tilting of the vortex by the mean flow. $\mathcal{S}^*$ is the stretching and tilting of the vortex on itself. $\mathcal{B}^*$ is the effect of the baroclinic torque and, finally, $\bar{\mathcal{D}}$ and $\mathcal{D}^*$ are the dissipations of the mean flow and vortex enstrophies, respectively.

3.5 Energy and enstrophy evolutions

Figure 3.3 presents typical evolutions of the kinetic and potential energies in (a), and of the enstrophy in (b), for $F_h = 0.5$, $k_z = \pi$, $U_S = 0.2$ and $Re = 6000$. The vertical kinetic energy is always small relative to its horizontal counterpart. This remains true throughout this dissertation. This is consistent with the fact that strong stratification inhibits vertical motions. The kinetic energy of the mean flow is nearly constant although it increases slightly owing to the transfer term T (see (3.12)). This is consistent with the fact that the velocity field of the mean flow remains close to the sinusoidal profile imposed initially (figure 3.2). In spite of the KH instability present at $t \simeq 24$ in this simulation, the global horizontal kinetic energy E_{kh}^* of the vortex decreases regularly and smoothly, following an approximately linear trend. Since the mean flow has an almost constant kinetic energy, the resulting variations of the total horizontal kinetic energy E_{kh} are very similar to those of the vortex horizontal kinetic energy.

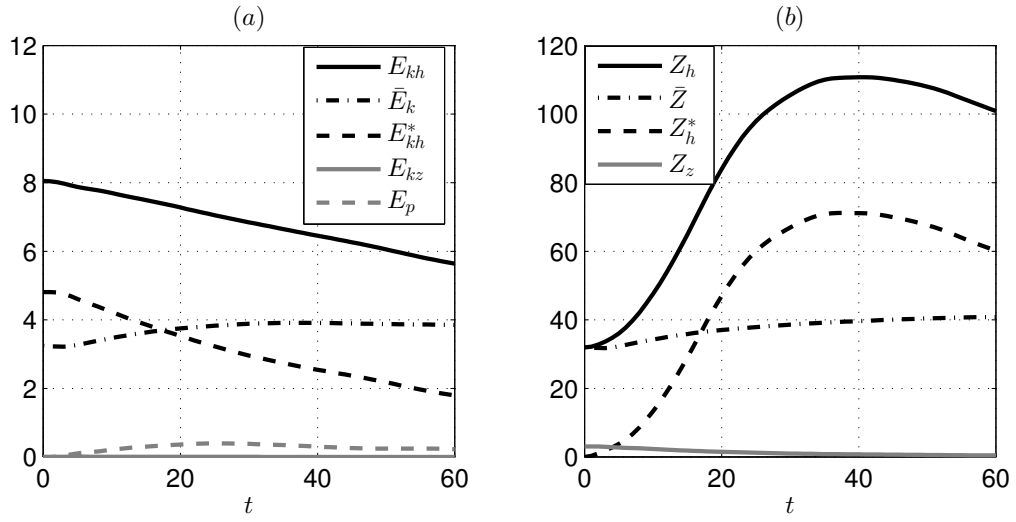

Figure 3.3: Evolutions of (a) the total horizontal kinetic energy (black solid line), the mean flow kinetic energy (black dash-dotted line), the vortex horizontal kinetic energy (black dashed line), the vertical kinetic energy (grey solid line), and the potential energy (grey dashed line) and of (b) the total horizontal enstrophy (black solid line), the enstrophy of the mean flow (black dash-dotted line), the vortex horizontal enstrophy (black dashed line), and the vertical enstrophy (grey solid line). The parameters are $F_h = 0.5$, $k_z = \pi$, $U_S = 0.2$ and $Re = 6000$.

The potential energy remains small compared to the horizontal kinetic energies. It exhibits a first regime where it grows regularly. Then, it saturates approximately when the KH instability develops. In the present case, the instability decays quite rapidly and disappears at $t \simeq 30$. Therefore, the plateau seen in the evolution of the potential energy persists after the decay of the instability. Ultimately, the potential energy slowly decays.

Regarding the enstrophy, that of the mean flow is almost constant as expected. In contrast, the global horizontal enstrophy of the vortex defined as

$$Z^*_h = \frac{1}{l_z}\int_\vartheta \frac{\boldsymbol{\omega}^{*2}_h}{2}\mathrm{d}\tau \tag{3.27}$$

strongly increases. Since the vertical velocity is small compared to the horizontal velocity, the horizontal enstrophy $\boldsymbol{\omega}^{*2}_h/2$ corresponds in very good approximation to the vertical shear of the horizontal velocity of the vortex:

$$\boldsymbol{\omega}^{*2}_h \simeq \left(\frac{\partial \boldsymbol{u}^*_h}{\partial z}\right)^2. \tag{3.28}$$

Therefore, Z^*_h is a measure of the vertical shear of the vortex. It grows since the vortex is progressively bent by the external shear flow. The vortex horizontal enstrophy saturates at $t \simeq 40$, i.e. well after the time $t \simeq 24$ when the KH instability is the most developed. The maximum horizontal enstrophy of the vortex is approximately twice the horizontal enstrophy of the mean flow. Thus, there is an approximate 200% increase of the total horizontal enstrophy. In contrast, the vertical enstrophy defined as

$$Z_z = Z^*_z = \frac{1}{l_z}\int_\vartheta \frac{\omega^{*2}_z}{2}\mathrm{d}\tau \tag{3.29}$$

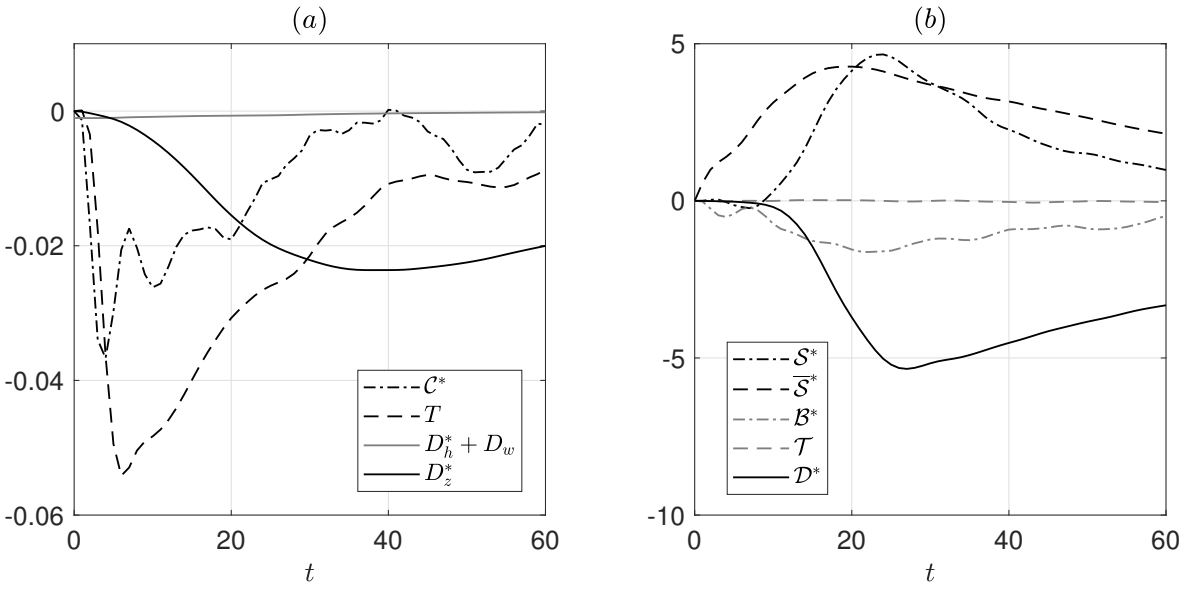

Figure 3.4: Source terms in (a) the kinetic energy budget (3.11) and in (b) the enstrophy budget (3.21). The parameters are the same as in figure 3.3.

decreases continuously.

3.6 Kinetic energy and enstrophy budgets of the vortex

Figures 3.4a,b show the source terms of the kinetic energy equation (3.11) and of the enstrophy equation (3.21) of the vortex, for the same run as presented in figure 3.3.

As seen in figure 3.4a, the kinetic energy of the vortex decreases because of three main effects. There are first a transfer to the potential energy ($\mathcal{C}^*$) and also a transfer to the shear flow (T). Later, these two terms decrease while the dissipation due to the vertical shear of the horizontal velocity (D_z^*) increases and saturates at $t \simeq 40$. The other dissipative terms are very small ($D_h^* + D_w$).

Figure 3.4b shows that the enstrophy of the vortex grows because of the stretching and tilting, first by the shear flow ($\bar{\mathcal{S}}^*$), and then by the vortex on itself ($\mathcal{S}^*$) also. In contrast, the baroclinic term ($\mathcal{B}^*$), the transfer to the enstrophy of the vortex ($\mathcal{T}$), and dissipation ($\mathcal{D}^*$) are all negative. All these terms saturate between $t \simeq 20$ and $t \simeq 30$. The dominant terms are the stretching $\bar{\mathcal{S}}^*$ and the dissipation $\mathcal{D}^*$ while the stretching $\mathcal{S}^*$ contributes also significantly to the budget but grows later and is at best of the order of $\bar{\mathcal{S}}^*$. Therefore, in order to estimate the maximum enstrophy of the vortex (figure 3.3a), we can, as a first approach, approximate the enstrophy equation of the vortex in the form

$$\frac{\mathrm{d}Z^*}{\mathrm{d}t} \simeq \bar{\mathcal{S}}^* + \mathcal{D}^*. \tag{3.30}$$

The enstrophy of the vortex thus saturates when $\bar{\mathcal{S}}^* \simeq -\mathcal{D}^*$. The order of magnitude of these two quantities can be estimated by introducing the scaling relations $||\boldsymbol{\omega}^*|| \sim 1/\delta$ where $1/\delta \sim \partial/\partial z$ is the vertical length scale associated to the vertical shear (non-dimensionalized by a_0), $||\partial u^*/\partial x|| \sim ||\partial v^*/\partial x|| \sim ||\partial u^*/\partial y|| \sim ||\partial v^*/\partial y|| \sim O(1)$ since the velocities and lengths have been non-dimensionalized by $|\Gamma|/2\pi a_0$ and

a_0, and $||\bar{\boldsymbol{\omega}}|| \sim k_z U_S$. This gives

$$\bar{\mathcal{S}}^* \sim l_x l_y \frac{k_z U_S}{\delta}, \quad \mathcal{D}^* \sim -l_x l_y \frac{1}{\delta^4 Re}, \tag{3.31}$$

where the factor $l_x l_y$ comes from the volume integration. Therefore, the relation $\bar{\mathcal{S}}^* \simeq -\mathcal{D}^*$ yields the order of magnitude

$$\delta \sim \frac{1}{(k_z U_S Re)^{1/3}} \tag{3.32}$$

when the enstrophy of the vortex saturates. Hence, the maximum enstrophy of the vortex is

$$\max(Z^*) \sim \frac{l_x l_y}{\delta^2} \sim l_x l_y (k_z U_S Re)^{2/3}. \tag{3.33}$$

This scaling is independent of the Froude number F_h as found by Deloncle et al. (2008). However, the scaling of Deloncle et al. (2008) is different and has been obtained by balancing $\mathcal{S}^*$ and $\mathcal{D}^*$ since there were no mean shear flow in their case. Since $\mathcal{S}^* \sim l_x l_y/\delta^2$, they have obtained $\delta \sim 1/\sqrt{Re}$ and $\max(Z^*) \propto Re$ instead of (3.32)-(3.33).

By assuming that the equation (3.30) holds approximately at any time, we can further obtain the typical time scale of the evolution of Z^*. Indeed, (3.31) can be rewritten

$$\bar{\mathcal{S}}^* \sim \sqrt{l_x l_y} k_z U_S \sqrt{Z^*}, \quad \mathcal{D}^* \sim -\frac{Z^{*2}}{l_x l_y Re}, \tag{3.34}$$

since $Z^* \sim l_x l_y/\delta^2$. Thus, the simplified equation (3.30) for the enstrophy budget of the vortex can be written

$$\frac{\mathrm{d}Z^*}{\mathrm{d}t} \simeq \sqrt{l_x l_y} k_z U_S \sqrt{Z^*} - \frac{Z^{*2}}{l_x l_y Re}. \tag{3.35}$$

By rescaling the enstrophy and the time as

$$Z^* = l_x l_y (k_z U_S Re)^{2/3} \hat{Z}, \quad t = \tau_v \hat{t}, \tag{3.36}$$

where $\tau_v = Re^{1/3}/(k_z U_S)^{2/3}$, (3.35) becomes:

$$\frac{\mathrm{d}\hat{Z}}{\mathrm{d}\hat{t}} \simeq \sqrt{\hat{Z}} - \hat{Z}^2. \tag{3.37}$$

This shows that the enstrophy of the vortex evolves as

$$\frac{Z^*}{l_x l_y (k_z U_S Re)^{2/3}} = \hat{Z} = \varphi\left(\frac{t}{\tau_v}\right). \tag{3.38}$$

If we neglect the transfer terms T and $\mathcal{C}^*$ in the kinetic energy budget (3.11), i.e.

$$\frac{\mathrm{d}E_k^*}{\mathrm{d}t} \simeq D_h^* + D_z^* + D_w \simeq -\frac{2Z^*}{Re}, \tag{3.39}$$

we see that the kinetic energy should also follow the self-similar law

$$\frac{\mathrm{d}E_k^*}{\mathrm{d}\hat{t}} \simeq -2 l_x l_y \varphi(\hat{t}) \tag{3.40}$$

giving

$$E_k^* = l_x l_y \Phi\left(\frac{t}{\tau_v}\right). \tag{3.41}$$

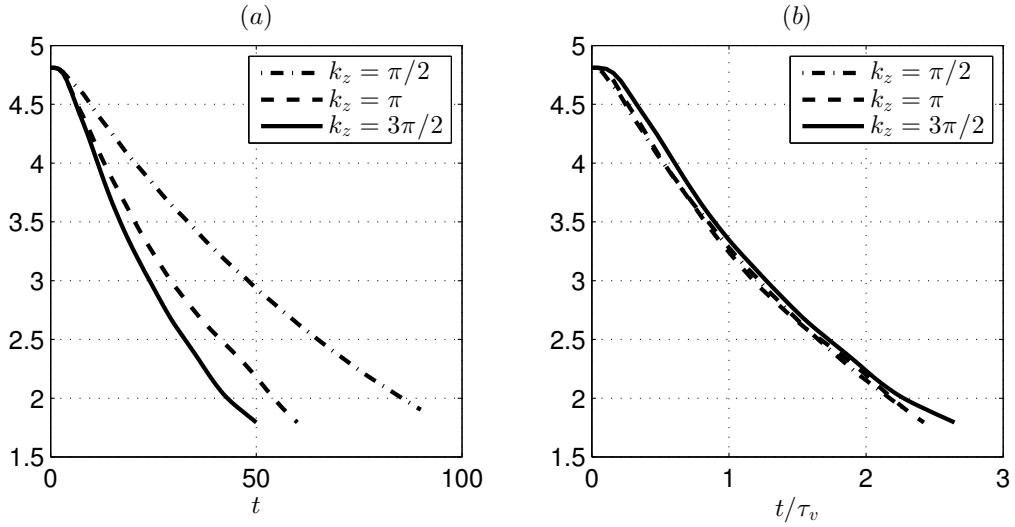

Figure 3.5: Kinetic energy of the vortex E_k^* for $F_h = 0.5$, $U_S = 0.2$, $Re = 6000$, for $k_z = \pi/2$ (dash-dotted line), $k_z = \pi$ (dashed line) and $k_z = 3\pi/2$ (solid line), as a function of (a) the time t and (b) the rescaled time t/τ_v.

3.7 Parametric analysis

We now test the self-similar laws (3.38) and (3.41) by varying the control parameters. We first consider the kinetic energy of the vortex and then the corresponding enstrophy.

3.7.1 Kinetic energy of the vortex

Figure 3.5a shows the temporal evolution of the kinetic energy of the vortex E_k^* for several wavenumbers k_z, for $F_h = 0.5$, $U_S = 0.2$ and $Re = 6000$. The decay is faster as k_z increases. When the time is rescaled by τ_v (figure 3.5b), the three curves collapse quite well confirming (3.41).

Similarly, figure 3.6 displays the evolution of the vortex kinetic energy for various U_S, for $F_h = 0.5$, $k_z = \pi$ and $Re = 6000$. Again, the rescaling of t by τ_v (figure 3.6b) leads to a self-similar decay in agreement with (3.41).

The effect of the Reynolds number is tested in figure 3.7 for $F_h = 0.5$, $k_z = \pi$ and $U_S = 0.2$. It is seen that the evolution of E_k^* weakly depends on the Reynolds number, especially the initial part $t \lesssim 20$. When t is rescaled by τ_v (figure 3.7b), the collapse of the three curves remains satisfactory. This is because τ_v depends on Re with the power law exponent $1/3$. Moreover, the relative variations of Re in figure 3.7 are smaller than for the two previous parameters.

All these results are consistent with (3.41). Remarkably, this relation is not only valid for large times but also for short times. This suggests that the transfer terms T and $\mathcal{C}^*$, although dominant at the beginning, do not have a so important effect.

3.7.2 Enstrophy of the vortex

The self-similar law for the enstrophy of the vortex (3.38) is now checked when the parameters k_z, U_S, and Re are varied as done for the kinetic energy. Figures 3.8, 3.9, and 3.10 show that the scaling (3.38) gathers relatively well the different curves. The

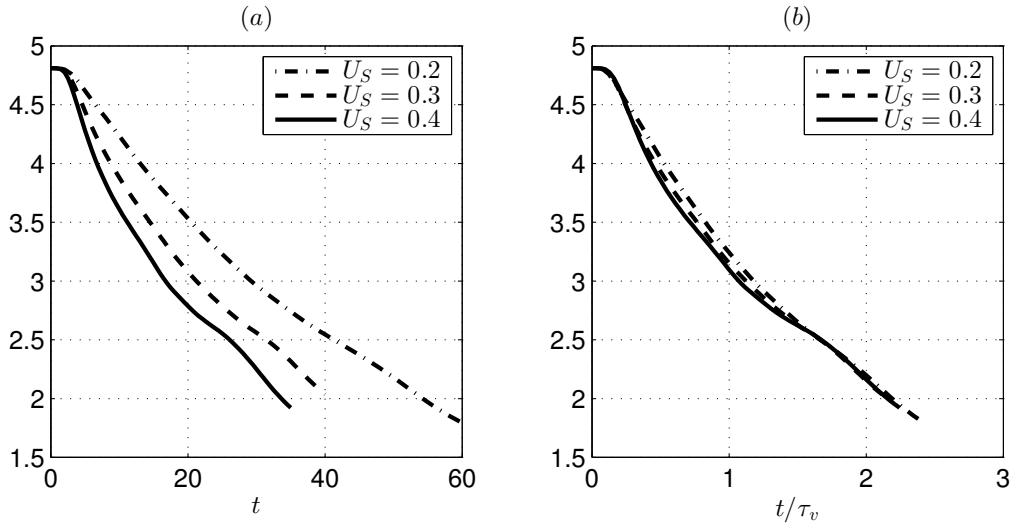

Figure 3.6: Kinetic energy E_k^* of the vortex for $F_h = 0.5$, $k_z = \pi$, $Re = 6000$, for $U_S = 0.2$ (dash-dotted line), $U_S = 0.3$ (dashed line) and $U_S = 0.4$ (solid line), as a function of (a) the time t and (b) the rescaled time t/τ_v.

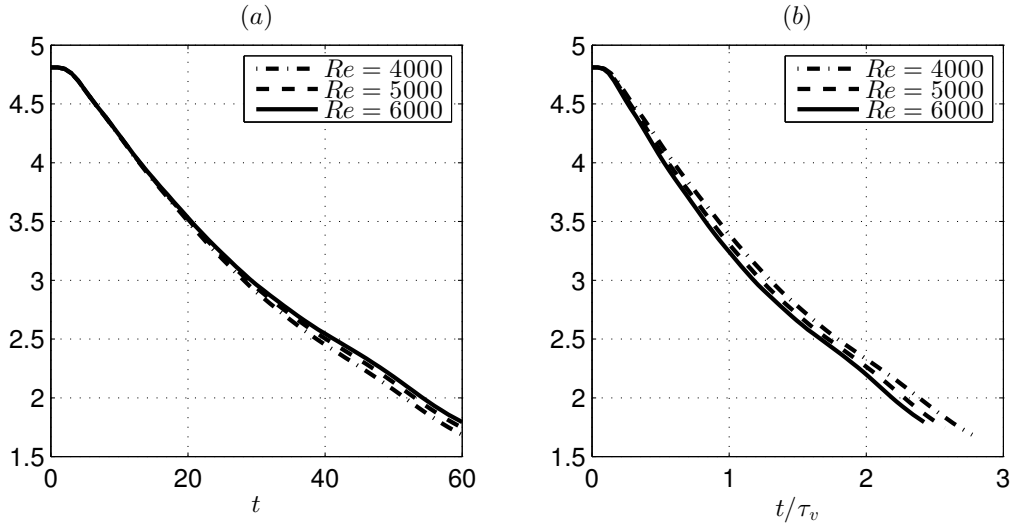

Figure 3.7: Kinetic energy E_k^* of the vortex for $F_h = 0.5$, $k_z = \pi$, $U_S = 0.2$, for $Re = 4000$ (dash-dotted line), $Re = 5000$ (dashed line) and $Re = 6000$ (solid line), as a function of (a) the time t and (b) the rescaled time t/τ_v.

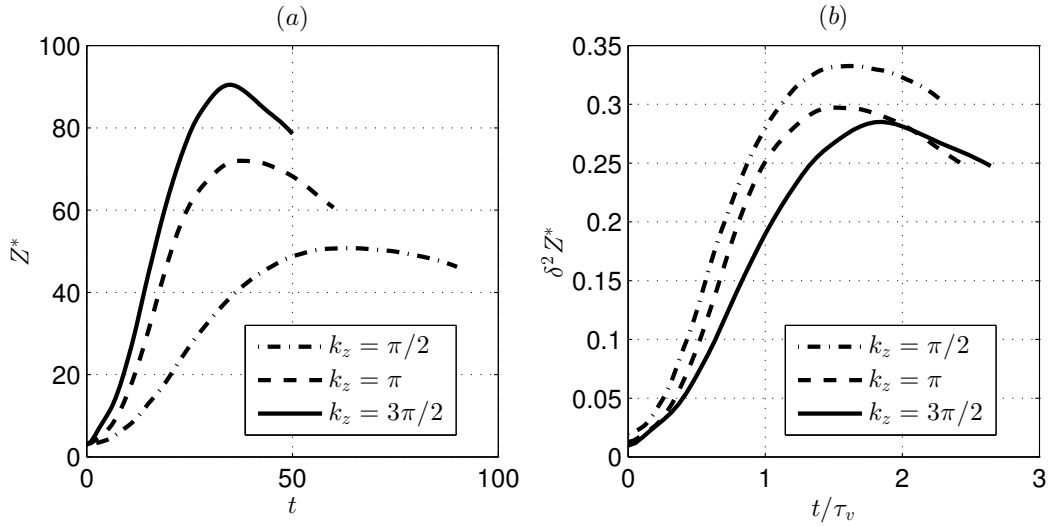

Figure 3.8: Enstrophy of the vortex for $F_h = 0.5$, $U_S = 0.2$, $Re = 6000$, for $k_z = \pi/2$ (dash-dotted line), $k_z = \pi$ (dashed line) and $k_z = 3\pi/2$ (solid line). The unscaled enstrophy Z^* is plotted against t in (a) and the rescaled enstrophy $\delta^2 Z^*$ is plotted against the rescaled time t/τ_v in (b).

maximum enstrophy of the vortex is approximately $\max(Z^*) \simeq 0.3/\delta^2$ and is attained at $t \simeq 1.6\tau_v$.

3.7.3 Effect of the Froude number

Finally, we examine the influence of F_h on the evolutions of E_k^* and Z^*. According to the self-similar laws (3.38) and (3.41), the Froude number should not have any effect. However, figure 3.11, which reports the evolution of E_k^* for different Froude numbers for $k_z = \pi$, $U_S = 0.2$, and $Re = 6000$, shows that the decay of E_k^* is more rapid at the beginning when F_h increases. Nevertheless, we can notice that the three curves are approximately parallel for long times $t \gtrsim 20$. This shows that the transfer terms T and $\mathcal{C}^*$ have, as a matter of fact, a non-negligible effect at the beginning while, after, the kinetic energy decay is mostly due to viscous effects. Figure 3.11b shows that the different kinetic energy evolutions collapse approximately if the time is rescaled by $\tau_v/F_h^{1/3}$.

Similarly, figure 3.12 illustrates the effect of F_h on Z^* for the same parameters as previously. Again, the Froude number is found to exert a strong influence on the variations of Z^*, thus invalidating (3.38). The different curves gather if Z^* is rescaled by $1/F_h^{1/3}$ but not the time (figure 3.12b), suggesting the modified self-similar law:

$$\frac{F_h^{1/3}\delta^2 Z^*}{l_x l_y} = \varphi\left(\frac{t}{\tau_v}\right). \tag{3.42}$$

We have not succeeded in obtaining an interpretation for the factor $F_h^{1/3}$ from the energy and enstrophy budgets. In particular, concerning the kinetic energy, the transfer towards potential energy weakens when the Froude number decreases. This explains qualitatively why the kinetic energy decay is less pronounced at the beginning for small Froude numbers. However, why this leads to the typical decay time $\tau_v/F_h^{1/3}$ remains unknown from the previous analysis of the enstrophy and energy budgets.

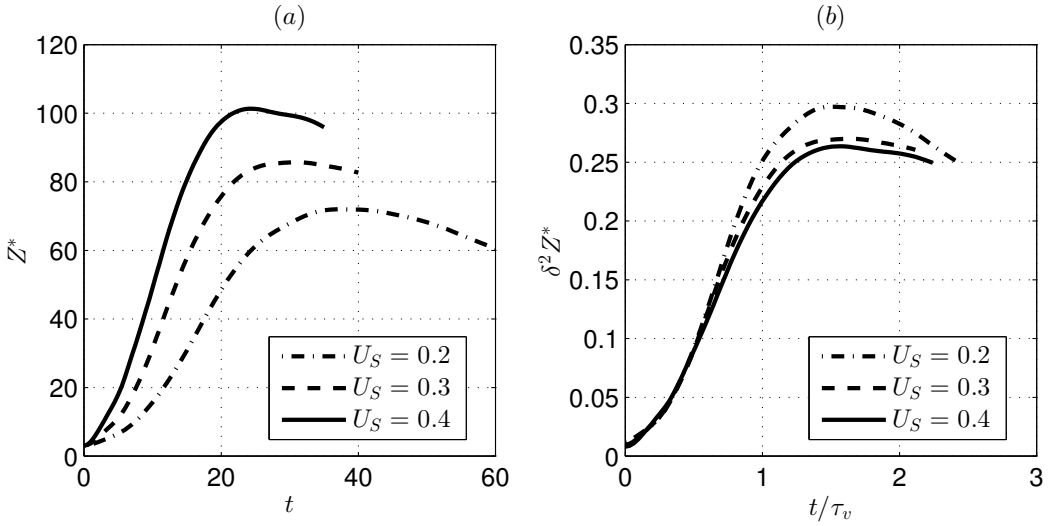

Figure 3.9: Enstrophy of the vortex for $F_h = 0.5$, $k_z = \pi$, $Re = 6000$, for $U_S = 0.2$ (dash-dotted line), $U_S = 0.3$ (dashed line) and $U_S = 0.4$ (solid line). The unscaled enstrophy Z^* is plotted against t in (a) and the rescaled enstrophy $\delta^2 Z^*$ is plotted against the rescaled time t/τ_v in (b).

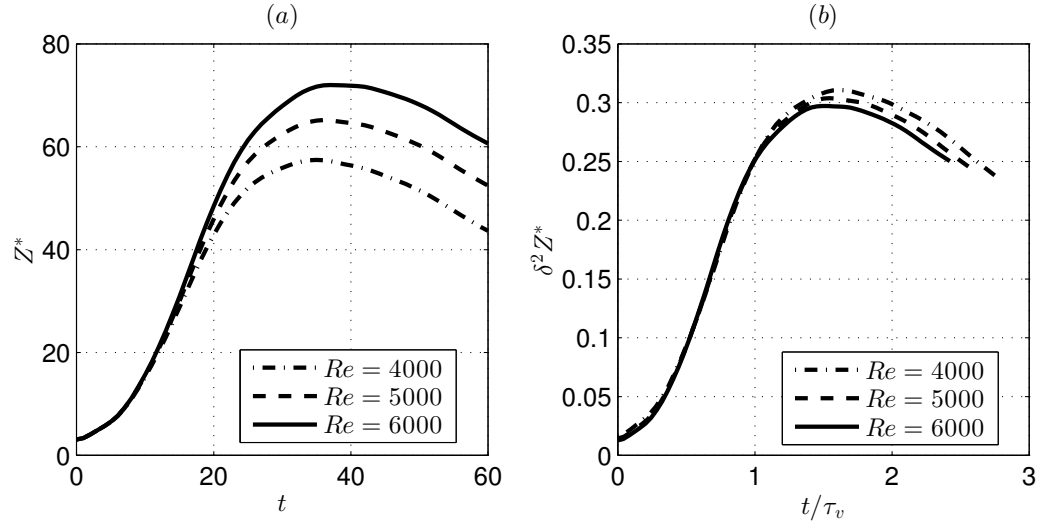

Figure 3.10: Enstrophy of the vortex for $F_h = 0.5$, $k_z = \pi$, $U_S = 0.2$, for $Re = 4000$ (dash-dotted line), $Re = 5000$ (dashed line) and $Re = 6000$ (solid line). The unscaled enstrophy Z^* is plotted against t in (a) and the rescaled enstrophy $\delta^2 Z^*$ is plotted against the rescaled time t/τ_v in (b).

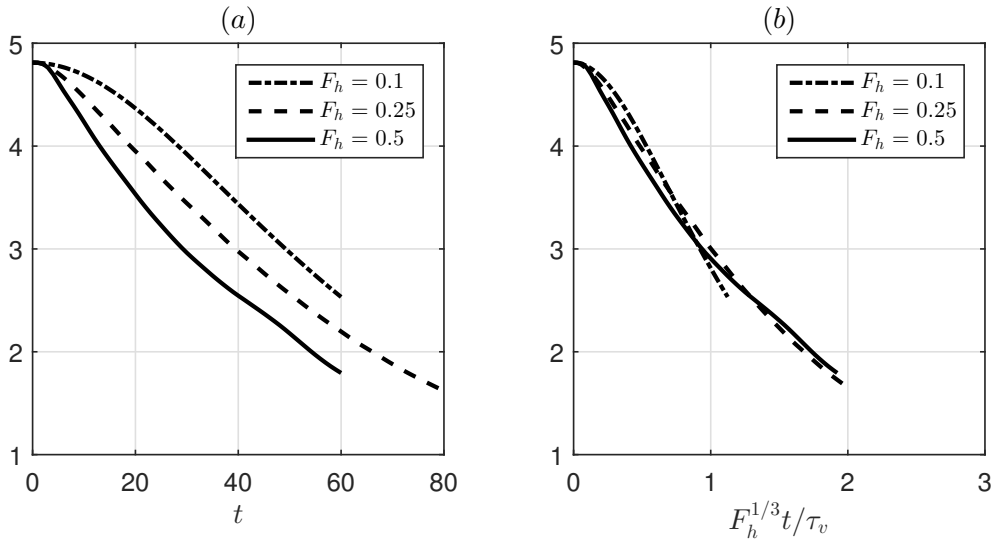

Figure 3.11: Kinetic energy E_k^* of the vortex for $k_z = \pi$, $U_S = 0.2$, $Re = 6000$, for $F_h = 0.1$ (dash-dotted line), $F_h = 0.25$ (dashed line) and $F_h = 0.5$ (solid line), as a function of (a) the time t and (b) the rescaled time $F_h^{1/3} t/\tau_v$.

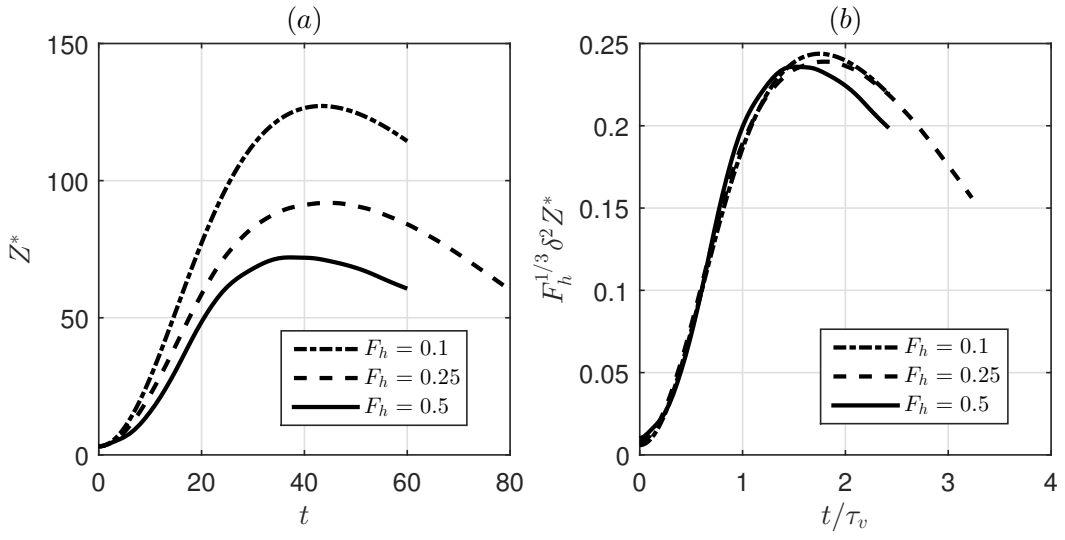

Figure 3.12: Enstrophy of the vortex for $k_z = \pi$, $U_S = 0.2$, $Re = 6000$, for $F_h = 0.1$ (dash-dotted line), $F_h = 0.25$ (dashed line) and $F_h = 0.5$ (solid line). The unscaled enstrophy Z^* is plotted against t in (a) and the rescaled enstrophy $F_h^{1/3}\delta^2 Z^*$ is plotted against the rescaled time t/τ_v in (b).

3.8 Conclusions

In the present chapter, we have investigated the global budgets of the volume-integrated kinetic energy and enstrophy in order to get some insight on the effect of the control parameters. The analysis of the budgets has provided an estimation of the minimum shear layer thickness δ which governs the maximum enstrophy of the vortex $Z^* \propto 1/\delta^2$. A scaling for the time scale that characterizes the viscous decay has also been obtained. These results have been shown to account for the influence of all the control parameters, except the horizontal Froude number. Indeed, the analysis of the budgets does not predict any dependency with respect to this parameter, although it strongly influences the variations of E_k^* and Z^*. This paradox has therefore motivated an in-depth investigation of the local dynamics in the next chapters.

Chapter 4

Evolution of a vortex in a strongly stratified shear flow. Part 1. Asymptotic analyses.

Article in preparation for submission to the *Journal of Fluid Mechanics*.

Abstract

In this chapter, we investigate the dynamics of an initially vertical vortex embedded in a shear flow in a stratified fluid by means of two asymptotic analyses. The ultimate goal is to determine, whether or not, the Kelvin-Helmholtz instability can develop as speculated by Lilly (1983). The analyses are mostly performed in the cases of the Lamb-Oseen vortex profile and a shear flow uniform in the horizontal and varying sinusoidally along the vertical.

The first asymptotic analysis is performed for small time: $t \ll 1$, and shows that the dynamics is initially non-hydrostatic until $t > 1/N$, where N is the Brunt-Väisälä frequency.

The second asymptotic analysis is conducted by assuming a small vertical wavenumber k_z rescaled by the horizontal Froude number F_h: $k_z F_h \ll 1$. The results show that the vortex axis is not only advected in the direction of the shear flow but also in the perpendicular direction owing to the self-induced motion of the vortex. In addition, internal waves are transiently excited at the beginning, explaining the non-hydrostatic regime evidenced in the first asymptotic analysis. Their effects on the displacements of the vortex axis are weak except at the beginning. The angular velocity of the vortex decays owing to dynamic and viscous effects. The former effect is due to the squeezing of isopycnals in the vortex core which implies a decrease of the vertical vorticity to satisfy potential vorticity conservation. In addition, a horizontal velocity field with an azimuthal wavenumber $m = 2$ is generated meaning that the shape of the vortex becomes slightly elliptical.

These predictions will be tested against Direct Numerical Simulations in chapter 5.

4.1 Introduction

Stratified turbulence is strongly anisotropic with predominantly horizontal motions but high shear along the vertical (Riley and Lelong, 2000). Such layered structure inherently promotes the shear instability which breaks down the layers into smaller-scale turbulence (Lilly, 1983; Riley and deBruynKops, 2003; Lindborg, 2006). This is one of the main mechanisms that accomplish the direct energy cascade towards small scales in stratified turbulence (Riley and deBruynKops, 2003; Brethouwer et al., 2007; Deloncle et al., 2008; Augier and Billant, 2011; Augier et al., 2012; Waite, 2013).

In his pioneering paper on strongly stratified flows, Lilly (1983) has conjectured a simple mechanism for the growth of the vertical shear. He considered a uniform horizontal flow directed along a given direction, let us say x, and vertically sheared: $\boldsymbol{U} = U(z)\boldsymbol{e}_x$ where z is the vertical coordinate. If a coherent structure with initial horizontal velocity $\boldsymbol{u}_{h0}(x, y, z)$ is embedded within this shear flow, it will be advected differentially depending on the vertical position:

$$\frac{\partial \boldsymbol{u}_h}{\partial t} = -U\frac{\partial \boldsymbol{u}_h}{\partial x}. \tag{4.1}$$

Lilly has further assumed that the coupling along the vertical is weak in the limit of strong stratification. When the vertical coupling is zero, the flow consists in a stack of horizontal two-dimensional flows evolving independently at each level z. Then, the solution at any time is simply: $\boldsymbol{u}_h(x, y, z, t) = \boldsymbol{u}_{h0}(x - U(z)t, y, z)$. This shows that

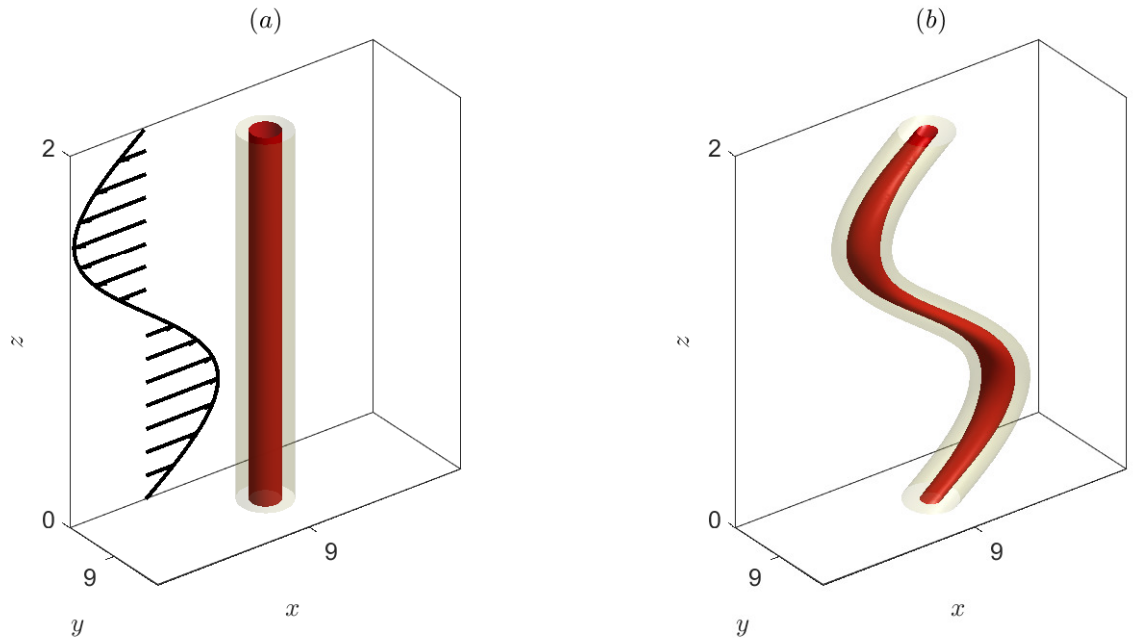

Figure 4.1: (a) Sketch of the flow configuration studied in this dissertation. The ambient shear flow $U(z)\boldsymbol{e}_x$ is represented by the black vectors. The red and yellow contours show two levels of the potential vorticity of the vortex at $t = 0$. (b) Potential vorticity contours at $t = 20$ obtained from a direct numerical simulation for the Froude and Reynolds numbers $F_h = 0.1$, $Re = 6000$ and the shear flow $U = U_S \sin(k_z z)$ with $U_S = 0.2$ and $k_z = \pi$. See chapter 5 for the definitions of these parameters and the details of the numerical simulations.

the vertical shear should grow algebraically with time according to

$$\frac{\partial \boldsymbol{u}_h}{\partial z} = -\frac{\mathrm{d}U}{\mathrm{d}z} t \frac{\partial \boldsymbol{u}_{h0}}{\partial x} + \frac{\partial \boldsymbol{u}_{h0}}{\partial z}. \tag{4.2}$$

On this basis, Lilly (1983) argued that the Richardson number should reach sooner or later the critical value 1/4 for the onset of the shear instability (Miles, 1961; Howard, 1961). However, a key assumption behind this conjecture is that there is no vertical coupling. This derives directly from Lilly's assumption that the vertical Froude number tends to zero in the limit of strong stratification. It is now acknowledged that the vertical Froude number remains of order unity because the typical vertical length scale scales like the buoyancy length scale in strongly stratified flows (Billant and Chomaz, 2001; Lindborg, 2006).

It is therefore unknown whether or not this mechanism for the growth of the vertical shear is valid. In order to answer this question, we have considered the particular case of an initially vertical vortex in an ambient vertically sheared flow in a stratified fluid. This flow configuration is sketched in figure 4.1 together with the example of a direct numerical simulation illustrating the vortex evolution. In the present chapter, we shall study the dynamics of this flow by asymptotic analyses while direct numerical simulations will be performed in chapter 5.

The dynamics of an isolated vortex in an ambient vertical shear has been studied before in stratified rotating fluids in order to understand the dynamics of atmospheric tropical cyclones (Jones, 1995, 2000a,b, 2004; Sutyrin and Morel, 1997; Frank and

Ritchie, 1999; Reasor et al., 2004; Päschke et al., 2012) or oceanic vortices (Vandermeirsch et al., 2001, 2002). In particular, Jones (1995), using a three-dimensional continuous hydrostatic primitive equation model, has shown that an initially barotropic vortex in a linear shear flow tilts in the shear direction but also executes a cyclonic rotation about its mid-level center. Päschke et al. (2012) have derived asymptotically the equations for the motion of the vortex center in the case of a weak shear flow.

The influence of a vertical shear on an initially aligned vortex has been also investigated by means of quasigeostrophic two-layer models (Marshall and Parthasarathy, 1993; DeMaria, 1996; Smith et al., 2000; Vandermeirsch et al., 2001, 2002). Marshall and Parthasarathy (1993) have reported two distinct evolutions depending on the strength of the vortices compared to the shear. When the advection by the shear is below a critical value, the vortices in each layer are offset and rotate about each other. Conversely, when the advection is sufficiently strong, the two vortices are continuously advected away from each other. These two regimes have been called non-tearing and tearing regimes, respectively.

In contrast, the dynamics of an isolated vortex subjected to a vertical shear in stratified non-rotating fluids has been little investigated so far. Boulanger et al. (2007, 2008) have considered the dynamics of a vortex slightly tilted with respect to the direction of stratification. However, the tilt of the vortex is not created by an external shear flow but by the method of generation of the vortex. Majda and Grote (1997) have studied the effect of a vertically sheared mean horizontal flow on a vortex pair but only by means of the reduced equations of Lilly (1983) which are valid in the limits of zero vertical and horizontal Froude numbers. Here and in chapter 5, we will study the dynamics of a Lamb-Oseen vortex in a sinusoidally sheared flow using the full Navier-Stokes equations under the Boussinesq approximation in the aim of testing Lilly's conjecture for the growth of vertical shear.

In the present chapter, two asymptotic analyses will be performed. The first analysis (§4.3) is an asymptotic expansion for small times starting from the initial conditions. It will be shown that the initial response of the vortex is non-hydrostatic whatever the magnitude of the stratification. The second asymptotic analysis (§4.4) is conducted for long vertical wavelength following a similar approach as used by Billant (2010) to describe the unstable interaction between columnar vortices in stratified-rotating fluids. This analysis will provide the governing equations for the displacements of the vortex center and its structure evolution due to the shear flow. We shall see that the vortex is not only advected in the direction of the shear flow but also in the orthogonal direction owing to its self-induced motion. In addition, it will be demonstrated that the vertical vorticity of the vortex decreases with time owing to dynamic and viscous effects. The initial non-hydrostatic regime evidenced in the first asymptotic analysis will be related to the transient excitation of internal waves at the start-up of the motion.

These asymptotic predictions will be compared to Direct Numerical Simulations (DNS) in chapter 5.

4.2 Formulation of the problem

4.2.1 Governing equations

We consider the incompressible Navier-Stokes equations written within the Boussinesq approximation

$$\boldsymbol{\nabla} \cdot \boldsymbol{u} = 0, \tag{4.3}$$

$$\frac{\partial \boldsymbol{u}}{\partial t} + (\boldsymbol{u} \cdot \boldsymbol{\nabla})\boldsymbol{u} = -\boldsymbol{\nabla}\left(\frac{p}{\rho_0}\right) + b\boldsymbol{e}_z + \nu \boldsymbol{\nabla}^2 \boldsymbol{u}, \tag{4.4}$$

$$\frac{\partial b}{\partial t} + \boldsymbol{u} \cdot \boldsymbol{\nabla} b + N^2 w = \kappa \nabla^2 b, \tag{4.5}$$

with $\boldsymbol{u} = (u, v, w)$ being the velocity field in cartesian coordinates (x, y, z), p the pressure, $b = -g\rho/\rho_0$ the buoyancy, g the gravity, $\boldsymbol{e}_z$ the vertical unit vector oriented upwards, ν the viscosity, and κ the mass diffusivity. The total density field ρ_t has been decomposed as $\rho_t(\boldsymbol{x}, t) = \rho_0 + \bar{\rho}(z) + \rho(\boldsymbol{x}, t)$, ρ_0 being a constant reference density, $\bar{\rho}$ a linear mean density profile varying with the vertical coordinate z, and $\rho(\boldsymbol{x}, t)$ a perturbation density. The Brunt-Väisälä frequency measuring the ambient stratification $N = \sqrt{-g/\rho_0 \mathrm{d}\bar{\rho}/\mathrm{d}z}$ is assumed constant.

4.2.2 Initial condition

The initial flow is made of a columnar vortex embedded in a sinusoidal shear flow of the form $\boldsymbol{U}_S = U(z)\boldsymbol{e}_x$, where $U(z) = \hat{U}_S \sin(\hat{k}_z z)$, $\boldsymbol{e}_x$ is the unit vector in the x direction, $\hat{U}_S$ the amplitude and $\hat{k}_z$ the vertical wavenumber.

The vortex is chosen to have a Lamb-Oseen profile:

$$\boldsymbol{u}_v = \frac{\Gamma}{2\pi r}\left[1 - \exp\left(-\frac{r^2}{a_0^2}\right)\right]\boldsymbol{e}_\theta, \tag{4.6}$$

where (r, θ, z) are cylindrical coordinates such that $x = r\cos(\theta)$ and $y = r\sin(\theta)$, Γ is the vortex circulation, a_0 its radius, and $\boldsymbol{e}_\theta$ the unit vector in the azimuthal direction.

The total initial flow is therefore:

$$\boldsymbol{u} = \boldsymbol{U}_S + \boldsymbol{u}_v. \tag{4.7}$$

4.2.3 Non-dimensionalization

The equations (4.3-4.5) are non-dimensionalized by the characteristics of the vortex: the length and time units are taken as the vortex radius a_0 and the turnover time scale $2\pi a_0^2/|\Gamma|$. Keeping the same notation for the non-dimensional variables, the dimensionless equations read

$$\boldsymbol{\nabla}_h \cdot \boldsymbol{u}_h + \frac{\partial w}{\partial z} = 0, \tag{4.8}$$

$$\frac{\partial \boldsymbol{u}_h}{\partial t} + (\boldsymbol{u}_h \cdot \boldsymbol{\nabla}_h)\boldsymbol{u}_h + w\frac{\partial \boldsymbol{u}_h}{\partial z} = -\boldsymbol{\nabla}_h p + \frac{1}{Re}\boldsymbol{\nabla}^2 \boldsymbol{u}_h, \tag{4.9}$$

$$\frac{\partial w}{\partial t} + \boldsymbol{u}_h \cdot \boldsymbol{\nabla}_h w + w\frac{\partial w}{\partial z} = -\frac{\partial p}{\partial z} + b + \frac{1}{Re}\nabla^2 w, \tag{4.10}$$

$$\frac{\partial b}{\partial t} + \boldsymbol{u}_h \cdot \boldsymbol{\nabla}_h b + w\frac{\partial b}{\partial z} = -\frac{w}{F_h^2} + \frac{1}{ReSc}\nabla^2 b, \tag{4.11}$$

where $\boldsymbol{u}_h$ denotes the horizontal velocity. The Reynolds and Froude numbers are defined as

$$Re = \frac{|\Gamma|}{2\pi\nu}, \quad F_h = \frac{|\Gamma|}{2\pi a_0^2 N}, \tag{4.12}$$

and $Sc = \nu/\kappa$ is the Schmidt number.

In non-dimensional form, the velocities of the shear flow and the vortex become

$$\boldsymbol{U}_S = U_S \sin(k_z z)\boldsymbol{e}_x, \quad \boldsymbol{u}_v = \frac{1-\exp(-r^2)}{r}\boldsymbol{e}_\theta, \tag{4.13}$$

where $U_S = \hat{U}_S/(|\Gamma|/2\pi a_0)$ and $k_z = \hat{k}_z a_0$. Without loss of generality, the vortex circulation has been considered positive. Indeed, a vortex with a negative circulation can be transformed into a positive one by simply changing the cartesian frame $(\boldsymbol{e}_x, \boldsymbol{e}_y, \boldsymbol{e}_z)$ into $(-\boldsymbol{e}_x, \boldsymbol{e}_y, -\boldsymbol{e}_z)$.

4.3 Initial dynamics of the vortex

4.3.1 Asymptotic problem

The initial dynamics of the vortex will be derived analytically from the equations (4.8-4.11) in the inviscid limit $Re = +\infty$ by expanding all the variables $\boldsymbol{q} = (u, v, w, p, b)$ in power series of t:

$$\boldsymbol{q}(x,y,z,t) = \boldsymbol{q}_0(x,y,z) + t\boldsymbol{q}_1(x,y,z) + t^2\boldsymbol{q}_2(x,y,z) + t^3\boldsymbol{q}_3(x,y,z) + O(t^4). \tag{4.14}$$

Then, each power of t can be solved successively. In the following, the shear flow and the vortex will be assumed to have the arbitrary profiles $\boldsymbol{U}_S = U(z)\boldsymbol{e}_x$ and $\boldsymbol{u}_v = u_\theta(r)\boldsymbol{e}_\theta$ as long as they do not need to be specified to solve the problem. The fluid domain is assumed unbounded in the horizontal direction.

Zeroth-order sub-problem

The zeroth-order problem reads

$$\boldsymbol{\nabla}\cdot\boldsymbol{u}_0 = 0, \tag{4.15}$$

$$\boldsymbol{u}_{h1} + u_0\frac{\partial \boldsymbol{u}_{h0}}{\partial x} + v_0\frac{\partial \boldsymbol{u}_{h0}}{\partial y} + w_0\frac{\partial \boldsymbol{u}_{h0}}{\partial z} = -\boldsymbol{\nabla}_h p_0, \tag{4.16}$$

$$w_1 + u_0\frac{\partial w_0}{\partial x} + v_0\frac{\partial w_0}{\partial y} + w_0\frac{\partial w_0}{\partial z} = -\frac{\partial p_0}{\partial z} + b_0, \tag{4.17}$$

$$b_1 + u_0\frac{\partial b_0}{\partial x} + v_0\frac{\partial b_0}{\partial y} + w_0\frac{\partial b_0}{\partial z} = -\frac{w_0}{F_h^2}. \tag{4.18}$$

As already explained in section 4.2.2, the initial flow is taken as the sum of the shear flow and the vortex velocity field, i.e.:

$$u_0 = -\sin(\theta)u_\theta(r) + U(z), \quad v_0 = \cos(\theta)u_\theta(r), \quad w_0 = 0, \quad b_0 = 0. \tag{4.19}$$

Although u_0 and v_0 are the horizontal velocity components in cartesian coordinates, it is more compact and convenient to express them in terms of the cylindrical coordinates (r, θ).

The solution (4.19) satisfies the divergence condition (4.15), and the density equation (4.18) immediately reduces to $b_1 = 0$. In order to find the remaining fields p_0, u_1, v_1 and w_1, the divergence of (4.16)-(4.17) is taken. This yields

$$\nabla^2 p_0 = 2\Omega \frac{\mathrm{d}r\Omega}{\mathrm{d}r}, \tag{4.20}$$

since $\boldsymbol{\nabla} \cdot \boldsymbol{u}_1 = 0$, where $\Omega = u_\theta / r$ is the vortex angular velocity. A solution is

$$p_0 = \int \xi \Omega^2(\xi) \mathrm{d}\xi, \tag{4.21}$$

which expresses the balance between the centrifugal force and the pressure gradient in the vortex. This balance is not affected by the presence of the shear flow at leading order because U is only a function of the vertical coordinate. Using (4.21), (4.16)-(4.17) yield the velocity field at first order:

$$u_1 = \frac{\sin(2\theta)}{2} r \frac{\mathrm{d}\Omega}{\mathrm{d}r} U(z), \quad v_1 = -\frac{1}{2}\left[\cos(2\theta) r \frac{\mathrm{d}\Omega}{\mathrm{d}r} + \zeta\right] U(z), \quad w_1 = 0, \tag{4.22}$$

with ζ the vertical vorticity:

$$\zeta = \frac{1}{r}\frac{\mathrm{d}r^2\Omega}{\mathrm{d}r}. \tag{4.23}$$

It is worth mentioning that (4.22) corresponds to a bending of the vortex as a whole without any deformation of its velocity distribution in the horizontal plane. Indeed, let us consider the translated vortex velocity

$$\boldsymbol{u}_v(\boldsymbol{x}, t) = \boldsymbol{u}_v(x - \Delta x(z,t), y - \Delta y(z,t)), \tag{4.24}$$

with Δx and Δy representing the cartesian displacements of the vortex center that are null at $t = 0$. For small Δx and Δy, we have:

$$\begin{aligned} \boldsymbol{u}_v(\boldsymbol{x}, t) &= \boldsymbol{u}_v(x, y) - \Delta x \frac{\partial \boldsymbol{u}_v}{\partial x} - \Delta y \frac{\partial \boldsymbol{u}_v}{\partial y} \\ &\quad + \frac{\Delta x^2}{2}\frac{\partial^2 \boldsymbol{u}_v}{\partial x^2} + \frac{\Delta y^2}{2}\frac{\partial^2 \boldsymbol{u}_v}{\partial y^2} + \Delta x \Delta y \frac{\partial^2 \boldsymbol{u}_v}{\partial x \partial y} + ... \end{aligned} \tag{4.25}$$

Since

$$\frac{\partial \boldsymbol{u}_v}{\partial x} = -\frac{\sin(2\theta)}{2} r \frac{\mathrm{d}\Omega}{\mathrm{d}r} \boldsymbol{e}_x + \frac{1}{2}\left[\cos(2\theta) r \frac{\mathrm{d}\Omega}{\mathrm{d}r} + \zeta\right] \boldsymbol{e}_y, \tag{4.26}$$

the velocity field at first order (4.22) is identical to the order $O(t)$ of (4.25) with the displacements $\Delta x = U(z)t$ and $\Delta y = 0$. It is important to stress that these results are valid for any vortex profile $u_\theta(r)$ and any shear flow profile $U(z)$.

First-order sub-problem

The set of equations at first order reads:

$$\boldsymbol{\nabla}_h \cdot \boldsymbol{u}_{h1} = 0, \tag{4.27}$$

$$2\boldsymbol{u}_{h2} + u_0 \frac{\partial \boldsymbol{u}_{h1}}{\partial x} + u_1 \frac{\partial \boldsymbol{u}_{h0}}{\partial x} + v_0 \frac{\partial \boldsymbol{u}_{h1}}{\partial y} + v_1 \frac{\partial \boldsymbol{u}_{h0}}{\partial y} = -\boldsymbol{\nabla}_h p_1, \tag{4.28}$$

$$2w_2 = -\frac{\partial p_1}{\partial z}, \tag{4.29}$$

$$b_2 = 0, \tag{4.30}$$

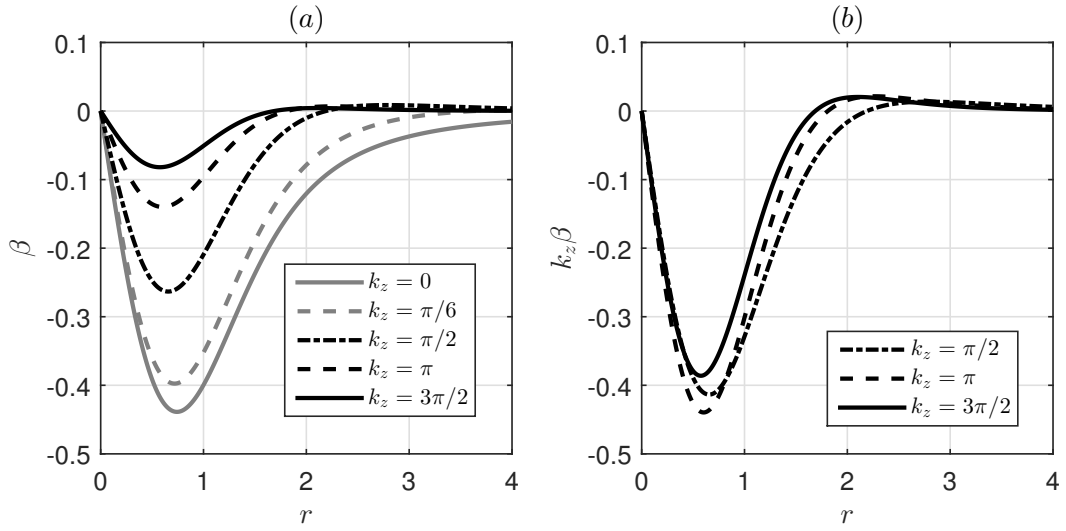

Figure 4.2: Variations of (a) β and (b) $k_z\beta$ against the radius r for different values of the vertical wavenumber: $k_z = 0$ (grey solid line), $k_z = \pi/6$ (grey dashed line), $k_z = \pi/2$ (black dash-dotted line), $k_z = \pi$ (black dashed line) and $k_z = 3\pi/2$ (black solid line).

since $w_1 = b_1 = 0$. Remarkably, (4.27-4.30) are independent of the Froude number. The divergence equation (4.27) is automatically satisfied. By imposing the divergence condition at second order $\boldsymbol{\nabla} \cdot \boldsymbol{u}_2 = 0$, we obtain from (4.28)-(4.29):

$$\nabla^2 p_1 = -2\cos(\theta)\frac{\mathrm{d}}{\mathrm{d}r}\left(\Omega\frac{\mathrm{d}r\Omega}{\mathrm{d}r}\right)U(z). \tag{4.31}$$

In order to solve this Poisson equation, we now have to specify the profile $U(z)$. In the following, we consider the sinusoidal shear flow $U(z) = U_S\sin(k_z z)$. The case of a linear shear flow is investigated in appendix A. We look for p_1 in the form

$$p_1 = \cos(\theta)\beta(r)U(z). \tag{4.32}$$

Then, (4.31) becomes:

$$\frac{\mathrm{d}^2\beta}{\mathrm{d}r^2} + \frac{1}{r}\frac{\mathrm{d}\beta}{\mathrm{d}r} - \left(k_z^2 + \frac{1}{r^2}\right)\beta = -\frac{\mathrm{d}}{\mathrm{d}r}\left(\frac{1}{r}\frac{\mathrm{d}r^2\Omega^2}{\mathrm{d}r}\right). \tag{4.33}$$

The solution is:

$$\beta(r) = -r\Omega^2(r) + \beta_b(r), \tag{4.34}$$

with

$$\beta_b(r) = k_z^2 I_1(k_z r)\int_r^{+\infty} K_1(k_z\xi)\xi^2\Omega^2(\xi)\mathrm{d}\xi + k_z^2 K_1(k_z r)\int_0^r I_1(k_z\xi)\xi^2\Omega^2(\xi)\mathrm{d}\xi, \tag{4.35}$$

where it has been imposed that β is not singular at $r = 0$ and vanishes at infinity. I_1 and K_1 are the modified Bessel functions of order one of the first and second kind, respectively. Figure 4.2 displays the function β for different vertical wavenumbers k_z in the case of the Lamb-Oseen profile (4.13). Starting from $k_z = 3\pi/2$, which corresponds to a dimensional vertical wavelength slightly larger than the vortex radius a_0, it is observed that β decreases as k_z diminishes to 0 (figure 4.2a). In the limit $k_z = 0$, we

have $\beta = -r\Omega^2$. For finite wavenumbers $\pi/2 \leqslant k_z \leqslant 3\pi/2$, figure 4.2*b* shows that $k_z\beta$ is almost independent of k_z. These values cover wavelengths ranging approximately from the vortex radius to four radii. Finally, using (4.34), (4.28)-(4.29) give the second-order velocities:

$$u_2 = -\frac{1}{4}\left[\frac{\mathrm{d}\beta_b}{\mathrm{d}r} + \frac{\beta_b(r)}{r} + \cos(2\theta)\left(\frac{\mathrm{d}\beta_b}{\mathrm{d}r} - \frac{\beta_b(r)}{r}\right)\right] U_S \sin(k_z z) + \frac{\sin(\theta)}{2}\left[\cos(2\theta)\frac{\mathrm{d}}{\mathrm{d}r}\left(\Omega - \frac{r}{2}\frac{\mathrm{d}\Omega}{\mathrm{d}r}\right) - \frac{\mathrm{d}}{\mathrm{d}r}\left(\frac{r}{2}\frac{\mathrm{d}\Omega}{\mathrm{d}r}\right)\right] U_S^2 \sin^2(k_z z), \tag{4.36}$$

$$v_2 = -\frac{\sin(2\theta)}{4}\left[\frac{\mathrm{d}\beta_b}{\mathrm{d}r} - \frac{\beta_b(r)}{r}\right] U_S \sin(k_z z) + \frac{\cos(\theta)}{2}\left[\cos(2\theta)\frac{\mathrm{d}}{\mathrm{d}r}\left(\frac{r}{2}\frac{\mathrm{d}\Omega}{\mathrm{d}r} - \Omega\right) + \frac{\mathrm{d}}{\mathrm{d}r}\left(\Omega + \frac{\zeta}{2}\right)\right] U_S^2 \sin^2(k_z z), \tag{4.37}$$

$$w_2 = -\frac{\cos(\theta)}{2}\beta(r) k_z U_S \cos(k_z z). \tag{4.38}$$

In contrast to its counterpart at first order, this second order velocity field does not correspond in general to a bending of the vortex without internal deformation. This is the case only in the limit $k_z \ll 1$ for which β_b can be neglected at leading order in (4.36)-(4.37) since

$$\beta_b = k_z^2\left[\frac{r}{2}\int_r^{+\infty} \xi\Omega^2(\xi)\mathrm{d}\xi + \frac{1}{2r}\int_0^r \xi^3\Omega^2(\xi)\mathrm{d}\xi\right] + O(k_z^4), \tag{4.39}$$

i.e. $\beta_b = O(k_z^2)$. The second order horizontal velocity field (4.36)-(4.37) is then equal to the order $O(t^2)$ of (4.25) with the displacements $\Delta x = U(z)t$ and $\Delta y = 0$ since

$$\frac{\partial^2 \boldsymbol{u}_v}{\partial x^2} = \sin(\theta)\left[\cos(2\theta)\frac{\mathrm{d}}{\mathrm{d}r}\left(\Omega - \frac{r}{2}\frac{\mathrm{d}\Omega}{\mathrm{d}r}\right) - \frac{\mathrm{d}}{\mathrm{d}r}\left(\frac{r}{2}\frac{\mathrm{d}\Omega}{\mathrm{d}r}\right)\right]\boldsymbol{e}_x + \cos(\theta)\left[\cos(2\theta)\frac{\mathrm{d}}{\mathrm{d}r}\left(\frac{r}{2}\frac{\mathrm{d}\Omega}{\mathrm{d}r} - \Omega\right) + \frac{\mathrm{d}}{\mathrm{d}r}\left(\Omega + \frac{\zeta}{2}\right)\right]\boldsymbol{e}_y. \tag{4.40}$$

Second-order sub-problem

At second order, we do not consider all the equations but only the buoyancy equation:

$$3b_3 = -\frac{w_2}{F_h^2}. \tag{4.41}$$

This yields the first non-zero term in the expansion of the buoyancy:

$$b_3 = \frac{k_z U_S}{6F_h^2}\cos(\theta)\beta(r)\cos(k_z z). \tag{4.42}$$

This shows that $w = w_2 t^2$ and $b = b_3 t^3$ at leading order. Using (4.41), the ratio of the vertical acceleration to the buoyancy is therefore

$$\left|\frac{1}{b}\frac{\mathrm{D}w}{\mathrm{D}t}\right| = 6\left(\frac{F_h}{t}\right)^2. \tag{4.43}$$

Hence, for small times such that $t \ll F_h$, the buoyancy is negligible relative to the vertical acceleration, meaning that the dynamics is initially non-hydrostatic. This

transient non-hydrostatic phase lasts until $t = O(F_h)$ whereas for $t \gg F_h$, a hydrostatic regime is expected to be recovered if $F_h < 1$. This subsequent hydrostatic regime will occur for $t \ll 1$ as assumed here, only if $F_h \ll 1$. We can further remark that the vertical velocity w_2 and the buoyancy b_3 are both proportional to $k_z\beta$. From the behaviour of the function β displayed in figure 4.2, we can deduce that these two quantities are therefore proportional to k_z for small k_z whereas they are weakly sensitive to the variation of the vertical wavenumber for $\pi/2 \leqslant k_z \leqslant 3\pi/2$.

4.3.2 Summary

The latter analysis shows that at first order in time, the vortex is simply advected as a whole in the x direction by $\Delta x = U(z)t$. Internal deformation and generation of vertical motions occur only at order $O(t^2)$. At this order, there is no displacement of the vortex implying that the higher orders in the displacements $(\Delta x, \Delta y)$ are at least $O(t^3)$ or higher. This agrees with Jones' observation (Jones, 1995) in stratified rotating fluids that the initial effect of the vertical shear is a bending of the vortex in the streamwise direction only. We can further remark that the flow field at order $O(t^2)$ does not depend on the Froude number but depends only on the vertical wavenumber k_z of the sinusoidal shear flow. In other words, the stratification has no effect on the initial dynamics of the vortex. We have not determined the flow field at order $O(t^3)$ but it is clear that it would also be independent of the Froude number. The stratification only intervenes in the buoyancy at order $O(t^3)$. These results show the existence of an initial transient non-hydrostatic regime whose duration scales like the Froude number.

In the next section, we shall conduct an asymptotic analysis for long vertical wavelengths which is valid for longer times. This investigation will show that the initial non-hydrostatic phase is due to the generation of internal waves and that the vortex is also displaced in the y direction for finite times.

4.4 Long-wavelength dynamics of the vortex

4.4.1 Formulation of the problem

In section §4.3, we have studied the initial dynamics of the vortex by means of an asymptotic expansion in powers of t for any vertical wavenumber. The dynamics of the vortex can be also described asymptotically for finite time in the limit of small vertical wavenumber. Indeed, when $k_z = 0$, i.e. in the two-dimensional limit, an exact solution is

$$\boldsymbol{u}_h = \boldsymbol{u}_{h0}(x - Ut, y) + U\boldsymbol{e}_x, \tag{4.44}$$

which means that the vortex is simply advected at constant speed U. This solution is expected to remain valid at leading order when $\varepsilon = k_z^2 F_h^2$ is such that $\varepsilon \ll 1$, i.e. when the vertical variations $\partial/\partial z$ of $U(z)$ rescaled by the Froude number F_h are weak:

$$\sqrt{\varepsilon} = O\left(F_h \frac{\partial}{\partial z}\right) \ll 1. \tag{4.45}$$

We consider that $k_z F_h$ is small and not simply that $k_z \ll 1$ because of the self-similarity of strongly stratified fluids (Billant and Chomaz, 2001). Indeed, this self-similarity implies that the horizontal velocity depends on F_h and k_z only through their product

$k_z F_h$ when $F_h \ll 1$. This means that the condition $\varepsilon \ll 1$ can be fulfilled either by having $k_z \ll 1$ or $F_h \ll 1$. In each case, the other parameter F_h or k_z can be large provided that $k_z F_h \ll 1$. We will keep the asymptotic analysis as general as possible in order to encompass both cases. Nevertheless, some parts of the analysis will assume $F_h \ll 1$ in order to simplify the calculations. Consistently with (4.45), we rescale the vertical coordinate and wavenumber as follows:

$$\tilde{z} = \frac{\sqrt{\varepsilon}}{F_h} z, \quad \tilde{k}_z = \frac{k_z F_h}{\sqrt{\varepsilon}}, \tag{4.46}$$

so that $\tilde{k}_z = O(1)$ and $\partial/\partial\tilde{z} = O(1)$. Then, we can look for the horizontal velocity in the form of an asymptotic expansion:

$$\boldsymbol{u}_h = \boldsymbol{u}_{h0}(x - U(\tilde{z})t - \delta x, y - \delta y, \tilde{\eta}, \tau) + U(\tilde{z})\boldsymbol{e}_x + \varepsilon \boldsymbol{u}_{h1}(x, y, \tilde{z}, t, \tilde{\eta}, \tau) + O(\varepsilon^2), \tag{4.47}$$

where $\delta x(\tilde{z}, \tilde{\eta}, \tau)$ and $\delta y(\tilde{z}, \tilde{\eta}, \tau)$ are corrections to the displacements of the vortex center varying along the vertical and with the slow time scale $\tau = \varepsilon t$. In contrast to classical multiscale expansions, the fast and slow times t and τ should not be viewed as completely independent variables. We shall see indeed that the slow time evolution depends on the fast time. The introduction of τ is simply a convenient way to separate the dynamics at different orders[1]. Similarly, a slow vertical length scale $\tilde{\eta} = \varepsilon\tilde{z}$ is introduced. We also define local horizontal cartesian coordinates $(\tilde{x}, \tilde{y})$ centered on the vortex center at the level $\tilde{z}$:

$$\tilde{x} = x - U(\tilde{z})t - \delta x(\tilde{z}, \tilde{\eta}, \tau), \quad \tilde{y} = y - \delta y(\tilde{z}, \tilde{\eta}, \tau). \tag{4.48}$$

The cylindrical coordinates associated to these new coordinates are denoted with a tilde $(\tilde{x}, \tilde{y}) = (\tilde{r}\cos(\tilde{\theta}), \tilde{r}\sin(\tilde{\theta}))$. In addition to the horizontal velocity, the other fields are expanded in the form:

$$p = p_0(\tilde{x}, \tilde{y}, \tilde{\eta}, \tau) + \varepsilon p_1(\tilde{x}, \tilde{y}, \tilde{z}, t, \tilde{\eta}, \tau) + O(\varepsilon^2), \tag{4.49}$$

$$w = \sqrt{\varepsilon} F_h \left[w_0(\tilde{x}, \tilde{y}, \tilde{z}, t, \tilde{\eta}, \tau) + \varepsilon w_1(\tilde{x}, \tilde{y}, \tilde{z}, t, \tilde{\eta}, \tau) + O(\varepsilon^2) \right], \tag{4.50}$$

$$b = \frac{\sqrt{\varepsilon}}{F_h} \left[b_0(\tilde{x}, \tilde{y}, \tilde{z}, t, \tilde{\eta}, \tau) + \varepsilon b_1(\tilde{x}, \tilde{y}, \tilde{z}, t, \tilde{\eta}, \tau) + O(\varepsilon^2) \right], \tag{4.51}$$

where the vertical velocity and the buoyancy have been scaled by $\sqrt{\varepsilon}F_h$ and $\sqrt{\varepsilon}/F_h$, respectively, for convenience. These scalings are equivalent to those of Billant and Chomaz (2001) for strongly stratified flows. Weak viscous effects will be also taken into account by assuming $1/Re = O(\varepsilon)$. Thus, we write:

$$\frac{1}{Re} = \frac{\varepsilon}{\tilde{Re}}, \tag{4.52}$$

where $\tilde{Re} = O(1)$.

The expansions (4.47, 4.49, 4.50, 4.51) will be introduced in the governing equations (4.8-4.11). It will be useful to consider also the equation for the vertical vorticity $\zeta = \partial v/\partial x - \partial u/\partial y$:

$$\frac{\partial \zeta}{\partial t} + \boldsymbol{u}_h \cdot \boldsymbol{\nabla}_h \zeta + w \frac{\partial \zeta}{\partial z} = \boldsymbol{\omega}_h \cdot \boldsymbol{\nabla}_h w + \zeta \frac{\partial w}{\partial z} + \frac{1}{Re} \nabla^2 \zeta, \tag{4.53}$$

[1]However, another possible choice for the scaling of the slow time is discussed at the end in the light of the final equations.

where $\boldsymbol{\omega}_h$ is the horizontal vorticity.

Because of the introduction of the local coordinates $(\tilde{x}, \tilde{y})$ that depend on t, τ, $\tilde{z}$ and $\tilde{\eta}$ (see (4.48)), the time and vertical derivatives of any quantity Λ in (4.8-4.11) and (4.53) become:

$$\frac{\partial \Lambda}{\partial t} = \left(\frac{\partial \Lambda}{\partial t}\right)_{\tilde{x},\tilde{y},\tau} - U(\tilde{z})\frac{\partial \Lambda}{\partial \tilde{x}} + \varepsilon\left[\left(\frac{\partial \Lambda}{\partial \tau}\right)_{\tilde{x},\tilde{y},t} - \frac{\partial \delta x}{\partial \tau}\frac{\partial \Lambda}{\partial \tilde{x}} - \frac{\partial \delta y}{\partial \tau}\frac{\partial \Lambda}{\partial \tilde{y}}\right], \tag{4.54}$$

$$\begin{aligned}\frac{\partial \Lambda}{\partial z} = {} & \frac{\sqrt{\varepsilon}}{F_h}\left[\left(\frac{\partial \Lambda}{\partial \tilde{z}}\right)_{\tilde{x},\tilde{y},\tilde{\eta}} - t\frac{\mathrm{d}U}{\mathrm{d}\tilde{z}}\frac{\partial \Lambda}{\partial \tilde{x}} - \left(\frac{\partial \delta x}{\partial \tilde{z}}\right)_{\tilde{\eta}}\frac{\partial \Lambda}{\partial \tilde{x}} - \left(\frac{\partial \delta y}{\partial \tilde{z}}\right)_{\tilde{\eta}}\frac{\partial \Lambda}{\partial \tilde{y}}\right] \\ & + \frac{\varepsilon\sqrt{\varepsilon}}{F_h}\left[\left(\frac{\partial \Lambda}{\partial \tilde{\eta}}\right)_{\tilde{x},\tilde{y},\tilde{z}} - \left(\frac{\partial \delta x}{\partial \tilde{\eta}}\right)_{\tilde{z}}\frac{\partial \Lambda}{\partial \tilde{x}} - \left(\frac{\partial \delta y}{\partial \tilde{\eta}}\right)_{\tilde{z}}\frac{\partial \Lambda}{\partial \tilde{y}}\right].\end{aligned} \tag{4.55}$$

It is important to remark the presence of the term $t\mathrm{d}U/\mathrm{d}\tilde{z}$ in (4.55). Because of this term, the long-wavelength assumption (4.45) is expected to be no longer valid when $\sqrt{\varepsilon}t\mathrm{d}U/\mathrm{d}\tilde{z} > 1$, i.e. when $k_z F_h U_S t > 1$ for the shear flow profile $U = U_S \sin(k_z z)$.

4.4.2 Leading order problem

At zeroth-order, equations (4.8-4.11) reduce to:

$$\boldsymbol{\nabla}_h \cdot \boldsymbol{u}_{h0} = 0, \tag{4.56}$$

$$(\boldsymbol{u}_{h0} \cdot \boldsymbol{\nabla}_h)\, \boldsymbol{u}_{h0} = -\boldsymbol{\nabla}_h p_0, \tag{4.57}$$

$$F_h^2\left[\left(\frac{\partial w_0}{\partial t}\right)_{\tilde{x},\tilde{y},\tau} + \boldsymbol{u}_{h0}\cdot\boldsymbol{\nabla}_h w_0\right] = -\frac{\partial p_0}{\partial \tilde{z}} + b_0, \tag{4.58}$$

$$\left(\frac{\partial b_0}{\partial t}\right)_{\tilde{x},\tilde{y},\tau} + \boldsymbol{u}_{h0}\cdot\boldsymbol{\nabla}_h b_0 = -w_0, \tag{4.59}$$

where the operator $\boldsymbol{\nabla}_h$ is with respect to $\tilde{x}$ and $\tilde{y}$, or equivalently $\tilde{r}$ and $\tilde{\theta}$. Note that the advection by the shear flow $U(\tilde{z})\partial/\partial\tilde{x}$ is absent in (4.57-4.59) since it cancels with the term coming from the time derivative (see (4.54)). The equations (4.56)-(4.57) are the steady two-dimensional Euler equations. Consistently with the initial conditions chosen in §4.2.2, we take an axisymmetric vortex at leading order, namely $\boldsymbol{u}_{h0} = \tilde{r}\Omega(\tilde{r}, \tilde{\eta}, \tau)\boldsymbol{e}_{\tilde{\theta}}$. Then, (4.57) reduces to:

$$\frac{\partial p_0}{\partial \tilde{r}} = \tilde{r}\Omega^2(\tilde{r}, \tilde{\eta}, \tau), \tag{4.60}$$

which is the balance between the centrifugal force and the radial pressure gradient as if the shear flow were absent. Therefore, the vertical pressure gradient is given by

$$\frac{\partial p_0}{\partial \tilde{z}} = \frac{\partial \tilde{r}}{\partial \tilde{z}}\frac{\partial p_0}{\partial \tilde{r}} = -\left[\cos(\tilde{\theta})\left(\frac{\mathrm{d}U}{\mathrm{d}\tilde{z}}t + \frac{\partial \delta x}{\partial \tilde{z}}\right) + \sin(\tilde{\theta})\frac{\partial \delta y}{\partial \tilde{z}}\right]\tilde{r}\Omega^2 \tag{4.61}$$

since we have at leading order:

$$\frac{\partial \tilde{r}}{\partial \tilde{z}} = -\cos(\tilde{\theta})\left(\frac{\mathrm{d}U}{\mathrm{d}\tilde{z}}t + \frac{\partial \delta x}{\partial \tilde{z}}\right) - \sin(\tilde{\theta})\frac{\partial \delta y}{\partial \tilde{z}}. \tag{4.62}$$

Using (4.61), the equations (4.58) and (4.59) can be written as

$$F_h^2\left[\frac{\partial w_0}{\partial t}+\Omega\frac{\partial w_0}{\partial\tilde{\theta}}\right]=b_0+\left[\cos(\tilde{\theta})\left(\frac{\mathrm{d}U}{\mathrm{d}\tilde{z}}t+\frac{\partial\delta x}{\partial\tilde{z}}\right)+\sin(\tilde{\theta})\frac{\partial\delta y}{\partial\tilde{z}}\right]\tilde{r}\Omega^2, \tag{4.63}$$

$$\frac{\partial b_0}{\partial t}+\Omega\frac{\partial b_0}{\partial\tilde{\theta}}=-w_0, \tag{4.64}$$

where the fact that the time derivative $\partial/\partial t$ is taken at constant $\tilde{x}$, $\tilde{y}$ and τ and the vertical derivative $\partial/\partial\tilde{z}$ at constant $\tilde{x}$, $\tilde{y}$ and $\tilde{\eta}$ will be no longer mentioned to simplify the notation. To solve (4.63)-(4.64), w_0 and b_0 are decomposed into two components:

$$w_0=w_f(\tilde{r},\tilde{\theta},\tilde{z},t,\tilde{\eta},\tau)+w_s(\tilde{r},\tilde{\theta},\tilde{z},\tilde{\eta},\tau),\quad b_0=b_f(\tilde{r},\tilde{\theta},\tilde{z},t,\tilde{\eta},\tau)+b_s(\tilde{r},\tilde{\theta},\tilde{z},\tilde{\eta},\tau), \tag{4.65}$$

that are solution of

$$F_h^2\left[\frac{\partial w_f}{\partial t}+\Omega\frac{\partial w_f}{\partial\tilde{\theta}}\right]=b_f+\cos(\tilde{\theta})\tilde{r}\Omega^2\frac{\mathrm{d}U}{\mathrm{d}\tilde{z}}t, \tag{4.66}$$

$$\frac{\partial b_f}{\partial t}+\Omega\frac{\partial b_f}{\partial\tilde{\theta}}=-w_f, \tag{4.67}$$

and

$$F_h^2\Omega\frac{\partial w_s}{\partial\tilde{\theta}}=b_s+\left[\cos(\tilde{\theta})\frac{\partial\delta x}{\partial\tilde{z}}+\sin(\tilde{\theta})\frac{\partial\delta y}{\partial\tilde{z}}\right]\tilde{r}\Omega^2, \tag{4.68}$$

$$\Omega\frac{\partial b_s}{\partial\tilde{\theta}}=-w_s. \tag{4.69}$$

Deriving the analytic expressions of the slowly evolving components (w_s, b_s) is straightforward:

$$w_s=\left[-\sin(\tilde{\theta})\frac{\partial\delta x}{\partial\tilde{z}}+\cos(\tilde{\theta})\frac{\partial\delta y}{\partial\tilde{z}}\right]\mathcal{C}\Omega, \tag{4.70}$$

$$b_s=-\left[\cos(\tilde{\theta})\frac{\partial\delta x}{\partial\tilde{z}}+\sin(\tilde{\theta})\frac{\partial\delta y}{\partial\tilde{z}}\right]\mathcal{C}, \tag{4.71}$$

where

$$\mathcal{C}(\tilde{r},\tilde{\eta},\tau)=\frac{\tilde{r}\Omega^2}{1-F_h^2\Omega^2} \tag{4.72}$$

has no critical point and is well-defined when $F_h<1$. Determining the fast components w_f and b_f is more difficult. They can be found in the form

$$w_f=w_p+w_w,\quad b_f=b_p+b_w, \tag{4.73}$$

where (w_p, b_p) is a particular solution of (4.66)-(4.67):

$$w_p=\left[\cos(\tilde{\theta})\mathcal{F}-t\sin(\tilde{\theta})\Omega\right]\mathcal{C}\frac{\mathrm{d}U}{\mathrm{d}\tilde{z}}, \tag{4.74}$$

$$b_p=-\left[2F_h\sin(\tilde{\theta})\mathcal{G}+t\cos(\tilde{\theta})\right]\mathcal{C}\frac{\mathrm{d}U}{\mathrm{d}\tilde{z}}, \tag{4.75}$$

with

$$\mathcal{F}(\tilde{r},\tilde{\eta},\tau)=\frac{1+F_h^2\Omega^2}{1-F_h^2\Omega^2},\quad \mathcal{G}(\tilde{r},\tilde{\eta},\tau)=\frac{F_h\Omega}{1-F_h^2\Omega^2}, \tag{4.76}$$

while (w_w, b_w) is a homogeneous solution of (4.66)-(4.67) corresponding to internal waves oscillating at the non-dimensional frequency $1/F_h$:

$$w_w = \frac{1}{F_h^2}\cos(\Omega t-\tilde\theta)\left[\mathcal{C}_1(\tilde r,\tilde z,\tilde\eta,\tau)\cos\left(\frac{t}{F_h}\right)+\mathcal{C}_2(\tilde r,\tilde z,\tilde\eta,\tau)\sin\left(\frac{t}{F_h}\right)\right] + \frac{1}{F_h^2}\sin(\Omega t-\tilde\theta)\left[\mathcal{S}_1(\tilde r,\tilde z,\tilde\eta,\tau)\cos\left(\frac{t}{F_h}\right)+\mathcal{S}_2(\tilde r,\tilde z,\tilde\eta,\tau)\sin\left(\frac{t}{F_h}\right)\right], \tag{4.77}$$

$$b_w = \frac{1}{F_h}\cos(\Omega t-\tilde\theta)\left[\mathcal{C}_2(\tilde r,\tilde z,\tilde\eta,\tau)\cos\left(\frac{t}{F_h}\right)-\mathcal{C}_1(\tilde r,\tilde z,\tilde\eta,\tau)\sin\left(\frac{t}{F_h}\right)\right] + \frac{1}{F_h}\sin(\Omega t-\tilde\theta)\left[\mathcal{S}_2(\tilde r,\tilde z,\tilde\eta,\tau)\cos\left(\frac{t}{F_h}\right)-\mathcal{S}_1(\tilde r,\tilde z,\tilde\eta,\tau)\sin\left(\frac{t}{F_h}\right)\right], \tag{4.78}$$

where $\mathcal{C}_1$, $\mathcal{C}_2$, $\mathcal{S}_1$ and $\mathcal{S}_2$ are arbitrary functions. They are deduced by imposing that the vertical velocity and the buoyancy are null at $t=\tau=0$ since the vortex is strictly vertical at the start-up of the evolution. This implies that $\delta x(\tilde z,\tilde\eta,0)=\delta y(\tilde z,\tilde\eta,0)=0$ so that w_s and b_s are zero at $\tau=0$. Therefore, we have to impose $w_f=b_f=0$ at $t=\tau=0$, yielding:

$$\mathcal{C}_1=-F_h^2\mathcal{C}\mathcal{F}\frac{\mathrm{d}U}{\mathrm{d}\tilde z},\quad \mathcal{S}_1=0,\quad \mathcal{C}_2=0,\quad \mathcal{S}_2=-2F_h^2\mathcal{C}\mathcal{G}\frac{\mathrm{d}U}{\mathrm{d}\tilde z}. \tag{4.79}$$

Strictly speaking, $\mathcal{C}_1$ and $\mathcal{S}_2$ are fixed at $\tau=0$ so that we should set $\mathcal{C}_1=-F_h^2\mathcal{C}(\tilde r,\tilde\eta,\tau=0)\mathcal{F}(\tilde r,\tilde\eta,\tau=0)\mathrm{d}U/\mathrm{d}\tilde z$ and similarly for $\mathcal{S}_2$. However, it is also legitimate to impose (4.79) whatever τ since the evolution over the slow time scale τ is a higher order effect. Finally, collecting (4.70)-(4.71), (4.74)-(4.75), and (4.77)-(4.78) give the complete expressions of w_0 and b_0:

$$w_0 = \left[\cos(\tilde\theta)\mathcal{F}-t\sin(\tilde\theta)\Omega-\mathcal{F}\cos(\Omega t-\tilde\theta)\cos\left(\frac{t}{F_h}\right)-2\mathcal{G}\sin(\Omega t-\tilde\theta)\sin\left(\frac{t}{F_h}\right)\right]\mathcal{C}\frac{\mathrm{d}U}{\mathrm{d}\tilde z} + \left[-\sin(\tilde\theta)\frac{\partial\delta x}{\partial\tilde z}+\cos(\tilde\theta)\frac{\partial\delta y}{\partial\tilde z}\right]\mathcal{C}\Omega, \tag{4.80}$$

$$b_0 = -F_h\left[2\sin(\tilde\theta)\mathcal{G}+\frac{t}{F_h}\cos(\tilde\theta)+2\mathcal{G}\sin(\Omega t-\tilde\theta)\cos\left(\frac{t}{F_h}\right) - \mathcal{F}\cos(\Omega t-\tilde\theta)\sin\left(\frac{t}{F_h}\right)\right]\mathcal{C}\frac{\mathrm{d}U}{\mathrm{d}\tilde z} - \left[\cos(\tilde\theta)\frac{\partial\delta x}{\partial\tilde z}+\sin(\tilde\theta)\frac{\partial\delta y}{\partial\tilde z}\right]\mathcal{C}. \tag{4.81}$$

The vertical velocity and buoyancy (4.80)-(4.81) contain three types of terms evolving on three different time scales:

1. the terms corresponding to w_p and b_p that grow linearly with the fast time t in response to the shear flow $U(\tilde z)$,
2. internal waves oscillating at the frequency $1/F_h$ (i.e. the Brunt-Väisälä frequency in dimensional units) that are generated at the onset of the motion,
3. the terms coming from w_s and b_s due to the slow evolution of the displacement corrections δx and δy.

In the limit $t\ll 1$, $\tau\ll 1$, (4.80)-(4.81) rescaled by $\sqrt{\varepsilon}F_h$ and $\sqrt{\varepsilon}/F_h$ become at leading order

$$\sqrt{\varepsilon}F_h w_0=\frac{1}{2}\cos(\theta)r\Omega^2\frac{\mathrm{d}U}{\mathrm{d}z}t^2+O(t^3,\tau), \tag{4.82}$$

$$\frac{\sqrt{\varepsilon}}{F_h}b_0=-\frac{1}{6F_h^2}\cos(\theta)r\Omega^2\frac{\mathrm{d}U}{\mathrm{d}z}t^3+O(t^4,\tau), \tag{4.83}$$

since δx and δy are at most $O(\tau) = O(\varepsilon t)$ for $\tau \ll 1$ because $\delta x(\tilde{z}, \tilde{\eta}, 0) = \delta y(\tilde{z}, \tilde{\eta}, 0) = 0$. When $U = U_S \sin(\tilde{k}_z \tilde{z})$, (4.82) and (4.83) are identical to the expressions (4.38) and (4.42) obtained for small time in §4.3 in the limit $k_z \ll 1$ since then $\beta = -r\Omega^2 + O(k_z^2)$.

It can be concluded that the initial transient non-hydrostatic regime found in §4.3 comes from the generation of internal waves of frequency $1/F_h$. Indeed, if the waves (4.77)-(4.78) were absent in (4.80)-(4.81), the vertical velocity and buoyancy would mostly grow linearly with time $w \propto F_h^2 t$ and $b \propto t$ according to (4.74)-(4.75). These scaling laws fulfill the typical scaling associated to the hydrostatic balance, $w = O(F_h^2 b)$ in contrast to the full solution (4.80)-(4.81). For large time, the amplitude of the waves w_w, b_w will become small relative to w_p, b_p that grow linearly with time. Hence, the hydrostatic balance will be recovered. In addition, (4.80)-(4.81) show that the waves are advected differentially by the azimuthal motion in the vortex (terms $\cos(\Omega t - \tilde{\theta})$ and $\sin(\Omega t - \tilde{\theta})$). We will see in §4.4.4 that their influence quickly dies out for this reason.

4.4.3 First-order problem

At first order, it is more convenient to consider the divergence equation and the equation for the vertical vorticity $\zeta_1 = \partial v_1/\partial \tilde{x} - \partial u_1/\partial \tilde{y}$:

$$\boldsymbol{\nabla}_h \cdot \boldsymbol{u}_{h1} = -\left[\frac{\partial w_0}{\partial \tilde{z}} + \frac{\partial \tilde{r}}{\partial \tilde{z}}\frac{\partial w_0}{\partial \tilde{r}} + \frac{\partial \tilde{\theta}}{\partial \tilde{z}}\frac{\partial w_0}{\partial \tilde{\theta}}\right], \tag{4.84}$$

$$\begin{aligned}\frac{\partial \zeta_1}{\partial t} + \boldsymbol{u}_{h0}\cdot\boldsymbol{\nabla}_h\zeta_1 + \boldsymbol{u}_{h1}\cdot\boldsymbol{\nabla}_h\zeta_0 = &-\frac{\partial \zeta_0}{\partial \tau} + \cos(\tilde{\theta})\frac{\partial \delta x}{\partial \tau}\frac{\partial \zeta_0}{\partial \tilde{r}} + \sin(\tilde{\theta})\frac{\partial \delta y}{\partial \tau}\frac{\partial \zeta_0}{\partial \tilde{r}} \\ &+ \left[\frac{\mathrm{d}U}{\mathrm{d}\tilde{z}} + \frac{\partial \tilde{r}}{\partial \tilde{z}}\frac{\partial u_0}{\partial \tilde{r}} + \frac{\partial \tilde{\theta}}{\partial \tilde{z}}\frac{\partial u_0}{\partial \tilde{\theta}}\right]\frac{\partial w_0}{\partial \tilde{y}} - \left[\frac{\partial \tilde{r}}{\partial \tilde{z}}\frac{\partial v_0}{\partial \tilde{r}} + \frac{\partial \tilde{\theta}}{\partial \tilde{z}}\frac{\partial v_0}{\partial \tilde{\theta}}\right]\frac{\partial w_0}{\partial \tilde{x}} \\ &+ \zeta_0\left[\frac{\partial w_0}{\partial \tilde{z}} + \frac{\partial \tilde{r}}{\partial \tilde{z}}\frac{\partial w_0}{\partial \tilde{r}} + \frac{\partial \tilde{\theta}}{\partial \tilde{z}}\frac{\partial w_0}{\partial \tilde{\theta}}\right] - w_0\frac{\partial \tilde{r}}{\partial \tilde{z}}\frac{\partial \zeta_0}{\partial \tilde{r}} \\ &+ \frac{\nabla^2\zeta_0}{\tilde{R}e},\end{aligned} \tag{4.85}$$

where $\zeta_0 = 2\Omega + \tilde{r}\partial\Omega/\partial\tilde{r}$ and

$$\frac{\partial \tilde{\theta}}{\partial \tilde{z}} = \frac{\sin(\tilde{\theta})}{\tilde{r}}\left[\frac{\mathrm{d}U}{\mathrm{d}\tilde{z}}t + \frac{\partial \delta x}{\partial \tilde{z}}\right] - \frac{\cos(\tilde{\theta})}{\tilde{r}}\frac{\partial \delta y}{\partial \tilde{z}} \tag{4.86}$$

at leading order while $\partial\tilde{r}/\partial\tilde{z}$ has been given previously in (4.62). The forcing terms in the left-hand side of (4.85) correspond to the slow evolution of ζ_0 and the displacements δx, δy (first row), the tilting of horizontal vorticity into vertical vorticity (second row), the stretching and vertical advection of vertical vorticity (third row), and viscous effects (last row).

The viscous term in (4.85) reads

$$\nabla^2\zeta_0 = \frac{\partial^2\zeta_0}{\partial\tilde{r}^2} + \frac{1}{\tilde{r}}\frac{\partial\zeta_0}{\partial\tilde{r}} + \frac{\varepsilon}{F_h^2}\frac{\partial^2\zeta_0}{\partial\tilde{z}^2}. \tag{4.87}$$

This expression suggests that we should neglect the second term since $\varepsilon \ll 1$. However, we will keep it for two reasons: first, the condition $\varepsilon \ll 1$ can be fulfilled either by having $k_z \ll 1$ or $F_h \ll 1$. In the latter case, the parameter $\varepsilon/F_h^2 = k_z^2$ can be large

since a wavenumber k_z of order unity or larger can satisfy the condition $k_z F_h \ll 1$. Secondly, because the vertical shear grows algebraically with time as shown by (4.62) and (4.86), the second term can become large when $\varepsilon/F_h^2(t\mathrm{d}U/\mathrm{d}\tilde{z})^2 > 1$[2]. Actually, this is the main reason why this term may have an important effect. Hence, we will take into account only the terms proportional to $t\mathrm{d}U/\mathrm{d}\tilde{z}$ in (4.62)-(4.86) and neglect the others to express the viscous term (4.87). This yields:

$$\begin{aligned}\nabla^2\zeta_0 &= \frac{\partial^2\zeta_0}{\partial\tilde{r}^2}+\frac{1}{\tilde{r}}\frac{\partial\zeta_0}{\partial\tilde{r}}+\frac{\varepsilon}{2F_h^2}\left(\frac{\partial^2\zeta_0}{\partial\tilde{r}^2}+\frac{1}{\tilde{r}}\frac{\partial\zeta_0}{\partial\tilde{r}}\right)\left(\frac{\mathrm{d}U}{\mathrm{d}\tilde{z}}\right)^2 t^2-\frac{\varepsilon}{F_h^2}\cos(\tilde{\theta})\frac{\partial\zeta_0}{\partial\tilde{r}}\frac{\mathrm{d}^2U}{\mathrm{d}\tilde{z}^2}t \\ &\quad+\frac{\varepsilon}{2F_h^2}\cos(2\tilde{\theta})\left(\frac{\partial^2\zeta_0}{\partial\tilde{r}^2}-\frac{1}{\tilde{r}}\frac{\partial\zeta_0}{\partial\tilde{r}}\right)\left(\frac{\mathrm{d}U}{\mathrm{d}\tilde{z}}\right)^2 t^2. \qquad (4.88)\end{aligned}$$

We emphasize again that the term $O(\varepsilon/F_h^2)$ is taken into account in order to encompass both cases $k_z \ll 1$ or $F_h \ll 1$. However, in the former case, this term is expected to be negligible as long as $k_z t\mathrm{d}U/\mathrm{d}\tilde{z} \ll 1$.

We see that the viscous term contains azimuthal modes $m = 0$, 1, and 2. In fact, the other forcing terms in (4.84) and (4.85) can be also decomposed into these three azimuthal modes. Looking for example at the divergence equation (4.84), we see two categories of forcing terms. First, the term $\partial w_0/\partial\tilde{z}$ will produce terms proportional to $\cos(\tilde{\theta})$ or $\sin(\tilde{\theta})$. Secondly, the terms $\partial\tilde{r}/\partial\tilde{z}\partial w_0/\partial\tilde{r}$ and $\partial\tilde{\theta}/\partial\tilde{z}\partial w_0/\partial\tilde{\theta}$ will give azimuthal modes of the form $\cos(m\tilde{\theta})$ and $\sin(m\tilde{\theta})$ with $m = 0$ or $m = 2$. The right-hand side of (4.85) can be decomposed similarly into the azimuthal modes $m = 0$, $m = 1$, and $m = 2$. For this reason, (4.84) and (4.85) can be re-written as follows:

$$\boldsymbol{\nabla}_h \cdot \boldsymbol{u}_{h1} = -\frac{\partial w_0}{\partial\tilde{z}} + \delta D_0 + \delta D_2, \qquad (4.89)$$

$$\begin{aligned}\frac{\partial\zeta_1}{\partial t}+\Omega\frac{\partial\zeta_1}{\partial\tilde{\theta}}+\boldsymbol{u}_{h1}\cdot\boldsymbol{\nabla}_h\zeta_0 &= \left[\cos(\tilde{\theta})\frac{\partial\delta x}{\partial\tau}+\sin(\tilde{\theta})\frac{\partial\delta y}{\partial\tau}\right]\frac{\partial\zeta_0}{\partial\tilde{r}}+\zeta_0\frac{\partial w_0}{\partial\tilde{z}} \\ &\quad-\frac{\varepsilon}{\tilde{R}eF_h^2}\cos(\tilde{\theta})\frac{\partial\zeta_0}{\partial\tilde{r}}\frac{\mathrm{d}^2U}{\mathrm{d}\tilde{z}^2}t+\delta Z_0+\delta Z_2, \qquad (4.90)\end{aligned}$$

where δZ_0 and δD_0 correspond to the axisymmetric forcing terms, while δZ_2 and δD_2 are the forcing terms proportional to $\cos(2\tilde{\theta})$ or $\sin(2\tilde{\theta})$. In contrast, the forcing terms written explicitly in the right-hand sides of (4.89) and (4.90) are all proportional to $\cos(\tilde{\theta})$ or $\sin(\tilde{\theta})$.

In order to solve (4.89) and (4.90), the horizontal velocity is decomposed into potential and rotational components by introducing a potential Φ_1 and a streamfunction ψ_1:

$$\boldsymbol{u}_{h1} = \boldsymbol{\nabla}_h\Phi_1 - \boldsymbol{\nabla}\times\psi_1\boldsymbol{e_z}. \qquad (4.91)$$

The potential and streamfunction are further decomposed into three components

$$\Phi_1 = \Phi_{10}+\Phi_{11}+\Phi_{12}, \quad \psi_1 = \psi_{10}+\psi_{11}+\psi_{12}, \qquad (4.92)$$

corresponding to the azimuthal modes $m = 0$, $m = 1$, and $m = 2$, respectively. They can be solved separately. We will begin by the components (Φ_{11}, ψ_{11}) which will provide the governing equations for the displacements $(\delta x, \delta y)$. The other components will be next determined in section 4.4.5.

[2] As for the slow time scale, another possible choice for the scaling of the Reynolds number is discussed at the end of the chapter.

4.4.4 Determination of Φ_{11} and ψ_{11}

We first determine the potential from (4.89):

$$\nabla_h^2 \Phi_{11} = -\frac{\partial w_0}{\partial \tilde{z}}. \tag{4.93}$$

Like the vertical velocity (4.80), Φ_1 is separated into three potentials evolving with the different time scales τ, t, and t/F_h (corresponding to internal waves):

$$\Phi_{11} = \Phi_s(\tilde{r}, \tilde{\theta}, \tilde{z}, \tilde{\eta}, \tau) + \Phi_p(\tilde{r}, \tilde{\theta}, \tilde{z}, t, \tilde{\eta}, \tau) + \Phi_w(\tilde{r}, \tilde{\theta}, \tilde{z}, t, \tilde{\eta}, \tau), \tag{4.94}$$

with

$$\nabla_h^2 \Phi_s = -\frac{\partial w_s}{\partial \tilde{z}}, \quad \nabla_h^2 \Phi_p = -\frac{\partial w_p}{\partial \tilde{z}}, \quad \nabla_h^2 \Phi_w = -\frac{\partial w_w}{\partial \tilde{z}}, \tag{4.95}$$

where w_s is defined in (4.70), w_p in (4.74), and w_w in (4.77). The potential varying on the slow time scale reads

$$\Phi_s = \frac{1}{2}\left[\sin(\tilde{\theta})\frac{\partial^2 \delta x}{\partial \tilde{z}^2} - \cos(\tilde{\theta})\frac{\partial^2 \delta y}{\partial \tilde{z}^2}\right] \Phi_{ps}, \tag{4.96}$$

with

$$\Phi_{ps}(\tilde{r}, \tilde{\eta}, \tau) = \tilde{r}\int_{+\infty}^{\tilde{r}} \Omega(\xi, \tilde{\eta}, \tau)\mathcal{C}(\xi, \tilde{\eta}, \tau)\mathrm{d}\xi - \frac{1}{\tilde{r}}\int_0^{\tilde{r}} \xi^2 \Omega(\xi, \tilde{\eta}, \tau)\mathcal{C}(\xi, \tilde{\eta}, \tau)\mathrm{d}\xi, \tag{4.97}$$

where it has been imposed that Φ_s is not singular at $\tilde{r} = 0$ and vanishes as $\tilde{r}$ tends to infinity. The two other potentials Φ_p and Φ_w can be derived similarly:

$$\Phi_p = \frac{1}{2}\left[-\cos(\tilde{\theta})\Phi_{pc} + t\sin(\tilde{\theta})\Phi_{ps}\right]\frac{\mathrm{d}^2 U}{\mathrm{d}\tilde{z}^2}, \tag{4.98}$$

$$\begin{aligned}\Phi_w = \frac{1}{2}\Bigg[&\tilde{r}\int_{+\infty}^{\tilde{r}} \mathcal{C}(\xi, \tilde{\eta}, \tau)\mathcal{F}(\xi, \tilde{\eta}, \tau)\cos(\Omega(\xi, \tilde{\eta}, \tau)t - \tilde{\theta})\mathrm{d}\xi \\ &- \frac{1}{\tilde{r}}\int_0^{\tilde{r}} \xi^2 \mathcal{C}(\xi, \tilde{\eta}, \tau)\mathcal{F}(\xi, \tilde{\eta}, \tau)\cos(\Omega(\xi, \tilde{\eta}, \tau)t - \tilde{\theta})\mathrm{d}\xi\Bigg]\cos\left(\frac{t}{F_h}\right)\frac{\mathrm{d}^2 U}{\mathrm{d}\tilde{z}^2} \\ &+ \Bigg[\tilde{r}\int_{+\infty}^{\tilde{r}} \mathcal{C}(\xi, \tilde{\eta}, \tau)\mathcal{G}(\xi, \tilde{\eta}, \tau)\sin(\Omega(\xi, \tilde{\eta}, \tau)t - \tilde{\theta})\mathrm{d}\xi \\ &- \frac{1}{\tilde{r}}\int_0^{\tilde{r}} \xi^2 \mathcal{C}(\xi, \tilde{\eta}, \tau)\mathcal{G}(\xi, \tilde{\eta}, \tau)\sin(\Omega(\xi, \tilde{\eta}, \tau)t - \tilde{\theta})\mathrm{d}\xi\Bigg]\sin\left(\frac{t}{F_h}\right)\frac{\mathrm{d}^2 U}{\mathrm{d}\tilde{z}^2},\end{aligned} \tag{4.99}$$

where

$$\Phi_{pc}(\tilde{r}, \tilde{\eta}, \tau) = \tilde{r}\int_{+\infty}^{\tilde{r}} \mathcal{C}(\xi, \tilde{\eta}, \tau)\mathcal{F}(\xi, \tilde{\eta}, \tau)\mathrm{d}\xi - \frac{1}{\tilde{r}}\int_0^{\tilde{r}} \xi^2 \mathcal{C}(\xi, \tilde{\eta}, \tau)\mathcal{F}(\xi, \tilde{\eta}, \tau)\mathrm{d}\xi. \tag{4.100}$$

The potential Φ_{11} being determined, an equation for the streamfunction ψ_{11} is obtained from the equation (4.90) for the vertical vorticity:

$$\begin{aligned}\left[\frac{\partial}{\partial t} + \Omega\frac{\partial}{\partial \tilde{\theta}}\right]\nabla_h^2 \psi_{11} - \frac{1}{\tilde{r}}\frac{\partial \zeta_0}{\partial \tilde{r}}\frac{\partial \psi_{11}}{\partial \tilde{\theta}} &= \left[\cos(\tilde{\theta})\frac{\partial \delta x}{\partial \tau} + \sin(\tilde{\theta})\frac{\partial \delta y}{\partial \tau} - \frac{\partial \Phi_{11}}{\partial \tilde{r}}\right]\frac{\partial \zeta_0}{\partial \tilde{r}} \\ &\quad + \zeta_0\frac{\partial w_0}{\partial \tilde{z}} - \frac{\varepsilon}{\tilde{R}eF_h^2}\cos(\tilde{\theta})\frac{\partial \zeta_0}{\partial \tilde{r}}\frac{\mathrm{d}^2 U}{\mathrm{d}\tilde{z}^2}t.\end{aligned} \tag{4.101}$$

The first two terms in the left-hand side of (4.101) come from the slow evolution of δx and δy. The third term is the advection of ζ_0 by the first order potential flow. The fourth term is the stretching of ζ_0. The last term corresponds to the dominant viscous effect. In order to solve (4.101), the streamfunction is decomposed as

$$\psi_{11} = \psi_{sd}(\tilde{r},\tilde{\theta},\tilde{z},\tau) + \psi_s(\tilde{r},\tilde{\theta},\tilde{z},\tilde{\eta},\tau) + \psi_p(\tilde{r},\tilde{\theta},\tilde{z},t,\tilde{\eta},\tau) + \psi_w(\tilde{r},\tilde{\theta},\tilde{z},t,\tilde{\eta},\tau), \quad (4.102)$$

where the different streamfunctions are solution of:

$$\Omega\frac{\partial\nabla_h^2\psi_{sd}}{\partial\tilde{\theta}} - \frac{1}{\tilde{r}}\frac{\partial\zeta_0}{\partial\tilde{r}}\frac{\partial\psi_{sd}}{\partial\tilde{\theta}} = \left[\cos(\tilde{\theta})\left(\frac{\partial\delta x}{\partial\tau} - \frac{\varepsilon t}{\tilde{R}eF_h^2}\frac{\mathrm{d}^2U}{\mathrm{d}\tilde{z}^2}\right) + \sin(\tilde{\theta})\frac{\partial\delta y}{\partial\tau}\right]\frac{\partial\zeta_0}{\partial\tilde{r}}, \quad (4.103)$$

$$\Omega\frac{\partial\nabla_h^2\psi_s}{\partial\tilde{\theta}} - \frac{1}{\tilde{r}}\frac{\partial\zeta_0}{\partial\tilde{r}}\frac{\partial\psi_s}{\partial\tilde{\theta}} = -\frac{\partial\zeta_0}{\partial\tilde{r}}\frac{\partial\Phi_s}{\partial\tilde{r}} - \zeta_0\nabla_h^2\Phi_s, \quad (4.104)$$

$$\left[\frac{\partial}{\partial t} + \Omega\frac{\partial}{\partial\tilde{\theta}}\right]\nabla_h^2\psi_p - \frac{1}{\tilde{r}}\frac{\partial\zeta_0}{\partial\tilde{r}}\frac{\partial\psi_p}{\partial\tilde{\theta}} = -\frac{\partial\zeta_0}{\partial\tilde{r}}\frac{\partial\Phi_p}{\partial\tilde{r}} - \zeta_0\nabla_h^2\Phi_p, \quad (4.105)$$

$$\left[\frac{\partial}{\partial t} + \Omega\frac{\partial}{\partial\tilde{\theta}}\right]\nabla_h^2\psi_w - \frac{1}{\tilde{r}}\frac{\partial\zeta_0}{\partial\tilde{r}}\frac{\partial\psi_w}{\partial\tilde{\theta}} = -\frac{\partial\zeta_0}{\partial\tilde{r}}\frac{\partial\Phi_w}{\partial\tilde{r}} - \zeta_0\nabla_h^2\Phi_w, \quad (4.106)$$

where Φ_s, Φ_p and Φ_w are given in (4.96), (4.98), and (4.99), respectively. The solutions of (4.103) and (4.104) which are non-singular are

$$\psi_{sd} = \left[-\sin(\tilde{\theta})\left(\frac{\partial\delta x}{\partial\tau} - \frac{\varepsilon t}{\tilde{R}eF_h^2}\frac{\mathrm{d}^2U}{\mathrm{d}\tilde{z}^2}\right) + \cos(\tilde{\theta})\frac{\partial\delta y}{\partial\tau}\right](\tilde{r} + \mu\tilde{r}\Omega), \quad (4.107)$$

$$\psi_s = \left[\cos(\tilde{\theta})\frac{\partial^2\delta x}{\partial\tilde{z}^2} + \sin(\tilde{\theta})\frac{\partial^2\delta y}{\partial\tilde{z}^2}\right]\left(\tilde{\psi}_s + \alpha\tilde{r}\Omega\right), \quad (4.108)$$

where μ and α are arbitrary functions of $\tilde{\eta}$ and τ and

$$\begin{aligned}\tilde{\psi}_s(\tilde{r},\tilde{\eta},\tau) &= \tilde{r}\Omega(\tilde{r},\tilde{\eta},\tau)\int_0^{\tilde{r}}\frac{1}{\eta^3\Omega^2(\eta,\tilde{\eta},\tau)}\int_0^{\eta}\xi^2\Omega^2(\xi,\tilde{\eta},\tau)\mathcal{C}(\xi,\tilde{\eta},\tau)\mathrm{d}\xi\mathrm{d}\eta \\ &\quad + \tilde{r}\Omega(\tilde{r},\tilde{\eta},\tau)\int_{+\infty}^{\tilde{r}}\mathcal{C}(\xi,\tilde{\eta},\tau)\mathrm{d}\xi - \frac{\tilde{r}}{2}\frac{\partial\Phi_{ps}}{\partial\tilde{r}}. \quad (4.109)\end{aligned}$$

The functions μ, α are arbitrary because $\tilde{r}\Omega\cos(\tilde{\theta})$ and $\tilde{r}\Omega\sin(\tilde{\theta})$ are homogeneous solutions of (4.103) and (4.104). These solutions derive from the translational invariance (Billant, 2010). In order to set μ and α, we need to use a normalisation condition. Here, we have chosen to impose that the mean displacement associated to the first order vorticity $\nabla_h^2\psi_{11}$ is zero, i.e.

$$\int_0^{2\pi}\int_0^{+\infty} x\nabla_h^2\psi_{11}\tilde{r}\mathrm{d}\tilde{r}\mathrm{d}\tilde{\theta} = 0, \quad \int_0^{2\pi}\int_0^{+\infty} y\nabla_h^2\psi_{11}\tilde{r}\mathrm{d}\tilde{r}\mathrm{d}\tilde{\theta} = 0. \quad (4.110)$$

In this way, only the displacements $U(\tilde{z})t + \delta x$ and δy of the leading order vorticity ζ_0 will contribute to the mean displacement of the vortex. This will ease the comparison with the numerical simulations performed in chapter 5 where the vortex displacements will be computed from vertical vorticity centroids. Hence, to enforce (4.110), we impose

$$\left\langle\nabla_h^2\psi_{sd},\tilde{r}\right\rangle = 0, \quad (4.111)$$

$$\left\langle\nabla_h^2\psi_s,\tilde{r}\right\rangle = 0, \quad (4.112)$$

where the scalar product is defined as

$$< f, g >= \int_0^{+\infty} fg\tilde{r}\mathrm{d}\tilde{r} \tag{4.113}$$

for any functions f and g. Equations (4.111) and (4.112) lead to

$$\mu = 0, \quad \alpha = -\frac{\left\langle \nabla^2_{\tilde{r}}\tilde{\psi}_s, \tilde{r} \right\rangle}{\left\langle \dfrac{\partial \zeta_0}{\partial \tilde{r}}, \tilde{r} \right\rangle}, \tag{4.114}$$

where the operator $\nabla^2_{\tilde{r}}$ is given by

$$\nabla^2_{\tilde{r}}\Lambda = \frac{\partial^2 \Lambda}{\partial \tilde{r}^2} + \frac{1}{\tilde{r}}\frac{\partial \Lambda}{\partial \tilde{r}} - \frac{\Lambda}{\tilde{r}^2} \tag{4.115}$$

for any function Λ. Determining ψ_p and ψ_w is more difficult because of the dependence of the forcings on the fast time t in (4.105)-(4.106). We first derive ψ_p analytically. Since the potential Φ_p evolves linearly with t (see (4.98)), we seek a solution in the form

$$\psi_p = -\left[\sin(\tilde{\theta})\left(\lambda_0 \tilde{r}\Omega + \lambda_1 \tilde{r} + \psi_{ps}(\tilde{r}, \tilde{\eta}, \tau)\right) + t\cos(\tilde{\theta})\left(\lambda_1 \tilde{r}\Omega + \psi_{pc}(\tilde{r}, \tilde{\eta}, \tau)\right)\right]\frac{\mathrm{d}^2 U}{\mathrm{d}\tilde{z}^2}, \tag{4.116}$$

where λ_0 and λ_1 are arbitrary functions of $\tilde{\eta}$ and τ. This leads to the following equations for ψ_{ps} and ψ_{pc}:

$$\Omega\nabla^2_{\tilde{r}}\psi_{pc} - \frac{1}{\tilde{r}}\frac{\partial \zeta_0}{\partial \tilde{r}}\psi_{pc} = -\frac{1}{2}\left[\frac{\partial \zeta_0}{\partial \tilde{r}}\frac{\partial \Phi_{ps}}{\partial \tilde{r}} + \zeta_0 \nabla^2_{\tilde{r}}\Phi_{ps}\right], \tag{4.117}$$

$$\Omega\nabla^2_{\tilde{r}}\psi_{ps} - \frac{1}{\tilde{r}}\frac{\partial \zeta_0}{\partial \tilde{r}}\psi_{ps} = -\frac{1}{2}\left[\frac{\partial \zeta_0}{\partial \tilde{r}}\frac{\partial \Phi_{pc}}{\partial \tilde{r}} + \zeta_0 \nabla^2_{\tilde{r}}\Phi_{pc}\right] - \nabla^2_{\tilde{r}}\psi_{pc}, \tag{4.118}$$

The solutions that are non-singular at $\tilde{r} = 0$ are:

$$\psi_{pc} = -\tilde{\psi}_s, \tag{4.119}$$

$$\begin{aligned}\psi_{ps}(\tilde{r}, \tilde{\eta}, \tau) = {} & \frac{\tilde{r}}{2}\frac{\partial \Phi_{pc}}{\partial \tilde{r}} - \tilde{r}\int_{+\infty}^{\tilde{r}} \mathcal{C}(\xi, \tilde{\eta}, \tau)\mathrm{d}\xi - 2F_h\tilde{r}\Omega\int_0^{\tilde{r}} \mathcal{C}(\xi, \tilde{\eta}, \tau)\mathcal{G}(\xi, \tilde{\eta}, \tau)\mathrm{d}\xi \\ & - 2F_h\tilde{r}\Omega\int_0^{\tilde{r}} \frac{1}{\eta^3\Omega^2(\eta, \tilde{\eta}, \tau)}\int_0^{\eta} \xi^2\Omega^2(\xi, \tilde{\eta}, \tau)\mathcal{C}(\xi, \tilde{\eta}, \tau)\mathcal{G}(\xi, \tilde{\eta}, \tau)\mathrm{d}\xi\mathrm{d}\eta \\ & + 2\tilde{r}\Omega\int_0^{\tilde{r}} \frac{1}{\eta^3\Omega^3(\eta, \tilde{\eta}, \tau)}\int_0^{\eta} \xi^2\Omega^2(\xi, \tilde{\eta}, \tau)\mathcal{C}(\xi, \tilde{\eta}, \tau)\mathrm{d}\xi\mathrm{d}\eta \\ & - \tilde{r}\int_0^{\tilde{r}} \frac{1}{\eta^3\Omega^2(\eta, \tilde{\eta}, \tau)}\int_0^{\eta} \xi^2\Omega^2(\xi, \tilde{\eta}, \tau)\mathcal{C}(\xi, \tilde{\eta}, \tau)\mathrm{d}\xi\mathrm{d}\eta,\end{aligned} \tag{4.120}$$

where $\tilde{\psi}_s$ is defined in (4.109). The two arbitrary functions λ_0 and λ_1 in (4.116) come from the homogeneous solution of (4.105) which is of the form

$$\psi_h = \tilde{r}\Omega\left[\cos(\tilde{\theta})f + \sin(\tilde{\theta})g\right] + \tilde{r}\left[\sin(\tilde{\theta})\frac{\partial f}{\partial t} - \cos(\tilde{\theta})\frac{\partial g}{\partial t}\right], \tag{4.121}$$

where f and g are arbitrary functions of $\tilde{z}$, t, $\tilde{\eta}$ and τ. In (4.116), we have taken $f(\tilde{z}, t, \tilde{\eta}, \tau) = -t\lambda_1(\tilde{\eta}, \tau)\mathrm{d}^2U/\mathrm{d}\tilde{z}^2$ and $g(\tilde{z}, \tilde{\eta}, \tau) = -\lambda_0(\tilde{\eta}, \tau)\mathrm{d}^2U/\mathrm{d}\tilde{z}^2$ in accordance with

the time dependence of this equation. As before, we impose the normalisation conditions

$$\left\langle \nabla^2_{\tilde{r}}\psi_{ps}, \tilde{r}\right\rangle + \lambda_0(\tilde{\eta},\tau)\left\langle \frac{\partial\zeta_0}{\partial\tilde{r}}, \tilde{r}\right\rangle = 0, \tag{4.122}$$

$$\left\langle \nabla^2_{\tilde{r}}\psi_{pc}, \tilde{r}\right\rangle + \lambda_1(\tilde{\eta},\tau)\left\langle \frac{\partial\zeta_0}{\partial\tilde{r}}, \tilde{r}\right\rangle = 0, \tag{4.123}$$

which enforce that the mean displacement associated to $\nabla^2_h\psi_p$ is zero. This sets λ_0 and λ_1 to:

$$\lambda_0 = -\frac{\langle\nabla^2_{\tilde{r}}\psi_{ps}, \tilde{r}\rangle}{\left\langle \frac{\partial\zeta_0}{\partial\tilde{r}}, \tilde{r}\right\rangle}, \quad \lambda_1 = -\frac{\langle\nabla^2_{\tilde{r}}\psi_{pc}, \tilde{r}\rangle}{\left\langle \frac{\partial\zeta_0}{\partial\tilde{r}}, \tilde{r}\right\rangle}. \tag{4.124}$$

Similarly, the solution of (4.106) is sought in the form

$$\begin{aligned}\psi_w &= -\left[\cos(\tilde{\theta})\left(\psi_{wc}(\tilde{r},t,\tilde{\eta},\tau) + \tilde{r}\Omega\mathcal{C}_w(t,\tilde{\eta},\tau) - \tilde{r}\frac{\partial\mathcal{S}_w}{\partial t}\right)\right.\\ &\quad\left. + \sin(\tilde{\theta})\left(\psi_{ws}(\tilde{r},t,\tilde{\eta},\tau) + \tilde{r}\Omega\mathcal{S}_w(t,\tilde{\eta},\tau) + \tilde{r}\frac{\partial\mathcal{C}_w}{\partial t}\right)\right]\frac{\mathrm{d}^2U}{\mathrm{d}\tilde{z}^2},\end{aligned} \tag{4.125}$$

where $\mathcal{C}_w$ and $\mathcal{S}_w$ are arbitrary functions while ψ_{wc} and ψ_{ws} satisfy

$$\frac{\partial\nabla^2_{\tilde{r}}\psi_{wc}}{\partial t} + \Omega\nabla^2_{\tilde{r}}\psi_{ws} - \frac{1}{\tilde{r}}\frac{\partial\zeta_0}{\partial\tilde{r}}\psi_{ws} = -\frac{\partial\zeta_0}{\partial\tilde{r}}\frac{\partial\Phi_{wc}}{\partial\tilde{r}} - \zeta_0\nabla^2_{\tilde{r}}\Phi_{wc}, \tag{4.126}$$

$$\frac{\partial\nabla^2_{\tilde{r}}\psi_{ws}}{\partial t} - \Omega\nabla^2_{\tilde{r}}\psi_{wc} + \frac{1}{\tilde{r}}\frac{\partial\zeta_0}{\partial\tilde{r}}\psi_{wc} = -\frac{\partial\zeta_0}{\partial\tilde{r}}\frac{\partial\Phi_{ws}}{\partial\tilde{r}} - \zeta_0\nabla^2_{\tilde{r}}\Phi_{ws}, \tag{4.127}$$

where the potentials Φ_{wc} and Φ_{ws} are given by:

$$\begin{aligned}\Phi_{wc}(\tilde{r},t,\tilde{\eta},\tau) &= \frac{1}{2}\left[\frac{1}{\tilde{r}}\int_0^{\tilde{r}}\xi^2\mathcal{C}(\xi,\tilde{\eta},\tau)\mathcal{F}(\xi,\tilde{\eta},\tau)\cos(\Omega(\xi,\tilde{\eta},\tau)t)\mathrm{d}\xi\right.\\ &\quad\left. - \tilde{r}\int_{+\infty}^{\tilde{r}}\mathcal{C}(\xi,\tilde{\eta},\tau)\mathcal{F}(\xi,\tilde{\eta},\tau)\cos(\Omega(\xi,\tilde{\eta},\tau)t)\mathrm{d}\xi\right]\cos\left(\frac{t}{F_h}\right)\\ &\quad + \left[\frac{1}{\tilde{r}}\int_0^{\tilde{r}}\xi^2\mathcal{C}(\xi,\tilde{\eta},\tau)\mathcal{G}(\xi,\tilde{\eta},\tau)\sin(\Omega(\xi,\tilde{\eta},\tau)t)\mathrm{d}\xi\right.\\ &\quad\left. - \tilde{r}\int_{+\infty}^{\tilde{r}}\mathcal{C}(\xi,\tilde{\eta},\tau)\mathcal{G}(\xi,\tilde{\eta},\tau)\sin(\Omega(\xi,\tilde{\eta},\tau)t)\mathrm{d}\xi\right]\sin\left(\frac{t}{F_h}\right),\end{aligned} \tag{4.128}$$

$$\begin{aligned}\Phi_{ws}(\tilde{r},t,\tilde{\eta},\tau) &= \frac{1}{2}\left[\frac{1}{\tilde{r}}\int_0^{\tilde{r}}\xi^2\mathcal{C}(\xi,\tilde{\eta},\tau)\mathcal{F}(\xi,\tilde{\eta},\tau)\sin(\Omega(\xi,\tilde{\eta},\tau)t)\mathrm{d}\xi\right.\\ &\quad\left. - \tilde{r}\int_{+\infty}^{\tilde{r}}\mathcal{C}(\xi,\tilde{\eta},\tau)\mathcal{F}(\xi,\tilde{\eta},\tau)\sin(\Omega(\xi,\tilde{\eta},\tau)t)\mathrm{d}\xi\right]\cos\left(\frac{t}{F_h}\right)\\ &\quad - \left[\frac{1}{\tilde{r}}\int_0^{\tilde{r}}\xi^2\mathcal{C}(\xi,\tilde{\eta},\tau)\mathcal{G}(\xi,\tilde{\eta},\tau)\cos(\Omega(\xi,\tilde{\eta},\tau)t)\mathrm{d}\xi\right.\\ &\quad\left. - \tilde{r}\int_{+\infty}^{\tilde{r}}\mathcal{C}(\xi,\tilde{\eta},\tau)\mathcal{G}(\xi,\tilde{\eta},\tau)\cos(\Omega(\xi,\tilde{\eta},\tau)t)\mathrm{d}\xi\right]\sin\left(\frac{t}{F_h}\right).\end{aligned} \tag{4.129}$$

Because the time and radial dependencies in Φ_{wc} and Φ_{ws} are not separated, it is not possible to solve (4.126) and (4.127) analytically. We have therefore implemented a numerical resolution of (4.126)-(4.127). The time advancement is performed by a forward Euler scheme, spatial derivatives are computed by centered finite differences, and the Laplacian operator is inverted by means of the tridiagonal algorithm. The imposed boundary conditions are $\psi_{ws} = \psi_{wc} = 0$ at $\tilde{r} = 0$ and that ψ_{ws} and ψ_{wc} vanish as $\tilde{r} \to +\infty$. Since the total streamfunction ψ_{11} should be zero at $t = \tau = 0$, the initial condition should be $\psi_w = -\psi_p$ because $\psi_s(\tilde{r}, \tilde{\theta}, \tilde{z}, \tilde{\eta}, \tau = 0) = 0$ and $\psi_{sd}(\tilde{r}, \tilde{\theta}, \tilde{z}, \tau = 0) = 0$ since $\delta x = \delta y = \partial \delta x/\partial \tau = \partial \delta y/\partial \tau = 0$ at $\tau = 0$. Thus, we impose at $t = \tau = 0$:

$$\psi_{wc} = 0, \quad \psi_{ws} = -\left[\psi_{ps} + \lambda_0 \tilde{r}\Omega + \lambda_1 \tilde{r} - \vartheta(\tilde{\eta}, \tau = 0)\tilde{r}\right], \tag{4.130}$$

where $\vartheta(\tilde{\eta}, \tau = 0)$ is set such that $\psi_{ws} \to 0$ as $\tilde{r} \to +\infty$ initially, as required to integrate (4.126) and (4.127) numerically. From the expression (4.120) of ψ_{ps}, we have:

$$\begin{aligned}
\vartheta(\tilde{\eta}, \tau) \;=\; & \lambda_1(\tilde{\eta}, \tau) - F_h \int_0^{+\infty} \xi^2 \Omega^2(\xi, \tilde{\eta}, \tau) \mathcal{C}(\xi, \tilde{\eta}, \tau) \mathcal{G}(\xi, \tilde{\eta}, \tau) \mathrm{d}\xi \\
& + \lim_{\tilde{R} \to +\infty} 2\Omega(\tilde{R}, \tilde{\eta}, \tau) \int_0^{\tilde{R}} \frac{1}{\eta^3 \Omega^3(\eta, \tilde{\eta}, \tau)} \int_0^{\eta} \xi^2 \Omega^2(\xi, \tilde{\eta}, \tau) \mathcal{C}(\xi, \tilde{\eta}, \tau) \mathrm{d}\xi \mathrm{d}\eta \\
& - \lim_{\tilde{R} \to +\infty} \int_0^{\tilde{R}} \frac{1}{\eta^3 \Omega^2(\eta, \tilde{\eta}, \tau)} \int_0^{\eta} \xi^2 \Omega^2(\xi, \tilde{\eta}, \tau) \mathcal{C}(\xi, \tilde{\eta}, \tau) \mathrm{d}\xi \mathrm{d}\eta.
\end{aligned} \tag{4.131}$$

There is no loss of generality in imposing that ψ_{ws} vanishes as $\tilde{r} \to +\infty$ initially because the function $\vartheta \tilde{r}$ belongs to the homogeneous solution of (4.106):

$$\psi_{wh} = \vartheta t \cos(\tilde{\theta}) \tilde{r}\Omega + \vartheta \tilde{r} \sin(\tilde{\theta}). \tag{4.132}$$

In other words, introducing the term $\vartheta \tilde{r}$ is equivalent to substituting $\mathcal{C}_w$ by $\mathcal{C}_w + \vartheta t$ in (4.125). After the numerical integration, we enforce that the mean displacement associated to $\nabla_h^2 \psi_w$ is zero, yielding:

$$\mathcal{C}_w(t, \tilde{\eta}, \tau) = -\frac{\langle \nabla_{\tilde{r}}^2 \psi_{wc}, \tilde{r} \rangle}{\left\langle \dfrac{\partial \zeta_0}{\partial \tilde{r}}, \tilde{r} \right\rangle}, \quad \mathcal{S}_w(t, \tilde{\eta}, \tau) = -\frac{\langle \nabla_{\tilde{r}}^2 \psi_{ws}, \tilde{r} \rangle}{\left\langle \dfrac{\partial \zeta_0}{\partial \tilde{r}}, \tilde{r} \right\rangle}. \tag{4.133}$$

Figures 4.3 and 4.4 show the streamfunctions ψ_{wc} and ψ_{ws} plotted against $\tilde{r}$ at different times, for $F_h = 0.1$ and $F_h = 0.5$ respectively, at $z = l_z/4$. In the next section, we will show that the angular velocity Ω does not evolve with τ in this plane. After an initial transient phase, the streamfunctions globally decay with time in the vortex core.

We have now fully determined the four components of the streamfunction at first order ψ_{11}. They all satisfy the boundary condition at $\tilde{r} = 0$. However, for large $\tilde{r}$, we see directly in (4.107) that ψ_{sd} grows like $\tilde{r}$. Similarly, it can be shown that the three other components behave as

$$\psi_s \sim \frac{\mathcal{A}}{2} \left[\cos(\tilde{\theta}) \frac{\partial^2 \delta x}{\partial \tilde{z}^2} + \sin(\tilde{\theta}) \frac{\partial^2 \delta y}{\partial \tilde{z}^2} \right] \tilde{r}, \tag{4.134}$$

$$\psi_p \sim \left[-\sin(\tilde{\theta}) \vartheta + \cos(\tilde{\theta}) \frac{\mathcal{A}t}{2} \right] \frac{\mathrm{d}^2 U}{\mathrm{d}\tilde{z}^2} \tilde{r}, \tag{4.135}$$

$$\psi_w \sim \left[\cos(\tilde{\theta}) \frac{\partial \mathcal{S}_w}{\partial t} - \sin(\tilde{\theta}) \frac{\partial \mathcal{C}_w}{\partial t} \right] \frac{\mathrm{d}^2 U}{\mathrm{d}\tilde{z}^2} \tilde{r}, \tag{4.136}$$

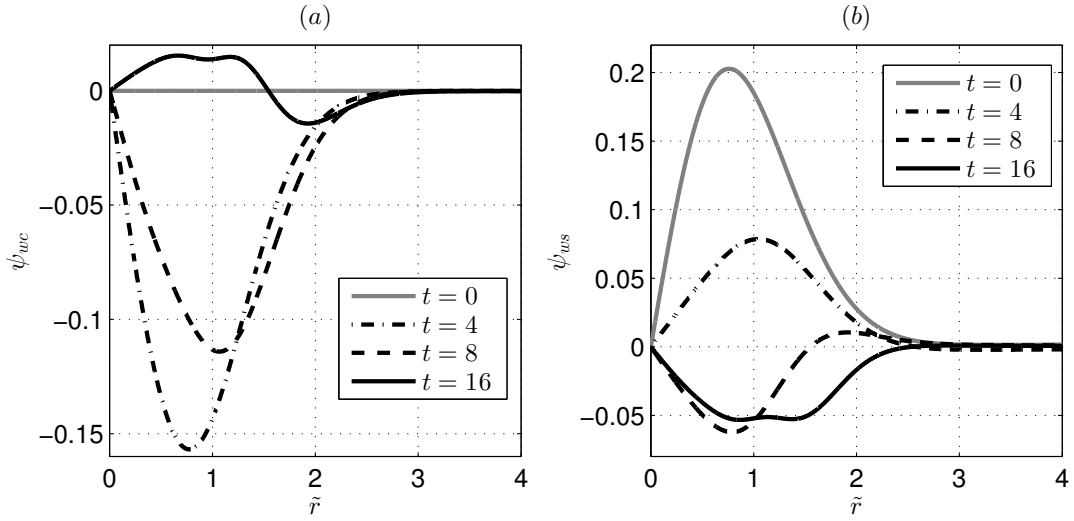

Figure 4.3: Streamfunctions ψ_{wc} (a) and ψ_{ws} (b) plotted against $\tilde{r}$ at $t = 0$ (grey solid line), $t = 4$ (black dash-dotted line), $t = 8$ (black dashed line) and $t = 16$ (black solid line), at $z = l_z/4$ where $\Omega = [1 - \exp(-\tilde{r}^2)]/\tilde{r}^2$ regardless of τ. The Froude number is $F_h = 0.1$.

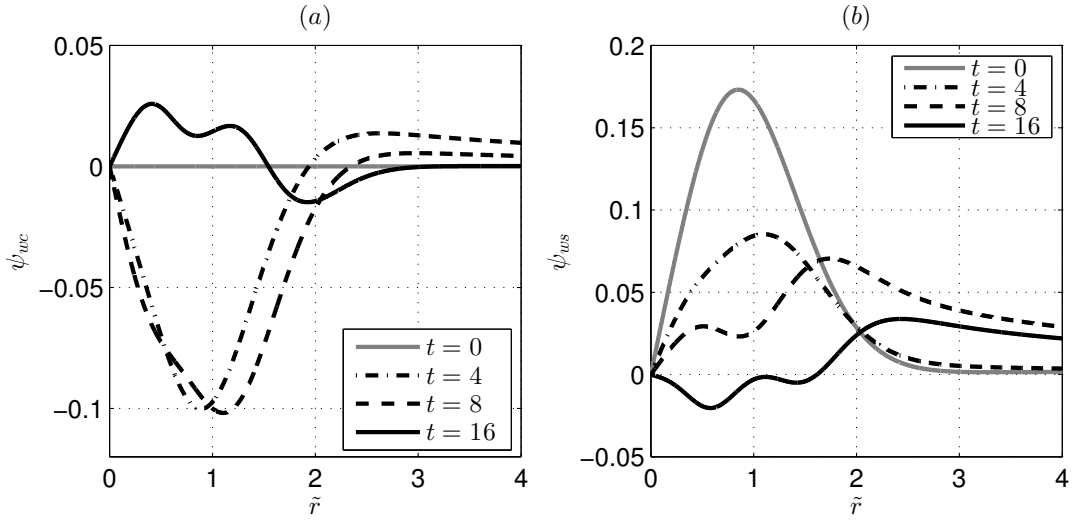

Figure 4.4: Same as figure 4.3 for $F_h = 0.5$.

where $\mathcal{A}$ is given by:

$$\mathcal{A}(\tilde{\eta},\tau)=\int_0^{+\infty}\xi^2\Omega^2(\xi,\tilde{\eta},\tau)\mathcal{C}(\xi,\tilde{\eta},\tau)\mathrm{d}\xi. \tag{4.137}$$

Note that we have used the fact that ψ_{wc} and ψ_{ws} tend to zero as $\tilde{r}\to+\infty$. In order to enforce the boundary condition $\psi_{11}\to 0$ as $\tilde{r}\to+\infty$, the sum of the four components should be zero, giving the governing equations for $(\delta x,\delta y)$:

$$\frac{\partial\delta x}{\partial\tau}=\frac{\mathcal{A}(\tilde{\eta},\tau)}{2}\frac{\partial^2\delta y}{\partial\tilde{z}^2}-\left[\vartheta(\tilde{\eta},\tau)+\frac{\partial\mathcal{C}_w}{\partial t}(t,\tilde{\eta},\tau)\right]\frac{\mathrm{d}^2U}{\mathrm{d}\tilde{z}^2}+\frac{\varepsilon t}{\tilde{R}eF_h^2}\frac{\mathrm{d}^2U}{\mathrm{d}\tilde{z}^2}, \tag{4.138}$$

$$\frac{\partial\delta y}{\partial\tau}=-\frac{\mathcal{A}(\tilde{\eta},\tau)}{2}\left[t\frac{\mathrm{d}^2U}{\mathrm{d}\tilde{z}^2}+\frac{\partial^2\delta x}{\partial\tilde{z}^2}\right]-\frac{\partial\mathcal{S}_w}{\partial t}(t,\tilde{\eta},\tau)\frac{\mathrm{d}^2U}{\mathrm{d}\tilde{z}^2}. \tag{4.139}$$

When $U=0$, these equations are identical to those found by Billant (2010) for the self-induction of an isolated vortex in stratified non-rotating fluids. Figure 4.5 shows $\mathcal{A}$ and ϑ as functions of F_h at $z=l_z/4$, where the angular velocity remains the same $\Omega=\left[1-\exp(-\tilde{r}^2)\right]/\tilde{r}^2$ whatever τ (see §4.4.6). They are almost independent of F_h for $F_h\lesssim 0.5$. The wave forcing terms $\mathcal{C}_w$ and $\mathcal{S}_w$ are also shown in figure 4.6 for two Froude numbers $F_h=0.1$ and $F_h=0.5$, at the same location. In appendix B, it is shown that they behave for small time as

$$\mathcal{C}_w=-\vartheta t+O(t^3),\quad \mathcal{S}_w=-\frac{\mathcal{A}}{4}t^2+O(t^4). \tag{4.140}$$

Then, they go through oscillations as seen in figure 4.6. These oscillations exhibit two typical periods: the period of rotation in the vortex core $T\sim 2\pi$ and the buoyancy period $T\sim 2\pi F_h$. For $F_h=0.5$ (figure 4.6*b*), these two periods are comparable so that $\mathcal{C}_w$ and $\mathcal{S}_w$ exhibit irregular oscillations while for $F_h=0.1$ (figure 4.6*a*), fast oscillations superimposed on slow oscillations can be clearly distinguished. For large times, $\mathcal{C}_w$ and $\mathcal{S}_w$ tend to constant values because the waves are increasingly sheared by the vortex rotation through the terms $\cos(\Omega t-\tilde{\theta})$ and $\sin(\Omega t-\tilde{\theta})$ in Φ_w (see (4.99)). As a result, their contributions $\partial\mathcal{C}_w/\partial t$ and $\partial\mathcal{S}_w/\partial t$ to the vortex displacements vanish as $t\to+\infty$.

In order to be able to solve (4.138)-(4.139) in general, we first need to know how the angular velocity evolves on the slow time τ. This will be determined in the next two sections while further analyses of (4.138)-(4.139) will be conducted in §4.4.7.

4.4.5 Determination of (Φ_{10},ψ_{10}) and (Φ_{12},ψ_{12})

We now determine (Φ_{10},ψ_{10}) and (Φ_{12},ψ_{12}) corresponding to the azimuthal modes $m=0$ and $m=2$ of the potential and streamfunction at first order (4.92).

In order to keep the calculations relatively simple, we will assume here that the Froude number is small so that the hydrostatic approximation is satisfied. The comparison with the DNS in chapter 5 will show that this assumption provides accurate predictions for $F_h\lesssim 1$. In the limit $F_h\to 0$, the vertical velocity and buoyancy

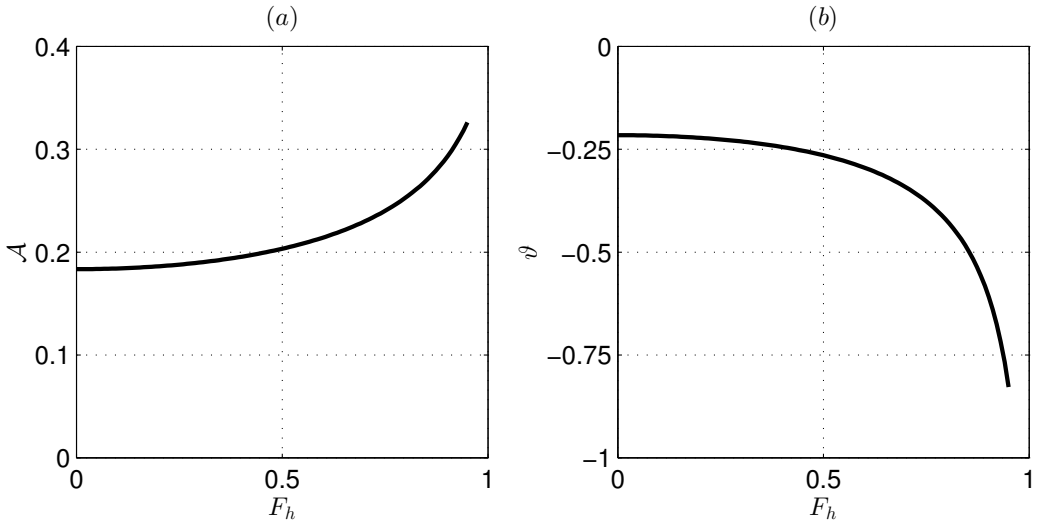

Figure 4.5: Variables (a) $\mathcal{A}$ and (b) ϑ plotted against F_h, at $z = l_z/4$ where $\Omega = [1 - \exp(-\tilde{r}^2)]/\tilde{r}^2$ regardless of τ.

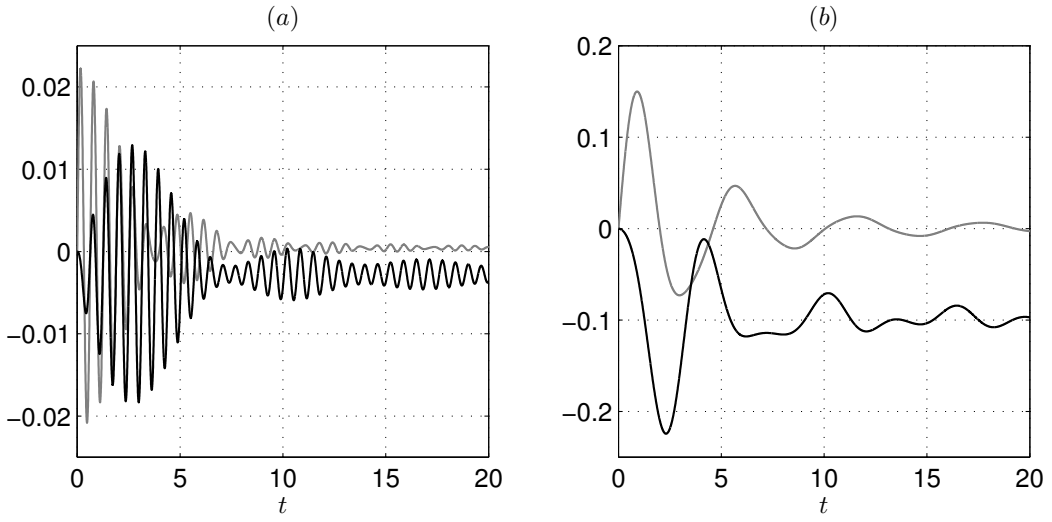

Figure 4.6: Forcings $\mathcal{C}_w$ (grey lines) and $\mathcal{S}_w$ (black lines) for (a) $F_h = 0.1$ and (b) $F_h = 0.5$, at $z = l_z/4$ where $\Omega = [1 - \exp(-\tilde{r}^2)]/\tilde{r}^2$ regardless of τ.

(4.80)-(4.81) reduce to:

$$w_0 = \left[\cos(\tilde{\theta}) - t\sin(\tilde{\theta})\Omega - \cos(\Omega t - \tilde{\theta})\cos\left(\frac{t}{F_h}\right)\right]\tilde{r}\Omega^2\frac{\mathrm{d}U}{\mathrm{d}\tilde{z}} + \left[-\sin(\tilde{\theta})\frac{\partial\delta x}{\partial\tilde{z}} + \cos(\tilde{\theta})\frac{\partial\delta y}{\partial\tilde{z}}\right]\tilde{r}\Omega^3, \tag{4.141}$$

$$b_0 = -t\cos(\tilde{\theta})\tilde{r}\Omega^2\frac{\mathrm{d}U}{\mathrm{d}\tilde{z}} - \left[\cos(\tilde{\theta})\frac{\partial\delta x}{\partial\tilde{z}} + \sin(\tilde{\theta})\frac{\partial\delta y}{\partial\tilde{z}}\right]\tilde{r}\Omega^2. \tag{4.142}$$

The only remaining term due to internal waves is the third term in (4.141). However, if the Froude number F_h were set to zero directly in (4.63)-(4.64), this term would be absent in (4.141). Furthermore, the previous section has shown that the effects due to these internal waves are restricted to the beginning of the evolution and are rather weak (see also chapter 5). For this reason, we will neglect the third term in (4.141) in the following. This will avoid lengthy calculations. In addition, the equations (4.138)-(4.139) for the displacement perturbations derived in the previous section show that $(\delta x, \delta y)$ remain small. Therefore, these displacements will be also neglected in (4.141)-(4.142). Hence, (4.141)-(4.142) are simplified as follows:

$$w_0 = \left[\cos(\tilde{\theta}) - t\sin(\tilde{\theta})\Omega\right]\tilde{r}\Omega^2\frac{\mathrm{d}U}{\mathrm{d}\tilde{z}}, \tag{4.143}$$

$$b_0 = -t\cos(\tilde{\theta})\tilde{r}\Omega^2\frac{\mathrm{d}U}{\mathrm{d}\tilde{z}}. \tag{4.144}$$

Using (4.143), it is now a simple matter to derive the azimuthal components $m = 0$ and $m = 2$ of the forcing terms of (4.89)-(4.90):

$$\delta D_0 = \left[\Omega^2 + \tilde{r}\Omega\frac{\partial\Omega}{\partial\tilde{r}}\right]t\left(\frac{\mathrm{d}U}{\mathrm{d}\tilde{z}}\right)^2, \tag{4.145}$$

$$\delta D_2 = \left[t\cos(2\tilde{\theta})\tilde{r}\Omega\frac{\partial\Omega}{\partial\tilde{r}} - \frac{3}{2}t^2\sin(2\tilde{\theta})\tilde{r}\Omega^2\frac{\partial\Omega}{\partial\tilde{r}}\right]\left(\frac{\mathrm{d}U}{\mathrm{d}\tilde{z}}\right)^2, \tag{4.146}$$

$$\delta Z_0 = -\frac{\partial\zeta_0}{\partial\tau} - \left[2t\Omega^3 + 3t\tilde{r}\Omega^2\frac{\partial\Omega}{\partial\tilde{r}}\right]\left(\frac{\mathrm{d}U}{\mathrm{d}\tilde{z}}\right)^2 + \frac{t}{2}\tilde{r}\Omega^2\frac{\partial\zeta_0}{\partial\tilde{r}}\left(\frac{\mathrm{d}U}{\mathrm{d}\tilde{z}}\right)^2 + \frac{\varepsilon t^2}{2\tilde{R}eF_h^2}\left[\frac{\partial^2\zeta_0}{\partial\tilde{r}^2} + \frac{1}{\tilde{r}}\frac{\partial\zeta_0}{\partial\tilde{r}}\right]\left(\frac{\mathrm{d}U}{\mathrm{d}\tilde{z}}\right)^2, \tag{4.147}$$

$$\delta Z_2 = \left[\sin(2\tilde{\theta})\tilde{r}\Omega\frac{\partial\Omega}{\partial\tilde{r}} + t\cos(2\tilde{\theta})\tilde{r}\Omega^2\frac{\partial\Omega}{\partial\tilde{r}} + t^2\sin(2\tilde{\theta})\tilde{r}\Omega^3\frac{\partial\Omega}{\partial\tilde{r}}\right]\left(\frac{\mathrm{d}U}{\mathrm{d}\tilde{z}}\right)^2 + \left[t\cos(2\tilde{\theta}) - \sin(2\tilde{\theta})\Omega t^2\right]\frac{\tilde{r}\Omega^2}{2}\frac{\partial\zeta_0}{\partial\tilde{r}}\left(\frac{\mathrm{d}U}{\mathrm{d}\tilde{z}}\right)^2 + \frac{\varepsilon t^2}{2\tilde{R}eF_h^2}\cos(2\tilde{\theta})\left[\frac{\partial^2\zeta_0}{\partial\tilde{r}^2} - \frac{1}{\tilde{r}}\frac{\partial\zeta_0}{\partial\tilde{r}}\right]\left(\frac{\mathrm{d}U}{\mathrm{d}\tilde{z}}\right)^2. \tag{4.148}$$

In (4.147), we have neglected the horizontal dissipation (first two terms in the right-hand side of (4.88)) and retained only the terms coming from the vertical dissipation (third term in the right-hand side of (4.88)) because the latter term grows like t^2 in contrast to the former.

We first determine the potentials Φ_{10} and Φ_{12}. They satisfy (see (4.89)):

$$\nabla_h^2\Phi_{10} = \delta D_0, \quad \nabla_h^2\Phi_{12} = \delta D_2. \tag{4.149}$$

The solutions that are not singular at $\tilde{r} = 0$ and that vanish at infinity are

$$\Phi_{10} = \frac{t}{2}\int_{+\infty}^{\tilde{r}} \xi\Omega^2(\xi,\tilde{\eta},\tau)\mathrm{d}\xi \left(\frac{\mathrm{d}U}{\mathrm{d}\tilde{z}}\right)^2, \tag{4.150}$$

$$\Phi_{12} = \left[t\cos(2\tilde{\theta})\Phi_{c2} - \frac{3}{2}t^2\sin(2\tilde{\theta})\Phi_{s2}\right]\left(\frac{\mathrm{d}U}{\mathrm{d}\tilde{z}}\right)^2, \tag{4.151}$$

where:

$$\Phi_{c2}(\tilde{r},\tilde{\eta},\tau) = \frac{1}{2\tilde{r}^2}\int_0^{\tilde{r}} \xi^3\Omega^2(\xi,\tilde{\eta},\tau)\mathrm{d}\xi, \quad \Phi_{s2}(\tilde{r},\tilde{\eta},\tau) = \frac{1}{3\tilde{r}^2}\int_0^{\tilde{r}} \xi^3\Omega^3(\xi,\tilde{\eta},\tau)\mathrm{d}\xi. \tag{4.152}$$

Then, we look for the streamfunctions ψ_{10} and ψ_{12}. Their equations are directly obtained from (4.90). Using (4.147), (4.148), (4.150) and (4.151):

$$\begin{aligned}\left[\frac{\partial}{\partial t} + \Omega\frac{\partial}{\partial\tilde{\theta}}\right]\nabla_h^2\psi_{10} - \frac{1}{\tilde{r}}\frac{\partial\zeta_0}{\partial\tilde{r}}\frac{\partial\psi_{10}}{\partial\tilde{\theta}} &= -\frac{\partial\zeta_0}{\partial\tau} - \left[2t\Omega^3 + 3t\tilde{r}\Omega^2\frac{\partial\Omega}{\partial\tilde{r}}\right]\left(\frac{\mathrm{d}U}{\mathrm{d}\tilde{z}}\right)^2 \\ &+ \frac{\varepsilon t^2}{2\tilde{Re}F_h^2}\left[\frac{\partial^2\zeta_0}{\partial\tilde{r}^2} + \frac{1}{\tilde{r}}\frac{\partial\zeta_0}{\partial\tilde{r}}\right]\left(\frac{\mathrm{d}U}{\mathrm{d}\tilde{z}}\right)^2, \end{aligned}\tag{4.153}$$

$$\begin{aligned}\left[\frac{\partial}{\partial t} + \Omega\frac{\partial}{\partial\tilde{\theta}}\right]\nabla_h^2\psi_{12} - \frac{1}{\tilde{r}}\frac{\partial\zeta_0}{\partial\tilde{r}}\frac{\partial\psi_{12}}{\partial\tilde{\theta}} &= \frac{\varepsilon t^2}{2\tilde{Re}F_h^2}\cos(2\tilde{\theta})\left[\frac{\partial^2\zeta_0}{\partial\tilde{r}^2} - \frac{1}{\tilde{r}}\frac{\partial\zeta_0}{\partial\tilde{r}}\right]\left(\frac{\mathrm{d}U}{\mathrm{d}\tilde{z}}\right)^2 \\ &+ \sin(2\tilde{\theta})\left[\tilde{r}\Omega\frac{\partial\Omega}{\partial\tilde{r}} + t^2\tilde{r}\Omega^3\frac{\partial\Omega}{\partial\tilde{r}} - \frac{t^2}{\tilde{r}^3}\frac{\partial\zeta_0}{\partial\tilde{r}}\int_0^{\tilde{r}}\xi^3\Omega^3(\xi,\tilde{\eta},\tau)\mathrm{d}\xi\right]\left(\frac{\mathrm{d}U}{\mathrm{d}\tilde{z}}\right)^2 \\ &+ t\cos(2\tilde{\theta})\left[\tilde{r}\Omega^2\frac{\partial\Omega}{\partial\tilde{r}} + \frac{1}{\tilde{r}^3}\frac{\partial\zeta_0}{\partial\tilde{r}}\int_0^{\tilde{r}}\xi^3\Omega^2(\xi,\tilde{\eta},\tau)\mathrm{d}\xi\right]\left(\frac{\mathrm{d}U}{\mathrm{d}\tilde{z}}\right)^2. \end{aligned}\tag{4.154}$$

Since ψ_{10} is axisymmetric, the left-hand side of (4.153) reduces to $\partial\nabla_h^2\psi_{10}/\partial t$. In addition, we should impose that

$$\left\langle\nabla_h^2\psi_{10},\zeta_0\right\rangle = 0 \tag{4.155}$$

in order that the vertical vorticity at order 1 is orthogonal to the vertical vorticity at leading order. Taking the scalar product of (4.153) with ζ_0 shows that $\partial\left\langle\nabla_h^2\psi_{10},\zeta_0\right\rangle/\partial t = 0$ only if

$$\frac{\partial\zeta_0}{\partial\tau} = -\left[2t\Omega^3 + 3t\tilde{r}\Omega^2\frac{\partial\Omega}{\partial\tilde{r}}\right]\left(\frac{\mathrm{d}U}{\mathrm{d}\tilde{z}}\right)^2 + \frac{\varepsilon t^2}{2\tilde{Re}F_h^2}\left[\frac{\partial^2\zeta_0}{\partial\tilde{r}^2} + \frac{1}{\tilde{r}}\frac{\partial\zeta_0}{\partial\tilde{r}}\right]\left(\frac{\mathrm{d}U}{\mathrm{d}\tilde{z}}\right)^2. \tag{4.156}$$

The streamfunction ψ_{12} will be sought in the form

$$\psi_{12} = \psi_{12}^* + \psi_{12}^\nu, \tag{4.157}$$

where ψ_{12}^ν is the solution forced by the viscous term in the right-hand side of (4.154) (first term) while ψ_{12}^* is the solution forced by all the other terms. We will first determine ψ_{12}^* in the form

$$\psi_{12}^* = \frac{1}{2}\left[-\cos(2\tilde{\theta})\psi_{2b} + t\sin(2\tilde{\theta})\psi_{2s} - t^2\cos(2\tilde{\theta})\psi_{2c}\right]\left(\frac{\mathrm{d}U}{\mathrm{d}\tilde{z}}\right)^2, \tag{4.158}$$

where the streamfunctions $\psi_{2b}(\tilde{r},\tilde{\eta},\tau)$, $\psi_{2s}(\tilde{r},\tilde{\eta},\tau)$, and $\psi_{2c}(\tilde{r},\tilde{\eta},\tau)$ are solution of

$$\frac{\nabla^{2*}_{\tilde{r}}\psi_{2s}}{2}+\Omega\nabla^{2*}_{\tilde{r}}\psi_{2b}-\frac{1}{\tilde{r}}\frac{\partial\zeta_0}{\partial\tilde{r}}\psi_{2b}=\tilde{r}\Omega\frac{\partial\Omega}{\partial\tilde{r}}, \tag{4.159}$$

$$-\nabla^{2*}_{\tilde{r}}\psi_{2c}+\Omega\nabla^{2*}_{\tilde{r}}\psi_{2s}-\frac{1}{\tilde{r}}\frac{\partial\zeta_0}{\partial\tilde{r}}\psi_{2s}=\tilde{r}\Omega^2\frac{\partial\Omega}{\partial\tilde{r}}+\frac{1}{\tilde{r}^3}\frac{\partial\zeta_0}{\partial\tilde{r}}\int_0^{\tilde{r}}\xi^3\Omega^2(\xi,\tilde{\eta},\tau)\mathrm{d}\xi, \tag{4.160}$$

$$\Omega\nabla^{2*}_{\tilde{r}}\psi_{2c}-\frac{1}{\tilde{r}}\frac{\partial\zeta_0}{\partial\tilde{r}}\psi_{2c}=\tilde{r}\Omega^3\frac{\partial\Omega}{\partial\tilde{r}}-\frac{1}{\tilde{r}^3}\frac{\partial\zeta_0}{\partial\tilde{r}}\int_0^{\tilde{r}}\xi^3\Omega^3(\xi,\tilde{\eta},\tau)\mathrm{d}\xi, \tag{4.161}$$

where $\nabla^{2*}_{\tilde{r}}$ is defined as:

$$\nabla^{2*}_{\tilde{r}}\varphi=\frac{\partial^2\varphi}{\partial\tilde{r}^2}+\frac{1}{\tilde{r}}\frac{\partial\varphi}{\partial\tilde{r}}-\frac{4\varphi}{\tilde{r}^2}. \tag{4.162}$$

It can be remarked that the decomposition (4.158) contains a constant term implying that ψ^*_{12} does not vanish at $t=0$. Yet, the total streamfunction at first order ψ_1 (4.92) should be zero at $t=0$ since there is no perturbation initially. Because ψ_{10} and ψ_{11} already fulfill this condition, it should be the case also for ψ^*_{12}. However, the simplified expression of the vertical velocity (4.143), which is at the origin of the inviscid forcing terms in (4.154) (see (4.85)), does not vanish either at $t=0$. This is a direct consequence of the fact that the term $\cos(\Omega t-\tilde{\theta})\cos(t/F_h)$, corresponding to internal waves, has been neglected in (4.143). Nevertheless, if this term had been kept, the vertical velocity would be zero at $t=0$ and ψ_1 would contain an additional contribution ψ^w_{12} due to this wave term. This contribution could be computed so that it cancels ψ^*_{12} at $t=0$, i.e. $\psi^*_{12}+\psi^w_{12}=0$ initially. This is the procedure that has been followed to compute ψ_{11} in §4.4.4. However, the contribution due to the internal waves rapidly decays as seen in figure 4.6. This is the reason why we have chosen to neglect this term here so as to simplify the calculations. However, this implies that w_0 and ψ^*_{12} are not exactly zero at $t=0$.

In (4.159-4.161), the angular velocity Ω and vertical vorticity ζ_0 evolve on the slow time according to (4.156). In the next section, it will be shown that this evolution can be very well accounted for by assuming that the vortex keeps a Lamb-Oseen profile but with time varying maximum angular velocity $\Omega_c(\tilde{\eta},\tau)$ and radius $\tilde{a}_e(\tilde{\eta},\tau)$:

$$\Omega=\Omega_c(\tilde{\eta},\tau)\bar{\Omega}(\bar{r}),\quad \bar{\Omega}=\frac{1-\exp(-\bar{r}^2)}{\bar{r}^2}, \tag{4.163}$$

where $\bar{r}=\tilde{r}/\tilde{a}_e$.

Then, by rescaling ψ_{2b}, ψ_{2s}, and ψ_{2c} as follows:

$$\psi_{2b}=\tilde{a}_e^2\Omega_c\bar{\psi}_{2b}(\bar{r}),\quad \psi_{2s}=\tilde{a}_e^2\Omega_c^2\bar{\psi}_{2s}(\bar{r}),\quad \psi_{2c}=\tilde{a}_e^2\Omega_c^3\bar{\psi}_{2c}(\bar{r}), \tag{4.164}$$

(4.159-4.161) become

$$\bar{\Omega}\left[\frac{\mathrm{d}^2\bar{\psi}_{2b}}{\mathrm{d}\bar{r}^2}+\frac{1}{\bar{r}}\frac{\mathrm{d}\bar{\psi}_{2b}}{\mathrm{d}\bar{r}}-\frac{4\bar{\psi}_{2b}}{\bar{r}^2}\right]-\frac{\mathrm{d}\bar{\zeta}_0}{\mathrm{d}\bar{r}}\frac{\bar{\psi}_{2b}}{\bar{r}}=\bar{r}\bar{\Omega}\frac{\mathrm{d}\bar{\Omega}}{\mathrm{d}\bar{r}}-\frac{1}{2}\left[\frac{\mathrm{d}^2\bar{\psi}_{2s}}{\mathrm{d}\bar{r}^2}+\frac{1}{\bar{r}}\frac{\mathrm{d}\bar{\psi}_{2s}}{\mathrm{d}\bar{r}}-\frac{4\bar{\psi}_{2s}}{\bar{r}^2}\right], \tag{4.165}$$

$$\begin{aligned}\bar{\Omega}\left[\frac{\mathrm{d}^2\bar{\psi}_{2s}}{\mathrm{d}\bar{r}^2}+\frac{1}{\bar{r}}\frac{\mathrm{d}\bar{\psi}_{2s}}{\mathrm{d}\bar{r}}-\frac{4\bar{\psi}_{2s}}{\bar{r}^2}\right]-\frac{\mathrm{d}\bar{\zeta}_0}{\mathrm{d}\bar{r}}\frac{\bar{\psi}_{2s}}{\bar{r}}&=\frac{\mathrm{d}^2\bar{\psi}_{2c}}{\mathrm{d}\bar{r}^2}+\frac{1}{\bar{r}}\frac{\mathrm{d}\bar{\psi}_{2c}}{\mathrm{d}\bar{r}}-\frac{4\bar{\psi}_{2c}}{\bar{r}^2}\\&\quad+\bar{r}\bar{\Omega}^2\frac{\mathrm{d}\bar{\Omega}}{\mathrm{d}\bar{r}}+\frac{1}{\bar{r}^3}\frac{\mathrm{d}\bar{\zeta}_0}{\mathrm{d}\bar{r}}\int_0^{\bar{r}}\xi^3\bar{\Omega}^2(\xi)\mathrm{d}\xi,\end{aligned} \tag{4.166}$$

$$\bar{\Omega}\left[\frac{\mathrm{d}^2\bar{\psi}_{2c}}{\mathrm{d}\bar{r}^2}+\frac{1}{\bar{r}}\frac{\mathrm{d}\bar{\psi}_{2c}}{\mathrm{d}\bar{r}}-\frac{4\bar{\psi}_{2c}}{\bar{r}^2}\right]-\frac{\mathrm{d}\bar{\zeta}_0}{\mathrm{d}\bar{r}}\frac{\bar{\psi}_{2c}}{\bar{r}}=\bar{r}\bar{\Omega}^3\frac{\mathrm{d}\bar{\Omega}}{\mathrm{d}\bar{r}}-\frac{1}{\bar{r}^3}\frac{\mathrm{d}\bar{\zeta}_0}{\mathrm{d}\bar{r}}\int_0^{\bar{r}}\xi^3\bar{\Omega}^3(\xi)\mathrm{d}\xi. \tag{4.167}$$

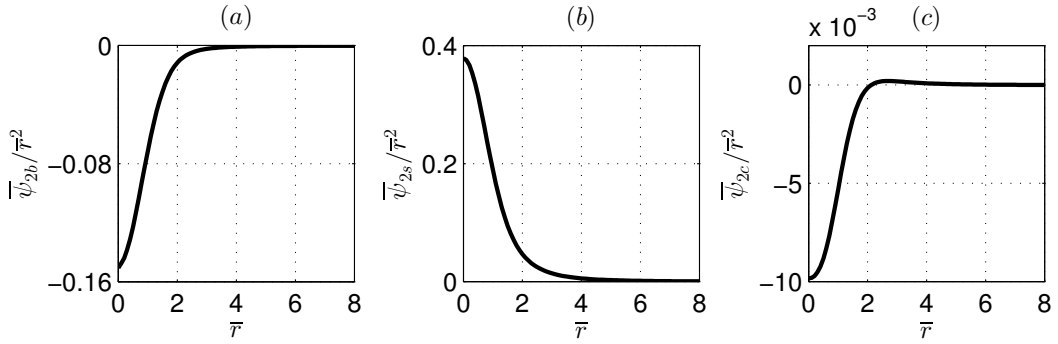

Figure 4.7: Streamfunctions $\bar{\psi}_{2b}$ (a), $\bar{\psi}_{2s}$ (b), and $\bar{\psi}_{2c}$ (c) rescaled by $\bar{r}^2$ as functions of $\bar{r}$. Note that they all rapidly vanish outside the vortex core.

These three equations share the same linear operator which admits a homogeneous solution behaving as $\psi_{2h} = \bar{r}^2$ for $\bar{r} \to +\infty$ and $\psi_{2h} = 2.524\bar{r}^2$ for $\bar{r} \to 0$ (Moore and Saffman, 1975; Le Dizès and Laporte, 2002). By using this homogeneous solution, it is possible to determine numerically complete solutions that vanish at infinity and are non-singular at $\bar{r} = 0$. They are shown in figure 4.7. For $\bar{r} \ll 1$, they behave as

$$\bar{\psi}_{2b} = \beta_2\bar{r}^2 + O(\bar{r}^4), \quad \bar{\psi}_{2s} = \sigma_2\bar{r}^2 + O(\bar{r}^4), \quad \bar{\psi}_{2c} = \chi_2\bar{r}^2 + O(\bar{r}^4), \tag{4.168}$$

with:

$$\beta_2 = -0.1506, \quad \sigma_2 = 0.3786, \quad \chi_2 = -9.830 \times 10^{-3}. \tag{4.169}$$

By using (4.164), this implies that the streamfunction ψ_{12}^* behaves in the vicinity of the vortex core as

$$\psi_{12}^* = \frac{\tilde{r}^2}{2}\left[-\beta_2\Omega_c\cos(2\tilde{\theta}) + \sigma_2\Omega_c^2\sin(2\tilde{\theta})t - \chi_2\Omega_c^3\cos(2\tilde{\theta})t^2\right]\left(\frac{\mathrm{d}U}{\mathrm{d}\tilde{z}}\right)^2 + O(\tilde{r}^4). \tag{4.170}$$

In chapter 5, this will allow us to determine the evolution of the vertical shear of the horizontal velocity on the vortex axis. A similar calculation is conducted in appendix C to determine ψ_{12}^ν. For $\tilde{r} \ll 1$, it is of the form:

$$\psi_{12}^\nu = \frac{\varepsilon\tilde{r}^2}{2\tilde{R}eF_h^2}\left[\frac{\beta_2^\nu}{\Omega_c}\sin(2\tilde{\theta}) + \chi_2^\nu t\cos(2\tilde{\theta}) + \sigma_2^\nu\Omega_c t^2\sin(2\tilde{\theta})\right]\left(\frac{\mathrm{d}U}{\mathrm{d}\tilde{z}}\right)^2 + O(\tilde{r}^4), \tag{4.171}$$

where

$$\beta_2^\nu = 10.66, \quad \chi_2^\nu = -5.376, \quad \sigma_2^\nu = -1.524. \tag{4.172}$$

4.4.6 Evolution of the angular velocity of the vortex

By rescaling the slow time, the vertical coordinate, and the Reynolds number, the evolution equation (4.156) can be re-written after some manipulations:

$$\frac{\partial\zeta_0}{\partial t} = -\frac{F_h^2}{\tilde{r}}\frac{\partial\tilde{r}^2\Omega^3}{\partial\tilde{r}}t\left(\frac{\mathrm{d}U}{\mathrm{d}z}\right)^2 + \frac{t^2}{2Re}\frac{1}{\tilde{r}}\frac{\partial}{\partial\tilde{r}}\left(\tilde{r}\frac{\partial\zeta_0}{\partial\tilde{r}}\right)\left(\frac{\mathrm{d}U}{\mathrm{d}z}\right)^2. \tag{4.173}$$

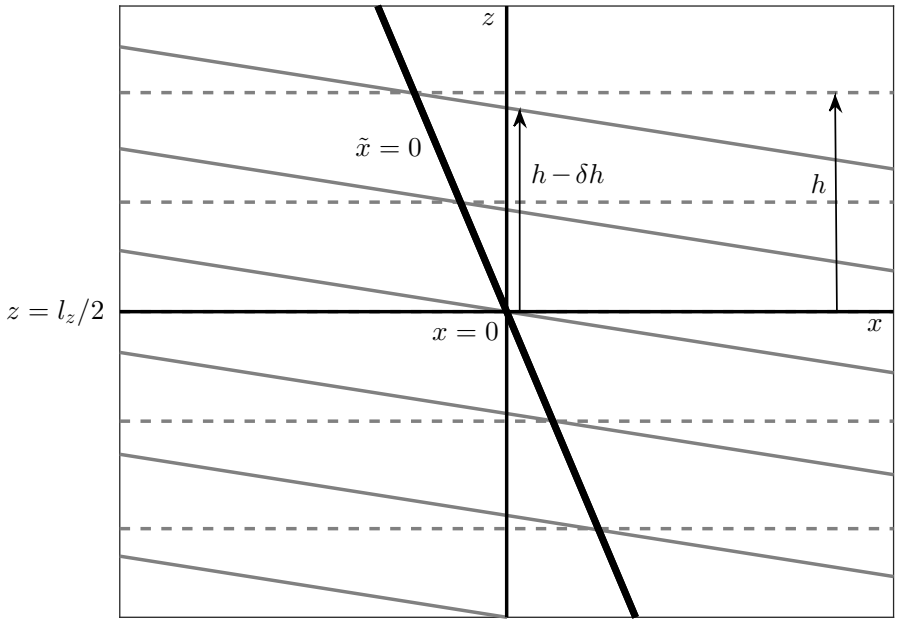

Figure 4.8: Lines of constant total buoyancy b_t near the point $x=0$, $z=l_z/2$ at $t=0$ (grey dashed lines) and $t=t_0$ (grey solid lines). The bold black solid line represents the vortex axis at $t=t_0$. δh is the height variation at $x=0$ of the iso-buoyancy line located at $z=h+l_z/2$ initially.

[3]Integrating in $\tilde{r}$ leads to an equation for Ω, namely

$$\frac{\partial\Omega}{\partial t}=\left[-F_h^2 t\Omega^3+\frac{t^2}{2Re\tilde{r}}\frac{\partial\zeta_0}{\partial\tilde{r}}\right]\left(\frac{\mathrm{d}U}{\mathrm{d}z}\right)^2. \tag{4.174}$$

This equation shows that the angular velocity of the vortex decays because of dynamic and viscous effects (first and second terms of the right-hand side, respectively). A physical interpretation of the origin of the dynamic effect can be gained by considering the conservation of potential vorticity near the vortex axis. First, let us consider the buoyancy at leading order $b=\sqrt{\varepsilon}b_0/F_h=-t\tilde{x}\Omega^2\mathrm{d}U/\mathrm{d}z$, where b_0 is given in (4.144) and $\tilde{x}=x-U(z)t$. Figure 4.8 sketches the lines of constant total buoyancy $b_t=b+z/F_h^2$ near the point $x=0$, $z=l_z/2$ at two times: $t=0$ (grey dashed lines) and $t=t_0$ (grey solid lines) where t_0 is small. At $t=t_0$, the vortex axis $\tilde{x}=0$ is inclined towards the left since $x=U(z)t_0\simeq -k_z U_S t_0(z-l_z/2)$ near $z=l_z/2$. The iso-buoyancy lines are also no longer horizontal but slanted downward towards the positive x direction. On the vortex axis $\tilde{x}=0$, they remain at the same vertical level while on the line $x=0$, they are displaced by

$$\delta h=-F_h^2\Omega^2 h t_0^2\left(\frac{\mathrm{d}U}{\mathrm{d}z}\right)^2 \tag{4.175}$$

where $h=z_0-l_z/2$ with z_0 the initial vertical level of the iso-buoyancy line. δh is therefore negative as clearly seen in figure 4.8. Since the vortex is inclined, the

[3]From this equation, it can be remarked that an alternative choice for the scaling of the slow time scale and Reynolds number could be $\tau=\sqrt{\varepsilon}t$, $1/ReF_h^2=\sqrt{\varepsilon}/\tilde{Re}_b$ where $\tilde{Re}_b=O(1)$. Introducing these scalings in (4.173) leads to an equation where only the slow time scale τ appears instead of both τ and t as in (4.156). However, the asymptotic analysis with these scalings would give identical results as the present one.

iso-buoyancy lines are indeed displaced towards the vortex axis where the pressure is minimum. This means that the vortex is squeezed near $x = 0$, $z = l_z/2$. The conservation of potential vorticity between the iso-density lines at $z = z_0$ and $z = l_z/2$ (figure 4.8)

$$\frac{\zeta}{h} = \frac{\zeta + \delta\zeta}{h + \delta h}, \tag{4.176}$$

implies that the vertical vorticity at $t = t_0$ will decrease by $\delta\zeta = \zeta\delta h/h$. The variation of vertical vorticity between $t = 0$ and $t = t_0$ is therefore

$$\frac{\partial\zeta}{\partial t} = \frac{\delta\zeta}{t_0} = -F_h^2\zeta\Omega^2 t_0 \left(\frac{\mathrm{d}U}{\mathrm{d}z}\right)^2. \tag{4.177}$$

This corresponds exactly to (4.174) for $Re = \infty$ since $\zeta = 2\Omega$ on the vortex axis. However, we stress that (4.174) is valid not only on the vortex axis near $z = l_z/2$ but everywhere. Both the dynamic and viscous decay of Ω are proportional to $(\mathrm{d}U/\mathrm{d}z)^2$. Hence, the decay will be maximum at $z = 0, l_z/2$ and will vanish at $z = l_z/4, 3l_z/4$ for the sinusoidal profile $U = U_S \sin(k_z z)$.

The equation (4.174) can be solved by a multiple scale analysis when the viscous effects are small. To do so, we introduce the time $\tilde{t} = (F_h t|\mathrm{d}U/\mathrm{d}z|)^3$. Then, (4.174) becomes

$$\frac{\partial\Omega}{\partial\tilde{t}} = -\frac{\Omega^3}{3\tilde{t}^{1/3}} + \frac{\gamma}{6\tilde{r}}\frac{\partial\zeta_0}{\partial\tilde{r}}, \quad \gamma = \frac{1}{ReF_h^3\left|\dfrac{\mathrm{d}U}{\mathrm{d}z}\right|}, \tag{4.178}$$

where γ is the only remaining control parameter. Assuming $\gamma \ll 1$, the angular velocity can be expanded as

$$\Omega = \Omega_0 + \gamma\Omega_1 + O(\gamma^2) \tag{4.179}$$

and we introduce a slow time scale $\upsilon = \gamma\tilde{t}$. At leading order, (4.178) becomes

$$\frac{\partial\Omega_0}{\partial\tilde{t}} = -\frac{\Omega_0^3}{3\tilde{t}^{1/3}} \tag{4.180}$$

whose solution is

$$\Omega_0 = \frac{\Omega_i(\tilde{r}, \upsilon)}{\sqrt{1 + \tilde{t}^{2/3}\Omega_i^2(\tilde{r}, \upsilon)}}, \tag{4.181}$$

where Ω_i is the angular velocity profile at $\tilde{t} = 0$. It can depend also on the slow time υ. At next order, we obtain:

$$\frac{\partial\Omega_1}{\partial\tilde{t}} + \frac{\partial\Omega_0}{\partial\upsilon} = -\frac{\Omega_0^2\Omega_1}{\tilde{t}^{1/3}} + \frac{1}{6\tilde{r}}\frac{\partial\zeta_0}{\partial\tilde{r}}. \tag{4.182}$$

After substituting (4.181) in this equation, its general solution is found to be:

$$\Omega_1 = \frac{\Theta - \dfrac{\partial\Omega_i}{\partial\upsilon} + \dfrac{1}{6\tilde{r}}\dfrac{\partial\zeta_i}{\partial\tilde{r}} - \dfrac{1}{2}\left(\dfrac{\partial\Omega_i}{\partial\tilde{r}}\right)^2\left[\dfrac{3\arctan(\Omega_i\tilde{t}^{1/3})}{\Omega_i^4} - \dfrac{3\tilde{t}^{1/3}}{\Omega_i^3} + \dfrac{\tilde{t}}{\Omega_i}\right]}{\left(1 + \tilde{t}^{2/3}\Omega_i^2\right)^{3/2}}, \tag{4.183}$$

where Θ is an arbitrary constant. This constant should be set to zero to ensure that $\Omega_1 \to 0$ as $\tilde{r} \to +\infty$. In addition, we have to impose that $\Omega = \Omega_i$ initially, implying that $\Omega_1 = 0$ at $\tilde{t} = 0$. This leads to an equation for Ω_i over the slow time υ:

$$\frac{\partial\Omega_i}{\partial\upsilon} = \frac{1}{6\tilde{r}}\frac{\partial\zeta_i}{\partial\tilde{r}}. \tag{4.184}$$

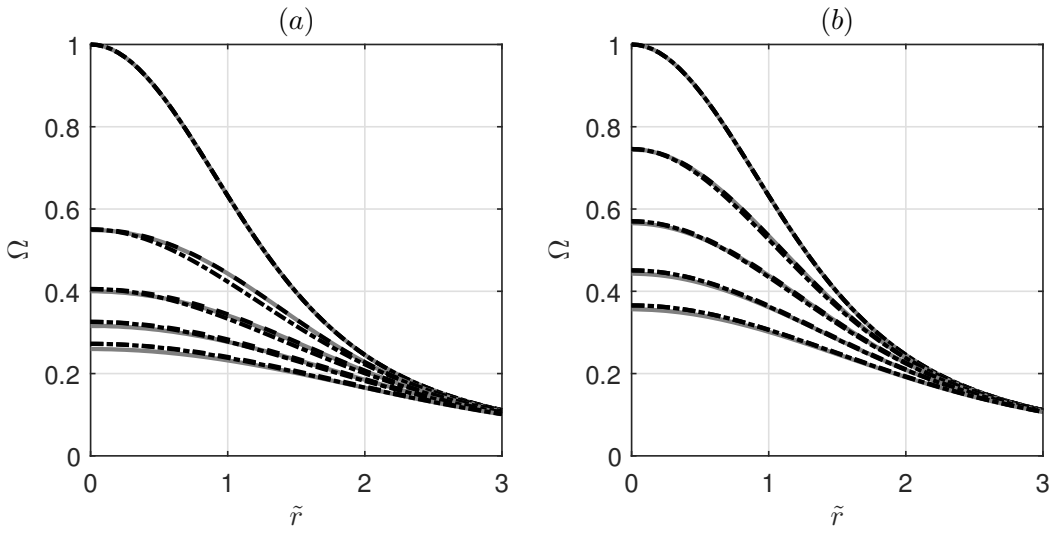

Figure 4.9: Angular velocity profile Ω computed numerically from (4.178) (grey solid lines) and predicted by (4.186) (black dashed lines) at different times for $\gamma = 0.1$ (a) and $\gamma = 1$ (b), as a function of $\tilde{r}$. The Lamb-Oseen profile (4.190) is also represented by black dash-dotted lines. The times shown are: (a) $\tilde{t} = 0$, $\tilde{t} = 2.65$, $\tilde{t} = 7.50$, $\tilde{t} = 13.8$, $\tilde{t} = 21.2$ and (b) $\tilde{t} = 0$, $\tilde{t} = 0.265$, $\tilde{t} = 0.750$, $\tilde{t} = 1.38$, $\tilde{t} = 2.12$, from top to bottom.

Since $\Omega_i(\tilde{r}, \upsilon = 0) = \left[1 - \exp(-\tilde{r}^2)\right]/\tilde{r}^2$, the solution of (4.184) is:

$$\Omega_i = \frac{1 - \exp(-\tilde{r}^2/\tilde{a}^2)}{\tilde{r}^2}, \tag{4.185}$$

with $\tilde{a}^2 = 1 + 2\upsilon/3$. Gathering the two orders and rescaling the slow time scale υ give the total expression of Ω:

$$\Omega = \frac{\Omega_i}{\sqrt{1 + \tilde{t}^{2/3}\Omega_i^2}} - \frac{\gamma}{2}\left(\frac{\partial \Omega_i}{\partial \tilde{r}}\right)^2 \frac{3\arctan(\Omega_i \tilde{t}^{1/3}) - 3\tilde{t}^{1/3}\Omega_i + \tilde{t}\Omega_i^3}{\Omega_i^4\left(1 + \tilde{t}^{2/3}\Omega_i^2\right)^{3/2}} + O(\gamma^2), \tag{4.186}$$

with

$$\Omega_i = \frac{1}{\tilde{r}^2}\left[1 - \exp\left(-\frac{\tilde{r}^2}{1 + 2\gamma\tilde{t}/3}\right)\right]. \tag{4.187}$$

Equation (4.186) implies that the angular velocity at the vortex center evolves as

$$\Omega_c = \frac{1}{\sqrt{\left(1 + 2\gamma\tilde{t}/3\right)^2 + \tilde{t}^{2/3}}} + O(\gamma^2), \tag{4.188}$$

i.e. in terms of t and the original parameters:

$$\Omega_c = \frac{1}{\sqrt{\left[1 + \dfrac{2t^3}{3Re}\left(\dfrac{\mathrm{d}U}{\mathrm{d}z}\right)^2\right]^2 + F_h^2 t^2 \left(\dfrac{\mathrm{d}U}{\mathrm{d}z}\right)^2}}. \tag{4.189}$$

Figure 4.9 compares the asymptotic solution (4.186) to the exact solution of (4.178) computed numerically at different times $\tilde{t}$. We see that the agreement is excellent for

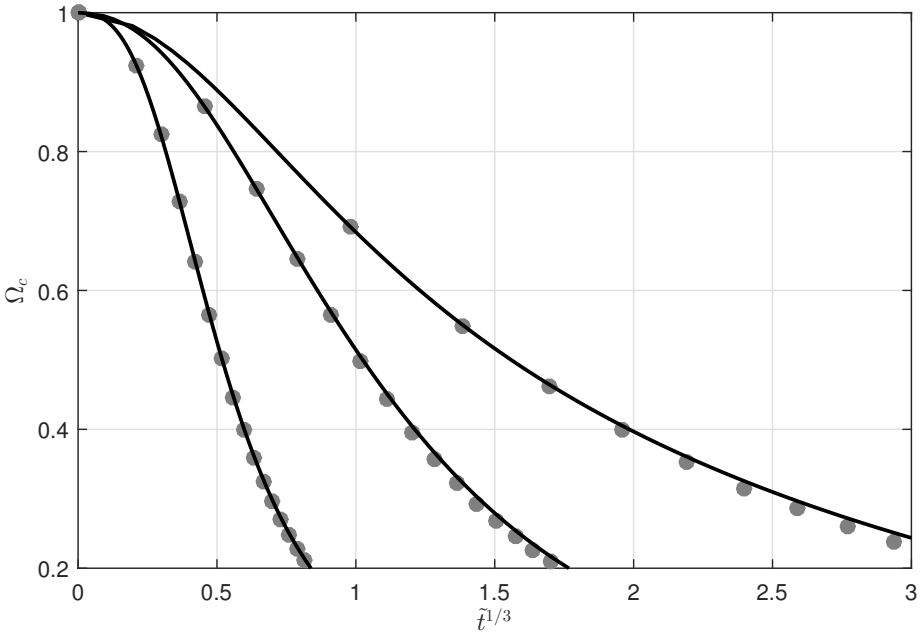

Figure 4.10: Evolution of the angular velocity at the vortex center Ω_c as a function of $\tilde{t}^{1/3}$ predicted by (4.188) (black solid lines) and computed numerically from (4.178) (grey circles) for $\gamma = 0.1$, $\gamma = 1$, and $\gamma = 10$ (top to bottom).

$\gamma = 0.1$ (figure 4.9*a*) and even for $\gamma = 1$ (figure 4.9*b*). There are only some slight discrepancies in the vortex core $\tilde{r} \lesssim 1$ when $\tilde{t} \gtrsim 1$. In practice, the asymptotic solution (4.186) turns out to be very accurate not only for small values of γ but also for large values such as $\gamma = 10$ (not shown). In figure 4.9, the Lamb-Oseen profile

$$\Omega_e = \frac{1 - \exp(-\tilde{r}^2/\tilde{a}_e^2)}{\tilde{r}^2} \tag{4.190}$$

with $\tilde{a}_e^2 = 1/\Omega_c$, where Ω_c is given by (4.188), has been also plotted with black dash-dotted lines. This profile is close to the asymptotic solution (4.186). This is the reason why the approximate profile (4.190) has been used to ease the numerical resolution of the streamfunction ψ_{12} (4.157).

Figure 4.10 shows the asymptotic angular velocity at the vortex center (4.188) and the exact solution obtained numerically, for different values of the control parameter γ. The agreement is very good not only for $\gamma = 0.1$ but also for $\gamma = 1$ and $\gamma = 10$. Therefore, (4.188) will be used to describe the evolution of Ω_c regardless of the value of γ.

4.4.7 Analysis of the vortex deformations

Having determined the evolution of Ω, we now come back to the study of the equations (4.138)-(4.139) for the vortex displacements.

Since $U = U_S \sin(\tilde{k}_z \tilde{z})$, we will look for the perturbation displacements in the form

$$\delta x(\tilde{z}, \tilde{\eta}, \tau) = \hat{X}(\tilde{\eta}, \tau) \sin(\tilde{k}_z \tilde{z}), \quad \delta y(\tilde{z}, \tilde{\eta}, \tau) = \hat{Y}(\tilde{\eta}, \tau) \sin(\tilde{k}_z \tilde{z}), \tag{4.191}$$

where $\hat{X}$ and $\hat{Y}$ are amplitudes that vary slowly along the vertical and with time.

Then, (4.138) and (4.139) become

$$\frac{\partial \hat{X}}{\partial \tau} = -\frac{\tilde{k}_z^2 \mathcal{A}(\tilde{\eta},\tau)}{2}\hat{Y}(\tilde{\eta},\tau) + \tilde{k}_z^2 U_S\left[\vartheta(\tilde{\eta},\tau) + \frac{\partial \mathcal{C}_w}{\partial t}(t,\tilde{\eta},\tau)\right] - \varepsilon\frac{\tilde{k}_z^2 U_S t}{\tilde{R}eF_h^2}, \tag{4.192}$$

$$\frac{\partial \hat{Y}}{\partial \tau} = \frac{\tilde{k}_z^2 \mathcal{A}(\tilde{\eta},\tau)}{2}\left[U_S t + \hat{X}(\tilde{\eta},\tau)\right] + \tilde{k}_z^2 U_S \frac{\partial \mathcal{S}_w}{\partial t}(t,\tilde{\eta},\tau). \tag{4.193}$$

It is convenient to further rescale the slow time τ and the vertical coordinate $\tilde{\eta}$ in terms of the time t and the vertical coordinate z:

$$\frac{\partial \hat{X}}{\partial t} = -\hat{\omega}(z,t)\hat{Y}(z,t) + (k_z F_h)^2 U_S\left[\vartheta(z,t) + \frac{\partial \mathcal{C}_w}{\partial t}(z,t)\right] - \frac{k_z^2 U_S t}{Re}, \tag{4.194}$$

$$\frac{\partial \hat{Y}}{\partial t} = \hat{\omega}(z,t)\left[U_S t + \hat{X}(z,t)\right] + (k_z F_h)^2 U_S \frac{\partial \mathcal{S}_w}{\partial t}(z,t), \tag{4.195}$$

where $\hat{\omega} = (k_z F_h)^2 \mathcal{A}/2$.

The solution of (4.194)-(4.195) can be decomposed as

$$\hat{X} = X^* + (k_z F_h)^2 U_S\left[\mathcal{C}_w + \int_0^t \vartheta(z,\upsilon)\mathrm{d}\upsilon\right] - \frac{k_z^2 U_S t^2}{2Re}, \tag{4.196}$$

$$\hat{Y} = Y^* + (k_z F_h)^2 U_S \mathcal{S}_w + U_S \int_0^t \hat{\omega}(z,\upsilon)\upsilon \mathrm{d}\upsilon, \tag{4.197}$$

giving

$$\frac{\partial X^*}{\partial t} = -\hat{\omega}Y^* + O\left[(k_z F_h)^4\right], \tag{4.198}$$

$$\frac{\partial Y^*}{\partial t} = \hat{\omega}X^* + O\left[(k_z F_h)^4, \frac{k_z^4 F_h^2}{Re}\right]. \tag{4.199}$$

Since (4.194)-(4.195) are valid up to order $O[(k_z F_h)^2]$ and $O[k_z^2/Re]$, it is indeed legitimate to neglect the terms $O[(k_z F_h)^4, k_z^4 F_h^2/Re]$ in (4.198)-(4.199). The general solution of (4.198)-(4.199) is

$$X^* = X_c^*(z)\cos\left(\int_0^t \hat{\omega}(z,\upsilon)\mathrm{d}\upsilon\right) + X_s^*(z)\sin\left(\int_0^t \hat{\omega}(z,\upsilon)\mathrm{d}\upsilon\right), \tag{4.200}$$

$$Y^* = -X_s^*(z)\cos\left(\int_0^t \hat{\omega}(z,\upsilon)\mathrm{d}\upsilon\right) + X_c^*(z)\sin\left(\int_0^t \hat{\omega}(z,\upsilon)\mathrm{d}\upsilon\right), \tag{4.201}$$

where X_c^* and X_s^* are arbitrary functions of z only. The initial conditions $\hat{X} = \hat{Y} = 0$ at $t = 0$ impose $X_c^* = X_s^* = 0$. Therefore, a solution of (4.194)-(4.195) valid up to order $O[(k_z F_h)^2]$ and $O[k_z^2/Re]$ is

$$\hat{X} = (k_z F_h)^2 U_S\left[\mathcal{C}_w + \int_0^t \vartheta(z,\upsilon)\mathrm{d}\upsilon\right] - \frac{k_z^2 U_S t^2}{2Re}, \tag{4.202}$$

$$\hat{Y} = (k_z F_h)^2 U_S \mathcal{S}_w + U_S \int_0^t \hat{\omega}(z,\upsilon)\upsilon \mathrm{d}\upsilon, \tag{4.203}$$

[4]These equations show that the vortex axis evolves because of four different effects in addition to the advection $Ut\boldsymbol{e}_x$ by the shear flow:

[4]With the alternative scalings proposed previously, $\tau = \sqrt{\varepsilon}t$, $1/ReF_h^2 = \sqrt{\varepsilon}/\tilde{R}e_b$, these solutions show that $\delta y = O(1)$ for $\tau = O(1)$ as assumed herein, while $\delta x = O(\sqrt{\varepsilon})$. However, the fast time would be still present in the wave terms.

1. the displacement due to internal waves (first terms in the right-hand side of (4.202)-(4.203))
2. the second term in the right-hand side of (4.202) describes a small delay (since ϑ is negative as seen in figure 4.5*b*) in the advection by the shear flow due to its three-dimensional character.
3. viscous effects (last term in the right-hand side of (4.202))
4. the self-induction (last term in the right-hand side of (4.203)). The shear flow bends the vortex in the x direction and, in turn, this creates a self-induced motion in the y direction.

Behaviour for small time

By substituting $\mathcal{C}_w$ and $\mathcal{S}_w$ in (4.194)-(4.195) by their asymptotic expressions (B.21)-(B.22) derived for small time (see appendix B), we find that the amplitudes of the perturbation displacements behave for $t \ll 1$ and in the inviscid limit as:

$$\hat{X} = k_z^2 U_S \varsigma t^3 + O(t^4), \quad \hat{Y} = k_z^2 U_S \sigma t^4 + O(t^5). \tag{4.204}$$

Remarkably, the initial evolution of $(\hat{X}, \hat{Y})$ is independent of the Froude number at leading order. At this order, $\hat{X}$ and $\hat{Y}$ vary like t^3 and t^4 respectively. This implies that the leading order buoyancy b_0 (4.81) varies like t^3 for small times consistently with the short time expansion of b derived in §4.3. However, it is not possible to compare quantitatively the order $k_z^2 t^3$ of the short time expansion to its counterpart in the long-wavelength expansion. Indeed, (4.204) shows that $\hat{X}$ and $\hat{Y}$ are of order k_z^2 for small times. Thus, the contribution of the perturbation displacements δx and δy in (4.81) is one order smaller in k_z^2 than the other terms. Hence, these contributions are actually of the same order as the next order term εb_1 in the expansion (4.51). Since b_1 will not be computed herein, the determination of the order k_z^2 of b is therefore incomplete.

It is interesting to compare the predictions (4.204) to those of a simple model where the advection by the shear flow is directly added to the equations of the self-induced motion of the single vortex, i.e.:

$$\frac{\partial \Delta\hat{X}}{\partial t} = -\hat{\omega}\hat{Y} + U_S, \tag{4.205}$$

$$\frac{\partial \hat{Y}}{\partial t} = \hat{\omega}\Delta\hat{X}, \tag{4.206}$$

where $\Delta\hat{X} = U_S t + \hat{X}$ is the total displacement of the vortex in the streamwise direction. Such phenomenological model can be obtained from (4.194)-(4.195) by assuming $Re \to \infty$ and by setting $\vartheta = \partial\mathcal{C}_w/\partial t = \partial\mathcal{S}_w/\partial t = 0$, i.e. by neglecting the waves effect and the three-dimensional correction of the advection by the base flow. The model (4.205)-(4.206) has been introduced for example by Marshall and Parthasarathy (1993) for two layer quasi-geostrophic flows, with constant coefficients. For small times $t \ll 1$, the solution of (4.205)-(4.206) is:

$$\hat{X} = -\frac{\hat{\omega}^2 U_S}{6} t^3 + O(t^4), \quad \hat{Y} = \frac{\hat{\omega} U_S}{2} t^2 + O(t^3). \tag{4.207}$$

Thus, $\hat{X}$ is initially of order $k_z^4 F_h^4 t^3$ instead of $k_z^2 t^3$ and $\hat{Y}$ is of order $k_z^2 F_h^2 t^2$ instead of $k_z^2 t^4$. This shows that internal waves have a strong effect on the initial dynamics of the vortex.

Evolution in the planes $z = l_z/4, 3l_z/4$

In the planes $z = l_z/4$, $z = 3l_z/4$, $\mathcal{A}$ and ϑ are independent of t because the initial angular velocity profile does not evolve at these locations since $\mathrm{d}U/\mathrm{d}z = 0$ (see (4.174)). Thus, (4.202)-(4.203) become

$$\hat{X} = (k_z F_h)^2 U_S \left[\mathcal{C}_w + \vartheta t\right] - \frac{k_z^2 U_S t^2}{2Re}, \tag{4.208}$$

$$\hat{Y} = \frac{U_S \hat{\omega} t^2}{2} + (k_z F_h)^2 U_S \mathcal{S}_w. \tag{4.209}$$

For large time $t \gg 1$, figure 4.6 shows that $\mathcal{C}_w$ and $\mathcal{S}_w$ tend to constant values $\mathcal{C}_w^\infty$ and $\mathcal{S}_w^\infty$ respectively. Hence, (4.208)-(4.209) become:

$$\hat{X} = (k_z F_h)^2 U_S \left[\mathcal{C}_w^\infty + \vartheta t\right] - \frac{k_z^2 U_S t^2}{2Re}, \tag{4.210}$$

$$\hat{Y} = \frac{U_S \hat{\omega} t^2}{2} + (k_z F_h)^2 U_S \mathcal{S}_w^\infty. \tag{4.211}$$

4.5 Conclusion

We have carried out two asymptotic analyses of the evolution of a columnar vortex in an ambient stratified shear flow. The vortex has initially a Lamb-Oseen profile while the shear flow is horizontally uniform and varies sinusoidally along the vertical: $U(z) = U_S \sin(k_z z)$. The Froude number F_h has been assumed to be lower than unity so that there is no critical layer where the angular velocity of the vortex is equal to the buoyancy frequency. The Reynolds number has been considered infinite in the first analysis and large in the second analysis. These asymptotic analyses highlight different aspects of the evolution of the vortex.

First, the asymptotic analysis for small time shows that the horizontal flow is independent of the stratification up to order t^3. At order t, the flow consists simply in a horizontal displacement of the vortex without deformation while at order t^2, internal deformations of the vortex occur for finite vertical wavenumber k_z. On the vertical, the dynamics is non-hydrostatic as long as $t < 1/N$.

The second asymptotic analysis is a long-wavelength analysis assuming that the rescaled vertical wavenumber $k_z F_h$ is small. This particular small parameter derives from the self-similarity of strongly stratified flows (Billant and Chomaz, 2001) according to which the vertical wavenumber always appears multiplied by the Froude number F_h in the Euler equations under the Boussinesq approximation.

This asymptotic analysis provides governing equations for the displacement of the vortex axis and for its angular velocity. The vortex axis is advected by the shear flow at leading order $\Delta x = U(z)t$ but four different effects influence its trajectory at order $(k_z F_h)^2$. First, the vortex axis deviates perpendicularly to the direction of the shear flow owing to the self-induction of the vortex when it is bent. Secondly, internal waves, which are generated at the start-up of the motion, influence the initial evolution of the vortex. These waves oscillate at the buoyancy pulsation N and explain why the dynamics is initially non-hydrostatic. Later, their effects on the vortex trajectory quickly decay off. The third and fourth effects are three-dimensional and viscous effects that slightly reduce the advection in the direction of the shear flow.

The angular velocity of the vortex decreases with time because of dynamic and viscous effects. The dynamic effect is due to the squeezing of the isopycnal surfaces when the vortex is inclined. To conserve potential vorticity, the core vertical vorticity has therefore to decrease. The viscous decay of the angular velocity is also quickly enhanced since the vertical shear increases algebraically with time. These two effects are not uniform along the vertical: they are maximum in the regions of high shear and vanish at the vertical levels where the shear is zero.

In addition, a horizontal velocity field with an azimuthal wavenumber $m = 2$ arises at order $(k_z F_h)^2$ implying that the vortex becomes slightly elliptical.

Chapter 5

Evolution of a vortex in a strongly stratified shear flow. Part 2. Numerical simulations.

Article in preparation for submission to the *Journal of Fluid Mechanics*.

Abstract

We conduct direct numerical simulations of an initially vertical Lamb-Oseen vortex in an ambient shear flow varying sinusoidally along the vertical in a stratified fluid. The Froude number F_h and the Reynolds number Re, based on the circulation Γ and radius a_0 of the vortex, have been varied in the ranges: $0.1 \leqslant F_h \leqslant 0.5$ and $3000 \leqslant Re \leqslant 10000$. The shear flow amplitude $\hat{U}_S$ and vertical wavenumber $\hat{k}_z$ lie in the ranges: $0.02 \leqslant 2\pi a_0 \hat{U}_S/|\Gamma| \leqslant 0.4$ and $0.1 \leqslant \hat{k}_z a_0 \leqslant 3\pi/2$. The results are analysed in the light of the asymptotic analyses performed in chapter 4.

The vortex is mostly advected in the direction of the shear flow but also in the perpendicular direction owing to the self-induction. The decay of potential vorticity is strongly enhanced in the regions of high shear. The shear instability is triggered only when the Froude number is moderate $F_h = 0.5$ and for sufficiently high Reynolds number and vertical wavenumber $\hat{k}_z$.

The initial non-hydrostatic dynamics is well captured by the short-time asymptotic analysis of chapter 4. The long-wavelength analysis predicts also very well the deformations of the vortex axis. The evolutions of the vertical shear of the horizontal velocity of the vortex and of the vertical gradient of the buoyancy at the location of maximum shear are in good agreement with the asymptotic predictions. These quantities saturate owing to both dynamic and viscous effects. The asymptotic Richardson number is shown to depend only on the initial Richardson number Ri_0 and the buoyancy Reynolds number $Re_b = ReF_h^2$. Its minimum value never goes below the critical value 1/4. This proves that the vertical shear cannot grow indefinitely in strongly stratified flows, contradicting the conjecture of Lilly (1983).

The asymptotic analysis is not able to predict the development of the shear instability for $F_h = 0.5$ because of the important effect of internal waves, partially neglected in the long-wavelength analysis.

5.1 Introduction

In this chapter, we continue the analysis of the evolution of a vortex embedded in a vertically sheared flow in a strongly stratified fluid. The main purpose is to determine if the vertical shear can grow indefinitely as speculated by Lilly (1983) and thus leads to the unconditional development of the shear instability.

This instability is thought to be an important process for the generation of small scales in stratified flows (Riley and deBruynKops, 2003; Lindborg, 2006; Brethouwer et al., 2007). In the case of a columnar counter-rotating vortex pair, Deloncle et al. (2008) and Waite and Smolarkiewicz (2008) have reported that the vertical shear generated by the zigzag instability can lead to the development of the shear instability. This occurs when the buoyancy Reynolds number $Re_b = ReF_h^2$ (Re is the classical Reynolds number and F_h the Froude number) is above a threshold since the minimum Richardson number is inversely proportional to Re_b (Riley and deBruynKops, 2003; Deloncle et al., 2008; Augier and Billant, 2011). The subsequent destabilization of the Kelvin-Helmholtz billows leads to small-scale turbulence with spectral characteristics similar to those of randomly forced stratified turbulence (Augier et al., 2012; Waite, 2013).

However, a counter-rotating vortex pair is a particular flow not frequently encountered in turbulent flows. Here, we consider the more generic configuration of

a single vortex in an ambient shear flow. In chapter 4, we have studied such flow by means of two asymptotic analyses. First, a short-time analysis has evidenced the existence of an initial non-hydrostatic regime. Secondly, a long-wavelength analysis has been carried out for $k_z F_h \ll 1$, where k_z is the vertical wavenumber of the sinusoidal shear flow. This analysis provides a complete description of the vortex dynamics: the evolution of the vortex axis and angular velocity as well as secondary flows created as the vortex is bent. In the present chapter, we will conduct DNS of this flow and analyse its dynamics in the light of the asymptotic analyses.

The chapter is organized as follows. The initial conditions, control parameters, and numerical method are described in §5.2. An overview of two typical simulations is first given in §5.3. Then, the initial evolution of the flow is compared to the results of the short-time asymptotic analysis in §5.4. In §5.5, the long-wavelength analysis is first briefly summarized in §5.5.1 and its predictions for the deformations of the vortex axis are compared to the numerical simulations in §5.5.2. We then focus on the evolution of the flow at the vortex center and the mid-vertical level where the vertical shear is maximum (§5.5.3). Again, the asymptotic analysis is used to rationalize the numerical results. Finally, section §5.5.4 concentrates on the Richardson number predicted by the long-wavelength analysis. Section §5.7 summarizes and discusses the results.

5.2 Formulation of the problem

5.2.1 Initial conditions and governing equations

As in chapter 4, the flow at $t = 0$ is chosen as

$$\boldsymbol{u} = \boldsymbol{U}_S + \boldsymbol{u}_v, \tag{5.1}$$

where $\boldsymbol{U}_S$ is a sinusoidal shear flow and $\boldsymbol{u}_v$ a columnar vortex with a Lamb-Oseen profile:

$$\boldsymbol{U}_S = U_S \sin(k_z z)\boldsymbol{e}_x, \quad \boldsymbol{u}_v = \frac{1-\exp(-r^2)}{r}\boldsymbol{e}_\theta, \tag{5.2}$$

where (x, y, z) and (r, θ, z) are cartesian and cylindrical coordinates, respectively. The associated unit vectors are $(\boldsymbol{e}_x, \boldsymbol{e}_y, \boldsymbol{e}_z)$ and $(\boldsymbol{e}_r, \boldsymbol{e}_\theta, \boldsymbol{e}_z)$.

In (5.2), the length and time have been non-dimensionalized by the vortex radius a_0 and the turnover time $2\pi a_0^2/|\Gamma|$ of the vortex. The shear amplitude U_S and wavenumber k_z are therefore non-dimensional: $U_S = \hat{U}_S/(|\Gamma|/2\pi a_0)$, $k_z = \hat{k}_z a_0$, where $\hat{U}_S$ and $\hat{k}_z$ are the corresponding dimensional quantities.

The governing equations are the incompressible Navier-Stokes equations under the Boussinesq approximation. They read in dimensionless form:

$$\boldsymbol{\nabla}_h \cdot \boldsymbol{u}_h + \frac{\partial w}{\partial z} = 0, \tag{5.3}$$

$$\frac{\partial \boldsymbol{u}_h}{\partial t} + (\boldsymbol{u}_h \cdot \boldsymbol{\nabla}_h)\,\boldsymbol{u}_h + w\frac{\partial \boldsymbol{u}_h}{\partial z} = -\boldsymbol{\nabla}_h p + \frac{1}{Re}\boldsymbol{\nabla}^2 \boldsymbol{u}_h, \tag{5.4}$$

$$\frac{\partial w}{\partial t} + \boldsymbol{u}_h \cdot \boldsymbol{\nabla}_h w + w\frac{\partial w}{\partial z} = -\frac{\partial p}{\partial z} + b + \frac{1}{Re}\nabla^2 w, \tag{5.5}$$

$$\frac{\partial b}{\partial t} + \boldsymbol{u}_h \cdot \boldsymbol{\nabla}_h b + w\frac{\partial b}{\partial z} = -\frac{w}{F_h^2} + \frac{1}{ReSc}\nabla^2 b, \tag{5.6}$$

F_h	Re	k_z	U_S	l_z	n_x	n_y	n_z	δt
0.1	6000	π	0.2	2	512	512	256	0.005
0.1	10000	2	0.2	3.142	512	512	256	0.005
0.1	6000	2	0.4	3.142	512	512	256	0.005
0.5	6000	0.3	0.2	20.94	384	384	448	0.01
0.5	6000	π	0.2	2	832	832	256	0.005
0.5	6000	$3\pi/2$	0.2	1.333	832	832	448	0.005

Table 5.1: Overview of the physical and numerical parameters of some typical simulations. For all simulations, the horizontal dimensions of the domain are $l_x = l_y = 18$.

where $\boldsymbol{u}_h = (u, v)$ and w are the horizontal and vertical velocities in cartesian coordinates, p the pressure, b the buoyancy, and

$$Re = \frac{|\Gamma|}{2\pi\nu}, \quad F_h = \frac{|\Gamma|}{2\pi a_0^2 N}, \quad Sc = \frac{\nu}{\kappa} \tag{5.7}$$

are the Reynolds, Froude and Schmidt numbers, with ν the viscosity, κ the diffusivity and N the Brunt-Väisälä frequency which is assumed constant.

5.2.2 Numerical method

Equations (5.3-5.6) are integrated numerically by means of a pseudo-spectral method with periodic boundary conditions and a fourth-order Runge-Kutta time advancement scheme (Deloncle et al., 2008). An elliptic truncation of the top one-third of the modes is applied. The viscous and diffusive terms are integrated exactly.

The horizontal size of the computational domain is taken large $l_x = l_y = 18$ in order to minimize the effect of the periodic boundary conditions. The vertical size is set to $l_z = 2\pi/k_z$, so that a single wavelength of the shear flow is simulated.

Table 5.1 lists the parameters of some typical simulations. The number of grid points in the x and y directions have been varied from $n_x = n_y = 384$ to $n_x = n_y = 832$ depending on the values of the Reynolds and Froude numbers. The number of grid points in the vertical direction ranges from $n_z = 256$ to $n_z = 448$ depending on the values of k_z, Re and F_h. Typically, a high resolution is required for the parameters where the shear instability develops because it generates small billows while a moderate resolution is sufficient for the other cases. When k_z increases, the horizontal and vertical resolutions have to be increased also since the vertical gradients are larger. The accuracy of the results has been checked by increasing the resolution or the domain horizontal sizes in several runs. The time step varies from $\delta t = 0.0025$ to $\delta t = 0.01$. All the numerical simulations have been carried out for $Sc = 1$. The Froude number has been always kept below unity so as to remain in the strongly stratified regime. The shear amplitude U_S is also always kept below unity meaning that the vortex is stronger than the shear flow. The vertical wavenumber has been varied in the range $0.1 \leqslant k_z \leqslant 3\pi/2$. The Reynolds number has been varied from $Re = 3000$ to $Re = 10000$.

5.3 Overview of the dynamics

5.3.1 Qualitative description

We first begin by a description of two different simulations in order to give a global overview of the flow dynamics.

Figures 5.1 and 5.2 display the potential vorticity at different times for $k_z = \pi$, $F_h = 0.1$ and $k_z = 3\pi/2$, $F_h = 0.5$, respectively, whereas U_S and Re are fixed to $U_S = 0.2$ and $Re = 6000$. The first column shows three-dimensional contours while the second column represents a corresponding horizontal cross-section at the vertical level $z = l_z/4$. The vortex is mostly displaced in the direction of the shear flow, but also slightly in the perpendicular direction as seen in the horizontal cross-sections. Hence, the vertical plane containing the vortex axis is actually oblique relative to the (x, z) plane. The displacement in the y direction is weaker in figure 5.1 than in figure 5.2.

A common feature of both simulations is that the potential vorticity decreases faster in the regions of high shear $z = 0, l_z/2$ than in the regions of weak shear $z = l_z/4, 3l_z/4$. Thus, the vortex seems to be torn apart into two separate pancake vortices (Beckers et al., 2001) at large times.

Figure 5.3 displays the corresponding total vertical shear of the horizontal velocity $\sqrt{S_z} = \sqrt{(\partial u/\partial z)^2 + (\partial v/\partial z)^2}$ (color) in the vertical cross-section at $y = 9$, i.e. passing through the vortex center at $t = 0$. The superimposed black lines show the total density ρ_t. For $k_z = \pi$, $F_h = 0.1$ (left column of figure 5.3), the shear is maximum in the vortex core at the point $x_c = 9$, $z_c = 0, l_z/2$ (note that these coordinates correspond to those of the computational domain where the vortex center is initially in the middle $x = 9$, $y = 9$). As the vortex is progressively bent, S_z grows monotonically with time and becomes rapidly much higher than the maximum ambient shear $\max(\bar{S}_z) = k_z^2 U_S^2$ (figure 5.3*a,c,e,g*). The iso-density lines remain nearly flat since the stratification is strong for this case.

Figure 5.4 shows that the minimum of the Richardson number (black solid line)

$$Ri = \frac{\dfrac{1}{F_h^2} + \dfrac{\partial b}{\partial z}}{S_z} \tag{5.8}$$

decreases with time down to $\min(Ri) = 3.7$ at $t = 22$ and then slowly re-increases. The quantity $\min(Ri)$ thus remains well above the critical value $1/4$ necessary for the development of the shear instability of a steady parallel inviscid shear flow (Miles, 1961; Howard, 1961).

For $k_z = 3\pi/2$, $F_h = 0.5$ (right column of figure 5.3), the growth of the maximum shear S_z is not monotonic. There is a first stage where the shear is very weak within the vortex core (see figure 5.3*b* at $t = 4$), i.e. the response of the vortex tends to cancel the ambient shear. Then, the vortex becomes tilted as for $k_z = \pi$, $F_h = 0.1$, and the maximum shear is encountered in the vicinity of $x_c = 9$, $z_c = 0, l_z/2$ (figure 5.3*d*). The regions of high shear are remarkably thin. Later on, the flow strongly dissipates in these regions and the shear becomes maximum at points away from (x_c, z_c) (figure 5.3*f,h*). During this evolution, the iso-density lines are strongly deformed in contrast to $k_z = \pi$, $F_h = 0.1$. Some overturns can even be seen in the regions of high shear at $t = 26$ (figure 5.3*f*). As seen in figure 5.4, the minimum Richardson number for this simulation (grey solid line) decreases below $Ri_c = 0.25$ for $11 \leqslant t \leqslant 37$. The (y, z)

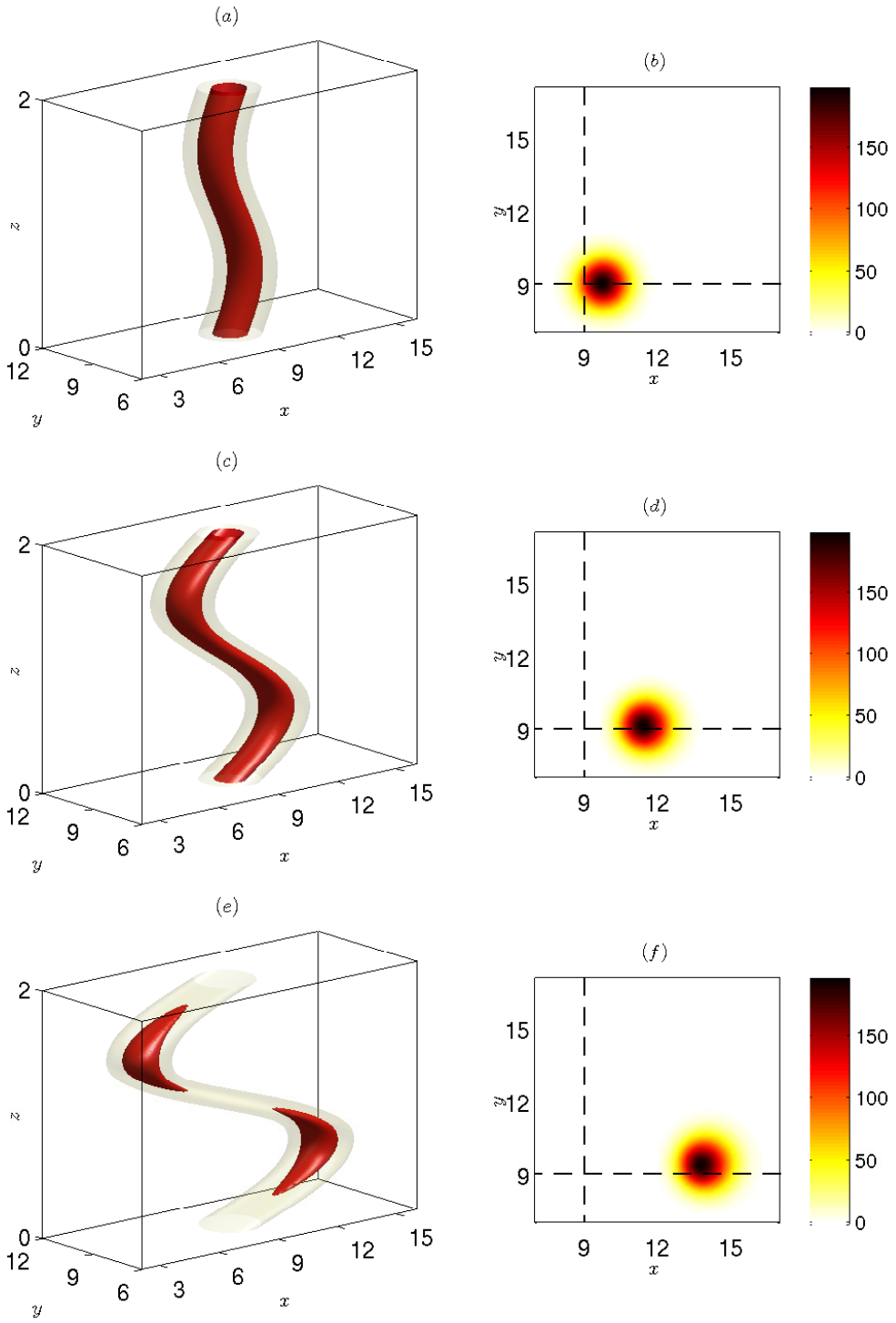

Figure 5.1: Left column: three-dimensional contours of the potential vorticity at different times for $F_h = 0.1$, $k_z = \pi$, $U_S = 0.2$ and $Re = 6000$. Right column: corresponding horizontal cross-sections in the plane $z = l_z/4$ where the advection is the most intense. The times shown are (a,b) $t = 4$, (c,d) $t = 13$, (e,f) $t = 26$. In (a,c,e), the isocontours correspond to 20% (yellow) and 60% (red) of the initial maximum value.

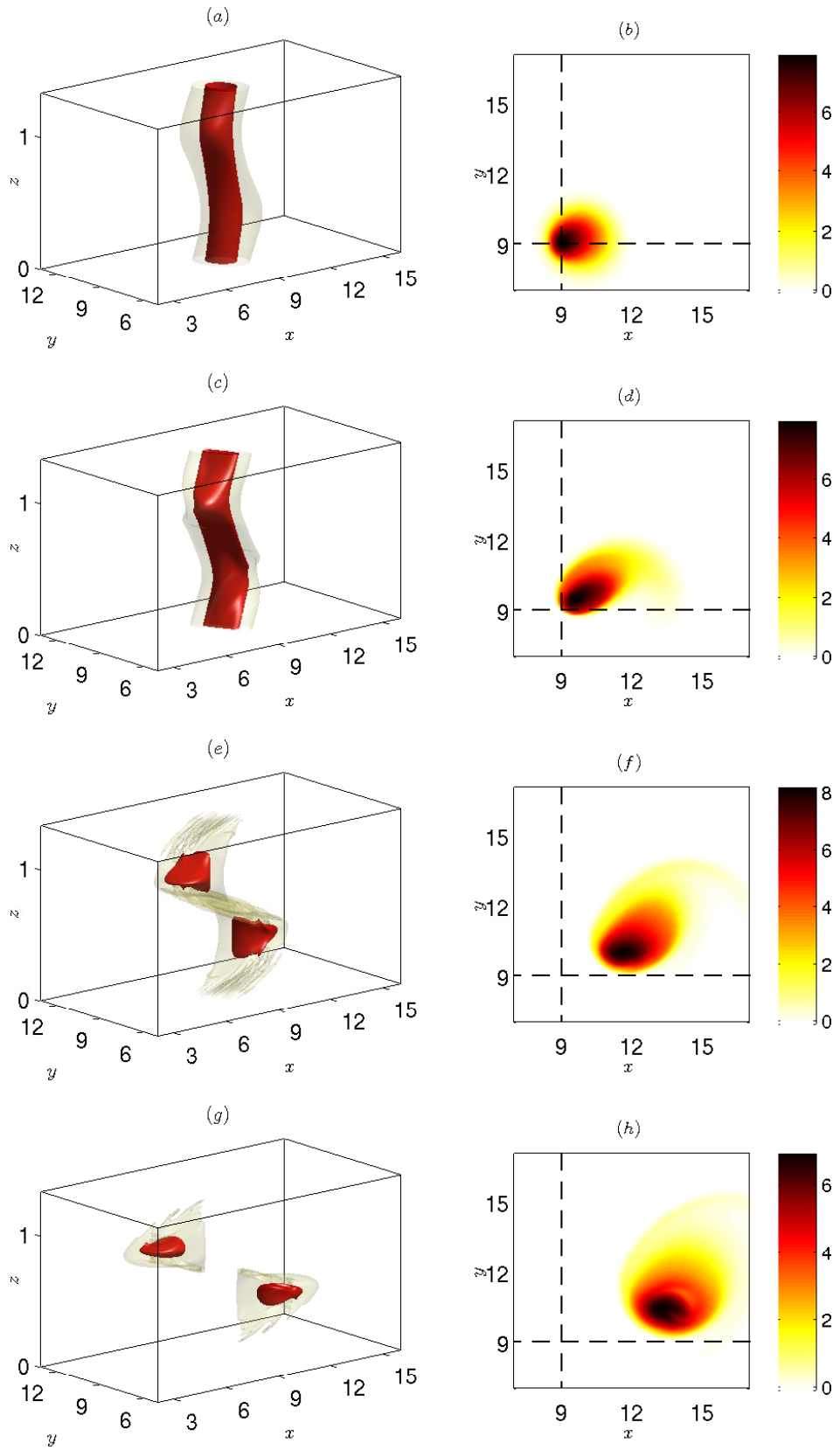

Figure 5.2: Same as figure 5.1 except that $F_h = 0.5$, $k_z = 3\pi/2$. The times shown are (a,b) $t = 4$, (c,d) $t = 13$, (e,f) $t = 26$, (g,h) $t = 36$.

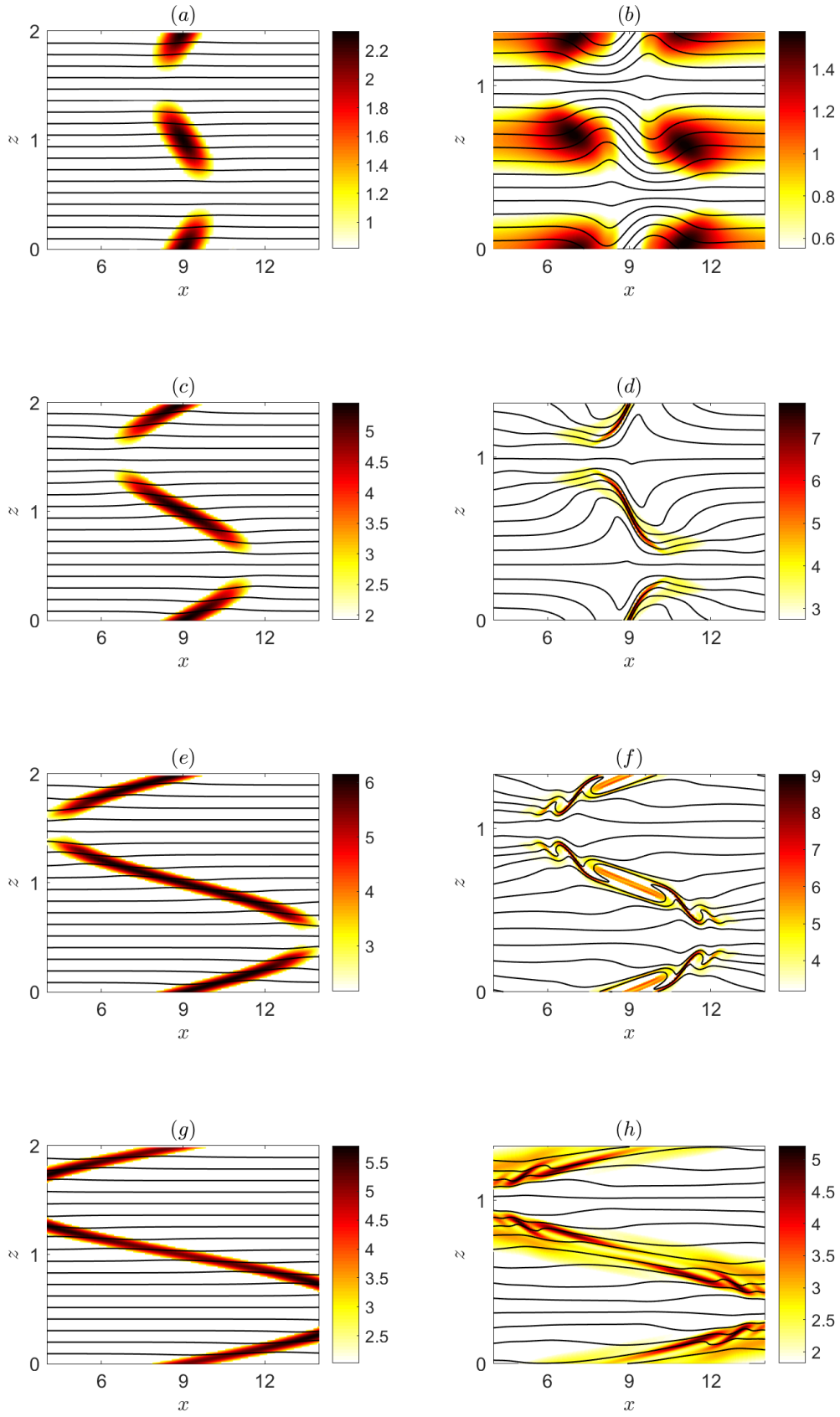

Figure 5.3: Vertical cross-sections of the shear $\sqrt{S_z}$ (color) and of the total density ρ_t (black contour lines) in the plane $y = 9$, for $F_h = 0.1$, $k_z = \pi$ (left column) and $F_h = 0.5$, $k_z = 3\pi/2$ (right column), for $U_S = 0.2$ and $Re = 6000$. The times shown are (a,b) $t = 4$, (c,d) $t = 13$, (e,f) $t = 26$, (g,h) $t = 36$.

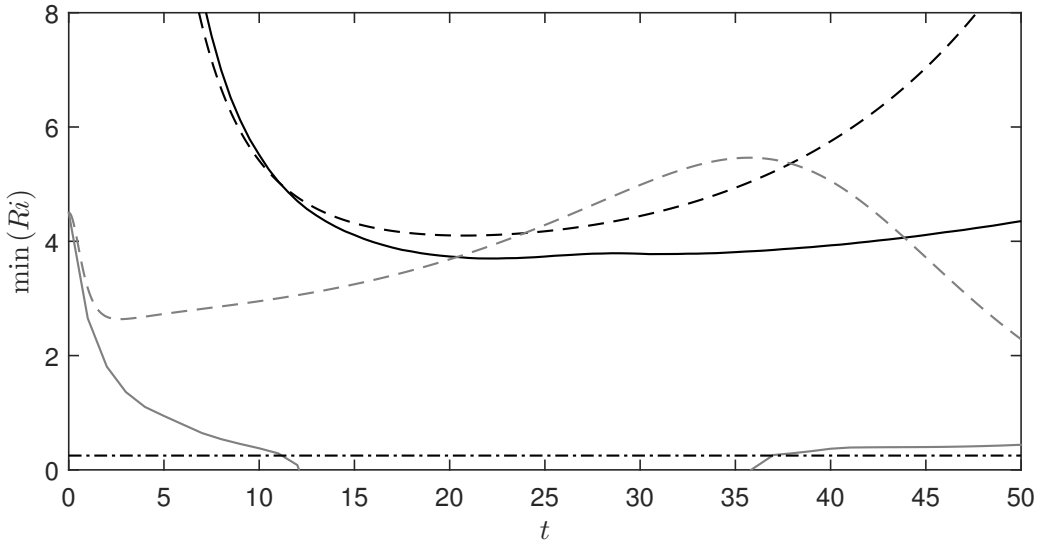

Figure 5.4: Minimum Richardson number as a function of time for $U_S = 0.2$, $Re = 6000$, and $F_h = 0.1$, $k_z = \pi$ (black solid line) and $F_h = 0.5$, $k_z = 3\pi/2$ (grey solid line) from the DNS. The asymptotic prediction (5.56) has been also plotted for both cases $F_h = 0.1$, $k_z = \pi$ (black dashed line) and $F_h = 0.5$, $k_z = 3\pi/2$ (grey dashed line). The horizontal black dash-dotted line shows the critical value $Ri_c = 0.25$.

cross-section at $x = 9$ of the buoyancy at $t = 26$ (figure 5.5b) confirms the presence of Kelvin-Helmholtz billows near $z = 0, l_z/2$. In contrast, no billows can be seen in these regions in the corresponding (x, z) cross-section at $y = 9$ (figure 5.5a). This means that the axes of the Kelvin-Helmholtz billows are mostly oriented in the x direction, i.e. they are parallel to the direction of the ambient shear flow. The black contours in figure 5.5 delineate the regions where $Ri < 0.25$. In addition to the unstable regions near (x_c, z_c), there exist also other unstable regions above and below each pancake vortex at $z = l_z/4$ and $z = 3l_z/4$. We can also see some billows in these regions (figures 5.5a and 5.3f) but in this case, their axes are perpendicular to the direction of the ambient shear. These unstable regions appear only in a second stage after those near (x_c, z_c).

5.3.2 Time evolution of the vertical shear at the center

For $k_z = \pi$, $F_h = 0.1$, the Richardson number is always minimum at the center point $(x_c = 9, y_c = 9, z_c = l_z/2)$ and at the symmetric point $(x_c = 9, y_c = 9, z_c = 0)$. For $k_z = 3\pi/2$, $F_h = 0.5$, the Kelvin-Helmholtz instability also develops first at these points. It is therefore interesting to investigate the evolution of the vertical shear at these locations.

To this end, we first decompose the flow into a mean flow varying only along the vertical and with time $\bar{\boldsymbol{u}}(z, t)$ and a complementary flow $\boldsymbol{u}^*$:

$$\boldsymbol{u} = \bar{\boldsymbol{u}} + \boldsymbol{u}^*, \tag{5.9}$$

where the overbar denotes the horizontal average over the computational domain, which for any quantity q is defined as

$$\bar{q} = \frac{1}{l_x l_y} \int_0^{l_y} \int_0^{l_x} q(x, y, z, t) \mathrm{d}x \mathrm{d}y. \tag{5.10}$$

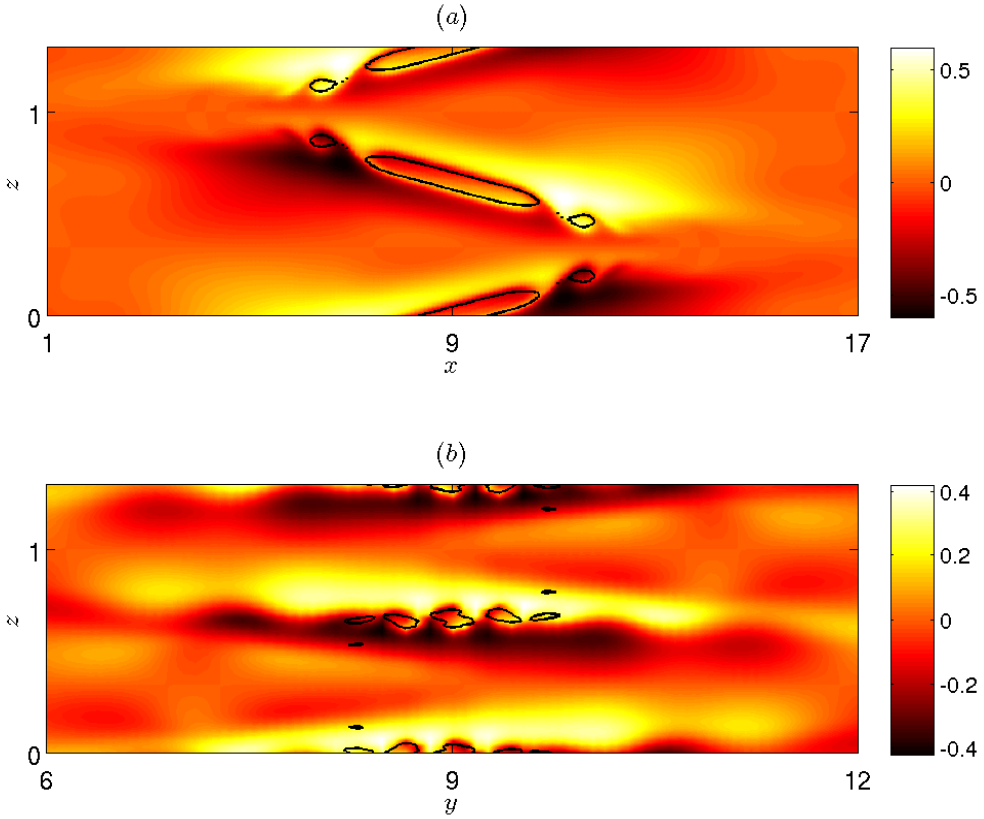

Figure 5.5: Vertical cross-sections of the buoyancy b at $t = 26$ in the planes $y = 9$ (a) and $x = 9$ (b) for $F_h = 0.5$, $k_z = 3\pi/2$, $U_S = 0.2$, and $Re = 6000$. The black contours represent the lines where $Ri = 0.25$.

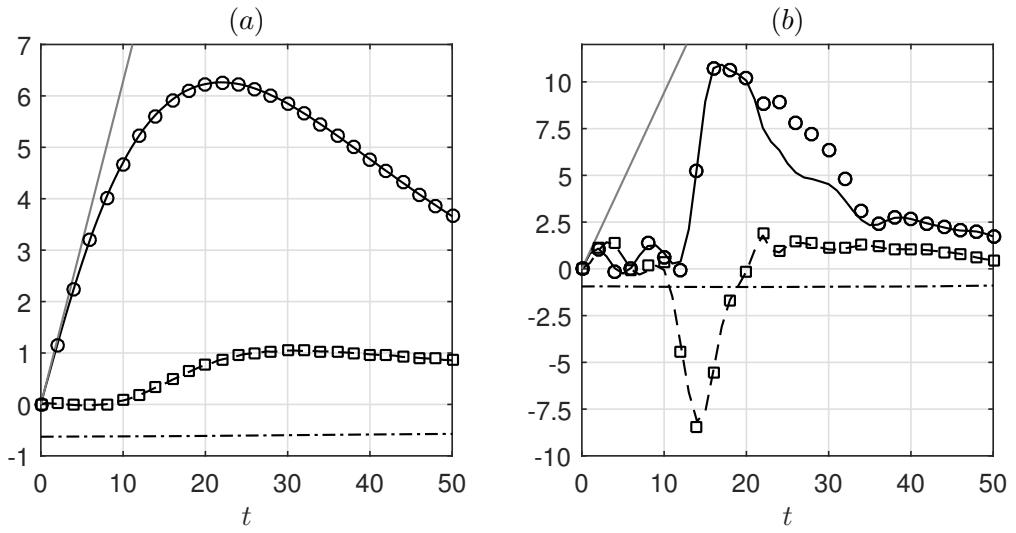

Figure 5.6: Time evolution of $\partial\bar{u}/\partial z$ (black dash-dotted lines), $\partial u^*/\partial z$ (black dashed lines), and $\partial v^*/\partial z$ (black solid lines) at the vortex center $x_c = 9$, $y_c = 9$, $z_c = l_z/2$ for (a) $F_h = 0.1$, $k_z = \pi$, and (b) $F_h = 0.5$, $k_z = 3\pi/2$ for $U_S = 0.2$ and $Re = 6000$. The straight grey lines represent the law $k_z U_S t$. The symbols show the horizontal vorticity components $-\omega_x^*$ (circles) and ω_y^* (squares).

At $t = 0$, we have $\bar{\boldsymbol{u}} = \boldsymbol{U}_S$ and $\boldsymbol{u}^* = \boldsymbol{u}_v$ so that $\bar{\boldsymbol{u}}$ and $\boldsymbol{u}^*$ will be called "shear flow" and "vortex flow", respectively.

Figure 5.6a shows the evolution of the different shear components $\partial\bar{u}/\partial z$, $\partial u^*/\partial z$, and $\partial v^*/\partial z$ at the center $(x_c = 9, y_c = 9, z_c = l_z/2)$ for $F_h = 0.1$, $k_z = \pi$, $U_S = 0.2$ and $Re = 6000$. The quantity $\partial\bar{v}/\partial z$ is always equal to zero at the center and is not plotted. More generally, $\partial\bar{v}/\partial z$ always remains very small at any vertical position compared to $\partial\bar{u}/\partial z$. We see that the mean shear $\partial\bar{u}/\partial z$ (dash-dotted line) remains almost constant and equal to $-k_z U_S = -0.6283$.

In contrast, the shear component $\partial v^*/\partial z$ (solid line) grows first linearly and then saturates at $t \simeq 22$ at the value $\partial v^*/\partial z = 6.3$, i.e. ten times the maximum ambient shear $|k_z U_S|$. The other component $\partial u^*/\partial z$ remains very weak up to $t = 10$ and then increases up to $\partial u^*/\partial z \simeq 1$ at $t = 30$. This quantity therefore saturates at a lower value and later than its counterpart $\partial v^*/\partial z$.

The initial behaviour of the vertical shear of the vortex $\partial u^*/\partial z$ and $\partial v^*/\partial z$ can be simply understood by considering that the vortex is displaced at the velocity $U(z)$ in the x direction, i.e. $\boldsymbol{u}_v(x - Ut, y)$, giving:

$$\frac{\partial \boldsymbol{u}_v}{\partial z} = -\frac{\mathrm{d}U}{\mathrm{d}z} t \frac{\partial \boldsymbol{u}_v}{\partial x}. \tag{5.11}$$

Since $\boldsymbol{u}_v = (-\Omega y, \Omega x)$, where $\Omega(r)$ is the angular velocity of the vortex, we have $\partial v_v/\partial x = \Omega = 1$ and $\partial u_v/\partial x = 0$ at the center $r = 0$. Thus, (5.11) yields

$$\frac{\partial u_v}{\partial z} = 0, \quad \frac{\partial v_v}{\partial z} = k_z U_S t \tag{5.12}$$

at $z = l_z/2$. The straight line in figure 5.6a confirms that $\partial v^*/\partial z$ increases initially at the rate $k_z U_S t$. This also explains why $\partial u^*/\partial z$ remains very small initially. The subsequent evolutions will be explained later thanks to the asymptotic analysis performed in chapter 4.

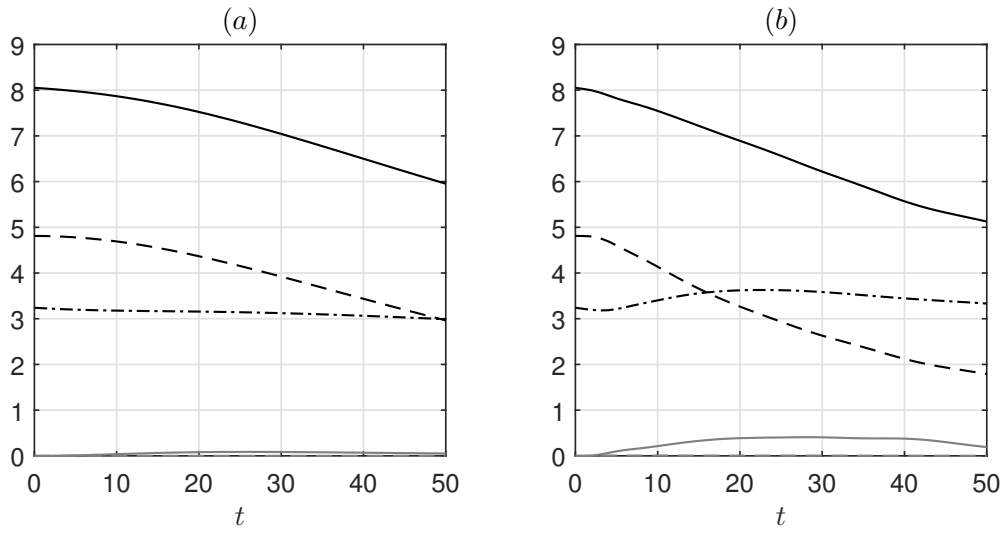

Figure 5.7: Time evolutions of the global kinetic energy $\bar{E}_k + E^*_{kh} + E^*_{kz}$ (black solid line), the mean flow kinetic energy $\bar{E}_k$ (black dash-dotted line), the vortex horizontal kinetic energy E^*_{kh} (black dashed line), the vortex vertical kinetic energy E^*_{kz} (grey dashed line) and the potential energy E_p (grey solid line) for (a) $F_h = 0.1$, $k_z = \pi$ and (b) $F_h = 0.5$, $k_z = 3\pi/2$ for $U_S = 0.2$, $Re = 6000$.

In figure 5.6a, we have also plotted with symbols the horizontal vorticity components $-\omega^*_x$ and ω^*_y where $\boldsymbol{\omega}^* = \boldsymbol{\nabla} \times \boldsymbol{u}^*$. They are nearly superposed to $\partial v^*/\partial z$ and $\partial u^*/\partial z$, respectively, because the vertical velocity is very small compared to the horizontal velocity. In other words, $\omega^*_x \simeq -\partial v^*/\partial z$ and $\omega^*_y \simeq \partial u^*/\partial z$.

Similarly, figure 5.6b displays the time evolution of $\partial \bar{u}/\partial z$, $\partial u^*/\partial z$, and $\partial v^*/\partial z$ at the center point for $F_h = 0.5$ and $k_z = 3\pi/2$, still for $U_S = 0.2$ and $Re = 6000$.

In contrast to the case $F_h = 0.1$, $k_z = \pi$ (figure 5.6a), $\partial v^*/\partial z$ follows the law (5.12) only at the very beginning $t \lesssim 2$. Instead, both shear components $\partial u^*/\partial z$ and $\partial v^*/\partial z$ first oscillate with a phase lag and with a period around 2π, i.e. the period corresponding to the angular velocity on the vortex axis $\Omega = 1$. Because of these oscillations, we can notice that $\partial v^*/\partial z$ goes back to zero around $t \simeq 4 - 5$ while $\partial u^*/\partial z$ is approximately opposite to $\partial \bar{u}/\partial z$. Thus, the total shear S_z is weak at the center as already observed in figure 5.3b at $t = 4$.

Then, $\partial u^*/\partial z$ and $\partial v^*/\partial z$ are both abruptly amplified up to an absolute value around 10. Remarkably, $\partial u^*/\partial z$ becomes now negative and saturates earlier than $\partial v^*/\partial z$. Later on, $|\partial u^*/\partial z|$ decreases very quickly while $|\partial v^*/\partial z|$ decays more slowly. The vorticity components $-\omega^*_x$ and ω^*_y have been also plotted in figure 5.6b. They are again almost identical to $\partial v^*/\partial z$ and $\partial u^*/\partial z$ except $-\omega^*_x$ for $21 \leqslant t \leqslant 35$. This corresponds to the time interval when the Kelvin-Helmholtz billows exist. They produce a finite vertical velocity w^*, making the term $\partial w^*/\partial y$ in ω^*_x no longer negligible. In contrast, the term $\partial w^*/\partial x$ is still negligible in ω^*_y, most probably because the axes of the Kelvin-Helmholtz billows are aligned with the x direction.

5.3.3 Global energy and enstrophy evolutions

Figure 5.7 presents the evolutions of the energies integrated over the whole computational domain for the two simulations for $k_z = \pi$, $F_h = 0.1$, and $k_z = 3\pi/2$, $F_h = 0.5$

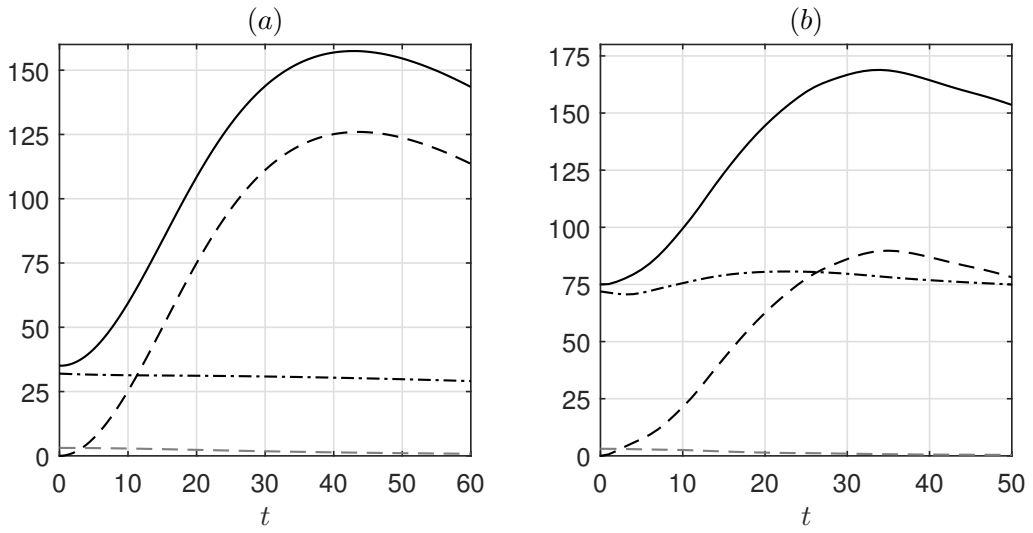

Figure 5.8: Time evolutions of the global total enstrophy $\bar{Z}+Z_h^*+Z_z^*$ (black solid line), the mean flow enstrophy $\bar{Z}$ (black dash-dotted line), the vortex horizontal enstrophy Z_h^* (black dashed line) and the vortex vertical enstrophy Z_z^* (grey dashed line) for (a) $F_h = 0.1$, $k_z = \pi$ and (b) $F_h = 0.5$, $k_z = 3\pi/2$ for $U_S = 0.2$, $Re = 6000$.

previously described. The kinetic energies have been decomposed into a mean part and a vortex part using the decomposition (5.9):

$$\bar{E}_k = \frac{1}{l_z}\int_V \frac{\bar{\boldsymbol{u}}^2}{2}\mathrm{d}V, \quad E_{kh}^* = \frac{1}{l_z}\int_V \frac{\boldsymbol{u}_h^{*2}}{2}\mathrm{d}V, \quad E_{kz}^* = \frac{1}{l_z}\int_V \frac{w^{*2}}{2}\mathrm{d}V. \tag{5.13}$$

The integral over the computational domain V is divided by l_z in order to enable the comparisons between simulations carried out with distinct vertical wavelengths. Similarly, the global potential energy per vertical length unit is:

$$E_p = \frac{1}{l_z}\int_V \frac{F_h^2 b^2}{2}\mathrm{d}V. \tag{5.14}$$

The kinetic energy of the mean flow $\bar{E}_k$ (black dash-dotted lines) remains approximately constant even if it increases slightly at the beginning mostly for $k_z = 3\pi/2$, $F_h = 0.5$ (figure 5.7b). In contrast, the horizontal kinetic energy of the vortex E_{kh}^* (black dashed lines) decreases regularly following an approximately linear trend. The vertical kinetic energy E_{kz}^* (grey dashed lines) and the potential energy E_p (grey solid lines) remain always very weak compared to the horizontal kinetic energy.

Likewise, figure 5.8 displays the evolutions of the global enstrophies per vertical length unit, decomposed using (5.9):

$$\bar{Z} = \frac{1}{l_z}\int_V \frac{\bar{\boldsymbol{\omega}}^2}{2}\mathrm{d}V, \quad Z_h^* = \frac{1}{l_z}\int_V \frac{\boldsymbol{\omega}_h^{*2}}{2}\mathrm{d}V, \quad Z_z^* = \frac{1}{l_z}\int_V \frac{\zeta^{*2}}{2}\mathrm{d}V. \tag{5.15}$$

The global horizontal enstrophy of the vortex Z_h^* (black dashed lines) increases and then decreases while its vertical counterpart Z_z^* (grey dashed lines) continuously decays. Unexpectedly, the growth of Z_h^* is much more pronounced for $k_z = \pi$, $F_h = 0.1$ than for $k_z = 3\pi/2$, $F_h = 0.5$ although the vertical wavenumber k_z is higher in this second case. The enstrophy of the mean shear $\bar{Z}$ remains approximately constant like the

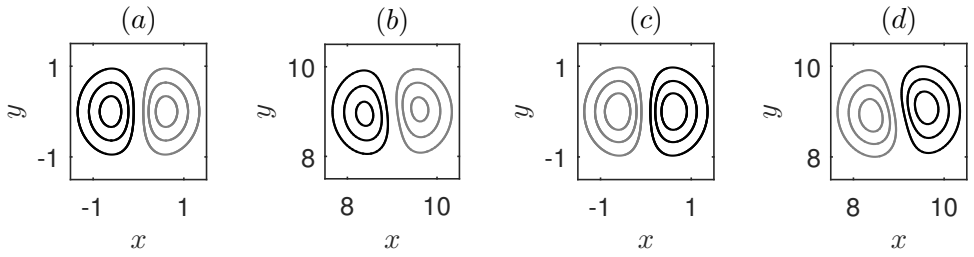

Figure 5.9: Horizontal cross-sections in the plane $z = l_z/2$ at $t = 0.4$ of the vertical velocity (*a,b*) and buoyancy (*c,d*) computed asymptotically (*a,c*) and numerically (*b,d*). The contour interval is 0.002 for w and 0.001 for b. The contour at the level zero is not drawn. The negative iso-contours are colored in grey. The parameters are $F_h = 0.5$, $k_z = \pi$, $U_S = 0.2$, and $Re = 6000$.

mean kinetic energy $\bar{E}_k$. Since the mean enstrophy $\bar{Z}$ for $k_z = 3\pi/2$ is more than twice the one for $k_z = \pi$, the maximum of the total enstrophy (solid lines) is comparable in the two simulations even if $\max(Z_h^*)$ is lower for $k_z = 3\pi/2$.

5.4 Comparison to the short-time asymptotic analysis

After this global description of two simulations, we turn to a detailed comparison of the initial dynamics with the predictions of the asymptotic analysis for small time performed in chapter 4 in the inviscid limit. The main result of this analysis is that the buoyancy and vertical velocity should behave initially as

$$b = t^3 \frac{k_z U_S}{6F_h^2} \beta(r) \cos(\theta) \cos(k_z z), \tag{5.16}$$

$$w = -t^2 \frac{k_z U_S}{2} \beta(r) \cos(\theta) \cos(k_z z), \tag{5.17}$$

where β is a function which depends on r and k_z (see (4.34)-(4.35) and figure 4.2 in chapter 4). The expressions (5.16)-(5.17) imply that the dynamics is non-hydrostatic, i.e. $b < w$, as long as $t < F_h$.

These asymptotic predictions will be first checked against a simulation for the parameters $F_h = 0.5$, $k_z = \pi$, $U_S = 0.2$, $Re = 6000$, and then a parametric study will be carried out.

5.4.1 A detailed comparison

Figures 5.9 and 5.10 compare the asymptotic predictions for w and b to the observed fields in the DNS at $z = l_z/2$, at two times $t = 0.4$ and $t = 1.6$, respectively. As seen in (5.16)-(5.17), $z = l_z/2$ is the vertical level where w and b are maximum. There is a good quantitative agreement between asymptotics and numerics at $t = 0.4$ both for the vertical velocity (figure 5.9*a,b*) and the buoyancy (figure 5.9*c,d*). We can notice that the buoyancy is in phase opposition with the vertical velocity. As expected, the asymptotics depart from the numerical results for $t > 1$ as can be seen in figure 5.10 at $t = 1.6$. Indeed, the wavenumber one pattern of the buoyancy has started to rotate in

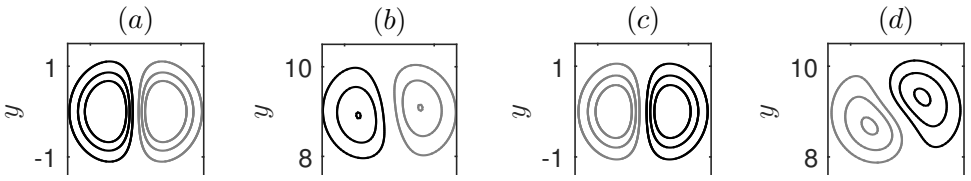

Figu
0.05

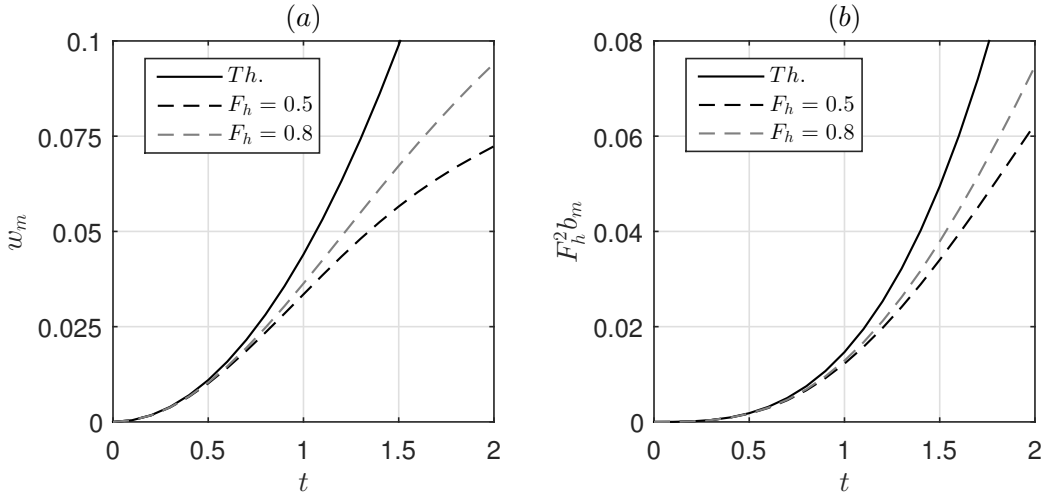

Figure 5.11: Temporal evolutions of w_m (a) and $F_h^2 b_m$ (b) for $k_z = \pi$, $U_S = 0.2$, and $Re = 6000$, for $F_h = 0.5$ (black dashed lines) and $F_h = 0.8$ (grey dashed lines) computed from the DNS and predicted asymptotically (black solid lines).

the numerical simulation (figure 5.10d), while such rotation is not reproduced by the asymptotic solution (figure 5.10c). Moreover, the extremum values predicted by the asymptotics no longer perfectly match those in the DNS. Nevertheless, the structure of the vertical velocity (figure 5.10a,b) is qualitatively similar in the asymptotics and numerics.

In order to estimate the time range of validity of the asymptotics, the evolutions of the peak values w_m and $F_h^2 b_m$ of the vertical velocity and buoyancy are plotted in figure 5.11. An excellent agreement between theory (black solid lines) and numerics for $F_h = 0.5$ (black dashed lines) is observed for $t \leqslant 0.8$ approximately. Beyond this time, the growth of the maximum vertical velocity and buoyancy is slowlier in the numerics than predicted by the asymptotics.

5.4.2 Effect of the Froude number

Figure 5.11 also shows w_m and $F_h^2 b_m$ from a DNS for the larger Froude number $F_h = 0.8$ (grey dashed lines). In agreement with the asymptotics, w_m and $F_h^2 b_m$ are independent of the Froude number for $t < 1$ whereas they become dependent for larger time.

According to (5.16)-(5.17), the buoyancy becomes larger than the vertical acceleration when $t > \sqrt{6} F_h$, i.e. sooner as the Froude number diminishes. In other words, the duration of the initial non-hydrostatic regime scales with the Froude number.

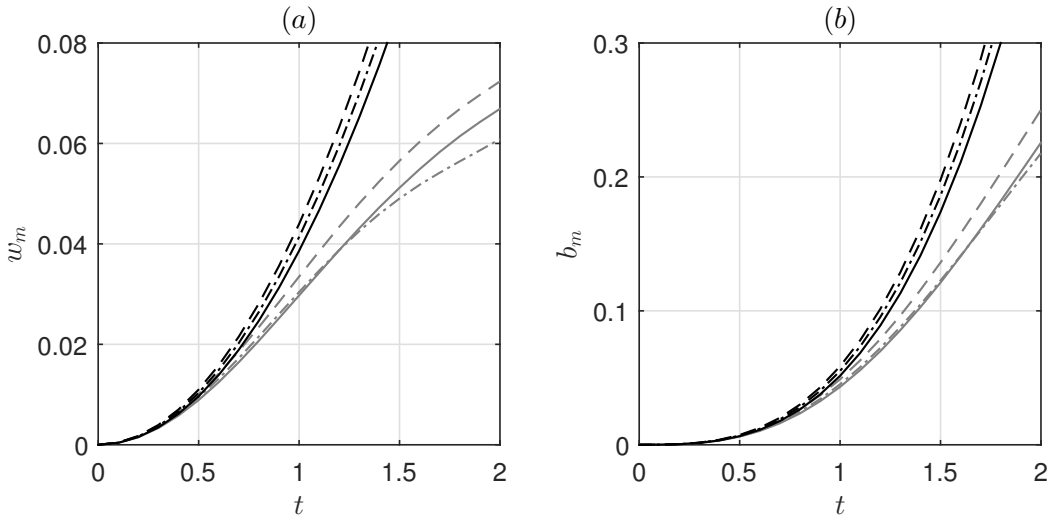

Figure 5.12: Temporal evolutions of (a) w_m and (b) b_m computed asymptotically (black lines) and numerically (grey lines) for $F_h = 0.5$, $U_S = 0.2$, and $Re = 6000$, for $k_z = \pi/2$ (dash-dotted lines), $k_z = \pi$ (dashed lines) and $k_z = 3\pi/2$ (solid lines).

5.4.3 Effect of the vertical wavenumber

The effect of the vertical wavenumber k_z on the maximum vertical velocity w_m and buoyancy b_m is investigated in figure 5.12. Both the asymptotic and the numerical results are almost distributed on a single curve. This is due to the fact that the factor $k_z\beta$ appearing in (5.16)-(5.17) is approximately independent of k_z in the range $\pi/2 \leqslant k_z \leqslant 3\pi/2$ as illustrated in figure 4.2 of chapter 4. In contrast, for small k_z, w_m and b_m are proportional to k_z since β is almost independent of the vertical wavenumber in that limit (not shown).

5.4.4 Effect of the shear flow amplitude U_S

The influence of the shear amplitude U_S is considered in figure 5.13. The maximum vertical velocity and buoyancy are both proportional to U_S in agreement with the asymptotic predictions. Even if there is a departure between the asymptotics and the numerics, it is remarkable that the scaling relations $w \propto U_S$ and $b \propto U_S$ hold very well in the DNS over the entire time range investigated.

5.5 Comparison to the long-wavelength asymptotic analysis

5.5.1 Reminder

In chapter 4, we have performed a long-wavelength asymptotic analysis for $k_z F_h \ll 1$, i.e. for small vertical Froude number $F_v = k_z F_h = |\Gamma|/(a_0 l_z N)$. Leading order viscous effects have been also taken into account. This analysis has provided evolution equations for the position of the vortex center at each level z:

$$\Delta x = U(z)t + \delta x(z,t), \tag{5.18}$$

$$\Delta y = \delta y(z,t), \tag{5.19}$$

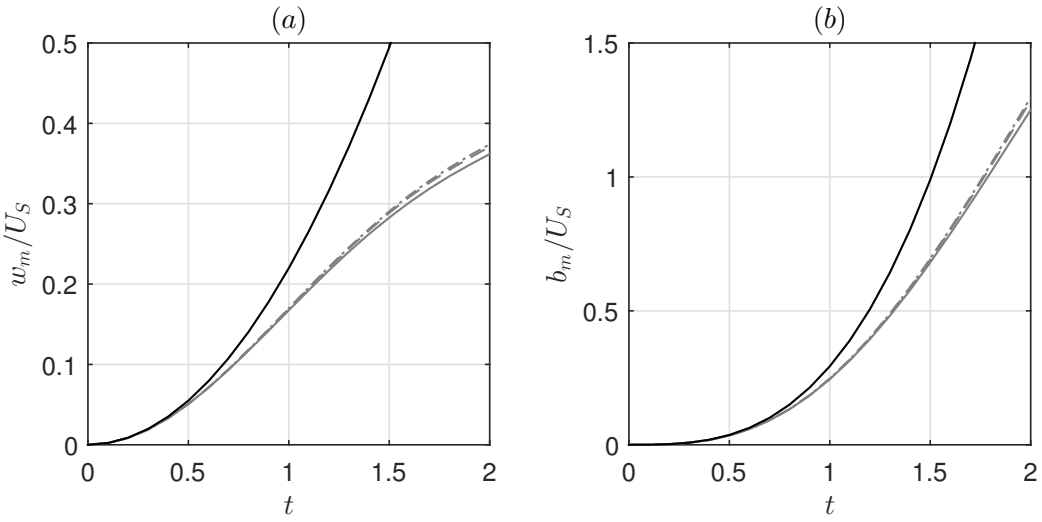

Figure 5.13: Temporal evolutions of (a) the rescaled maximum vertical velocity w_m/U_S and (b) the rescaled maximum buoyancy b_m/U_S computed analytically (black lines) and numerically (grey lines) for $F_h = 0.5$, $k_z = \pi$, and $Re = 6000$, for $U_S = 0.02$ (dash-dotted lines), $U_S = 0.1$ (dashed lines), and $U_S = 0.2$ (solid lines).

where

$$\delta x = \hat{X}(z,t)\sin(k_z z), \tag{5.20}$$

$$\delta y = \hat{Y}(z,t)\sin(k_z z). \tag{5.21}$$

The amplitudes $(\hat{X}, \hat{Y})$ follow the equations

$$\hat{X} = (k_z F_h)^2 U_S \left[\mathcal{C}_w + \int_0^t \vartheta(z,\upsilon)\mathrm{d}\upsilon\right] - \frac{k_z^2 U_S t^2}{2Re}, \tag{5.22}$$

$$\hat{Y} = (k_z F_h)^2 U_S \mathcal{S}_w + U_S \int_0^t \hat{\omega}(z,\upsilon)\upsilon \mathrm{d}\upsilon, \tag{5.23}$$

where $\mathcal{C}_w$ and $\mathcal{S}_w$ are the effects of internal waves excited at $t = 0$ and that decay quickly afterwards. The parameters $\hat{\omega}$ and ϑ correspond to the self-induction of the vortex and an advection correction, respectively. The last term in the right-hand side of (5.22) is the leading viscous effect. The expressions of all the parameters in (5.22)-(5.23) are given in chapter 4.

In addition, the asymptotic analysis has shown that the vortex remains axisymmetric at leading order but its angular velocity evolves according to

$$\frac{\partial \Omega}{\partial t} = \left[-F_h^2 t \Omega^3 + \frac{t^2}{2Re\tilde{r}}\frac{\partial \zeta_0}{\partial \tilde{r}}\right]\left(\frac{\mathrm{d}U}{\mathrm{d}z}\right)^2, \tag{5.24}$$

where $\zeta_0 = (1/\tilde{r})\partial \tilde{r}^2 \Omega/\partial \tilde{r}$ is the vertical vorticity and $\tilde{r}$ is the local radius with respect to the center of the vortex at the level z:

$$\tilde{r}^2 = (x - U(z)t - \delta x)^2 + (y - \delta y)^2. \tag{5.25}$$

The associated local angle is denoted $\tilde{\theta}$. The first term in the right-hand side of (5.24) ensures the conservation of potential vorticity while the second term describes

the leading viscous effect. This effect is proportional to t^2 because the vertical shear grows like $t\mathrm{d}U/\mathrm{d}z$ at leading order. In chapter 4, the equation (5.24) has been solved asymptotically when

$$\gamma = \frac{1}{ReF_h^3 \left|\dfrac{\mathrm{d}U}{\mathrm{d}z}\right|} \tag{5.26}$$

is small. In particular, an analytic expression for the angular velocity on the vortex axis has been obtained:

$$\Omega_c = \frac{1}{\sqrt{\left(1+2\gamma T^3/3\right)^2 + T^2}}, \tag{5.27}$$

where $T = F_h t|\mathrm{d}U/\mathrm{d}z|$. This expression is in very good agreement with the exact result obtained by numerical integration of (5.24). It will be therefore used in the following.

A last prediction of the asymptotic analysis is that the horizontal velocity of the vortex at order $O[(k_z F_h)^2]$ is of the form

$$\boldsymbol{u}_{h1} = \boldsymbol{\nabla}_h \Phi_1 - \boldsymbol{\nabla} \times \psi_1 \boldsymbol{e}_z, \tag{5.28}$$

with

$$\Phi_1 = \Phi_{10} + \Phi_{11} + \Phi_{12}, \quad \psi_1 = \psi_{11} + \psi_{12}. \tag{5.29}$$

The potential Φ_{10} does not depend on $\tilde{\theta}$ and thus corresponds to an axisymmetric velocity field in the local reference frame with origin at the vortex center. In contrast, (Φ_{11}, ψ_{11}) and (Φ_{12}, ψ_{12}) are contributions with an azimuthal wavenumber $m = 1$ or $m = 2$, respectively. They correspond to a displacement and an elliptic deformation of the vortex, respectively. All these functions have been determined in chapter 4.

These results will enable us to obtain predictions for the evolution of the vertical shear of the horizontal velocity in section §5.5.3. Before, we begin by presenting in the next section a comparison between the asymptotic predictions for the vortex center (5.18)-(5.19) and the DNS.

5.5.2 Deformations of the vortex axis

In order to estimate the position of the vortex center in the numerical simulations, we have used two methods: one based on the potential vorticity $\Pi = \boldsymbol{\omega} \cdot [\boldsymbol{\nabla} b + N^2 \boldsymbol{e_z}]$ and the other on the vertical vorticity ζ. In each case, the displacements of the vortex center have been estimated from vorticity centroids:

$$\Delta x_c^{\Pi}(z,t) = \frac{\langle x\Pi \rangle_h}{\langle \Pi \rangle_h}, \quad \Delta y_c^{\Pi}(z,t) = \frac{\langle y\Pi \rangle_h}{\langle \Pi \rangle_h}, \tag{5.30}$$

or

$$\Delta x_c^{\zeta}(z,t) = \frac{\langle x\zeta \rangle_h}{\langle \zeta \rangle_h}, \quad \Delta y_c^{\zeta}(z,t) = \frac{\langle y\zeta \rangle_h}{\langle \zeta \rangle_h}, \tag{5.31}$$

where the brackets denote

$$\langle \varphi \rangle_h = \int_{\varphi > \varphi_c} \varphi \mathrm{d}x\mathrm{d}y. \tag{5.32}$$

The horizontal integration is carried out only in the regions where the vorticity is larger than a critical value Π_c, ζ_c in order to avoid taking into account the small background vorticity due to the fact that the total vorticity is zero owing to the use of periodic boundary conditions. The values $\Pi_c = 0.05 \max_{t=0}(\Pi)$ and $\zeta_c = 0.05 \max_{t=0}(\zeta)$ have

been chosen as they provide results almost independent of the size of the computational domain and the particular values of the thresholds.

The tracking method based on the potential vorticity seems more natural since it is a transported quantity in the inviscid limit. However, we shall see that the method based on the vertical vorticity will enable a closer comparison to the asymptotic results. This is because the condition used to normalize the streamfunction at first order implies

$$\Delta x_c^{\zeta} = \frac{\langle x\zeta \rangle_h}{\langle \zeta \rangle_h} = \frac{\langle x\zeta_0(\tilde{r}) \rangle_h}{\langle \zeta_0 \rangle_h} = \Delta x, \tag{5.33}$$

and, similarly $\Delta y_c^{\zeta} = \Delta y$, where $(\Delta x, \Delta y)$ are the asymptotic displacements (5.18)-(5.19).

In the next sections, we compare the asymptotic and numerical results for different parameters.

In-depth analysis of a simulation

Figure 5.14 compares the total displacements $\Delta x = U_S t + \delta x$ and δy as predicted by the asymptotics to the positions Δx_c and Δy_c of the vortex estimated from the vertical vorticity and potential vorticity centroids at the level $z = l_z/4$ for $F_h = 0.5$, $k_z = 0.3$, $U_S = 0.2$, and $Re = 6000$. The agreement is excellent even at $t = 20$. The dominant displacement is in the x direction (figure 5.14*a*) and given by $U_S t$ while the deviations δx and δy are much smaller.

Figures 5.14*b*,*c* display the y displacement of the vortex estimated from the vertical vorticity, Δy_c^{ζ}, and from the potential vorticity, Δy_c^{Π}, respectively. They are both in very good agreement with the asymptotic prediction δy even if a small discrepancy arises after $t \simeq 12$. However, if we focus on the initial evolution of Δy_c^{ζ} and Δy_c^{Π} (figure 5.14*d*), we see that they are actually different for $t \leqslant 4$.

The displacement Δy_c^{ζ} (crosses) is first slightly negative for $t \leqslant 2$ in excellent agreement with the asymptotic prediction δy (black solid line). In contrast, the y displacement estimated from the potential vorticity Δy_c^{Π} (open circles) increases monotonically. The estimation of the vortex center from the vertical vorticity is in much better agreement with the asymptotics than the estimation from the potential vorticity because the normalisation condition used in the asymptotic analysis is based on the vertical vorticity.

Nevertheless, if the effects of the internal waves are neglected (i.e. $\mathcal{C}_w = \mathcal{S}_w = 0$), the asymptotic prediction (black dashed line) is then close to Δy_c^{Π}. This confirms that internal waves play a key role at the start-up of the flow evolution. Because of these waves, the initial evolution of δy is of the form $\delta y = k_z^2 U_S \sigma t^4$, where $\sigma = -3.826 \times 10^{-3}$ is a constant, as shown by the grey solid line in figure 5.14*d*. In contrast, when internal waves are neglected, δy evolves initially as $\delta y \propto t^2$ (black dashed line).

We have also compared the vertical velocity and buoyancy fields predicted by the asymptotics against their numerical counterparts. Figures 5.15 and 5.16 display horizontal cross-sections of w and b, respectively, in the plane $z = l_z/2$ where they are maximum. A very good qualitative and quantitative agreement is observed even at $t = 18$ (figures 5.15*c*,*f* and 5.16*c*,*f*) apart from the existence of small wave-like disturbances in the DNS that are absent in the asymptotics. We can remark that the vertical velocity and buoyancy are approximately in phase opposition at $t = 2$ (figures 5.15*a*,*d* and 5.16*a*,*d*) as observed for short times (figures 5.9, 5.10) while for $t = 6$ and $t = 18$,

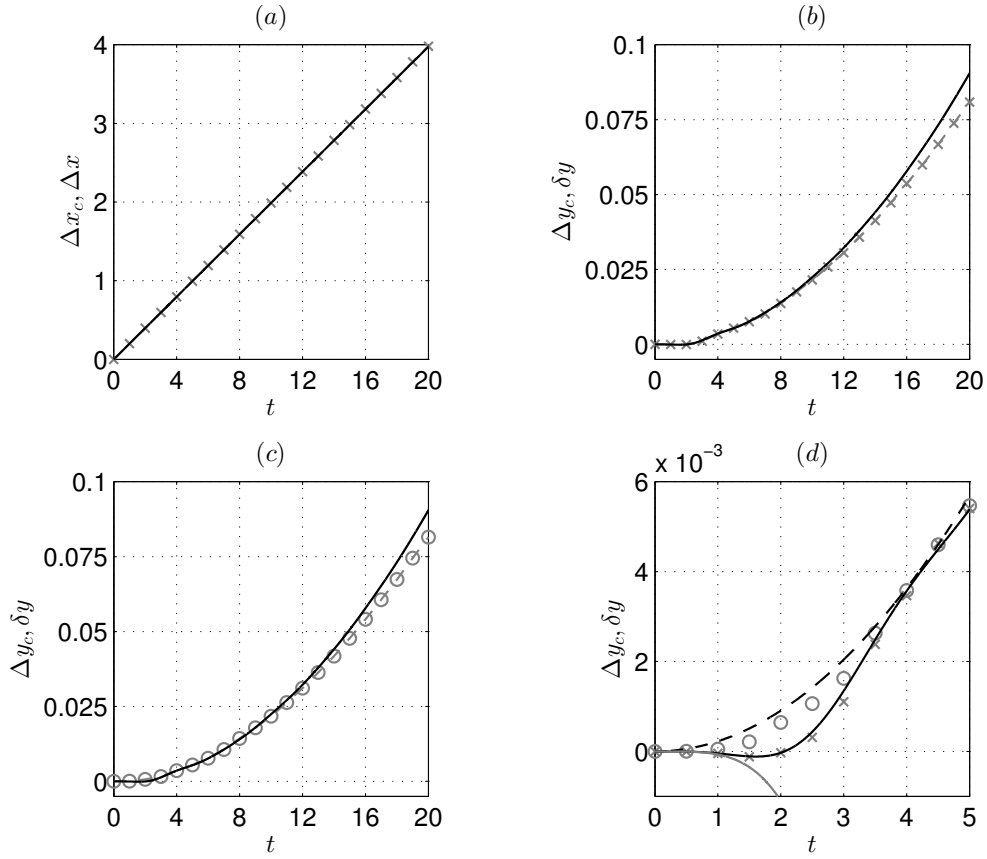

Figure 5.14: (a,b) Comparison between the vertical vorticity centroids Δx_c^ζ and Δy_c^ζ (grey dashed lines with crosses) and the asymptotic predictions for the displacements Δx (a) and δy (b) (black solid lines) in the plane $z = l_z/4$. (c) displays the same comparison as in (b) except that the grey dashed line marked with open circles now represents the potential vorticity centroid Δy_c^Π. (d) displays a close-up view of the initial evolution of Δy_c^ζ (grey crosses), Δy_c^Π (grey open circles), and δy (black solid line). The asymptotic prediction in the absence of internal waves, i.e. by setting $\mathcal{C}_w = \mathcal{S}_w = 0$ in (5.22)-(5.23) has been also reported (black dashed line). The short-time asymptotic prediction for δy has been plotted as well (grey solid line). The parameters are $F_h = 0.5$, $k_z = 0.3$, $U_S = 0.2$, and $Re = 6000$.

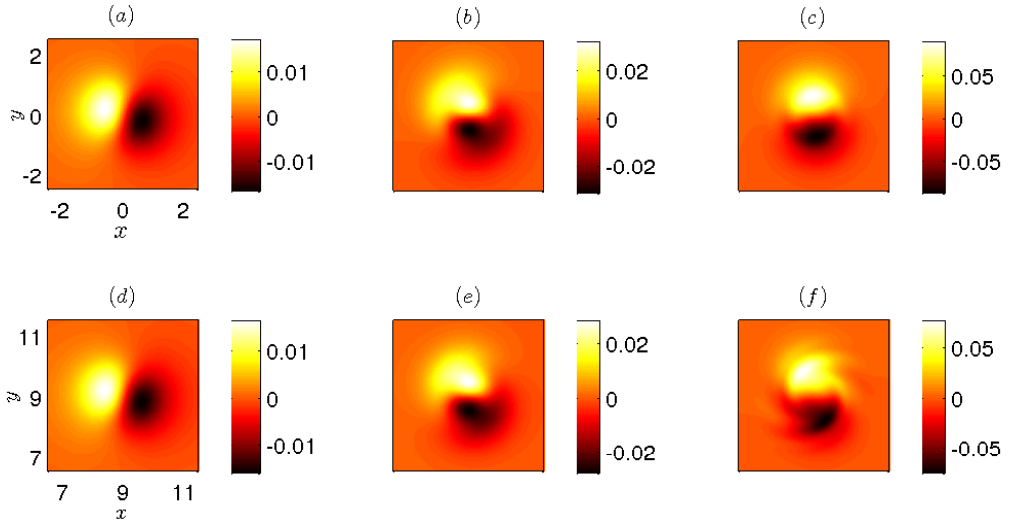

Figure 5.15: Horizontal cross sections in the plane $z = l_z/2$ of (a,b,c) the vertical velocity calculated asymptotically and (d,e,f) in the DNS for $F_h = 0.5$, $k_z = 0.3$, $U_S = 0.2$, and $Re = 6000$ at $t = 2$ (a,d), $t = 6$ (b,e) and $t = 18$ (c,f).

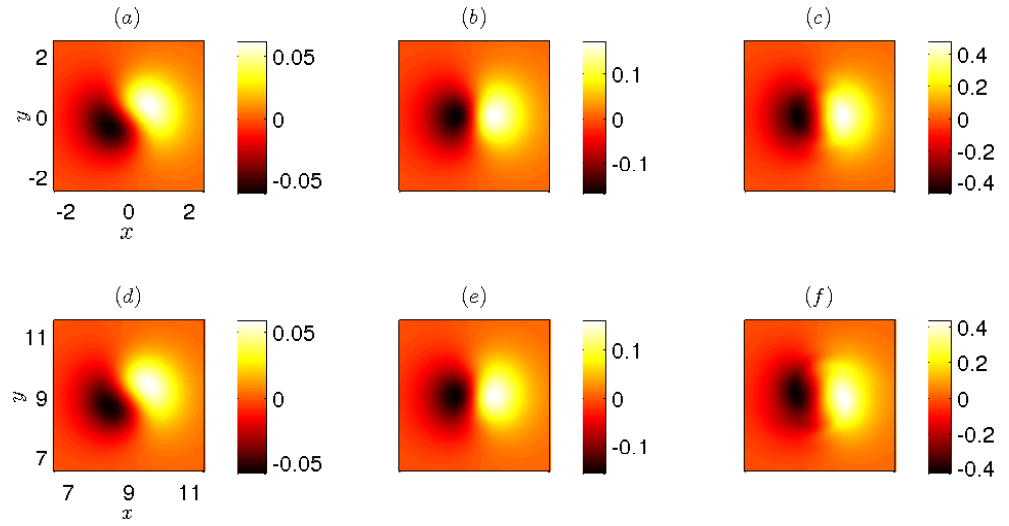

Figure 5.16: Horizontal cross sections in the plane $z = l_z/2$ of (a,b,c) the buoyancy calculated asymptotically and (d,e,f) in the DNS for $F_h = 0.5$, $k_z = 0.3$, $U_S = 0.2$, and $Re = 6000$ at $t = 2$ (a,d), $t = 6$ (b,e) and $t = 18$ (c,f).

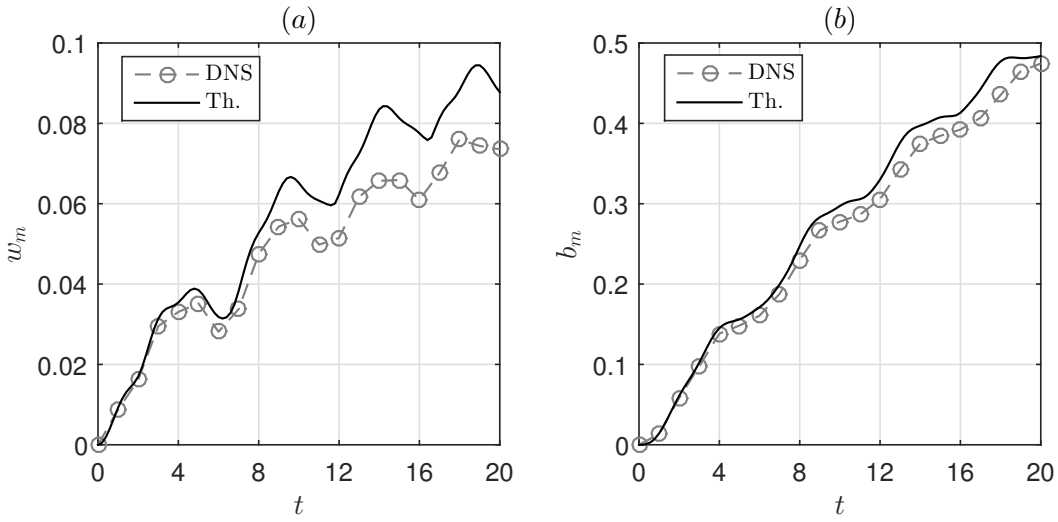

Figure 5.17: Evolution of the maximum values of (a) the vertical velocity w_m and (b) the buoyancy b_m in the DNS (grey dashed lines with open circles) and predicted by the asymptotics (black solid lines), for $F_h = 0.5$, $k_z = 0.3$, $U_S = 0.2$, and $Re = 6000$.

they have a $\pi/2$ phase difference. The close agreement between the asymptotic and numerical results can be further seen in the temporal variations of the maximum values of w and b (figure 5.17). The asymptotic and numerical results begin to slightly depart from each other only at $t \simeq 10$. The slowly growing discrepancy as time increases is probably due to the fact that the vertical derivative grows like $k_z U_S t$ at leading order owing to the shear flow. Hence, the long wavelength assumption $F_h \partial/\partial z \ll 1$ is expected to be less and less valid as time increases. The maximum values of w and b increase approximately linearly with oscillations superimposed. These oscillations are due to the internal waves excited at $t = 0$. Two periods $T = 2\pi F_h = \pi$ and $T = \Omega(r = 0) = 1$ are mixed explaining why the oscillations look somewhat irregular, especially for w_m (figure 5.17a).

Parametric study

We now examine the effects of the parameters F_h, k_z, and U_S.

Figure 5.18a presents the evolution of the y displacement for a different Froude number and wavenumber $F_h = 0.1$, $k_z = 1.5$ such that the product $k_z F_h = 0.15$ is the same as in figure 5.14. The shear flow amplitude and Reynolds number have been kept to the same values $U_S = 0.2$ and $Re = 6000$. As expected, the evolution of δy (black solid line) is similar to the one for $k_z = 0.3$, $F_h = 0.5$ (shown again by a black dashed line in figure 5.18a for reference). This confirms that the relevant main control parameter is $k_z F_h$ and not k_z and F_h, separately. There is a small difference between the curves for $F_h = 0.1$, $k_z = 1.5$ and $F_h = 0.5$, $k_z = 0.3$ because the functions $\hat{\omega}$, ϑ, $\mathcal{C}_w$ and $\mathcal{S}_w$ depend on the Froude number. However, this dependence is weak when $F_h \lesssim 0.5$.

In contrast, if only F_h (figure 5.18b) or only k_z (figure 5.18c) are varied relative to the reference case, the y displacement differs since $k_z F_h$ has changed. We can notice that the agreement of the asymptotic predictions δy with the measured y displacement of the vertical vorticity centroids is slightly better than for the reference case since $k_z F_h$ is lower. Finally, lowering the shear flow amplitude to $U_S = 0.1$ while keeping the

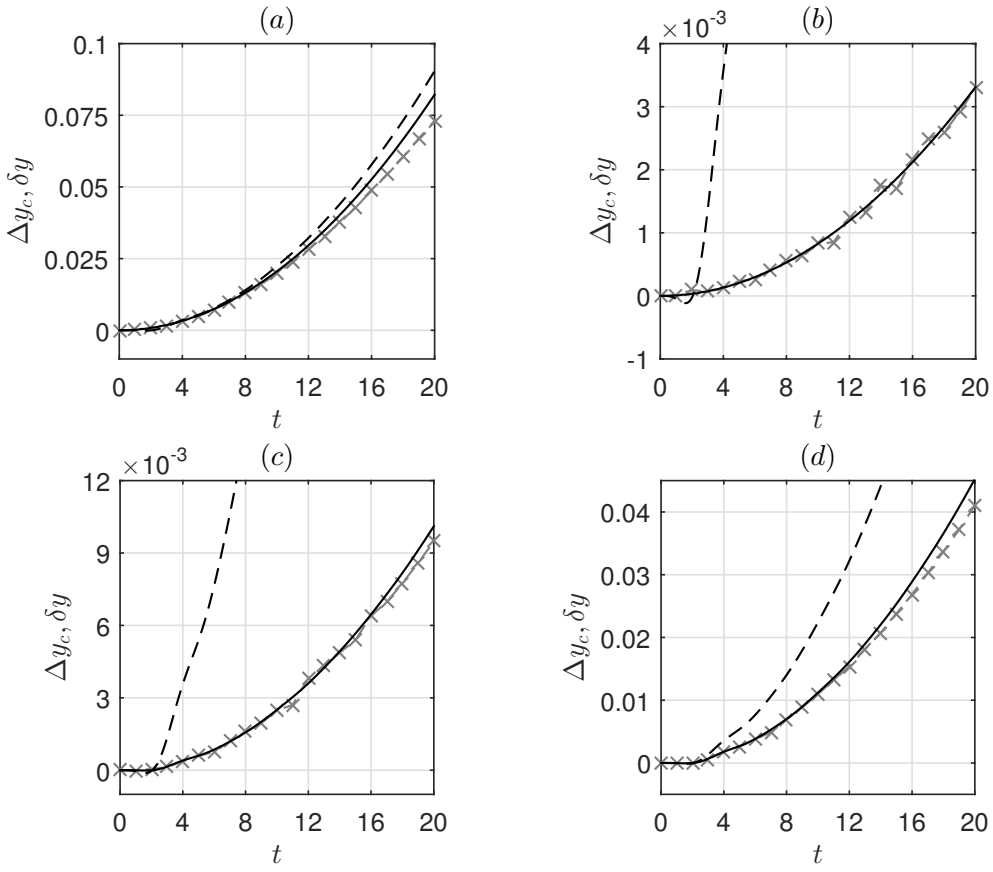

Figure 5.18: Comparison between the y displacements of the vertical vorticity centroids Δy_c^{ζ} (grey dashed lines with crosses) and the asymptotic predictions δy (black solid lines) in the plane $z = l_z/4$, for $Re = 6000$, for (a) $F_h = 0.1$, $k_z = 1.5$, $U_S = 0.2$, (b) $F_h = 0.1$, $k_z = 0.3$, $U_S = 0.2$, (c) $F_h = 0.5$, $k_z = 0.1$, $U_S = 0.2$, and (d) $F_h = 0.5$, $k_z = 0.3$, $U_S = 0.1$. The black dashed lines represent δy for the reference case $F_h = 0.5$, $k_z = 0.3$, $U_S = 0.2$ already shown in figure 5.14.

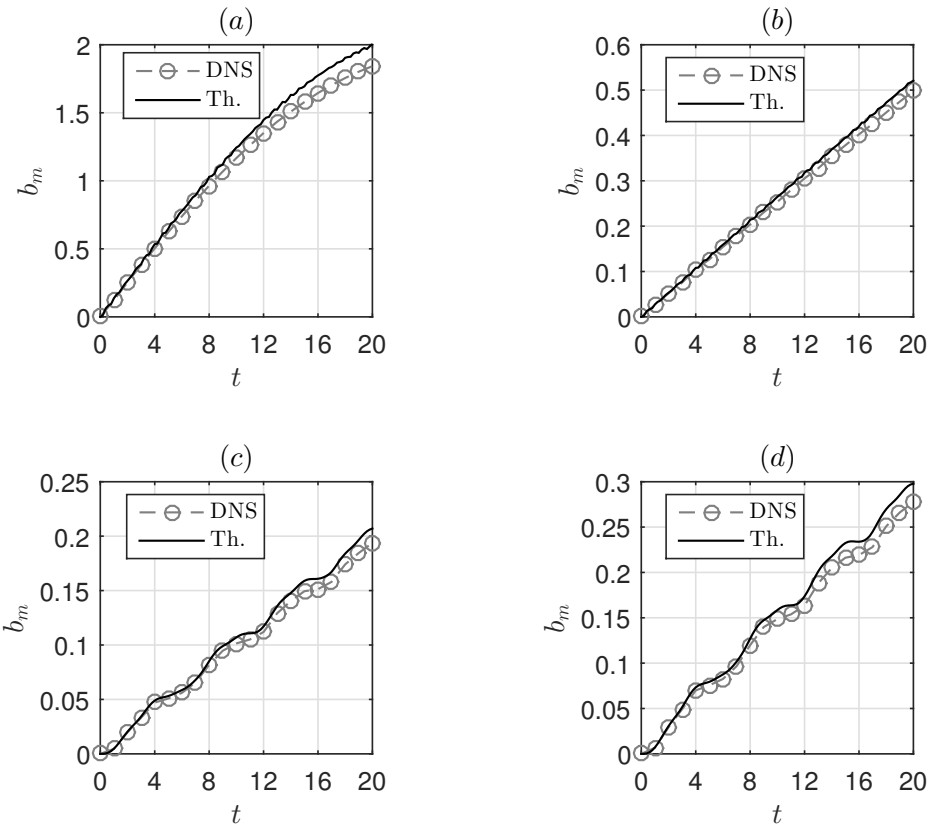

Figure 5.19: Evolution of the maximum buoyancy b_m in the DNS (grey dashed lines with grey open circles) and from the asymptotic predictions (black solid lines) for $Re = 6000$, for (a) $F_h = 0.1$, $k_z = 1.5$, $U_S = 0.2$, (b) $F_h = 0.1$, $k_z = 0.3$, $U_S = 0.2$, (c) $F_h = 0.5$, $k_z = 0.1$, $U_S = 0.2$, and (d) $F_h = 0.5$, $k_z = 0.3$, $U_S = 0.1$.

other parameters constant (figure 5.18d) reduces the y displacement as expected. The agreement between the theoretical prediction and the numerical results is as good as for the reference case (figure 5.14).

Figure 5.19 shows the evolution of the maximum buoyancy for the same four set of parameters as in figure 5.18. Once again, the asymptotics closely follow the numerics for all times investigated in the four cases all the more than $k_z F_h$ is low. We can notice that the oscillations are strongly reduced when $F_h = 0.1$ (figure 5.19a,b) compared to $F_h = 0.5$ (figure 5.19c,d). This is because the amplitude of the internal waves in the buoyancy scales as the Froude number. Hence, they vanish in the hydrostatic limit $F_h = 0$.

5.5.3 Evolution of the vertical shear

We now investigate the evolution of the flow at the vortex center $\tilde{r} = 0$ and at the levels $z_c = 0, l_z/2$ where the ambient shear is maximum. As seen in section §5.3, these are the locations where the Richardson number reaches its minimum or where the Kelvin-Helmholtz instability first appears.

Using the asymptotic expressions of the velocity and buoyancy fields, it is possible to obtain simple predictions for the vertical shear of the horizontal velocity and the buoyancy at these locations. This should enable us to predict the evolution of the Richardson number and the occurrence of the Kelvin-Helmholtz instability.

The horizontal velocity of the vortex has been written in the asymptotic analysis in the general form

$$\boldsymbol{u}_h \equiv \boldsymbol{u}_h(\tilde{x}, \tilde{y}, z, t), \tag{5.34}$$

where we recall that $(\tilde{x}, \tilde{y})$ are the local cartesian horizontal coordinates with origin at the vortex center at the level z. Hence, differentiating with respect to z leads to

$$\frac{\partial \boldsymbol{u}_h}{\partial z} = -\frac{\partial \Delta x}{\partial z}\frac{\partial \boldsymbol{u}_h}{\partial \tilde{x}} - \frac{\partial \Delta y}{\partial z}\frac{\partial \boldsymbol{u}_h}{\partial \tilde{y}} + \left(\frac{\partial \boldsymbol{u}_h}{\partial z}\right)_{\tilde{x},\tilde{y}}. \tag{5.35}$$

At the vortex center $\tilde{x} = \tilde{y} = 0$ and the level $z = l_z/2$, we have $(\partial \boldsymbol{u}_h/\partial z)_{\tilde{x},\tilde{y}} = 0$. In addition, we can assume $\partial \Delta x/\partial z \simeq t\mathrm{d}U/\mathrm{d}z$, $\partial \Delta y/\partial z \simeq 0$ since the displacement corrections $(\delta x, \delta y)$ are small compared to $U(z)t$ as seen in the previous section. Hence, (5.35) reduces to

$$\frac{\partial \boldsymbol{u}_h}{\partial z}(\tilde{r} = 0, z = l_z/2) = -t\frac{\mathrm{d}U}{\mathrm{d}z}\frac{\partial \boldsymbol{u}_h}{\partial \tilde{x}} = k_z U_S t\frac{\partial \boldsymbol{u}_h}{\partial \tilde{x}}. \tag{5.36}$$

Therefore, only the $\tilde{x}$ derivatives of the horizontal velocity field are needed to compute the vertical shear of the vortex at $\tilde{r} = 0$, $z = l_z/2$. In the asymptotic analysis, its horizontal velocity has been written in the form

$$\boldsymbol{u}_h = \boldsymbol{u}_{h0} + (k_z F_h)^2 \boldsymbol{u}_{h1} + O\left[(k_z F_h)^4\right], \tag{5.37}$$

with

$$u_0 = -\Omega(\tilde{r}, z, t)\tilde{y}, \quad v_0 = \Omega(\tilde{r}, z, t)\tilde{x} \tag{5.38}$$

while $\boldsymbol{u}_{h1}$ is defined in (5.28). This leads to

$$\frac{\partial u}{\partial \tilde{x}}(\tilde{r} = 0, z = l_z/2) = (k_z F_h U_S)^2 \left[\left(\frac{3}{4} - \sigma_2\right) t\Omega_c^2 - \frac{1}{ReF_h^2}\left(\frac{\beta_2^\nu}{\Omega_c} + \sigma_2^\nu t^2 \Omega_c\right)\right], \tag{5.39}$$

$$\frac{\partial v}{\partial \tilde{x}}(\tilde{r} = 0, z = l_z/2) = \Omega_c - (k_z F_h U_S)^2 \left[\beta_2 \Omega_c + \left(\frac{1}{4} + \chi_2\right) t^2 \Omega_c^3 - \frac{\chi_2^\nu t}{ReF_h^2}\right], \tag{5.40}$$

where $\Omega_c(t)$ is the angular velocity at the vortex center and σ_2, β_2, χ_2, β_2^ν, σ_2^ν and χ_2^ν are constants given in chapter 4. Using (5.36), we therefore obtain

$$\frac{\partial u}{\partial z}(\tilde{r} = 0, z = l_z/2) = (k_z U_S)^3 F_h^2 t \left[\left(\frac{3}{4} - \sigma_2\right) t\Omega_c^2 - \frac{1}{ReF_h^2}\left(\frac{\beta_2^\nu}{\Omega_c} + \sigma_2^\nu t^2 \Omega_c\right)\right], \tag{5.41}$$

$$\frac{\partial v}{\partial z}(\tilde{r} = 0, z = l_z/2) = k_z U_S t\Omega_c - (k_z U_S)^3 F_h^2 t \left[\beta_2 \Omega_c + \left(\frac{1}{4} + \chi_2\right) t^2 \Omega_c^3 - \frac{\chi_2^\nu t}{ReF_h^2}\right]. \tag{5.42}$$

Similarly, the vertical gradient of the buoyancy can be obtained as

$$\frac{\partial b}{\partial z}(\tilde{r} = 0, z = l_z/2) = -\frac{\partial \Delta x}{\partial z}\frac{\partial b}{\partial \tilde{x}} \tag{5.43}$$

by neglecting $(\delta x, \delta y)$ and because $(\partial b/\partial z)_{\tilde{x},\tilde{y}} = 0$ at $\tilde{r} = 0$. Using the leading order expression of the buoyancy in the hydrostatic limit, we have

$$\frac{\partial b}{\partial \tilde{x}}(\tilde{r} = 0, z = l_z/2) = k_z U_S t\Omega_c^2 \tag{5.44}$$

giving therefore

$$\frac{\partial b}{\partial z} = (k_z U_S t\Omega_c)^2. \tag{5.45}$$

We now compare these predictions to the results of the DNS presented in section §5.3 for $F_h = 0.1$, $k_z = \pi$, $U_S = 0.2$, and $Re = 6000$.

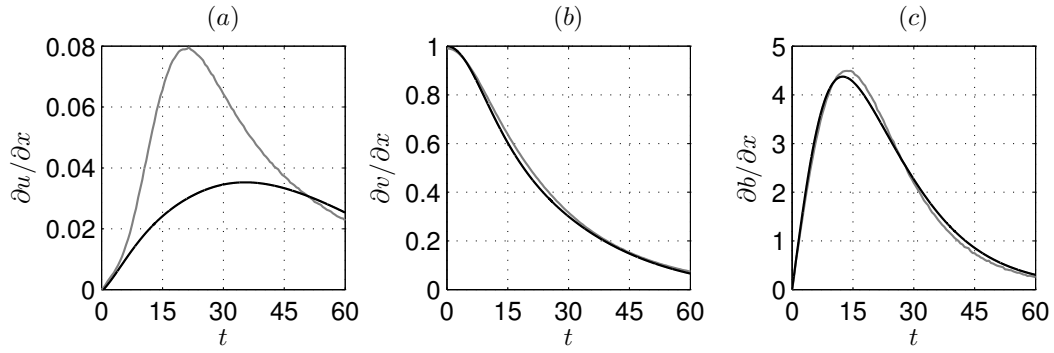

Figure 5.20: Evolution of (a) $\partial u/\partial x$, (b) $\partial v/\partial x$, and (c) $\partial b/\partial x$ at $\tilde{r}=0$, $z=l_z/2$ from the DNS (grey solid lines) and predicted from the asymptotics (black solid lines), for $F_h=0.1$, $k_z=\pi$, $U_S=0.2$, $Re=6000$, i.e. $\gamma\simeq 0.27$.

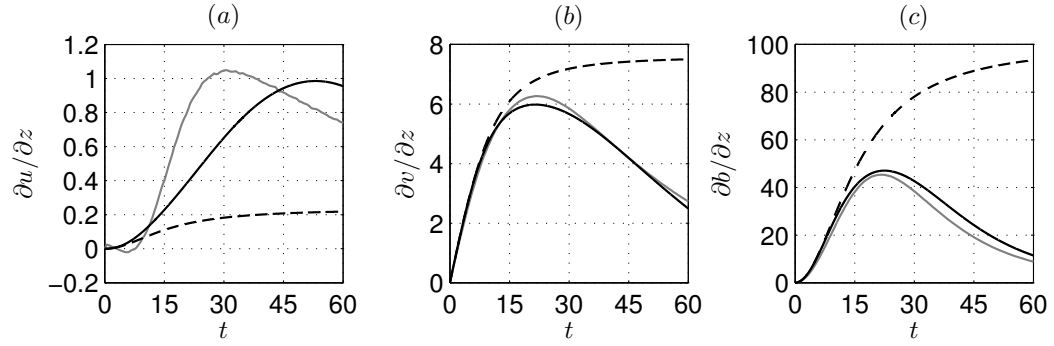

Figure 5.21: Evolution of (a) $\partial u/\partial z$, (b) $\partial v/\partial z$ and (c) $\partial b/\partial z$ at $\tilde{r}=0$, $z=l_z/2$ from the DNS (grey solid lines) and predicted from the asymptotics (black solid lines). The inviscid solutions (black dashed lines) corresponding to $\Omega_c=1/\sqrt{1+(k_zF_hU_St)^2}$ have been also reported. The parameters are $F_h=0.1$, $k_z=\pi$, $U_S=0.2$, $Re=6000$, i.e. $\gamma\simeq 0.27$.

Detailed comparisons for a reference case

Figure 5.20 compares $\partial u/\partial x$, $\partial v/\partial x$, and $\partial b/\partial x$ at the vortex center and at $z_c=l_z/2$ predicted by (5.39), (5.40), and (5.44), respectively, to their counterparts from the DNS. Apart from $\partial u/\partial x$, the agreement is excellent over the entire time range investigated. In particular, the saturation of the buoyancy gradient is properly accounted for (figure 5.20c). The beginning of the evolution of $\partial u/\partial x$ is well predicted by the asymptotics until $t\simeq 5$ but not later. This discrepancy might be due to the fact that the asymptotic model is not uniformly asymptotic in time, since the long-wavelength assumption is expected to be no longer valid when $k_zF_hU_St>1$.

Figure 5.21 compares $\partial u/\partial z$, $\partial v/\partial z$ and $\partial b/\partial z$ at the vortex center and at $z_c=l_z/2$ from the DNS and predicted by (5.41), (5.42) and (5.45). Except for $\partial u/\partial z$ once again, a very good agreement is observed at all times. In particular, the times and levels of saturations of $\partial v/\partial z$ and $\partial b/\partial z$ are both accurately estimated. Note that $\partial v/\partial z$ and $\partial b/\partial z$ saturate simultaneously because these two quantities are functions of a unique arrangement, namely $t\Omega_c$, except the small viscous term in (5.42). As already seen in figure 5.6a, the level of saturation of $\partial u/\partial z$ is much lower than for $\partial v/\partial z$. From (5.41)-(5.42), we can see that this is because $\partial u/\partial z$ is one order smaller in $(k_zF_h)^2$

than $\partial v/\partial z$. This comes from the fact that the leading order velocity is such that $\partial u_0/\partial \tilde{x} = 0$ while $\partial v_0/\partial \tilde{x} = \Omega_c$.

In figure 5.21, we have also plotted with black dashed lines the evolution of each asymptotic quantity in the inviscid limit, i.e. for $Re = \infty$. In this limit, the angular velocity at the vortex center follows the law

$$\Omega_c = \frac{1}{\sqrt{1 + (k_z F_h U_S t)^2}}. \tag{5.46}$$

Remarkably, we see in figure 5.21 that the three quantities grow monotonically but tend to finite values in the limit $t \to \infty$:

$$\lim_{Re,t\to\infty} \frac{\partial u}{\partial z} = \left(\frac{3}{4} - \sigma_2\right) k_z U_S, \tag{5.47}$$

$$\lim_{Re,t\to\infty} \frac{\partial v}{\partial z} = \frac{1}{F_h}\left[1 - \beta_2 (k_z F_h U_S)^2 - \left(\frac{1}{4} + \chi_2\right)\right], \tag{5.48}$$

$$\lim_{Re,t\to\infty} \frac{\partial b}{\partial z} = \frac{1}{F_h^2}. \tag{5.49}$$

This clearly demonstrates that the vertical shear cannot grow indefinitely in strongly stratified flows even for $Re = \infty$, contradicting the conjecture of Lilly (1983). We will see later whether or not the bounds (5.47-5.49) are sufficiently high to reach the threshold $Ri = 1/4$ necessary for the development of the shear instability. Before, we will conduct a parametric study in order to check if the maxima of the vertical gradients of u, v and b are always well predicted by the asymptotic formulas (5.41), (5.42) and (5.45).

As already remarked, $\partial v/\partial z$ and $\partial b/\partial z$ are one order higher than $\partial u/\partial z$ (see figure 5.21 and (5.41), (5.42), (5.45)). Equations (5.42) and (5.45) show that the quantities $\partial v/\partial z$ and $\partial b/\partial z$ both depend only on the product $\Lambda = t\Omega_c$ except the viscous term in (5.42) but which is small. Therefore, they both reach their maxima when

$$\frac{\mathrm{d}\Lambda}{\mathrm{d}t} = 0. \tag{5.50}$$

The time of saturation is therefore given by $T_{sat} = k_z F_h U_S t_{sat} = (3/4\gamma)^{1/3}$ where γ is defined in (5.26), i.e.

$$t_{sat} = \frac{1}{k_z F_h U_S}\left(\frac{3}{4\gamma}\right)^{1/3} = \left(\frac{3Re}{4k_z^2 U_S^2}\right)^{1/3}. \tag{5.51}$$

At this time, the angular velocity is

$$\Omega_c = \Omega_{sat} = \frac{2}{3\sqrt{1 + \left(\frac{2}{9\gamma}\right)^{2/3}}}. \tag{5.52}$$

It is then straightforward to obtain the maxima of $\partial v/\partial z$ and $\partial b/\partial z$:

$$\max\left(\frac{\partial v}{\partial z}\right) = \mathcal{M}_v = \frac{\eta}{F_h}\left[1 - \beta_2 (k_z F_h U_S)^2 - \left(\frac{1}{4} + \chi_2\right)\eta^2\right] + \frac{k_z U_S}{Re F_h^2}\chi_2^\nu \left(\frac{3}{4\gamma}\right)^{2/3}, \tag{5.53}$$

$$\max\left(\frac{\partial b}{\partial z}\right) = \mathcal{M}_b = \frac{\eta^2}{F_h^2}, \tag{5.54}$$

where η is a function of the single parameter γ, namely

$$\eta = \frac{2}{3\sqrt{1+\left(\frac{2}{9\gamma}\right)^{2/3}}}\left(\frac{3}{4\gamma}\right)^{1/3}. \tag{5.55}$$

In contrast, the viscous term in (5.41) governs the level of saturation of $\partial u/\partial z$ as seen in figure 5.21*a*. The maximum $\mathcal{M}_u$ of $\partial u/\partial z$ is reached at $t^*_{sat} \neq t_{sat}$. Since it is not possible to derive simple analytic expressions for t^*_{sat} and $\mathcal{M}_u$, these two quantities have been determined numerically using the asymptotic formulas (5.27) and (5.41).

Effect of k_z

Figure 5.22 shows the evolution of $\partial u/\partial z$, $\partial v/\partial z$, and $\partial b/\partial z$ at the vortex center and $z = l_z/2$ in numerical simulations for different vertical wavenumbers k_z, for $F_h = 0.1$, $U_S = 0.2$, and $Re = 6000$. As k_z increases, these quantities saturate earlier and at a higher level (figure 5.22*a,c,e*). The right plots (figure 5.22*b,d,f*) show the same curves when each quantity is rescaled by its asymptotic maximum $\mathcal{M}_u$, $\mathcal{M}_v$ (5.53), $\mathcal{M}_b$ (5.54), the time t being rescaled by the corresponding saturation time t^*_{sat} or t_{sat}.

The different curves of $\partial v/\partial z$ and $\partial b/\partial z$ collapse very well with rescaled maxima close to unity and reached when $t/t_{sat} = 1$. The time of saturation is thus proportional to $k_z^{-2/3}$ as seen in (5.51).

Regarding $\partial u/\partial z$ (figure 5.22*b*), the level of saturation is correctly predicted by the asymptotics and the three rescaled curves reach their respective peaks at the same time $t/t^*_{sat} \simeq 0.6$ different from unity. The fact that the theory does not predict the exact saturation time is not surprising given the discrepancy observed in figure 5.21*a*. However, it is noticeable that the scaling of the saturation time as well as the maximum of $\partial u/\partial z$ are properly estimated.

Effect of U_S

As for k_z, figure 5.23 displays the evolution of $\partial u/\partial z$, $\partial v/\partial z$, and $\partial b/\partial z$ at $\tilde{r} = 0$, $z = l_z/2$ in numerical simulations for different values of U_S. Enhancing the shear amplitude again leads to higher saturation levels that are reached earlier. When rescaled (figure 5.23*d,f*), $(\partial v/\partial z)/\mathcal{M}_v$ and $(\partial b/\partial z)/\mathcal{M}_b$ saturate around unity at $t/t_{sat} = 1$. As seen in (5.51), the time of saturation thus scales like $U_S^{-2/3}$. Regarding $\partial u/\partial z$, the rescaling aligns the peaks around $t/t^*_{sat} \simeq 0.6$ and their levels are again close to unity as observed for k_z.

Effect of Re

Figure 5.24 shows that increasing the Reynolds number delays the saturation of $\partial u/\partial z$, $\partial v/\partial z$ and $\partial b/\partial z$ at $\tilde{r} = 0$, $z = l_z/2$ and slightly increases the peak values. This is consistent with (5.51), since this equation shows that t_{sat} is weakly affected by the Reynolds number because Re intervenes only to the power $1/3$ instead of $-2/3$ for k_z and U_S.

The rescaling of $\partial v/\partial z$ and $\partial b/\partial z$ by their asymptotic maxima and of the time by t_{sat} (figure 5.24*d,f*) accurately collapses the evolution and saturation of these quantities.

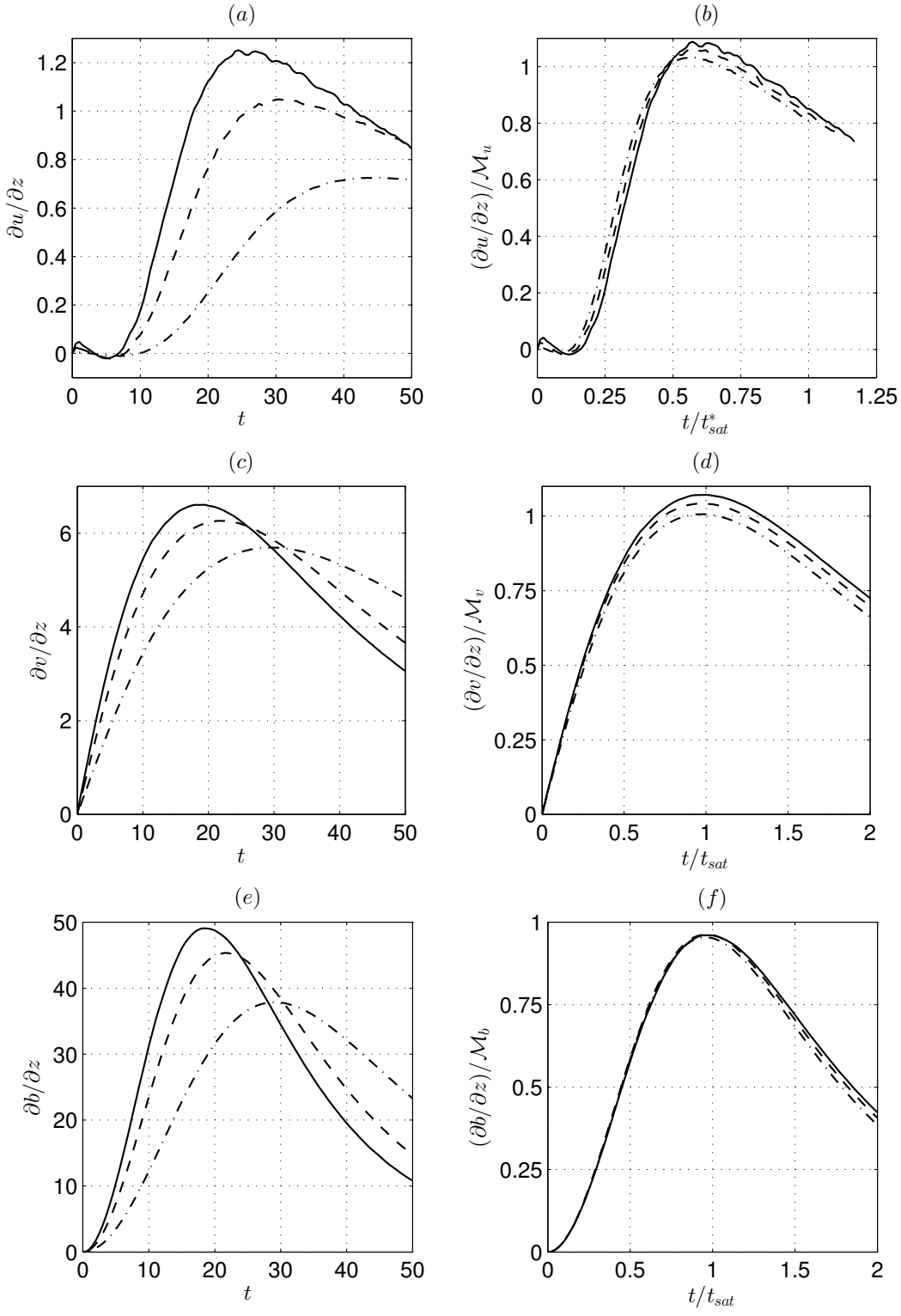

Figure 5.22: Evolution of $\partial u/\partial z$ (a,b), $\partial v/\partial z$ (c,d), and $\partial b/\partial z$ (e,f) at $\tilde{r} = 0$, $z = l_z/2$, for $F_h = 0.1$, $U_S = 0.2$, and $Re = 6000$, for $k_z = 2$ (dash-dotted lines), $k_z = \pi$ (dashed lines), and $k_z = 4$ (solid lines). The quantities $\partial u/\partial z$, $\partial v/\partial z$, $\partial b/\partial z$ are plotted against the physical time t in (a), (c), (e), respectively, whereas (b), (d), (f) show $(\partial u/\partial z)/\mathcal{M}_u$ against t/t^*_{sat}, and $(\partial v/\partial z)/\mathcal{M}_v$, $(\partial b/\partial z)/\mathcal{M}_b$ against t/t_{sat}, respectively.

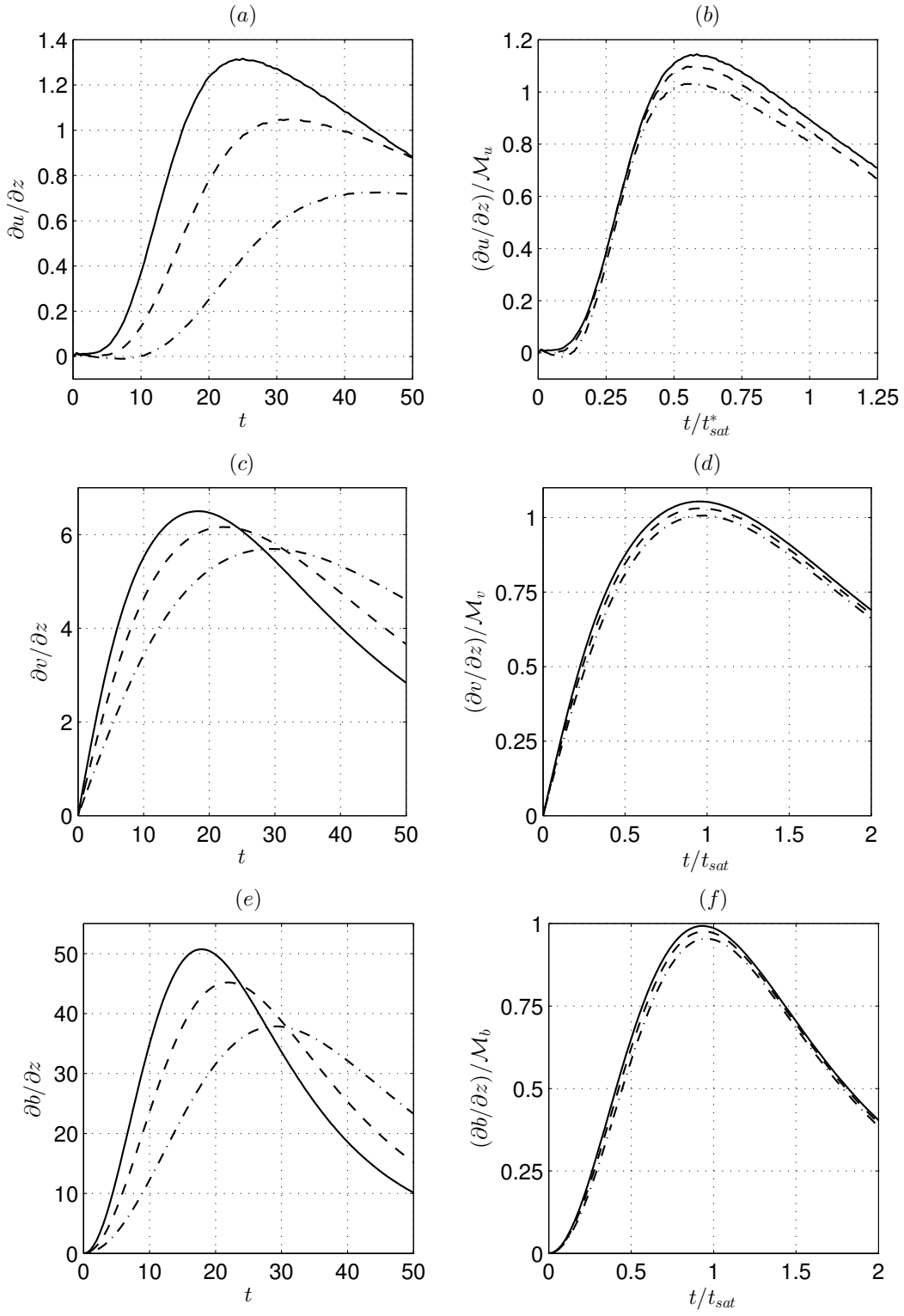

Figure 5.23: Evolution of $\partial u/\partial z$ (a,b), $\partial v/\partial z$ (c,d), and $\partial b/\partial z$ (e,f) at $\tilde{r} = 0$, $z = l_z/2$, for $F_h = 0.1$, $k_z = 2$, and $Re = 6000$, for $U_S = 0.2$ (dash-dotted lines), $U_S = 0.3$ (dashed lines), and $U_S = 0.4$ (solid lines). The quantities $\partial u/\partial z$, $\partial v/\partial z$, $\partial b/\partial z$ are plotted against the physical time t in (a), (c), (e), respectively, whereas (b), (d), (f) show $(\partial u/\partial z)/\mathcal{M}_u$ against t/t^*_{sat}, and $(\partial v/\partial z)/\mathcal{M}_v$, $(\partial b/\partial z)/\mathcal{M}_b$ against t/t_{sat}, respectively.

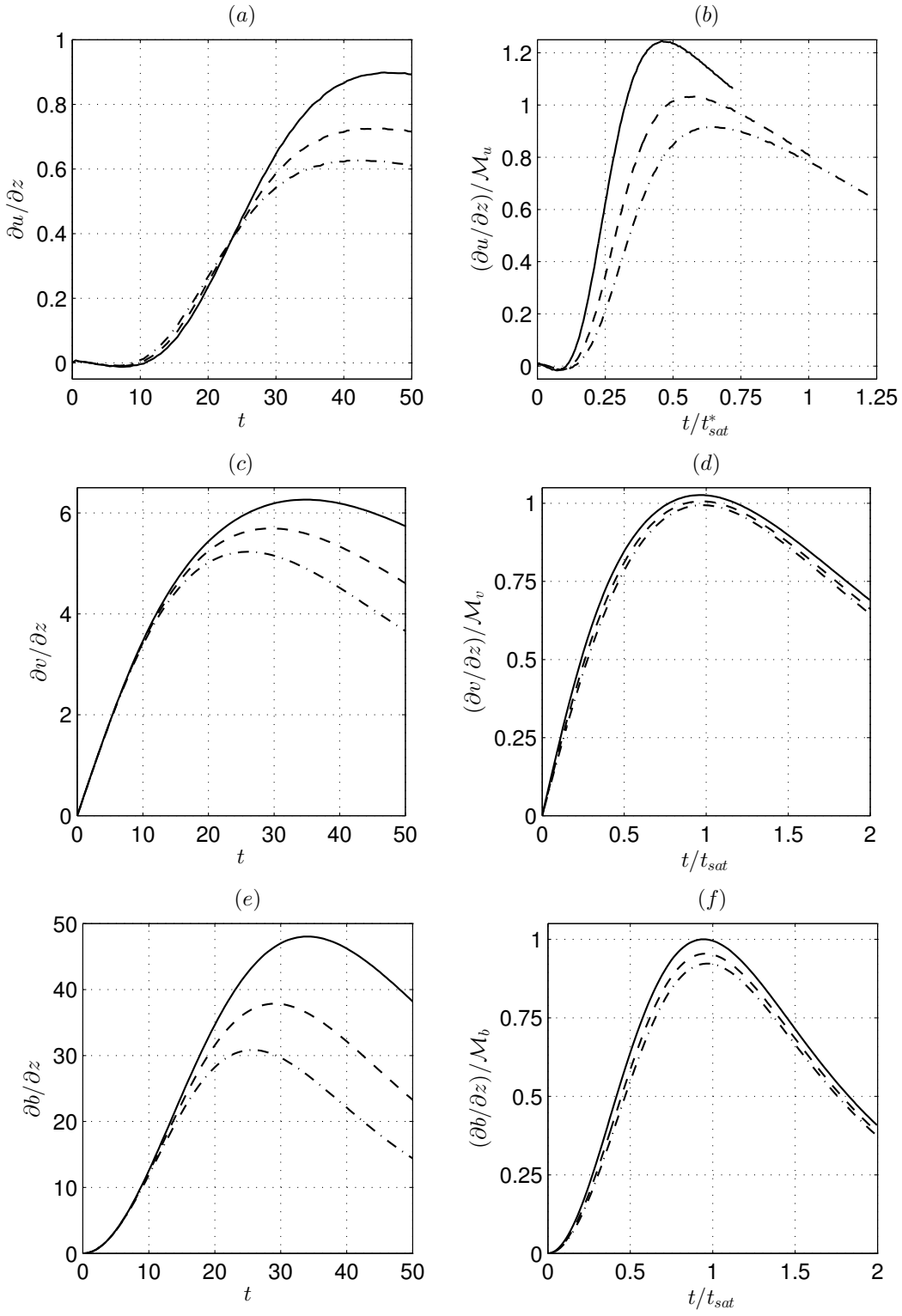

Figure 5.24: Evolution of $\partial u/\partial z$ (a,b), $\partial v/\partial z$ (c,d), and $\partial b/\partial z$ (e,f) at $\tilde{r} = 0$, $z = l_z/2$, for $F_h = 0.1$, $k_z = 2$, and $U_S = 0.2$, for $Re = 4000$ (dash-dotted lines), $Re = 6000$ (dashed lines), and $Re = 10000$ (solid lines). The quantities $\partial u/\partial z$, $\partial v/\partial z$, $\partial b/\partial z$ are plotted against the physical time t in (a), (c), (e), respectively, whereas (b), (d), (f) show $(\partial u/\partial z)/\mathcal{M}_u$ against t/t^*_{sat}, and $(\partial v/\partial z)/\mathcal{M}_v$, $(\partial b/\partial z)/\mathcal{M}_b$ against t/t_{sat}, respectively.

The prediction of the saturation of $\partial u/\partial z$ is less satisfying this time. Indeed, the curve corresponding to the highest Reynolds number $Re = 10000$ departs from the other ones (figure 5.24b). Nevertheless, the two other curves still saturate at $t/t^*_{sat} \simeq 0.6$ and their peaks are both close to unity as for k_z and U_S.

Effect of F_h

Eventually, we examine the influence of the horizontal Froude number in figure 5.25. When F_h is increased, from $F_h = 0.1$ to $F_h = 0.5$, $\partial v/\partial z$ and $\partial b/\partial z$ at the vortex center at $z = l_z/2$ decrease (figure 5.25c,e) while $\partial u/\partial z$ increases (figure 5.25a). In addition, large oscillations are present for $F_h = 0.5$. When the curves are rescaled as before, the collapse is less satisfactory than for the other parameters investigated previously, especially for the case $F_h = 0.5$. Two reasons can explain these discrepancies. First, as F_h increases, the parameter $k_z F_h$ goes from 0.2 to 1. Thus, the hypothesis of the long-wavelength analysis, i.e. $k_z F_h \ll 1$, is less and less valid as F_h increases. Secondly, the law for the evolution of the angular velocity has been derived under the hydrostatic approximation, i.e. equivalently $F_h \ll 1$, in order to simplify the calculations. This assumption implies, in particular, that the internal waves excited at $t = 0$ are neglected. However, it is likely that these internal waves are responsible for the oscillations seen for $F_h = 0.5$ in figure 5.25. To test this claim, it could be therefore interesting to derive the evolution of the angular velocity without making the hydrostatic approximation.

5.5.4 Evolution of the Richardson number

Having validated the asymptotics for the evolution of the vertical shear of the vortex and the vertical gradient of the buoyancy at the vortex center at $z = l_z/2$, we now consider the evolution of the asymptotic Richardson number at this location:

$$Ri = \frac{\dfrac{1}{F_h^2} + \dfrac{\partial b}{\partial z}}{\left(-k_z U_S + \dfrac{\partial u}{\partial z}\right)^2 + \left(\dfrac{\partial v}{\partial z}\right)^2}, \tag{5.56}$$

where $\partial u/\partial z$, $\partial v/\partial z$ and $\partial b/\partial z$ are given by (5.41), (5.42), and (5.45).

In figure 5.4, we have plotted (5.56) for the two sets of parameters considered in section §5.3. The agreement with the numerical results is good for $k_z = \pi$, $F_h = 0.1$, while for $k_z = 3\pi/2$, $F_h = 0.5$, the initial decrease of the asymptotic Richardson number is well captured but subsequently, it re-increases instead of decreasing. As discussed above, this discrepancy comes probably from the oscillations due to internal waves that are present at $F_h = 0.5$ in the numerical simulations. These oscillations are absent in the asymptotics because of the use of the hydrostatic approximation. Hence, the asymptotics are expected to be valid only if the Froude number is below $F_h \simeq 0.25$.

To study the minimum value of (5.56) depending on the control parameters k_z, U_S, F_h, Re, it can be first remarked that (5.41), (5.42), and (5.45) can be written in the

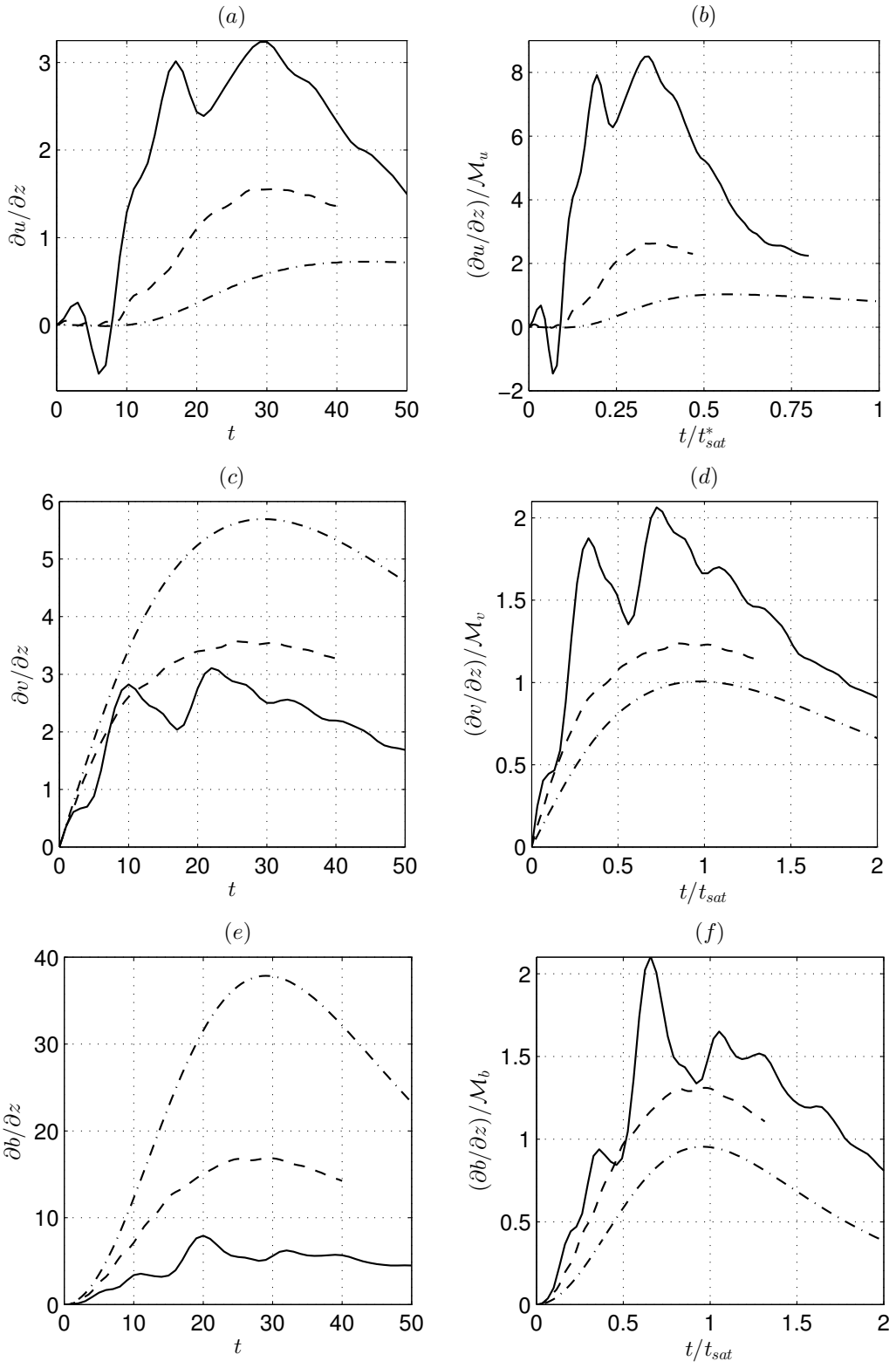

Figure 5.25: Evolution of $\partial u/\partial z$ (*a*,*b*), $\partial v/\partial z$ (*c*,*d*), and $\partial b/\partial z$ (*e*,*f*) at $\tilde{r} = 0$, $z = l_z/2$, for $k_z = 2$, $U_S = 0.2$, $Re = 6000$, for $F_h = 0.1$ (dash-dotted lines), $F_h = 0.25$ (dashed lines), and $F_h = 0.5$ (solid lines). The quantities $\partial u/\partial z$, $\partial v/\partial z$, $\partial b/\partial z$ are plotted against the physical time t in (*a*), (*c*), (*e*), respectively, whereas (*b*), (*d*), (*f*) show $(\partial u/\partial z)/\mathcal{M}_u$ against t/t^*_{sat}, and $(\partial v/\partial z)/\mathcal{M}_v$, $(\partial b/\partial z)/\mathcal{M}_b$ against t/t_{sat}, respectively.

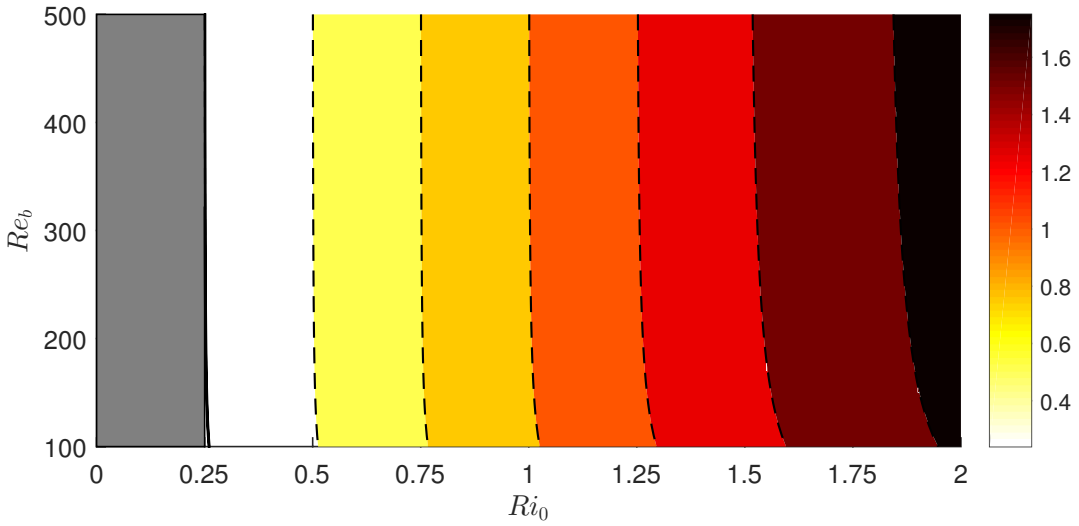

Figure 5.26: Contours of the minimum Richardson number as a function of its initial value Ri_0 and the buoyancy Reynolds number Re_b. The grey domain corresponds to $Ri_0 < 0.25$ i.e. where the shear flow is unstable by itself. The black solid line shows the threshold $\min(Ri) = 0.25$.

form

$$\frac{\partial u}{\partial z} = k_z U_S \mathcal{F}_u(k_z F_h U_S, Re_b, t), \tag{5.57}$$

$$\frac{\partial v}{\partial z} = \frac{1}{F_h}\mathcal{F}_v(k_z F_h U_S, Re_b, t), \tag{5.58}$$

$$\frac{\partial b}{\partial z} = \frac{1}{F_h^2}\mathcal{F}_b(k_z F_h U_S, Re_b, t), \tag{5.59}$$

where $Re_b = ReF_h^2$ is the buoyancy Reynolds number. Hence, the Richardson number can be re-written

$$Ri = \frac{1 + \mathcal{F}_b}{(k_z F_h U_S)^2 (\mathcal{F}_u - 1)^2 + \mathcal{F}_v^2}, \tag{5.60}$$

meaning that it is a function of only three parameters: $k_z F_h U_S$, Re_b, and t. This greatly simplifies its study. Thereby, figure 5.26 shows the minimum of the Richardson number over time as a function of the initial Richardson number $Ri_0 = 1/(k_z F_h U_S)^2$ and Re_b. Only the domain $Ri_0 > 0.25$ is of interest since below the ambient shear is unstable by itself. The threshold $\min(Ri) = 0.25$ is indicated by the black solid line. For $Re_b \sim 100$, this line is tangent and already very close to the boundary $Ri_0 = 0.25$. When Re_b is increased, it quickly crosses the limit $Ri_0 = 0.25$ meaning that $\min(Ri) \leqslant 0.25$ only if already initially, $Ri_0 \leqslant 0.25$.

The limit for $Re_b \gg 1$ can be studied by considering the expressions (5.47), (5.48) and (5.49) of $\partial u/\partial z$, $\partial v/\partial z$ and $\partial b/\partial z$ when $Re \to \infty$ and $t \to \infty$. This yields

$$\min(Ri) = \frac{2Ri_0}{\left(\sigma_2 + \frac{1}{4}\right)^2 + Ri_0\left(\frac{3}{4} - \chi_2 - \frac{\beta_2}{Ri_0}\right)^2}. \tag{5.61}$$

This relation implies that $\min(Ri) < 0.25$ only if $Ri_0 \lesssim 0.12$. Therefore, the Richardson number will go below the threshold $Ri = 0.25$ in the inviscid limit only if the initial

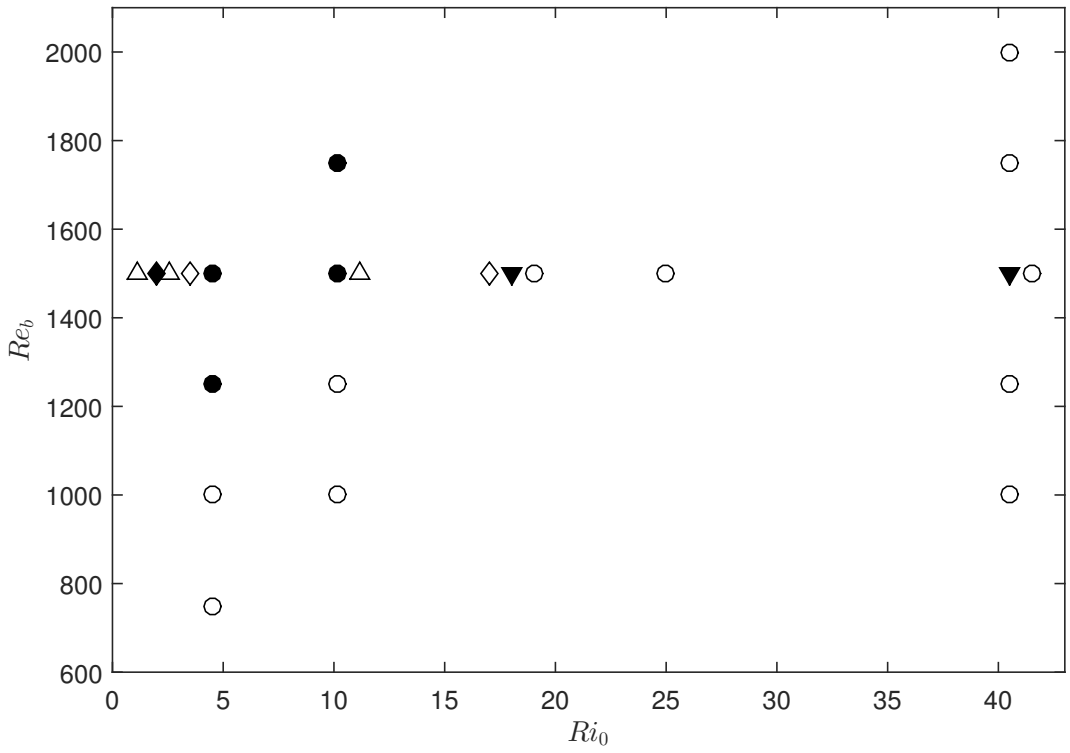

Figure 5.27: Summary of the runs performed at $F_h = 0.5$, in the plane $(Ri_0, Re_b = ReF_h^2)$. Empty symbols correspond to cases where the Kelvin-Helmholtz does not develop, while filled symbols correspond to unstable runs. The symbols are associated with constant values of the ambient shear flow amplitude: downward triangles correspond to $U_S = 0.1$, open circles to $U_S = 0.2$, diamonds to $U_S = 0.3$, and upward triangles to $U_S = 0.4$.

Richardson number is already below this critical value, i.e. only if the ambient shear flow is unstable by itself.

5.6 Occurrence of the shear instability at $F_h = 0.5$

Since the shear instability has been only observed in the numerical simulations performed at $F_h = 0.5$, it is worth clarifying when it occurs at this particular Froude number, depending on the other control parameters k_z, U_S, Re.

To do so, and following the same idea as in §5.5.4, we have plotted in figure 5.27 a map discriminating stable cases from their unstable counterparts in the plane (Ri_0, Re_b). For a given U_S, the instability develops only if the buoyancy Reynolds number is sufficiently high and Ri_0 sufficiently low (see the circles for $U_S = 0.2$). However, this marginal stability line varies with U_S: it moves towards lower Ri_0 as U_S increases. Indeed, for $Re_b = 1500$, the instability develops for $U_S = 0.1$ even if Ri_0 is as high as $Ri_0 = 40$, while for $U_S = 0.2$ and $U_S = 0.3$, it occurs only for $Ri_0 \lesssim 10$ and $Ri_0 \lesssim 2$, respectively. For $U_S = 0.4$, no instability has been observed even at $Ri_0 \simeq 1$. Therefore, at this Froude number, the occurrence of the Kelvin-Helmholtz instability cannot be predicted on the basis of Ri_0 and Re_b only as suggested by the asymptotics. Nevertheless, there is no contradiction with the asymptotic predictions because of the effect of the internal waves in the moderately stratified regime.

5.7 Conclusion

We have performed direct numerical simulations of the evolution of an initially columnar vortex in an ambient shear flow in a strongly stratified fluid. The numerical results have been compared to the asymptotic analyses carried out in chapter 4.

The DNS show that the vortex is progressively bent in the direction of the shear flow but the vortex core also deviates in the orthogonal direction. The decay of its potential vorticity is enhanced in the regions of high shear. For $F_h = 0.5$ and sufficiently high Reynolds number Re and vertical wavenumber k_z, the Kelvin-Helmholtz instability is first triggered in the center of the vortex at the vertical levels where the ambient vertical shear is maximum. For the lower Froude numbers investigated $F_h = 0.1$ and $F_h = 0.25$, the Kelvin-Helmholtz instability has never been detected but the Richardson number reaches its minimum at the same location. We have therefore concentrated our efforts on the understanding of the evolution of the flow at this location thanks to the long-wavelength asymptotic analysis performed for $k_z F_h \ll 1$ in chapter 4. Besides, we have first shown that the short-time and the long-wavelength analyses account very well for the initial non-hydrostatic regime and the deformation of the vortex axis, respectively.

For $F_h \lesssim 0.25$, the long-wavelength asymptotic analysis turns out to predict very well the evolution of the vertical shear of the vortex in the spanwise direction $\partial v/\partial z$ and of the vertical gradient of the buoyancy $\partial b/\partial z$ at the vortex center and $z = l_z/2$ for all the parameters investigated. The prediction for the streamwise shear of the vortex $\partial u/\partial z$ is less accurate but this is not too dramatic since it is one order smaller in $(k_z F_h)^2$ than $\partial v/\partial z$ and $\partial b/\partial z$.

The long-wavelength asymptotic analysis reveals that the growth of these three quantities is bounded owing to the conservation of potential vorticity and by viscous effects. Thereby, the maxima of $\partial v/\partial z$ and $\partial b/\partial z$ at leading order are of the form $\mathcal{M}_v = \mathcal{F}_v(\gamma)/F_h$ and $\mathcal{M}_b = \mathcal{F}_b(\gamma)/F_h^2$, where $\gamma = 1/(ReF_h^3 k_z U_S) = \sqrt{Ri_0}/Re_b$, and where $Re_b = ReF_h^2$ is the buoyancy Reynolds number and $Ri_0 = 1/(k_z F_h U_S)^2$ the initial Richardson number. For small γ (i.e. near the inviscid limit), the functions $\mathcal{F}_v$ and $\mathcal{F}_b$ tend to constants close to unity, while for large γ, they behave as

$$\mathcal{F}_v(\gamma) \sim \frac{1}{\gamma^{1/3}} \sim F_h (k_z U_S Re)^{1/3}, \tag{5.62}$$

$$\mathcal{F}_b(\gamma) \sim \frac{1}{\gamma^{2/3}} \sim F_h^2 (k_z U_S Re)^{2/3}, \tag{5.63}$$

at leading order.

The Richardson number at the vortex center and $z = l_z/2$ based on the asymptotic expressions of $\partial u/\partial z$, $\partial v/\partial z$, and $\partial b/\partial z$ is in good agreement with the DNS provided that the Froude number is small $F_h \lesssim 0.25$. This limitation comes from the fact that the hydrostatic approximation has been assumed in some parts of the long-wavelength analysis.

The minimum asymptotic Richardson number depends only on the two parameters Ri_0 and Re_b. For large Re_b, it can be lower than the critical value 1/4 necessary for the development of the shear instability only if the initial Richardson number is already smaller than this value.

This result puts into question the idea that the shear instability is easily triggered in strongly stratified shear flows. It also demonstrates that the mechanism proposed by Lilly (1983), according to which the vertical shear should grow algebraically with

time without bounds, is not valid for the flow studied herein. Because of the vertical coupling, neglected by Lilly (1983), the flow actually decays in the regions of high shear, thereby limiting the maximum vertical shear attainable. This is due to potential vorticity conservation and enhanced viscous effects.

The shear instability has been only observed for $F_h = 0.5$ and sufficiently high Re and k_z. The role played by oscillations due to the transient internal waves excited at the start-up of the motion seems crucial for the development of the shear instability in this case. These oscillations are indeed of particularly large amplitudes for $F_h = 0.5$ and high k_z. Hence, the development of the shear instability for $F_h = 0.5$ might be specific to the particular configuration and initial conditions chosen here. However, in stratified turbulent flows, although the structures can be continuously vertically sheared, it is unlikely that a coherent structure will be impulsively sheared at a given time. As seen in section §5.4, this impulsive start-up leads to a transient non-hydrostatic regime and to the generation of large internal waves when F_h is not small. In contrast, the shearing process is expected to be much more continuous and smooth in stratified turbulent flows, limiting the generation of internal waves.

Chapter 6

Conclusions and perspectives

The purpose of the present dissertation has been to understand the different facets of the response of an initially vertical vortex embedded in an environmental vertically sheared flow, in presence of a strong stratification. To do so, we have considered the case of a model flow comprising a straight Lamb-Oseen vortex at $t = 0$ subjected to a flow uniform in the horizontal but varying sinusoidally along the vertical. Under the effect of the differential advection due to the shear flow, the vortex is progressively decorrelated along the vertical, this process being at the origin of the existence of localized regions of intense vertical shear. This investigation therefore enables testing Lilly's conjecture (Lilly, 1983) that the vertical shear should grow algebraically with time, leading to the generation of small scales through the shear instability for large enough times. More generally, the present study has aimed at clarifying many facets of the dynamics of the vortex: its displacements, its structure evolution, and notably the variations of the density as well as the vertical shear of the horizontal velocity in the vortex core.

In this regard, a first approach has been based on the analysis of the global budgets of energy and enstrophy (see chapter 3). We have been able to determine an estimation of the minimum shear layer thickness that is associated with the peak value attained by the global enstrophy of the vortex.

Remarkably, the scaling which has been obtained for the maximum enstrophy in terms of the control parameters indicates that it is proportional to the Reynolds number to the power 2/3, suggesting that the minimum Richardson number is in turn inversely proportional to $Re^{2/3}$. This result questions former estimations stating that the minimum Richardson number scales as the inverse of the buoyancy Reynolds number ReF_h^2 (Riley and deBruynKops, 2003; Deloncle et al., 2008). In fact, the exponent 2/3 comes from the presence of the ambient shear flow: the dynamics is not the same as in freely decaying flows.

This is not the only remarkable result of this investigation. Indeed, the theoretical scalings derived in chapter 3 account for the effect of all the control parameters except the Froude number: the interpretations presented in this chapter do not predict any dependency with respect to this parameter although it clearly influences the decay of the kinetic energy as well as the variations of enstrophy.

In order to overcome this paradox, we have carried out local investigations of the dynamics based on asymptotic analyses in chapters 4 and 5. First, the study of the short-time dynamics has shown that the initial response of the vortex to the ambient shear flow is non-hydrostatic regardless of the level of stratification. After this transient

stage however, the hydrostatic balance is progressively recovered. The initial non-hydrostatic regime arises because of the excitation of internal waves at the beginning of the flow evolution.

Another central result of these analyses is that the core angular velocity of the vortex decays because of dynamic and viscous effects. Notably, this decay is not uniform in the vertical: it is maximum in the regions of maximum vertical shear whereas it cancels at the locations where the vertical shear is close to zero. The decrease of the angular velocity actually modulates the growth of the vertical shear of the horizontal velocity which, in turn, cannot grow indefinitely as speculated by Lilly (1983): it has an upper bound accurately estimated by the asymptotics. A key factor in this process of modulation is the vertical velocity, which had been ignored by Lilly. The asymptotics have not only enabled us to obtain analytic predictions regarding the saturation of the different quantities but also for their global temporal variations, thus providing a comprehensive description of the dynamics.

Nevertheless, these analytic results have been obtained in the asymptotic limit of long vertical wavelength and strong stratification, hence allowing to use the hydrostatic approximation for the sake of simplicity. Their use in the moderately stratified regime has shown that they still account for the observed dynamics qualitatively, but are no longer valuable quantitatively. In particular, we have shown that the dependence of the vertical shear of horizontal velocity with respect to the Froude number is quite complex. Nevertheless, the effect of this parameter has been understood thanks to the local analyses presented in chapters 4 and 5, since the formulas derived in these chapters capture quite well the physics provided that the stratification is strong. Hence, these advances offer the possibility of explaining the effect of the Froude number on the variations of the volume-integrated energy and enstrophy, which remained unexplained in chapter 3, by integrating the local equations obtained via the asymptotics over the entire fluid domain.

Beyond the effect of the Froude number, the analytic predictions of chapter 4 yield an accurate expression for the local Richardson number in chapter 5. A major result is that, for strong stratification, its minimum is a function of time only, and of two well-identified parameters: the Richardson number associated with the ambient shear flow only, and the buoyancy Reynolds number. In this case, we have shown that the shear instability can be triggered only if the ambient shear flow is itself unstable in the sense of the Miles & Howard criterion (Miles, 1961; Howard, 1961). Thus, our results prove that the process of vertical decorrelation itself is insufficient to trigger the shear instability in strongly stratified fluids, in strong contrast with Lilly's hypothesis. However, we have shown that the shear instability develops for moderate stratification and large enough vertical wavenumber even if the advection by the ambient shear flow is not that strong.

Globally, the present investigations offer a variety of perspectives for future works on related issues. First, the present long-wavelength analysis could be improved and probably extended to the moderately stratified case by taking into account the wave terms that have been neglected herein when tackling the problem of the evolution of the vortex structure. More generally, the asymptotic method presented in chapter 4 could be replicated to other model cases, for example by assuming that the ambient shear flow varies linearly along the vertical, or by considering that a rapid background rotation is present over the stratification. The latter configuration should be interesting because there would no longer be any excitation of internal waves in this case. Thus,

the dynamics should be significantly different from that observed in the purely stratified case. In addition, our results prove that the decay of the core angular velocity is of utmost importance in order to model the evolution of the vertical shear of horizontal velocity properly. This could have important implications for two-layer models (or multi-layer models more generally). Indeed, they usually ignore this effect and, as such, may elude central physical processes, making them insufficiently representative of the real physics.

Appendix A

Study of a linear shear flow

This appendix generalizes the short time asymptotic analysis of chapter 4 (§4.3), to the case of a linear shear flow. The starting point of the present discussion is the equation (4.31), since it is valid for any vortex profile $u_\theta(r)$ and any shear flow profile $U(z)$.

We consider the linear shear flow given by:

$$U(z) = U_S \frac{z}{l_z}. \tag{A.1}$$

As in §4.3, we look for a solution of (4.31) in the form (4.32). Then, β is found to satisfy:

$$\frac{1}{r}\frac{\mathrm{d}}{\mathrm{d}r}\left(r\frac{\mathrm{d}\beta}{\mathrm{d}r}\right) - \frac{\beta(r)}{r^2} = -\frac{\mathrm{d}}{\mathrm{d}r}\left(\frac{1}{r}\frac{\mathrm{d}r^2\Omega^2}{\mathrm{d}r}\right). \tag{A.2}$$

A solution to this equation that is not singular at $r = 0$ and that vanishes at infinity is:

$$\beta(r) = -r\Omega^2. \tag{A.3}$$

Note that this solution has been derived without specifying the profile $u_\theta(r)$. As in the case of the sinusoidal shear flow, we have $w = w_2 t^2$ and $b = b_3 t^3$ at leading order for $t \ll 1$. However, in the present case, the expressions of w_2 and b_3 are:

$$w_2 = -\frac{U_S}{2l_z}\cos(\theta)\beta(r), \quad b_3 = \frac{U_S}{6F_h^2 l_z}\cos(\theta)\beta(r). \tag{A.4}$$

Thus, a transient non-hydrostatic regime also exists at the start-up of the motion when $t \ll F_h$. A striking difference with the sinusoidal shear flow (§4.3) is that w and b are now proportional to $1/l_z$ whatever its value. As for the second-order horizontal velocities, they read:

$$u_2 = \frac{\sin(\theta)}{2}\left[\cos(2\theta)\frac{\mathrm{d}}{\mathrm{d}r}\left(\Omega - \frac{r}{2}\frac{\mathrm{d}\Omega}{\mathrm{d}r}\right) - \frac{\mathrm{d}}{\mathrm{d}r}\left(\frac{r}{2}\frac{\mathrm{d}\Omega}{\mathrm{d}r}\right)\right]U^2(z), \tag{A.5}$$

$$v_2 = \frac{\cos(\theta)}{2}\left[\cos(2\theta)\frac{\mathrm{d}}{\mathrm{d}r}\left(\frac{r}{2}\frac{\mathrm{d}\Omega}{\mathrm{d}r} - \Omega\right) + \frac{\mathrm{d}}{\mathrm{d}r}\left(\Omega + \frac{\zeta}{2}\right)\right]U^2(z). \tag{A.6}$$

These expressions can be retrieved by assuming that the vortex is translated by $\Delta x(z,t) = U(z)t$ and $\Delta y(z,t) = 0$. The second-order horizontal velocity field therefore corresponds to a displacement of the vortex as a whole unlike (4.36)-(4.37) for the sinusoidal shear flow.

Appendix B

Derivation of the streamfunction ψ_w for small time

In this appendix, we derive analytically the streamfunction ψ_w associated to internal waves for small time. This will allow us to obtain the asymptotic expressions of $\mathcal{C}_w$ and $\mathcal{S}_w$ for $t \ll 1$.

It is first useful to rewrite the right-hand side of the equation for ψ_p (4.105) in the form

$$\mathcal{F}_p = -\left[\cos(\tilde{\theta}) f_{pc}(\tilde{r}) + t\sin(\tilde{\theta}) f_{ps}(\tilde{r})\right] \frac{\mathrm{d}^2 U}{\mathrm{d}\tilde{z}^2}, \tag{B.1}$$

where:

$$f_{pc}(\tilde{r}) = -\zeta_0 \mathcal{C}\mathcal{F} - \frac{1}{2}\frac{\partial \zeta_0}{\partial \tilde{r}}\left[\int_{+\infty}^{\tilde{r}} \mathcal{C}\mathcal{F} + \frac{1}{\tilde{r}^2}\int_0^{\tilde{r}} \xi^2 \mathcal{C}\mathcal{F}\right], \tag{B.2}$$

$$f_{ps}(\tilde{r}) = \zeta_0 \mathcal{C}\Omega + \frac{1}{2}\frac{\partial \zeta_0}{\partial \tilde{r}}\left[\int_{+\infty}^{\tilde{r}} \mathcal{C}\Omega + \frac{1}{\tilde{r}^2}\int_0^{\tilde{r}} \xi^2 \mathcal{C}\Omega\right]. \tag{B.3}$$

In the limit $t \to 0$, the right-hand side of (4.106) reads

$$\mathcal{F}_w = -\mathcal{F}_p + \left[t^2 \cos(\tilde{\theta})\frac{f_2(\tilde{r})}{4F_h^2} + t^3 \sin(\tilde{\theta})\frac{f_3(\tilde{r})}{12F_h^2} + O(t^4)\right]\frac{\mathrm{d}^2 U}{\mathrm{d}\tilde{z}^2}, \tag{B.4}$$

where:

$$f_2(\tilde{r}) = 2\tilde{r}\zeta_0\Omega^2 + \frac{\partial \zeta_0}{\partial \tilde{r}}\left[\int_{+\infty}^{\tilde{r}} \xi\Omega^2 + \frac{1}{\tilde{r}^2}\int_0^{\tilde{r}} \xi^3\Omega^2\right], \tag{B.5}$$

$$f_3(\tilde{r}) = 2\tilde{r}\zeta_0\Omega^3 + \frac{\partial \zeta_0}{\partial \tilde{r}}\left[\int_{+\infty}^{\tilde{r}} \xi\Omega^3 + \frac{1}{\tilde{r}^2}\int_0^{\tilde{r}} \xi^3\Omega^3\right]. \tag{B.6}$$

Accordingly, the solution ψ_w of (4.106) is expressed as:

$$\begin{aligned}
\psi_w \;=\; & -\left[\cos(\tilde{\theta})\left(\tilde{r}\Omega\mathcal{C}_w(t) - \tilde{r}\frac{\mathrm{d}\mathcal{S}_w}{\mathrm{d}t}\right) + \sin(\tilde{\theta})\left(\tilde{r}\Omega\mathcal{S}_w(t) + \tilde{r}\frac{\mathrm{d}\mathcal{C}_w}{\mathrm{d}t}\right)\right]\frac{\mathrm{d}^2 U}{\mathrm{d}\tilde{z}^2} \\
& - \Big[\sin(\tilde{\theta})\psi_{w0}(\tilde{r}) + t\cos(\tilde{\theta})\psi_{w1}(\tilde{r}) + t^2\sin(\tilde{\theta})\psi_{w2}(\tilde{r}) + t^3\cos(\tilde{\theta})\psi_{w3}(\tilde{r}) \\
& + t^4\sin(\tilde{\theta})\psi_{w4}(\tilde{r}) + O(t^5)\Big]\frac{\mathrm{d}^2 U}{\mathrm{d}\tilde{z}^2}.
\end{aligned} \tag{B.7}$$

Inserting this expansion in (4.106) yields the sequence of equations:

$$\nabla^2_{\tilde{r}}\psi_{w1} + \Omega\nabla^2_{\tilde{r}}\psi_{w0} - \frac{1}{\tilde{r}}\frac{\partial\zeta_0}{\partial\tilde{r}}\psi_{w0} = -f_{pc}, \tag{B.8}$$

$$2\nabla^2_{\tilde{r}}\psi_{w2} - \Omega\nabla^2_{\tilde{r}}\psi_{w1} + \frac{1}{\tilde{r}}\frac{\partial\zeta_0}{\partial\tilde{r}}\psi_{w1} = -f_{ps}, \tag{B.9}$$

$$3\nabla^2_{\tilde{r}}\psi_{w3} + \Omega\nabla^2_{\tilde{r}}\psi_{w2} - \frac{1}{\tilde{r}}\frac{\partial\zeta_0}{\partial\tilde{r}}\psi_{w2} = -\frac{f_2}{4F_h^2}, \tag{B.10}$$

$$4\nabla^2_{\tilde{r}}\psi_{w4} - \Omega\nabla^2_{\tilde{r}}\psi_{w3} + \frac{1}{\tilde{r}}\frac{\partial\zeta_0}{\partial\tilde{r}}\psi_{w3} = -\frac{f_3}{12F_h^2}. \tag{B.11}$$

These equations can be resolved successively. We first impose

$$\psi_{w0} = -\left[\psi_{ps} + \lambda_0\tilde{r}\Omega + (\lambda_1 - \vartheta)\tilde{r}\right] \tag{B.12}$$

in order to satisfy the same initial condition (4.130) as for the solution computed numerically. Note that ψ_{ps} is defined in (4.120). Then, (B.8) gives

$$\psi_{w1} = -\left[\psi_{pc} + (\lambda_1 - \vartheta)\tilde{r}\Omega + \frac{\mathcal{A}}{2}\tilde{r}\right], \tag{B.13}$$

where ψ_{pc} is defined in (4.119) and where it has been also imposed that $\psi_{w1} \to 0$ as $\tilde{r} \to +\infty$. In turn, (B.9) and (B.10) yield

$$\psi_{w2} = \frac{\mathcal{A}}{4}\tilde{r}\Omega, \quad \psi_{w3} = -\frac{\tilde{\psi}_3}{12F_h^2}, \tag{B.14}$$

with

$$\tilde{\psi}_3(\tilde{r}) = \tilde{r}\Omega\int_{+\infty}^{\tilde{r}}\xi\Omega^2 + \frac{\Omega}{\tilde{r}}\int_0^{\tilde{r}}\xi^3\Omega^2 - \tilde{r}\int_{+\infty}^{\tilde{r}}\xi\Omega^3 - \frac{1}{\tilde{r}}\int_0^{\tilde{r}}\xi^3\Omega^3 + 4\tilde{r}\int_{+\infty}^{\tilde{r}}\frac{\Omega}{\eta^3}\int_0^{\eta}\xi^3\Omega^2, \tag{B.15}$$

where the constants of integration have been chosen so that ψ_{w3} vanishes at infinity. At fourth order, only $\nabla^2_{\tilde{r}}\psi_{w4}$ will be needed: it is not necessary to derive ψ_{w4}. From (B.11) and (B.14), we have directly:

$$\nabla^2_{\tilde{r}}\psi_{w4} = \frac{\zeta_{w4}}{48F_h^2}, \tag{B.16}$$

where

$$\zeta_{w4}(\tilde{r}) = \frac{1}{\tilde{r}}\frac{\partial\zeta_0}{\partial\tilde{r}}\tilde{\psi}_3 - \Omega f_2 - f_3. \tag{B.17}$$

Finally, we impose that the mean displacement associated to $\nabla^2_h\psi_w$ is zero, giving

$$\mathcal{C}_w(t) = (\lambda_1 - \vartheta)\,t + \frac{\langle\nabla^2_{\tilde{r}}\psi_{pc}, \tilde{r}\rangle}{\left\langle\dfrac{\partial\zeta_0}{\partial\tilde{r}}, \tilde{r}\right\rangle}t + \frac{\varsigma}{F_h^2}t^3 + O(t^5), \tag{B.18}$$

and

$$\mathcal{S}_w(t) = \lambda_0 + \frac{\langle\nabla^2_{\tilde{r}}\psi_{ps}, \tilde{r}\rangle}{\left\langle\dfrac{\partial\zeta_0}{\partial\tilde{r}}, \tilde{r}\right\rangle} - \frac{\mathcal{A}}{4}t^2 + \frac{\sigma}{F_h^2}t^4 + O(t^5), \tag{B.19}$$

where

$$\varsigma = \frac{1}{12}\frac{\langle f_2, \tilde{r}\rangle}{\left\langle \frac{\partial \zeta_0}{\partial \tilde{r}}, \tilde{r} \right\rangle} = -3.554 \times 10^{-2}, \quad \sigma = -\frac{1}{48}\frac{\langle \zeta_{w4}, \tilde{r}\rangle}{\left\langle \frac{\partial \zeta_0}{\partial \tilde{r}}, \tilde{r} \right\rangle} = -3.826 \times 10^{-3} \tag{B.20}$$

for the Lamb-Oseen profile. Then, using (4.124), (B.18) and (B.19) finally reduce to:

$$\mathcal{C}_w(t) = -\vartheta t + \frac{\varsigma}{F_h^2} t^3 + O(t^5), \tag{B.21}$$

$$\mathcal{S}_w(t) = -\frac{\mathcal{A}}{4} t^2 + \frac{\sigma}{F_h^2} t^4 + O(t^5). \tag{B.22}$$

Appendix C

Determination of ψ_{12}^{ν}

In this appendix, we compute the streamfunction ψ_{12}^{ν} forced by the viscous term in (4.154).

By writing it in the form

$$\psi_{12}^{\nu} = \frac{\varepsilon}{2\tilde{R}eF_h^2}\left[\psi_{2b}^{\nu}\sin(2\tilde{\theta}) + \psi_{2c}^{\nu}t\cos(2\tilde{\theta}) + \psi_{2s}^{\nu}t^2\sin(2\tilde{\theta})\right]\left(\frac{\mathrm{d}U}{\mathrm{d}\tilde{z}}\right)^2, \tag{C.1}$$

the viscous part of (4.154) becomes

$$\nabla_{\tilde{r}}^{2*}\psi_{2c}^{\nu} + 2\Omega\nabla_{\tilde{r}}^{2*}\psi_{2b}^{\nu} - \frac{2}{\tilde{r}}\frac{\partial\zeta_0}{\partial\tilde{r}}\psi_{2b}^{\nu} = 0, \tag{C.2}$$

$$\nabla_{\tilde{r}}^{2*}\psi_{2s}^{\nu} - \Omega\nabla_{\tilde{r}}^{2*}\psi_{2c}^{\nu} + \frac{1}{\tilde{r}}\frac{\partial\zeta_0}{\partial\tilde{r}}\psi_{2c}^{\nu} = 0, \tag{C.3}$$

$$\Omega\nabla_{\tilde{r}}^{2*}\psi_{2s}^{\nu} - \frac{1}{\tilde{r}}\frac{\partial\zeta_0}{\partial\tilde{r}}\psi_{2s}^{\nu} = \frac{1}{2}\left[\frac{\partial^2\zeta_0}{\partial\tilde{r}^2} - \frac{1}{\tilde{r}}\frac{\partial\zeta_0}{\partial\tilde{r}}\right]. \tag{C.4}$$

Like for the determination of the streamfunction ψ_{12}^{*}, we assume that the angular velocity follows the law (4.163). Under this hypothesis, ψ_{2b}^{ν}, ψ_{2c}^{ν} and ψ_{2s}^{ν} are rescaled as follows:

$$\psi_{2b}^{\nu} = \frac{\bar{\psi}_{2b}^{\nu}(\bar{r})}{\Omega_c^2}, \quad \psi_{2c}^{\nu} = \frac{\bar{\psi}_{2c}^{\nu}(\bar{r})}{\Omega_c}, \quad \psi_{2s}^{\nu} = \bar{\psi}_{2s}^{\nu}(\bar{r}). \tag{C.5}$$

Then, (C.2-C.4) yield:

$$\nabla_{\bar{r}}^{2*}\bar{\psi}_{2c}^{\nu} + 2\bar{\Omega}\nabla_{\bar{r}}^{2*}\bar{\psi}_{2b}^{\nu} - \frac{2}{\bar{r}}\frac{\mathrm{d}\bar{\zeta}_0}{\mathrm{d}\bar{r}}\bar{\psi}_{2b}^{\nu} = 0, \tag{C.6}$$

$$\nabla_{\bar{r}}^{2*}\bar{\psi}_{2s}^{\nu} - \bar{\Omega}\nabla_{\bar{r}}^{2*}\bar{\psi}_{2c}^{\nu} + \frac{1}{\bar{r}}\frac{\mathrm{d}\bar{\zeta}_0}{\mathrm{d}\bar{r}}\bar{\psi}_{2c}^{\nu} = 0, \tag{C.7}$$

$$\bar{\Omega}\nabla_{\bar{r}}^{2*}\bar{\psi}_{2s}^{\nu} - \frac{1}{\bar{r}}\frac{\mathrm{d}\bar{\zeta}_0}{\mathrm{d}\bar{r}}\bar{\psi}_{2s}^{\nu} = \frac{1}{2}\left[\frac{\mathrm{d}^2\bar{\zeta}_0}{\mathrm{d}\bar{r}^2} - \frac{1}{\bar{r}}\frac{\mathrm{d}\bar{\zeta}_0}{\mathrm{d}\bar{r}}\right]. \tag{C.8}$$

These three equations admit the same homogeneous solution as (4.165-4.167). The complete solutions that vanish at infinity and are non-singular at $\bar{r} = 0$ have been computed numerically and are shown in figure C.1. For $\bar{r} \ll 1$, they behave as

$$\bar{\psi}_{2b}^{\nu} = \beta_2^{\nu}\bar{r}^2 + O(\bar{r}^4), \quad \bar{\psi}_{2c}^{\nu} = \chi_2^{\nu}\bar{r}^2 + O(\bar{r}^4), \quad \bar{\psi}_{2s}^{\nu} = \sigma_2^{\nu}\bar{r}^2 + O(\bar{r}^4), \tag{C.9}$$

with:

$$\beta_2^{\nu} = 10.66, \quad \chi_2^{\nu} = -5.376, \quad \sigma_2^{\nu} = -1.524, \tag{C.10}$$

leading to (4.171).

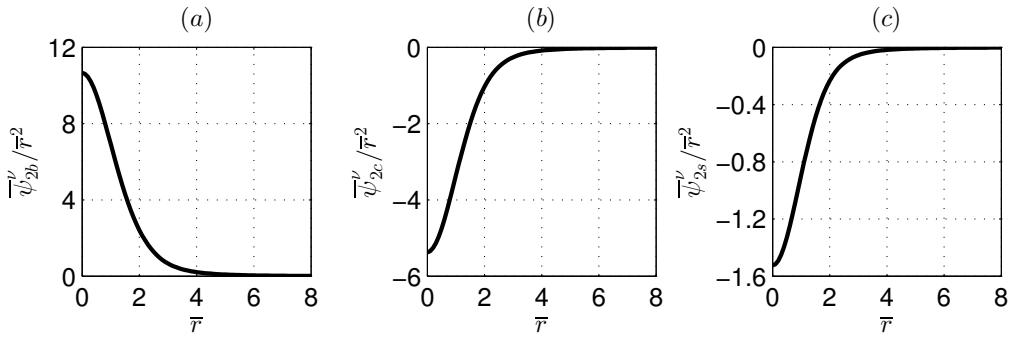

Figure C.1: Streamfunctions $\bar{\psi}^{\nu}_{2b}$ (a), $\bar{\psi}^{\nu}_{2c}$ (b), and $\bar{\psi}^{\nu}_{2s}$ (c) rescaled by $\bar{r}^2$ as functions of $\bar{r}$.

Bibliography

Augier, P.
2011. *Turbulence en milieu stratifié, étude des mécanismes de la cascade*. PhD thesis, Ecole polytechnique.

Augier, P. and P. Billant
2011. Onset of secondary instabilities on the zigzag instability in stratified fluids. *J. Fluid Mech.*, 682:120–131.

Augier, P., J.-M. Chomaz, and P. Billant
2012. Spectral analysis of the transition to turbulence from a dipole in stratified fluid. *J. Fluid Mech.*, 713:86–108.

Bartello, P.
2010. Quasigeostrophic and stratified turbulence in the atmosphere. In *IUTAM Symposium on Turbulence in the Atmosphere and Oceans*, Pp. 117–130. Springer Netherlands.

Bartello, P., O. Métais, and M. Lesieur
1994. Coherent structures in rotating three-dimensional turbulence. *J. Fluid Mech.*, 273:1–29.

Bartello, P. and S. M. Tobias
2013. Sensitivity of stratified turbulence to the buoyancy Reynolds number. *J. Fluid Mech.*, 725:1–22.

Beckers, M., R. Verzicco, H. J. H. Clercx, and G. J. F. V. Heijst
2001. Dynamics of pancake-like vortices in a stratified fluid: experiments, model and numerical simulations. *J. Fluid Mech.*, 433:1–27.

Billant, P.
2010. Zigzag instability of vortex pairs in stratified and rotating fluids. Part 1. General stability equations. *J. Fluid Mech.*, 660:354–395.

Billant, P. and J.-M. Chomaz
2000a. Experimental evidence for a new instability of a vertical columnar vortex pair in a strongly stratified fluid. *J. Fluid Mech.*, 418:167–188.

Billant, P. and J.-M. Chomaz
2000b. Theoretical analysis of the zigzag instability of a vertical columnar vortex pair in a strongly stratified fluid. *J. Fluid Mech.*, 419:29–63.

Billant, P. and J.-M. Chomaz
2000c. Three-dimensional stability of a vertical columnar vortex pair in a stratified fluid. *J. Fluid Mech.*, 419:65–91.

Billant, P. and J.-M. Chomaz
2001. Self-similarity of strongly stratified inviscid flows. *Phys. Fluids*, 13:1645–1651.

Billant, P., A. Deloncle, J.-M. Chomaz, and P. Otheguy
2010. Zigzag instability of vortex pairs in stratified and rotating fluids. Part 2. Analytical and numerical analyses. *J. Fluid Mech.*, 660:396–429.

Boulanger, N., P. Meunier, and S. Le Dizès
2007. Structure of a stratified tilted vortex. *J. Fluid Mech.*, 583:443–458.

Boulanger, N., P. Meunier, and S. Le Dizès
2008. Tilt-induced instability of a stratified vortex. *J. Fluid Mech.*, 596:1–20.

Brethouwer, G., P. Billant, E. Lindborg, and J.-M. Chomaz
2007. Scaling analysis and simulation of strongly stratified turbulent flows. *J. Fluid Mech.*, 585:343–368.

Charney, J. G.
1971. Geostrophic turbulence. *J. Atmos. Sci.*, 28:1087–1095.

Cho, J. Y. N. and E. Lindborg
2001. Horizontal velocity structure functions in the upper troposphere and lower stratosphere: 1. observations. *Journal of Geophysical Research: Atmospheres*, 106:10223–10232.

Cushman-Roisin, B. and J.-M. Beckers
2011. *Introduction to Geophysical Fluid Dynamics: Physical and Numerical Aspects.* Academic Press.

Delbende, I.
1998. *Réponse impulsionnelle dans les jets tournants et les sillages plans : analyse spatio-temporelle par simulation numérique directe.* PhD thesis, Ecole polytechnique.

Deloncle, A.
2007. *Three-dimensional instabilities in stratified fluids.* PhD thesis, Ecole polytechnique.

Deloncle, A.
2014. *NS3D v2.14: user's manual.* Ecole polytechnique.

Deloncle, A., P. Billant, and J.-M. Chomaz
2008. Nonlinear evolution of the zigzag instability in stratified fluids: a shortcut on the route to dissipation. *J. Fluid Mech.*, 599:299–239.

DeMaria, M.
1996. The effect of vertical shear on tropical cyclone intensity change. *J. Atmos. Sci.*, 53:2076–2088.

Deusebio, E., G. Boffetta, E. Lindborg, and S. Musacchio
2014. Dimensional transition in rotating turbulence. *Phys. Rev. E*, 90:023005.

Deusebio, E., A. Vallgren, and E. Lindborg
2013. The route to dissipation in strongly stratified and rotating flows. *J. Fluid Mech.*, 720:66–103.

Drazin, P. G.
1970. Kelvin-helmholtz instability of finite amplitude. *J. Fluid Mech.*, 42:321–335.

Ferrari, R. and C. Wunsch
2009. Ocean circulation kinetic energy: Reservoirs, sources, and sinks. *Annual Review of Fluid Mechanics*, 41:253–282.

Frank, W. M. and E. A. Ritchie
1999. Effects of environmental flow upon tropical cyclone structure. *Mon. Wea. Rev.*, 127:2044–2061.

Gage, K. S.
1979. Evidence for a $k^{-5/3}$ law inertial range in mesoscale two-dimensional turbulence. *J. Atmos. Sci.*, 36:1950–1954.

Gill, A.
1982. *Atmosphere-Ocean Dynamics*. Academic Press.

Godeferd, F. S. and C. Staquet
2003. Statistical modelling and direct numerical simulations of decaying stably stratified turbulence. Part 2. Large-scale and small-scale anisotropy. *J. Fluid Mech.*, 486:115–159.

Godoy-Diana, R., J.-M. Chomaz, and P. Billant
2004. Vertical length scale selection for pancake vortices in strongly stratified viscous fluids. *J. Fluid Mech.*, 504:229–238.

Herring, J. R. and O. Métais
1989. Numerical experiments in forced stably stratified turbulence. *J. Fluid Mech.*, 202:97–115.

Howard, L. N.
1961. Note on a paper of John W. Miles. *J. Fluid Mech.*, 10:509–512.

Jones, S. C.
1995. The evolution of vortices in vertical shear. I: Initially barotropic vortices. *Quart. J. Roy. Meteor. Soc*, 121:821–851.

Jones, S. C.
2000a. The evolution of vortices in vertical shear. II: Large-scale asymmetries. *Quart. J. Roy. Meteor. Soc*, 126:3137–3159.

Jones, S. C.
2000b. The evolution of vortices in vertical shear. III: Baroclinic vortices. *Quart. J. Roy. Meteor. Soc*, 126:3161–3185.

Jones, S. C.
2004. On the ability of dry tropical-cyclone-like vortices to withstand vertical shear. *J. Atmos. Sci.*, 61:114–119.

Kolmogorov, A. N.
1941. The local structure of turbulence in incompressible viscous fluids for very large Reynolds numbers. *Compt. Rend. Acad. Sci. (USSR)*, 30:301–305.

Kraichnan, R. H.
1967. Inertial ranges in two-dimensional turbulence. *Phys. Fluids*, 10:1417–1423.

Kraichnan, R. H.
1971. Inertial-range transfer in two- and three-dimensional turbulence. *J. Fluid Mech.*, 47:525–535.

Le Dizès, S. and F. Laporte
2002. Theoretical predictions for the elliptical instability in a two-vortex flow. *J. Fluid Mech.*, 471:169–201.

Lesieur, M.
2008. *Turbulence in Fluids*. Springer Netherlands.

Lilly, D. K.
1969. Numerical simulation of two-dimensional turbulence. *Phys. Fluids*, 12:240–249.

Lilly, D. K.
1983. Stratified turbulence and the mesoscale variability of the atmosphere. *J. Atmos. Sci.*, 40:749–761.

Lilly, D. K., G. Bassett, K. Droegemeier, and P. Bartello
1998. Stratified turbulence in the atmospheric mesoscales. *Theoretical and Computational Fluid Dynamics*, 11:139–153.

Lindborg, E.
1999. Can the atmospheric kinetic energy spectrum be explained by two-dimensional turbulence? *J. Fluid Mech.*, 388:259–288.

Lindborg, E.
2005. The effect of rotation on the mesoscale energy cascade in the free atmosphere. *Geophysical Research Letters*, 32.

Lindborg, E.
2006. The energy cascade in a strongly stratified fluid. *J. Fluid Mech.*, 550:207–242.

Lindborg, E. and G. Brethouwer
2007. Stratified turbulence forced in rotational and divergent modes. *J. Fluid Mech.*, 586:83–108.

Lumley, J. L.
1964. The spectrum of nearly inertial turbulence in a stably stratified fluid. *J. Atmos. Sci.*, 21:99–102.

Majda, A. J. and M. J. Grote
1997. Model dynamics and vertical collapse in decaying strongly stratified flows. *Phys. Fluids*, 9:2932–2940.

Marshall, J. S. and B. Parthasarathy
1993. Tearing of an aligned vortex by a current difference in two-layer quasi-geostrophic flow. *J. Fluid Mech.*, 255:157–182.

Métais, O., P. Bartello, E. Garnier, J. Riley, and M. Lesieur
1996. Inverse cascade in stably stratified rotating turbulence. *Dynamics of Atmospheres and Oceans*, 23:193–203.

Métais, O. and J. R. Herring
1989. Numerical simulations of freely evolving turbulence in stably stratified fluids. *J. Fluid Mech.*, 202:117–148.

Miles, J. W.
1961. On the stability of heterogeneous shear flows. *J. Fluid Mech.*, 10:496–508.

Molemaker, M., J. McWilliams, and I. Yavneh
2005. Baroclinic instability and loss of balance. *Journal of Physical Oceanography*, 35:1505–1517.

Moore, D. W. and P. G. Saffman
1975. The instability of a straight vortex filament in a strain field. *Proceedings of the Royal Society of London. Series A, Mathematical and Physical Sciences*, 346(1646):413–425.

Müller, P., J. McWilliams, and J. Molemaker
2005. Routes to dissipation in the ocean: The 2D/3D turbulence conundrum. *Marine Turbulence*, Pp. 397–405.

Orszag, S. A.
1971. On the elimination of aliasing in finite-difference schemes by filtering high-wavenumber components. *J. Atmos. Sci.*, 28:1074–1074.

Otheguy, P., P. Billant, and J.-M. Chomaz
2007. Theoretical analysis of the zigzag instability of a vertical co-rotating vortex pair in a strongly stratified fluid. *J. Fluid Mech.*, 584:103–123.

Otheguy, P., J.-M. Chomaz, and P. Billant
2006. Elliptic and zigzag instabilities on co-rotating vertical vortices in a stratified fluid. *J. Fluid Mech.*, 553:253–272.

Park, Y.-G., J. A. Whitehead, and A. Gnanadeskian
1994. Turbulent mixing in stratified fluids: layer formation and energetics. *J. Fluid Mech.*, 279:279–311.

Päschke, E., P. Marschalik, A. Z. Owinoh, and R. Klein
2012. Motion and structure of atmospheric mesoscale baroclinic vortices: dry air and weak environmental shear. *J. Fluid Mech.*, 701:137–170.

Pedlosky, J.
1987. *Geophysical Fluid Dynamics*. Springer.

Pouquet, A. and R. Marino
2013. Geophysical turbulence and the duality of the energy flow across scales. *Phys. Rev. Lett.*, 111:234501.

Pradeep, D. S. and F. Hussain
2004. Effects of boundary condition in numerical simulations of vortex dynamics. *J. Fluid Mech.*, 516:115–124.

Reasor, P. D., M. T. Montgomery, and L. D. Grasso
2004. A new look at the problem of tropical cyclones in vertical shear flow: vortex resiliency. *J. Atmos. Sci.*, 61:3–22.

Rennich, S. C. and S. K. Lele
1997. Numerical method for incompressible vortical flows with two unbounded directions. *Journal of Computational Physics*, 137:101–129.

Riley, J. J. and S. M. deBruynKops
2003. Dynamics of turbulence strongly influenced by buoyancy. *Phys. Fluids*, 15:2047–2059.

Riley, J. J. and M.-P. Lelong
2000. Fluid motions in the presence of strong stable stratification. *Annual Review of Fluid Mechanics*, 32:613–657.

Riley, J. J. and E. Lindborg
2008. Stratified turbulence: A possible interpretation of some geophysical turbulence measurements. *J. Atmos. Sci.*, 65:2416–2424.

Riley, J. J., R. W. Metcalfe, and M. A. Weissman
1981. Direct numerical simulations of homogeneous turbulence in density-stratified fluids. In *American Institute of Physics Conference Series*, volume 76 of *American Institute of Physics Conference Series*, Pp. 79–112.

Smith, R. K., W. Ulrich, and G. Sneddon
2000. On the dynamics of hurricane-like vortices in vertical-shear flows. *Quart. J. Roy. Meteor. Soc*, 126:2653–2670.

Smyth, W. D. and J. N. Moum
2000. Length scales of turbulence in stably stratified mixing layers. *Phys. Fluids*, 12:1327–1342.

Sutyrin, G. G. and Y. G. Morel
1997. Intense vortex motion in a stratified fluid on the beta-plane: an analytical theory and its validation. *J. Fluid Mech.*, 336:203–220.

Thorpe, S. A.
1968. A method of producing a shear flow in a stratified fluid. *J. Fluid Mech.*, 32:693–704.

Vallgren, A., E. Deusebio, and E. Lindborg
2011. Possible explanation of the atmospheric kinetic and potential energy spectra. *Phys. Rev. Lett.*, 107:268501.

Vallis, G. K.
2006. *Atmospheric and Oceanic Fluid Dynamics*. Cambridge, U.K.: Cambridge University Press.

Van Dyke, M.
1982. *An album of Fluid Motion*. Parabolic Press.

Vandermeirsch, F., Y. Morel, and G. Sutyrin
2001. The net advective effect of a vertically sheared current on a coherent vortex. *J. Phys. Oceanogr.*, 31:2210–2225.

Vandermeirsch, F., Y. Morel, and G. Sutyrin
2002. Resistance of a coherent vortex to a vertical shear. *J. Phys. Oceanogr.*, 32:3089–3100.

Waite, M. L.
2013. The vortex instability pathway in stratified turbulence. *J. Fluid Mech.*, 716:1–4.

Waite, M. L. and P. Bartello
2004. Stratified turbulence dominated by vortical motion. *J. Fluid Mech.*, 517:281–308.

Waite, M. L. and P. K. Smolarkiewicz
2008. Instability and breakdown of a vertical vortex pair in a strongly stratified fluid. *J. Fluid Mech.*, 606:239–273.

Résumé détaillé de la thèse

Contexte Cette thèse étudie un processus de décorrélation d'un tourbillon initialement rectiligne par un écoulement externe cisaillé sinusoïdalement selon la verticale, dans un fluide stratifié. Il a été proposé qu'un tel mécanisme devrait déclencher des instabilités de cisaillement et ainsi contribuer à la production de petites échelles en turbulence fortement stratifiée, que l'on rencontre dans l'atmosphère et les océans dans une gamme d'échelles où la force de Coriolis est négligeable.

Plus précisément, Lilly (1983) a émis l'idée qu'en présence d'une forte stratification, toute structure cohérente soumise à un champ de cisaillement de la forme $U(z)$, avec z la coordonnée verticale, devrait présenter un cisaillement vertical de vitesse horizontale augmentant avec le temps en raison de l'advection différentielle selon la verticale. En d'autres termes, la forte stratification tend à "scinder" l'écoulement en un empilement de couches dont les dynamiques sont indépendantes. En effet, la conjecture de Lilly suppose que la structure est advectée sans génération de vitesse verticale et que tout éventuel couplage vertical de son champ de vitesse est négligé. L'équation mathématique modélisant cette dynamique s'écrit :

$$\frac{\partial \boldsymbol{u}_h}{\partial t} = -U(z)\frac{\partial \boldsymbol{u}_h}{\partial x}$$

où l'on a supposé que l'écoulement ambiant est porté par un axe $\boldsymbol{e}_x$ associé à la coordonnée x, avec $\boldsymbol{u}_h$ le champ de vitesse (horizontal) de la structure considérée. La solution est

$$\boldsymbol{u}_h(x, y, z, t) = \boldsymbol{u}_{h0}(x - U(z)t, y, z)$$

avec $\boldsymbol{u}_{h0}$ le champ de vitesse $\boldsymbol{u}_h$ initial, si bien que le cisaillement vertical de vitesse horizontale

$$\frac{\partial \boldsymbol{u}_h}{\partial z} = \frac{\partial \boldsymbol{u}_{h0}}{\partial z} - t\frac{\mathrm{d}U}{\mathrm{d}z}\frac{\partial \boldsymbol{u}_{h0}}{\partial x}$$

croît algébriquement avec le temps t. On s'attend donc à une décroissance continue du nombre de Richardson, celui-ci étant inversement proportionnel au carré du cisaillement vertical de vitesse horizontale. La transition sous le seuil critique $1/4$, condition nécessaire au déclenchement d'une instabilité de cisaillement, devrait ainsi être inconditionnelle et l'instabilité devrait donc se développer après un certain laps de temps dépendant notamment de l'intensité de l'advection U.

Ce mécanisme, bien que fréquemment invoqué dans les études de turbulence fortement stratifiée, n'a pourtant jamais été testé en pratique. Cette thèse vise à le caractériser dans le cas d'un écoulement modèle comprenant un tourbillon de Lamb-Oseen soumis à un écoulement ambiant de profil de vitesse $U(z) = U_S \sin(k_z z)$.

Résultats La première partie est dédiée à l'analyse des évolutions des énergie cinétique et enstrophie totales du tourbillon calculées au moyen de Simulations Numériques

Directes (DNS), en fonction des paramètres de contrôle. Cette étude montre que la dynamique est différente de celle des écoulements libres non cisaillés : du fait de la présence de l'écoulement ambiant, la condition de saturation entre les termes d'étirement et de dissipation dans le bilan d'enstrophie globale implique que l'enstrophie maximale du tourbillon sature comme $Re^{2/3}$, Re étant le nombre de Reynolds, et non pas proportionnellement à Re comme pour les écoulements sans cisaillement ambiant. Néanmoins, cette condition de saturation ne rend pas compte de l'effet observé de la stratification.

Afin de comprendre cet effet, la dynamique locale du tourbillon a fait l'objet de deux analyses asymptotiques présentées dans une deuxième partie. Une première étude pour temps courts prouve que la réponse initiale du tourbillon est non-hydrostatique quelle que soit la stratification. Il est également démontré que, de manière remarquable, la stratification n'influence en réalité que très peu la dynamique initiale. Une deuxième analyse pour grande longueur d'onde fournit les équations qui décrivent l'évolution de la vitesse angulaire du tourbillon et des déformations de son axe. L'excitation d'ondes internes au début de l'évolution est à l'origine du régime non-hydrostatique initial. Le tourbillon est principalement advecté dans la direction du cisaillement ambiant mais aussi perpendiculairement du fait de son auto-induction. Sa vitesse angulaire décroît à cause d'effets dynamique et visqueux. La décroissance dynamique est dûe à un resserrement des lignes isopycnes dans le coeur du tourbillon, qui implique une atténuation de la vorticité verticale afin que la vorticité potentielle se conserve. Enfin, un champ de vitesse associé à un mode azimuthal $m = 2$ est généré, indiquant que le tourbillon devient légèrement elliptique.

Dans une troisième et dernière partie, des DNS révèlent que l'instabilité de cisaillement se développe seulement lorsque la stratification est modérée et la longueur d'onde du cisaillement ambiant suffisamment petite. Les résultats numériques sont comparés aux prédictions asymptotiques. Les déformations du tourbillon sont prédites avec précision. Les ondes internes influencent fortement le mouvement du tourbillon au début de l'évolution mais leur effet s'estompe rapidement. L'axe du tourbillon ne se déforme pas de façon purement sinusoïdale : il subit une torsion verticale. Par ailleurs, les évolutions du cisaillement vertical de vitesse horizontale et du gradient vertical de flottabilité sont prédites de manière fine et exhaustive par l'analyse asymptotique pour grande longueur d'onde lorsque le nombre de Froude est petit, c'est-à-dire dans la limite fortement stratifiée. Le nombre de Richardson asymptotique admet un minimum qui n'est pratiquement jamais inférieur au seuil critique 1/4 nécessaire au déclenchement de l'instabilité de cisaillement. La saturation du cisaillement vertical est dûe au déclin accéléré du tourbillon dans les régions où le cisaillement ambiant est maximal.

Conclusions Les résultats asymptotiques dans la limite des grandes longueurs d'onde permettent d'aboutir à une expression analytique du nombre de Richardson local, qui permet de le prédire finement lorsque la stratification est forte. On démontre, grâce à cette expression, que ce nombre ne peut être inférieur au seuil critique 1/4 nécessaire pour que l'instabilité de cisaillement se développe, à moins que l'écoulement ambiant ne soit lui-même instable. Ce résultat est cohérent avec les simulations numériques, celles-ci n'ayant jamais permis d'observer l'instabilité pour de petits nombres de Froude.

Ce comportement est lié à la saturation du cisaillement vertical de vitesse horizontale, qui résulte du déclin accéléré du tourbillon dans les régions où $|\mathrm{d}U/\mathrm{d}z|$ est maximal. Cette saturation entre en contradiction directe avec l'hypothèse formulée

par Lilly. On soulignera que la décroissance dynamique de la vitesse angulaire du tourbillon suffit à provoquer une saturation des cisaillements verticaux.

Au vu de ces résultats pour un tourbillon, il est conclu que les processus de décorrélation d'une structure cohérente par un champ de cisaillement ambiant semblent insuffisants, en fluide fortement stratifié, pour déclencher des instabilités de cisaillement, et donc pour participer à la génération de petites échelles, contrairement à la conjecture de Lilly (1983).

université PARIS-SACLAY
ÉCOLE DOCTORALE
Sciences mécaniques et énergétiques, matériaux et géosciences (SMEMAG)

Titre : Décorrélation verticale d'un tourbillon soumis à un champ de cisaillement dans un fluide fortement stratifié

Mots clés : décorrélation, tourbillon, cisaillement, stratification

Résumé : Cette thèse étudie la décorrélation verticale d'un tourbillon initialement rectiligne par un écoulement cisaillé sinusoïdalement dans un fluide stratifié. Il a été proposé qu'un tel mécanisme devrait déclencher des instabilités de cisaillement et ainsi contribuer à la production de petites échelles en turbulence fortement stratifiée, présente dans l'atmosphère et les océans dans une gamme d'échelles où la force de Coriolis est négligeable.
La première partie étudie les évolutions des énergies et enstrophie totales du tourbillon calculées au moyen de Simulations Numériques Directes (DNS). La dynamique est différente de celle des écoulements libres non cisaillés : du fait de la présence de l'écoulement ambiant, la condition de saturation entre les termes d'étirement et de dissipation dans le bilan d'enstrophie globale implique que l'enstrophie maximale du tourbillon est proportionnelle au nombre de Reynolds à la puissance 2/3. Néanmoins, cette condition de saturation ne rend pas compte de l'effet observé de la stratification.
Afin de l'expliquer, la dynamique locale a été étudiée théoriquement dans une deuxième partie pour temps courts ou grande longueur d'onde. Cette dernière analyse asymptotique fournit les équations d'évolution de la vitesse angulaire du tourbillon et des déformations de son axe. On montre principalement que la vitesse angulaire décroît à cause d'effets dynamique et visqueux. La décroissance dynamique est dûe à un resserrement des lignes isopycnes dans le coeur du tourbillon, qui implique une atténuation de la vorticité verticale afin que la vorticité potentielle se conserve.
Dans une troisième partie, des DNS révèlent que l'instabilité de cisaillement apparaît seulement lorsque la stratification est modérée. Les évolutions du cisaillement vertical de vitesse horizontale et du gradient vertical de flottabilité sont finement prédites par l'analyse asymptotique lorsque la stratification est forte. Le nombre de Richardson asymptotique est toujours supérieur au seuil critique 1/4 nécessaire au déclenchement de l'instabilité de cisaillement. La saturation du cisaillement vertical est dûe au déclin accéléré du tourbillon dans les régions où le cisaillement ambiant est maximal.
Ces résultats suggèrent que l'instabilité de cisaillement est difficilement déclenchée par des processus de décorrélation dans les écoulements fortement stratifiés, contredisant ainsi les conjectures précédemment formulées dans la littérature.

Title : Vertical decorrelation of a vortex by a strongly stratified shear flow

Keywords : decorrelation, vortex, shear, stratification

Abstract : This thesis studies the vertical decorrelation of an initially straight vortex by an ambient sinusoidal shear flow in a stratified fluid. It has been conjectured that such process should trigger shear instabilities and, as such, contribute to the generation of small scales in strongly stratified turbulence, which is encountered in the atmosphere and the oceans in an intermediate range of scales where Coriolis effects are negligible.
The first part analyses the evolutions of the total energies and enstrophy of the vortex in Direct Numerical Simulations (DNS). The dynamics differs from free unsheared flows: because of the presence of the ambient shear flow, the balance between stretching and dissipation terms in the global enstrophy budget implies that the maximum enstrophy of the vortex is proportional to the Reynolds number to the power 2/3. However, such simplified balance does not account for the observed effect of the stratification.
Thus, the local dynamics has been investigated theoretically in a second part for short time or long-wavelength. The latter asymptotic analysis provides the governing equations for the evolution of the angular velocity of the vortex and the deformations of its axis. We mainly show that the angular velocity decays because of dynamic and viscous effects. The dynamic decay results from the squeezing of the isopycnals in the vortex core which implies a decrease of the vertical vorticity to conserve potential vorticity.
In a third part, the DNS show that the shear instability is only triggered for a moderate stratification. The evolutions of the vertical shear of horizontal velocity and of the vertical buoyancy gradient are finely captured by the asymptotics in the strongly stratified limit. The asymptotic Richardson number always remains larger than the critical threshold 1/4 necessary for the development of the shear instability. The saturation of the vertical shear is due to the accelerated decay of the vortex in the regions of maximum ambient shear.
These results suggest that the shear instability is not easily triggered by decorrelation processes in strongly stratified flows in contradiction with previous conjectures.

Université Paris-Saclay
Espace Technologique / Immeuble Discovery
Route de l'Orme aux Merisiers RD 128 / 91190 Saint-Aubin, France